UNIVERSITÀ DEGLI STUDI DI PADOVA

Sede Amministrativa: **UNIVERSITÀ DEGLI STUDI DI PADOVA**
DIPARTIMENTO DI FISICA TECNICA

SCUOLA DI DOTTORATO DI RICERCA IN INGEGNERIA INDUSTRIALE
INDIRIZZO: FISICA TECNICA
CICLO XXI

SCAMBIO TERMICO E FLUIDODINAMICA DURANTE I DEFLUSSI BIFASE E MONOFASE SU SUPERFICI ESTESE E IN MICROGEOMETRIE

TWO-PHASE AND SINGLE-PHASE HEAT TRANSFER AND FLUID FLOW THROUGH ENHANCED SURFACES AND IN MICROGEOMETRIES

Direttore della Scuola: Ch.mo Prof. Paolo Francesco Bariani

Supervisore: Ch.mo Prof. Luisa Rossetto

Dottorando: Simone Mancin

"... e veramente parmi che saria
cosa ridicola il credere,
che allora comincino ad esser
le cose della natura,
quando noi cominciamo
a scoprirle ed intenderle.
Ma quando pure l'interder degl'uomini
dovesse esser cagione
della esistenza delle cose, bisognerebbe,
o che le medesime cose fussero
ed insieme non fussero
(fussero, per quelli che le intendono;
e non fussero,
per quelli che non le intendono),
o vero per l'intender di pochi,
ed anco di un solo,
bastasse per farle essere."

Galileo Galilei, Opere XI, 108

"La Scienza ha radici nell'Immanente ma porta l'uomo verso il Trascendente"

Giovanni Paolo II

...A chi mi ha Amato fin dal Primo giorno...

...A chi ha imparato ad Amarmi...

...A chi, oggi, mi Ama...

S.M.

PREFACE

In the last decades, heat transfer issues have become more and more important and strategic in several different daily life and industrial applications. The continuous improvement of electronic devices and the ecological issues linked to refrigeration and air conditioning have stimulated applied researchers to find new technological solutions to better the heat transfer efficiency of the existing systems and developing new ones.

The enhancement of the heat transfer efficiency has been analyzed during this Ph. D. work, where two important technological solutions created to improve two-phase and single-phase heat transfer have been experimentally studied.

The condensation phenomenon is involved in several industrial and home applications, since every vapour compression and absorption refrigeration system or air conditioning machine is implemented with a condenser. Improving condenser efficiency contributes to improve system efficiency too, saving energy and respecting the environment. Condensation heat transfer efficiency can be enhanced using a microfin tube, a device which has been used for air conditioning and refrigeration applications since the eighties.

In the first part of this Ph. D. thesis, the two-phase heat transfer coefficients and pressure drops measured during the condensation of R410A inside a microfin tube will be presented and then discussed. With this work, a new model useful for the design of this kind of air or water cooled condensers with microfin tubes is suggested. This model, which permits to determine the condensation heat transfer coefficient inside microfin tubes, has been developed using a wide experimental heat transfer database. The most important results related to this model will be presented at the end of this first part of the thesis.

The second part of the thesis documents the design, development and building of a new test facility for the thermal-fluid-dynamic characterization of several different enhanced surfaces and microgeometries during single-phase air forced convection. This new experimental test rig has been designed to permit the study and development of new enhanced heat transfer surfaces for electronics cooling applications which allow to overcome the upper limits of air cooling.

Since air is the safest and cheapest working fluid for electronics cooling applications, there is a great demand for new heat transfer surfaces to improve its poor heat transfer properties. Metal foams have been suggested as alternative air heat transfer surfaces, but their effective

heat transfer and fluid flow behaviours have not been deeply investigated experimentally. In this second part of the work, several aluminum metal foams have been acquired and then experimentally characterized using the new test facility. First of all, their most important geometrical characteristics have been measured: the results will be reported in a dedicated chapter.

The global heat transfer coefficients and the pressure drops measured during single-phase air forced convection will be reported and discussed in order to understand the effective heat transfer capabilities of these new enhanced surfaces. Finally, the experimental results found for the aluminum foams will be compared with those obtained for a traditional finned surface chosen as a benchmark solution for electronics cooling applications.

SOMMARIO

Lo scambio termico tra due fluidi o tra un fluido e una superficie, sia esso monofase o bifase, è profondamente legato alle caratteristiche geometriche delle superfici di scambio con le quali i fluidi stessi sono in contatto. Aumentare la superficie di scambio termico significa, in generale, incrementare lo scambio termico globale. Se poi questa superficie viene sviluppata per migliorare l'efficienza dello scambio termico, le prestazioni possono crescere ulteriormente. Il raffreddamento di componenti elettronici, la refrigerazione e il condizionamento dell'aria richiedono scambiatori di calore sempre più efficienti e compatti, pertanto lo sviluppo di nuove superfici di scambio termico risulta essere un obiettivo fondamentale della ricerca.

In questo lavoro di tesi sono stati affrontati, sia sperimentalmente che analiticamente, due argomenti connessi allo scambio termico su superfici estese. In particolare, si sono studiati la condensazione all'interno di tubi micro-alettati e la convezione forzata di aria su schiume metalliche e su superfici alettate tradizionali. Per quanto riguarda lo scambio termico bifase, sono stati misurati i coefficienti di scambio termico e le perdite di carico durante la condensazione di R410A all'interno di un tubo micro-alettato, alla temperatura di saturazione di 40 °C. Le prove sono state realizzate utilizzando l'impianto presente presso il Dipartimento di Fisica Tecnica dell'Università di Padova.

Successivamente, utilizzando un database contenente più di 4000 dati sperimentali, è stato sviluppato un nuovo modello per la stima del coefficiente di scambio termico durante la condensazione di refrigeranti naturali e sintetici all'interno di tubi micro-alettati.

Con riferimento allo scambio termico monofase, un nuovo impianto sperimentale è stato sviluppato, progettato e costruito presso il Dipartimento di Fisica Tecnica dell'Università di Padova. Questo apparato permette di eseguire accurate misure di scambio termico e perdite di carico durante la convezione forzata di aria attraverso superfici estese, quali tradizionali superfici alettate, schiume metalliche, microgeometrie, ecc. L'impianto sperimentale è stato calibrato testando una superficie alettata tradizionale per il raffreddamento di componenti elettronici. Successivamente, sono stati misurati i coefficienti di scambio e le perdite di carico di cinque schiume di alluminio durante il deflusso di aria. Tutti i provini sono stati riscaldati elettricamente imponendo differenti flussi temici tra 150 W e 400 W. I risultati sperimentali sono stati confrontati con quelli ottenuti per la superficie alettata tradizionale.

ABSTRACT

The heat transfer between two fluids or between a fluid and a surface, during both single-phase and two-phase flow, is intimately linked to the geometrical characteristic of the heat transfer surface involved. Generally speaking, if the heat transfer area increases, the global heat transfer also increases, but if the surface is developed to improve heat transfer, the overall performance can be higher.

Compact and efficient heat exchangers and heat sinks are more and more demanded for electronics cooling applications, refrigeration and air conditioning systems. For this reason, the development of new enhanced surfaces is a critical issue of thermal research.

In this Ph. D. thesis, two arguments connected with enhanced heat transfer surfaces have been experimentally and analytically studied. In particular, the condensation of R410A inside a microfin tube and air forced convection through different enhanced surfaces have been analysed.

With respect to two-phase flow, the heat transfer coefficients and the pressure drops during the condensation of R410A at 40 °C of saturation temperature inside a microfin tube have been measured. The experimental analysis have been carried out at the Dipartimento di Fisica Tecnica of the University of Padova.

Using a database of 4000 experimental data points, a new correlation for the computation of the heat transfer coefficient during the condensation of several natural and synthetic refrigerants inside different enhanced microfinned tubes has been developed.

With respect to single-phase flow, a new experimental test rig has been developed, designed and built at the laboratory of the Dipartimento di Fisica Tecnica of the University of Padova. This test rig allows to carry out accurate heat transfer and pressure drop measurements during air forced convection through different enhanced surfaces, such as traditional finned surfaces, metal foams and microgeometries, etc.

The apparatus has been calibrated by testing a traditional finned surface for electronics cooling applications. Then, the heat transfer coefficients and the pressure drops during air forced convection through five different aluminum foams have been measured. All tested samples have been heated by imposing different heat fluxes, which have been varied between 150 W and 400 W. The experimental results have been compared with those obtained for the traditional finned surface.

Table of Contents

List of Figures

List of Tables

1

Part 1:

Two Phase Enhanced Heat Transfer

1.1 Introduction

1.1.1 Condensation Process

The condensation process is involved in a large number of daily and industrial applications such as air conditioning and refrigeration, electronics cooling systems, electric power plants and more others. Moreover, the condensation phenomenon is a natural event that can be observed in foggy days or in steamed up windows.

When a vapour contacts a surface held below its saturation temperature, it condenses by releasing its latent energy. Thereupon, a condensate is formed, which, as a result of its contact with the wall surface, is subcooled, then a further vapour can condense upon the previous condensate.

Therefore, the condensation of vapour is always associated with a mass transfer, during which the vapour flows to the phase interface and is converted into the liquid phase [1].

In the presence of pure refrigerant, if the condensation process evolves at constant pressure, it is also isothermal.

Actual condensation can take place in very different ways: if the condensate forms a continuous film then one speaks of film condensation; the laminar flow Nusselt theory is used for calculation. Instead of in the film form, condensate can occur in the form of drops: this type of process is called dropwise condensation. As shown by Figure 1.Figure 1, the condensation process may occur in one of two ways, depending on the condition of the surface.

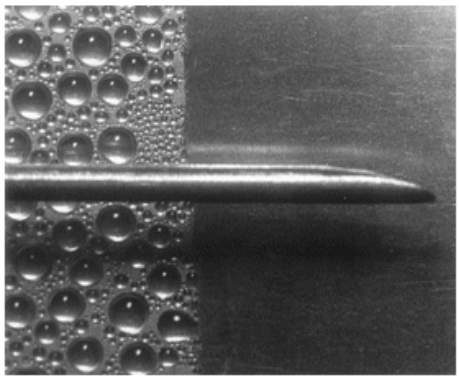

Figure 1. Steam at atmospheric pressure condensing on a copper plate. Dropwise condensation (on the left) and film condensation (on the right).(J. F. Welch and J. W. Westwater, Department of Chemical Engineering, University of Illinois, Urbana).

In the dropwise condensation not all of the cold surface is wet and the drops form in cracks, pits, and cavities on the surface and may grow and coalesce through condensation. Typically, more than 90% of the surface is covered by drops, ranging from those having a diameter of a few micrometers to agglomerations visible to the naked eye. This heat transfer mechanism is very efficient and the heat transfer rates may be more than an order of magnitude larger than those associated with film condensation.

Although it is desirable to achieve dropwise condensation in industrial applications, it is often difficult to maintain this condition. For this reason and because the convection heat transfer coefficients for film condensation are smaller than those for the dropwise case, condenser design calculations are often based on the assumption of film condensation [2].

Figure 2. Close-up of condensation plume from Mount St. Helens. USGS Photograph taken on December 19, 2006, by John Pallister.

Another vapour to liquid phase change possibility is the homogeneous condensation, in which the condensate is contained in the vapour phase (e.g. fog phenomena or cloud formation). In this mode the vapour has to be under its saturation temperature (Figure 2). Finally, the direct contact condensation involves a vapour that condenses over a cold liquid.

The thermal resistance can be present in the vapour phase or in the liquid phase or at the liquid-vapour interface.

In several civil and industrial applications regarding air conditioning and refrigeration, the condensation process takes place inside tubes. It is the binding choice for air cooled and evaporative condensers, but it is also used with water cooled condensers in reversible heat pumps and tube-in-tube condensers. It may be the best choice also in shell-and-tube heat exchangers in large equipments operated with high-pressure refrigerants [3].

In the intube condensation other important issues have to be considered. In fact, when a vapour condenses inside a tube, the vapour applies a shear stress to the liquid interface.

This force, combined with the gravity force, determines the two-phase flow pattern that influences the condensation heat transfer and pressure drops.

Among the possible two-phase flows, the liquid-vapour is the most interesting and complicated because the interface is deformable and a phase, that of gas, is compressible.

In the last decades, in-tube condensation has been widely studied by different research groups all over the world. This part of the work regards the experimental results concerning the heat transfer coefficients and the pressure drops measured during condensation inside a microfin tube.

The experimental data points have been collected in the laboratory of the Dipartimento di Fisica Tecnica of the University of Padova.

1.1.2 Microfin Tube

In the last thirty years it has become common to enhance condensation heat transfer inside horizontal tubes by employing finned surfaces. In fact, since Fujie et al. [4] invention, microfin tubes have received a lot of attention because they ensure a large heat transfer enhancement (80-180%) when compared to equivalent smooth tubes under the same operating conditions, with relatively small increase in pressure drop (20-80%) [5].

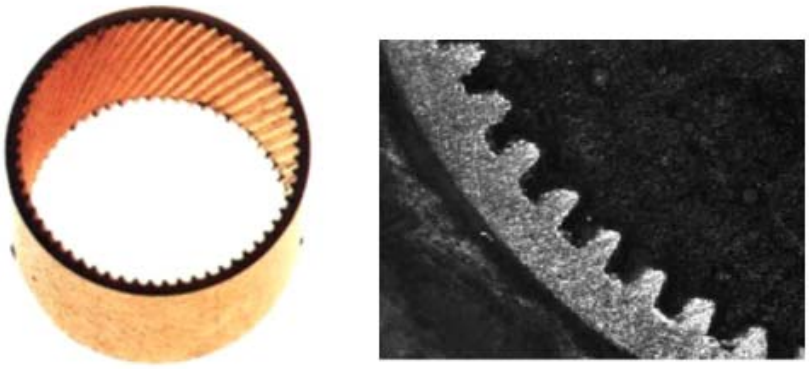

Figure 3. Two photos of a microfin tube.

Two photos of a microfin tube section are reported in Figure 3. Microfin tubes are typically made of copper and have an outside diameter from 4 to 15 mm, a single set of 50-70 fins with helix angle (β) from 6 to 30°, fin height (h) from 0.1 to 0.25 mm, triangular or trapezoidal fin shapes with an apex angle (γ) from 25 to 90° (Figure 4).

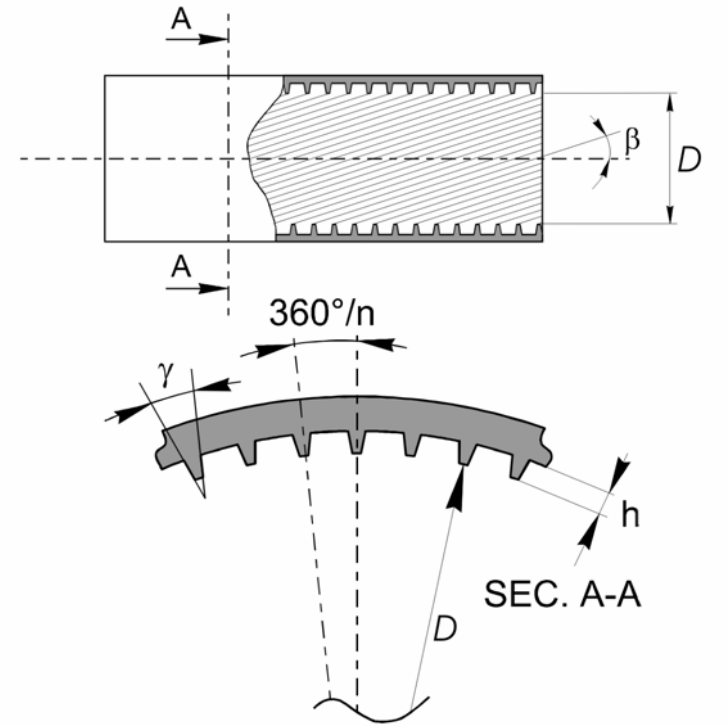

Figure 4. Two sections of a microfin tube: D internal fin tip diameter, β helical angle, γ apex angle and h fin height.

Heat transfer and pressure drop enhancements are partly due to the simple increase in the effective exchange area, and additionally to the turbulence induced in the liquid film by the micro-fins and to the surface tension effect on the condensate drainage [6].

In particular, in the open literature there is agreement that the mechanisms of heat transfer are intimately linked with the prevailing two-phase flow regime. During condensation in a microfin tube, the formed liquid is drained into the spiral groove by combined surface tension, centrifugal and gravity forces, while vapour shear forces drive the condensate in the downstream direction. The combination of these two actions promotes and extends the range of annular flow which is associated to heat transfer coefficients higher than those exhibit in the gravity-controlled flow pattern (stratified and wavy stratified flow, paragraph 1.1.4) [7, 8].

The main geometrical characteristics of the microfin tube tested in this experimental work are summarized in Table 1.

Table 1. Geometrical characteristic of the tested tube.

Microfin Tube	
Fin Tip Diameter, D	7.69 mm
Outside Diameter	11.6 mm
Number of Fins, n_g	60
Fin Height, h	0.23 mm
Apex Angle, γ	43°
Helix Angle, β	13°
$A_{MICROFIN}/A_{SMOOTH}$	1.8
A_{eff}	49.76 mm^2

1.1.3 R410A as Refrigerant

R410A is a quasi-azeotropic mixture of HFC-32-125 (50/50**%** by mass). R410A has recently been employed as an alternative working fluid for R22 in air conditioning equipment.

Table 2. R236ea, R134a and R410A thermophysical properties at t_{sat}=40 °C obtained using RefProp 7.0 by NIST [9].

Fluid	**R236ea**	**R134a**	**R410A**
t_{sat} [°C]	40	40	40
$p_{sat\,L}$ [MPa]	0.338	1.016	2.425
$p_{sat\,G}$ [MPa]	0.338	1.016	2.418
ρ_L [kg m^{-3}]	1375.1	1146.7	975.33
ρ_G [kg m^{-3}]	21.997	50.085	103.27
λ_L [Wm^{-1}K^{-1}] 10^{-3}	74.33	74.71	85.66
λ_G [Wm^{-1}K^{-1}]10^{-3}	15.72	15.44	19.51
μ_L [Pa s] 10^{-6}	313.01	161.45	98.076
μ_G [Pa s] 10^{-6}	11.353	12.373	16.012

Table 2 reports the thermophysical properties of three halogenated refrigerants at 40 °C of saturation temperature. R410A is a high pressure refrigerant because at t_{SAT}=40 °C it presents a pressure of 2.4 Mpa, while R134a and R236ea present a pressure of 1.0 MPa and 0.3 MPa respectively.

R410A is a fluid with liquid density and dynamic viscosity lower than those of R134a and R236ea, while its vapour density is higher than those of the other considered fluids. These thermophysical properties improve the fluid dynamic behaviour of R410A that exhibits two-phase pressure drops lower than those of R134a and R236ea.

Although R410A is classified as non azeotropic mixture, it presents a very low temperature glide. At 40 °C, the dew to bubble temperature difference is around 0.15 °C, so that it can be considered as a pure refrigerant.

Figure 5 plots the thermodynamic diagram for R410A.

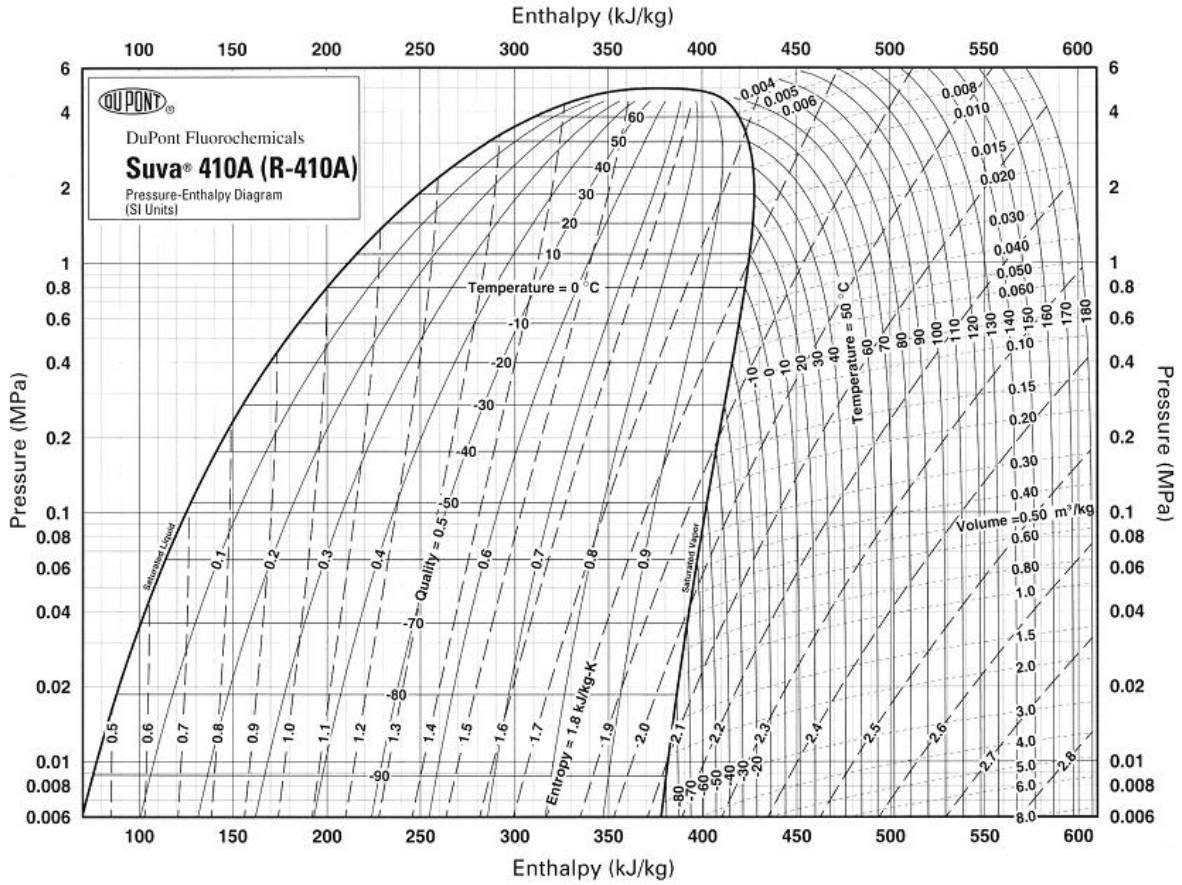

Figure 5. Thermodynamic p vs. h diagram for R410A.

1.1.4 Two-Phase Flow

Both condensation and vaporization involve a phase change process with heat transfer and pressure drop closely linked to the two-phase flow configurations.

During in-tube condensation, the vapour condenses all around the tube and is driven in the downstream direction by the gravity force resulting in an asymmetrically distribution of the phases.

The two-phase flow pattern is controlled by the equilibrium between the gravity force and the shear stress, this forces balance depends on the operating conditions, the working fluid and the geometrical characteristics of the tube.

Considering the refrigerant and the operating conditions, the mass flow rate, the vapour quality and the reduced pressure are the most important controlling parameters. The inner tube diameter, its inclination and its inside surface shape, too, are very important for the flow pattern definition.

Moreover, it is very difficult to analytically describe and predict the two-phase flow pattern during condensation or vaporization inside a tube. For this reason, several research groups have experimentally investigated the two-phase flow with different experimental techniques.

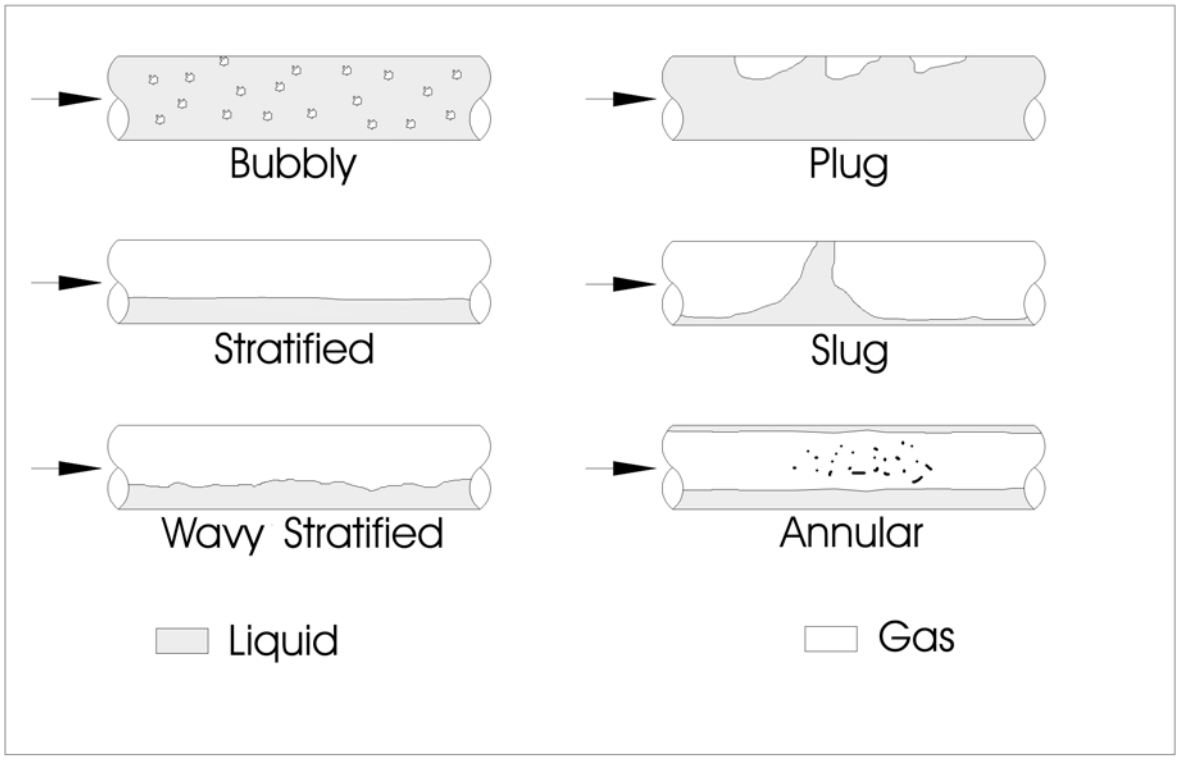

Figure 6. Observed two-phase flow patterns in a horizontal tube.

Figure 6 reports a drawing of the generally accepted flow patterns in a horizontal smooth tube, as described by Collier and Thome [10], these are:

Bubbly flow: the vapour phase is distributed in the form of discrete and uniform bubbles in a continuous liquid phase.

Plug flow: the gas bubbles are approximately as big as the pipe diameter and tend to travel in the upper half of the pipe.

Stratified flow: in this flow pattern the two phases flow separately with a relatively smooth interface. The pattern is controlled by the gravity force and it occurs at very low liquid and vapour velocities.

Wavy stratified flow: when the vapour velocity increases the liquid-gas interface becomes disturbed by waves travelling in the direction of the flow.

Slug flow: as the velocity increases, the shear stress at the interface promotes the waves growth and they reach the upper part of the tube forming slugs. These slugs are propagated along the channel at a high velocity.

Annular flow: A still higher vapour velocity produces a gas core with some entrained liquid droplets, while the liquid forms a film all around the perimeter of the tube wall. Due to the presence of the gravity force, the film thickness results to be asymmetrically distributed around the pipe and it is thicker at the base.

As highlighted before, flow regimes strongly influence the heat and momentum transfer processes, therefore any sound prediction of two phase heat transfer during condensation must be based on the analysis of the occurring flow pattern. This may be accomplished by recurring to an appropriate two-dimensional flow pattern map [11].

Although two-phase flow patterns in plain tubes have been largely studied, two-phase flow observations on enhanced tubes are few. Therefore, in open literature there are several flow pattern maps for plain tubes, among which those of Taitel and Dukler [12], Breber et al. [13] and Tandon et al. [14]. These maps report the transition boundaries between different flow regimes; unfortunately, most of them do not exhibit the same flow regime predictions at the same operative conditions. Recently, Cavallini et al. [11] have proposed a model for the prediction of condensation heat transfer coefficient inside smooth tubes. This model, based on 600 experimental data points, refers to a flow pattern map which is a composite of selected flow transition criteria proposed by other Authors.

In Figure 7 the map proposed by Cavallini et al. [11] for two-phase flow in a smooth tube is reported as an example of a flow regime diagram. In this map the non-dimensional gas velocity (J_G) is plotted against the Lockhart-Martinelli parameter (X_{tt}).
The adimensional gas velocity is defined as:

$$J_G = \frac{G \cdot x}{\sqrt{g \cdot D \cdot \rho_G \cdot (\rho_L - \rho_G)}} \qquad \textbf{Eq. 1}$$

While the Lockhart-Martinelli parameter can be calculated with Eq. 2:

$$X_{tt} = \left(\frac{1-x}{x}\right)^{0.9} \cdot \left(\frac{\rho_G}{\rho_L}\right)^{0.5} \cdot \left(\frac{\mu_L}{\mu_G}\right)^{0.1} \qquad \textbf{Eq. 2}$$

More recently, Cavallini et al. [15, 16] have proposed a simplified flow regime based heat transfer model in which the two-phase flow in a smooth tube is subdivided into two regions: one ΔT dependent and one ΔT independent (see Figure 8).

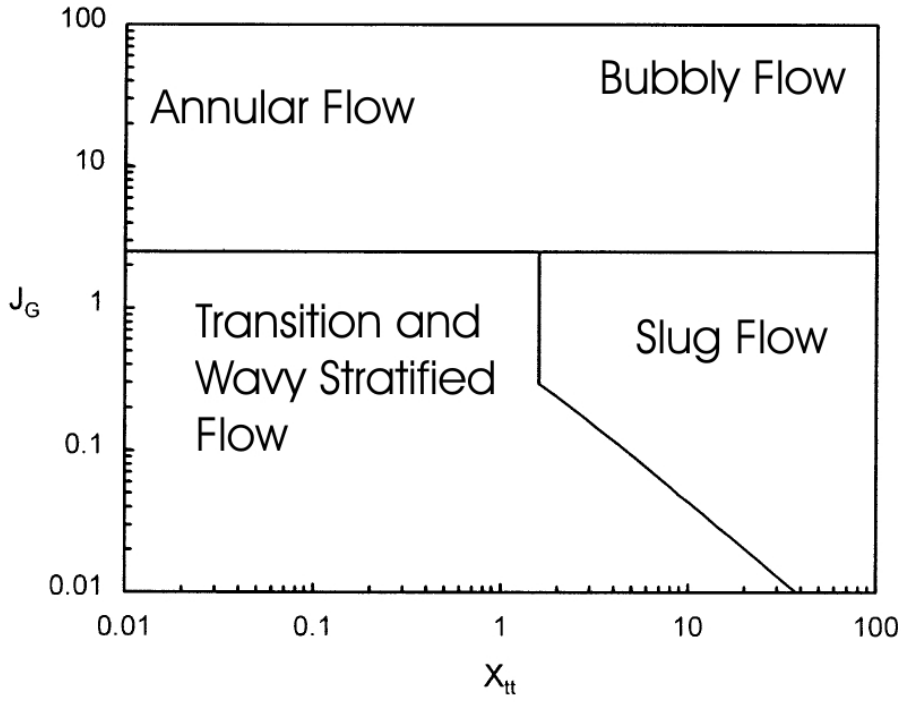

Figure 7. Cavallini et al. [10] flow regime map.

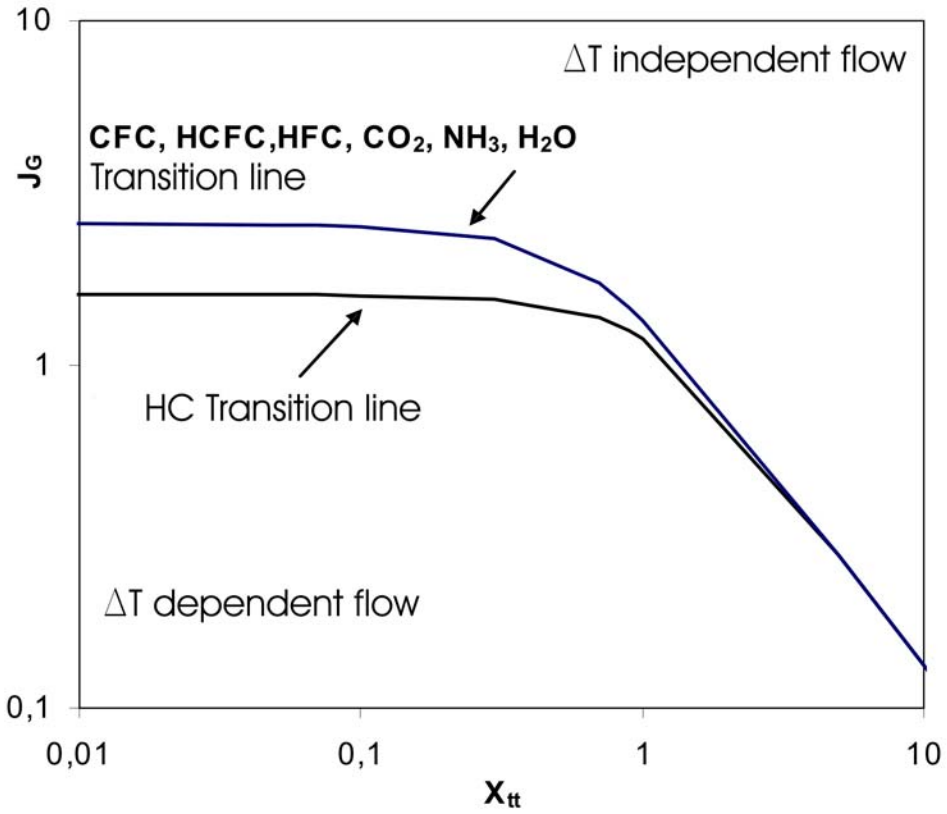

Figure 8. Cavallini et al. [15, 16] simplified flow regime map for a smooth tube.

Flow characteristics of condensate in a horizontal microfin tube would become more complex than in a smooth tube. This may be caused by the micro-fins: the condensate formed on a fin surface is drained into the spiral groove by combined surface tension and gravity forces, and then the condensate is driven through the groove by the vapour shear force in the downstream direction.

As for the smooth tube, the effect of gravity force may be negligible in comparison with the other two forces in a high vapour velocity region. In a low vapour mass quality region, on the other hand, the stratification of the condensate due to the gravity force may occur in the lower part of the tube.

Flow regimes observations inside microfin tubes have been conducted by Nozu et al. [17], Yu et al. [18], Censi et al. [19] and Doretti et al. [20].

Nozu et al. [17] reported a flow regime study carried out during condensation of R11 inside a microfin tube. From their observations, the Authors suggested that micro-fins play an important role in the condensation heat transfer mechanism.

Yu et al. [18] experimentally studied the two-phase heat transfer and flow pattern during the boiling of R134a in both microfin and plain tubes. The Authors tried to link the flow pattern to the heat transfer.

Considering a microfin tube, Yu et al. [18] found an early transition to annular flow in respect to a smooth tube. Moreover, during intermittent flow the local heat transfer coefficients measured in three cross-sectional locations, top, side and bottom, are relatively close. This behaviour confirms that in the intermittent flow the top and the side portions of the tube section are wet.

Doretti et al. [20] conducted a large amount of flow pattern visualizations during two-phase flow of several halogenated refrigerants, R410A, R134a and R236ea, inside both smooth and microfin tubes.

As one can see in Figure 9, the microfin tube promotes an early transition from the stratified flow to the annular flow. In fact, the transition occurs at $J_G \approx 1.5$ in a microfin tube, at $J_G \approx 2.5$ in a smooth tube. Furthermore, as it appears from the visualizations, the plain tube presents the wavy stratified flow pattern with negligible thickness of the liquid film in the upper part of the tube section.

Doretti et al. [20] verified that the visualization data points concerning transition were distributed along a line which started from J_G=1.5 and followed the trend predicted by the model presented in Cavallini et al. [15, 16].

Cavallini et al. [7] reported a complete experimental analysis on the two-phase condensation heat transfer inside a microfin tube, linking the flow pattern to the heat transfer enhancement.

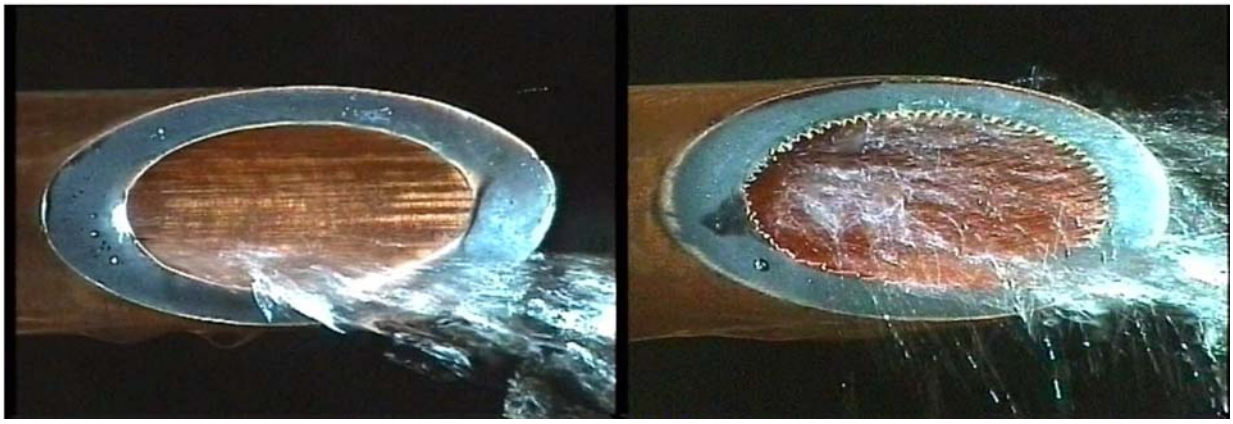

Figure 9. Smooth vs. microfin: flow pattern visualizations by Doretti et al. [20] during two-phase flow of R410A at t_{sat}=40 °C, G=252 kg $m^{-2}s^{-1}$, x=0.5 and J_G=1.5 (smooth tube: left – microfin tube: right).

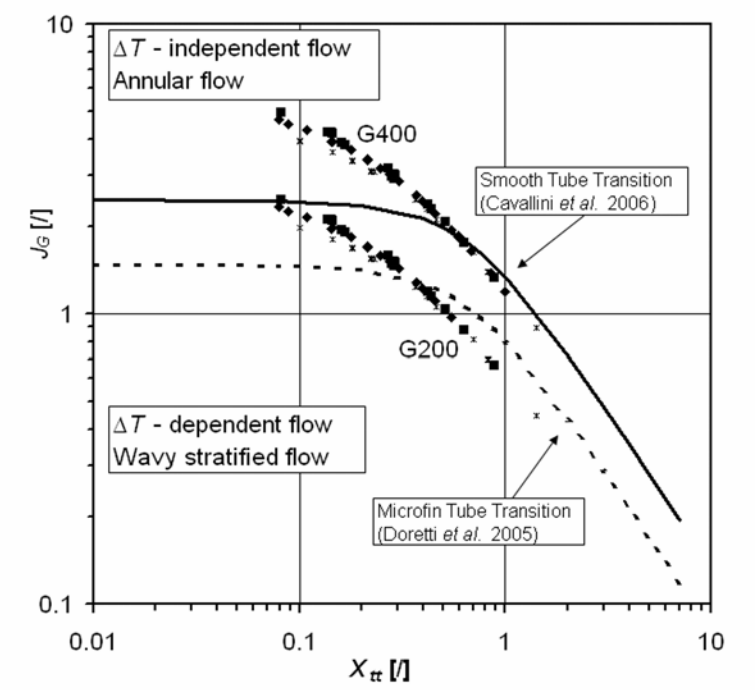

Figure 10. Cavallini et al. [8,9] simplified flow regime map for microfin tubes.

The same Authors [7, 8] have proposed a new flow regime map based on the one for smooth tubes as drawn in Figure 10. As one can see, besides the transition line, experimental data points taken during R410A, R22 and R134a condensation inside a microfin tube have also been reported.

The transition line plotted in Figure 10 (dot line) is defined as:

$$J_G^* = 0.6 \cdot \left\{ \left[\frac{7.5}{4.3 X_{tt}^{1.111} + 1} \right]^{-3} + 2.5^{-3} \right\}^{-0.3333} \qquad \textbf{Eq. 3}$$

1.2 Experimental Set-up

1.2.1 Overview

The experimental set-up is located in the laboratory of the Dipartimento di Fisica Tecnica of the University of Padova. In this apparatus it is possible to study both the condensation and the vaporization heat transfer behaviour of several high and low pressure halogenated refrigerants inside different test tubes, both plain and enhanced.

In particular, this work concerns the experimental heat transfer coefficient and pressure drop measurements during the condensation of R410A inside a helical microfin tube. The test tube has been described in paragraph 1.1.2.

The experimental test rig can be subdivided into three independent circuits: the refrigerant loop, the cooling water loop and the hot water loop. This test equipment is different from a vapour-compression cycle because the refrigerant evolves at constant pressure and the compressor is substituted by a gear pump which supplies the desired mass flow rate.

Following, it is reported a brief presentation of the test facility, drawn in Figure 11.

1.2.2 Refrigerant Loop

As highlighted before, the refrigerant evolves at constant pressure and the magnetically coupled gear pump, equipped with an inverter, ensures the desired mass flow rate by compensating pressure losses.

Travelling along the refrigerant circuit (Figure 11) the operating fluid is pumped through five different heat exchangers; the first two are an evaporator and a superheater which are followed by a pre-condenser. After that, the refrigerant arrives in the test section, a condenser. Finally, it is subcooled in a water cooled brazed plate heat exchanger which is located before the magnetically coupled gear pump.

The evaporator and the superheater are two counter-current tube-in-tube heat exchangers where the refrigerant flows in the inner tube while the hot water exchanges in the annulus. In this part of the test apparatus, the subcooled liquid is vaporised and 7-10 °C superheated.

Then, R410A is partially condensed in a tube-in-tube heat exchanger, fed with the cold water to achieve the desired vapour quality at the inlet of the test section. When the refrigerant arrives in the test condenser, it releases the latent heat of condensation to the cold water and finally it is subcooled before it reaches the pump again.

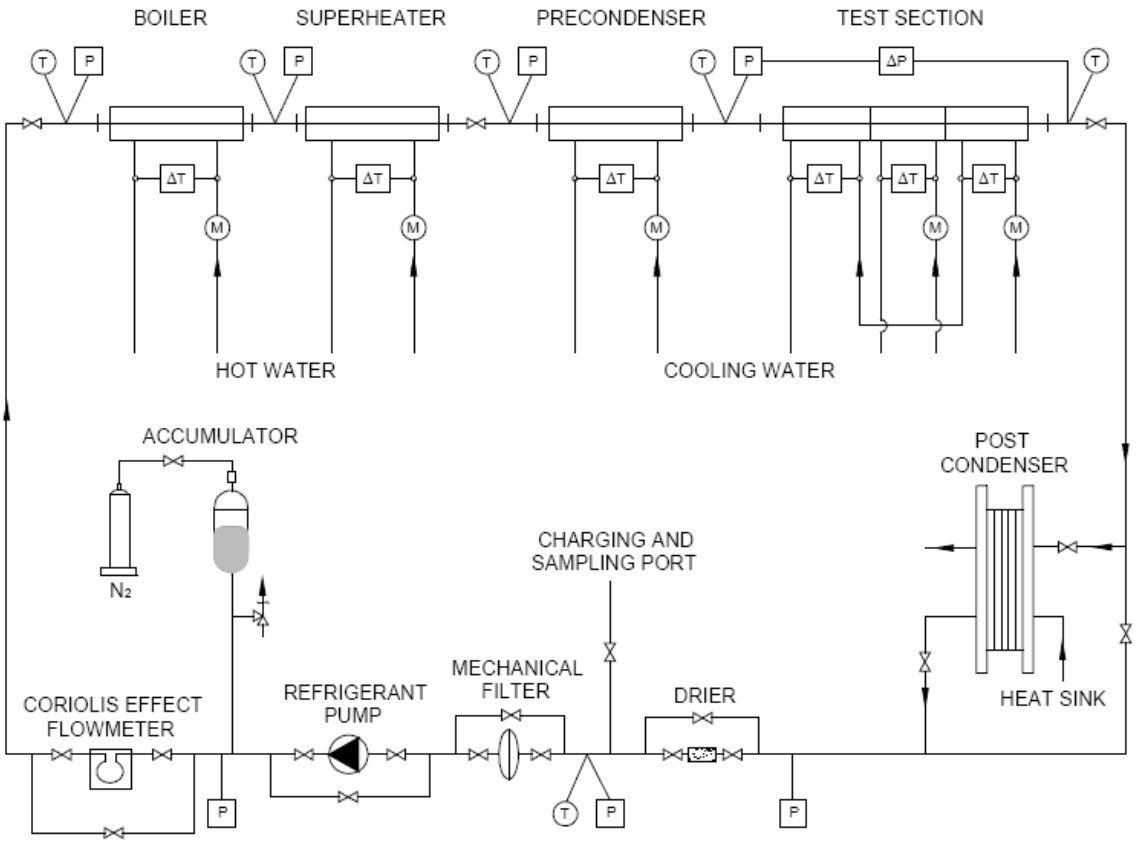

Figure 11. A schematic of the test facility.

The refrigerant pressure is controlled by a nitrogen accumulator inserted between the pump and the evaporator where it is also implemented a Coriolis effect mass flowmeter. A mechanical filter and a drier are inserted before the pump to eliminate oil, non-condensable fluids or particulate materials.

In order to analyse the refrigerant status all over the circuit, its temperature and pressure are measured at inlet and outlet of each heat exchanger.

1.2.3 Hot Water Loop

The hot water loop supplies the necessary heat to vaporize and superheat the subcooled liquid which comes from the magnetically coupled gear pump.

As plotted in Figure 12, the hot water loop consists in an electric shell-and-tube heat exchanger that warms the water up to 85-90 °C. The hot water is then pumped through the superheater and the boiler where it exchanges with the refrigerant.

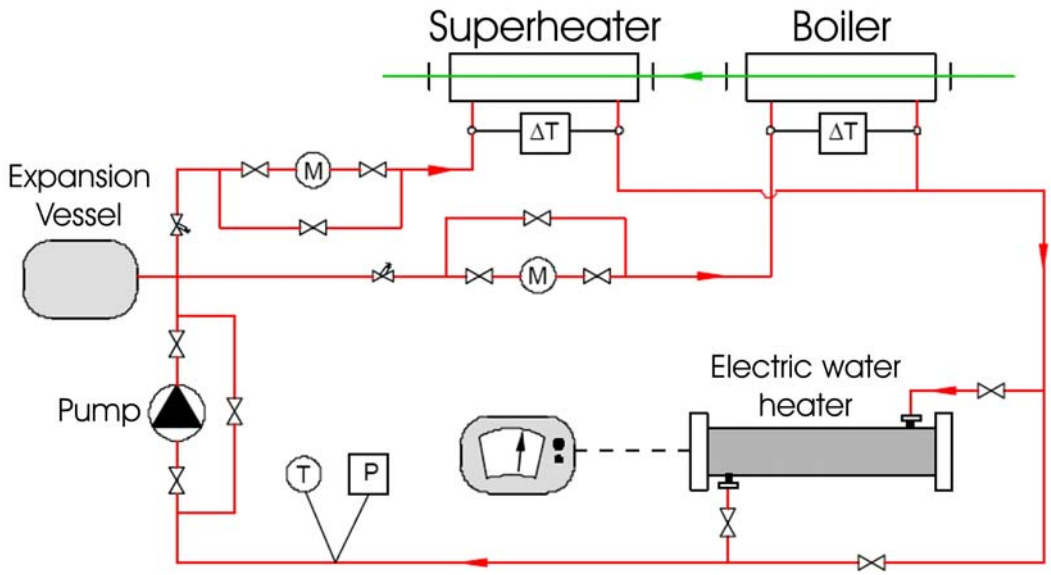

Figure 12. Hot water loop.

1.2.4 Cold Water Loop

The cold water loop feeds the test section and the pre-condenser with two independent water flow rates.

The first water flow rate is used, in the pre-condenser, to set up the desired vapour quality at the inlet of the test section while the second one exchanges in the test section.

As it appears from Figure 13, since the water circuits are independents, the temperature of the two water flow rates can be set at different values.

Again, two different cooling systems can be used to reach the desired water temperature set points:

- a R407C chiller which is used at high heat fluxes and low temperatures;
- a plate heat exchanger fed with well water which is used at low heat fluxes.

The first PID (PID 1) regulates the water tank temperature by controlling the electric heater power released to the water, which, with the heat flux from the test section, balances the heat removed by the chiller or the plate heat exchanger. The second water temperature level can be achieved using the second PID (PID 2), which is connected to another electric water heater.

Finally, the water flow rates at the inlet of the pre-condenser and of the test section are measured by means of three volumetric flowmeters.

Water temperature differences are measured by means of four calibrated thermopiles with an accuracy of 0.03 K.

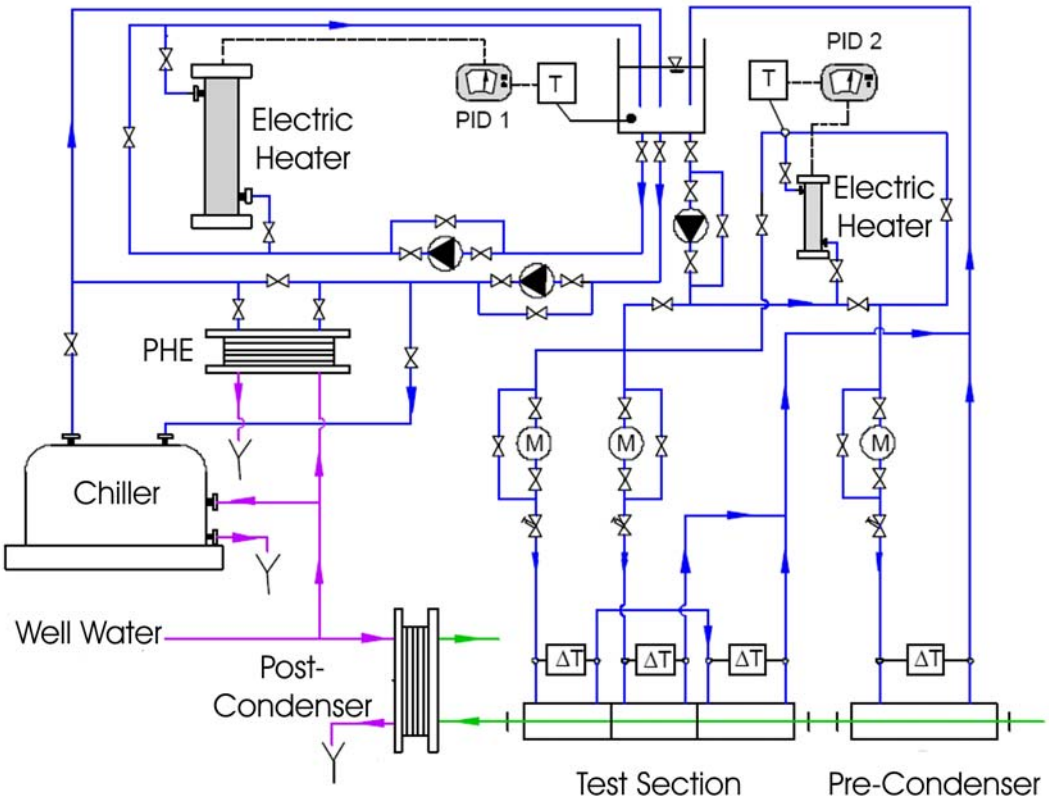

Figure 13. Cold water loop.

1.2.5 The Test Section

The test section consists in a 1.4 m long microfin tube subdivided in three sectors: a 600 mm pre-condenser, a 300 mm actual measuring part and a 200 mm post-condenser. It is a counter flow tube-in-tube condenser, with the refrigerant condensing in the inner tube and cold water flowing in the annulus. The experimental quasi-local condensation heat transfer coefficient is referred to the middle sector, where occurs a vapour quality change of 10-25% depending on the mass flux velocity and the heat flux.

According to the scheme drawn in Figure 14, the two-phase fluid, coming from the pre-condenser, reaches the first 600 mm tube-in-tube heat exchanger where the desired vapour quality value is set. Then, the refrigerant condenses in the test section and finally it exchanges with the cold water in the last sector of the test tube.

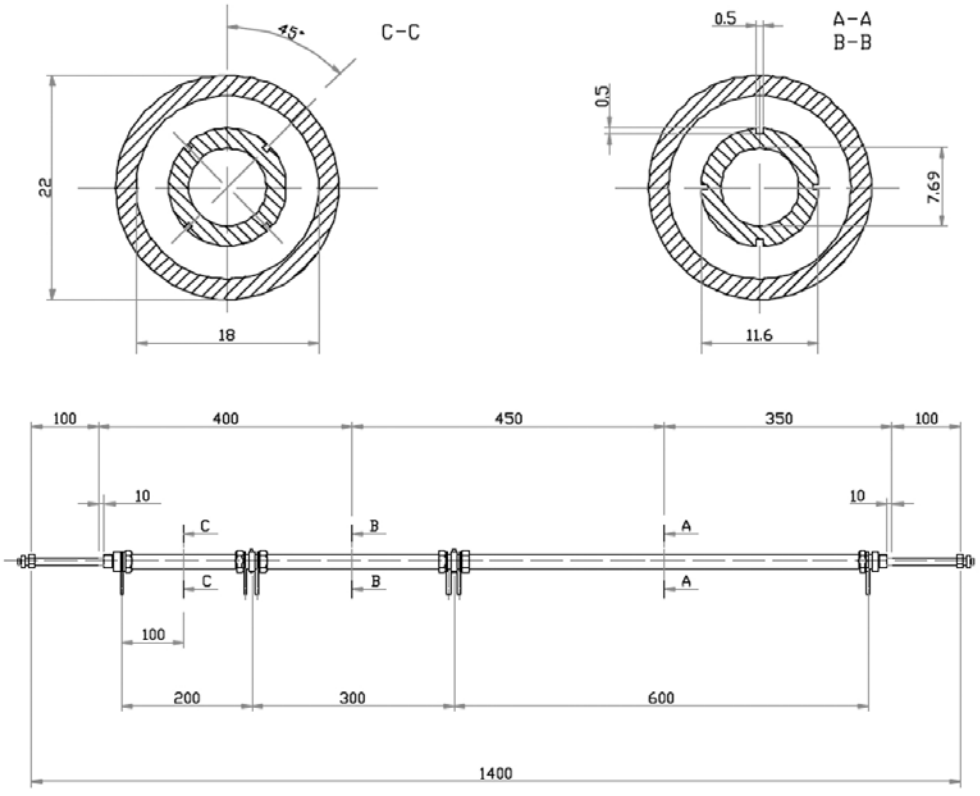

Figure 14. Microfin test section tube.

All the test parts are instrumented with four T-Type copper-constantan thermocouples embedded in the middle tube wall. As it appears from Figure 14 (section B-B), four thermocouples are soldered to draw a cross shape in the circumference.

The geometrical characteristics of the tested microfin tube are summarized in Table 1, paragraph 1.1.2.

The temperatures of the refrigerant at the inlet and outlet of the test section are measured by means of two adiabatic sectors equipped with three calibrated T-Type thermocouples inserted into both the refrigerant flow and the tube wall.

The absolute pressure of the refrigerant is measured at the inlet of the test tube by means of an absolute pressure transducer connected to two static pressure taps drilled in the connection flange.

Other two static pressure taps have been drilled in the outlet flange and connected to a differential pressure transducer to measure the refrigerant pressure drop.

The measuring test sector and the other test sections, the pre-condenser and the post-condenser, are fed with two independent water flow rates, measured by two magnetic flowmeters. The water temperature gain is obtained by means of three four-junction copper-constantan thermopiles installed into five mixing chambers to assure a perfect mixing of the water.

1.2.6 Acquisition System

The experimental apparatus is connected to a real-time acquisition system which permits to control the principal parameters directly measured by the instruments, such as: refrigerant temperatures and pressures, water temperatures or water flow rates. The real time acquisition system also displays the elaborated indirect measures, such as: vapour qualities, exchanged heat fluxes, etc.

The signals coming from the experimental transducers are recorded with an acquisition system consisting in a voltmeter, a digital switch multimeter connected to a PC.

Recorded signals are elaborated and displayed by an acquisition program developed with Labview 6.0 which permits to control all the process parameters.

The thermophysical properties of the refrigerant are calculated using RefProp 7.0, developed by NIST (National Institute of Standard and Technologies) [9].

The acquisition program displayes the direct and the indirect measurements in terms of graphs or numerical strings of the rielaborated electric signals.

In fact, the graphs report the desired parameter as a function of the lectures and they are updated at each new reading.

Once experimental steady state conditions are reached, it is possible to record the data; two consecutive readings are taken to ensure the repeatability of the test point. A measure consists of a mean of ten runs.

The acquisition system compiles two independent result files: one reports the effective data points, whilst in the other the standard deviations of each ten readings group are written.

This second file is very important to understand the effective test conditions and gives useful information concerning the possible presence of any systematic error during the experimental work.

The steady state condition has to be maintained during the acquisition process, otherwise the experimental data point will be eliminated and re-collected.

Table 3 reports a list of the instruments implemented in the test rig and their location in the plant; moreover, it gives the number of the acquisition channels and the output signal unit.

The principal transducers are:

- T-Type copper-constantan thermocouples to measure the temperatures. These present an uncertainty of ± 0.05 K as the whole measuring chain, comprehensive of the ice point reference and of the Voltmeter/Data logger, is calibrated against a Pt 100 thermistor with an accuracy of ± 0.02 K. The temperature of the refrigerant is measured at the inlet and outlet of each heat exchanger by means of adiabatic sectors inserted to eliminate from the measures the possible axial conduction effect.
- Four-junction T-Type copper-constantan thermopiles with an accuracy of ± 0.03 K, used to measure water temperature gains in the heat exchangers. The junctions are inserted into mixers ensuring that the water mixes at the inlet and outlet of each heat exchanger. The accuracy of the thermopile is higher than that of the thermocouple, so that it's useful when only a temperature difference is needed.
- A Micro Motion Coriolis mass flowmeter, with an uncertainty of ± 0.2% of reading, used to measure the refrigerant mass flow rate.
- Three Danfoss volumetric flowmeters, inserted to measure the water flow rate pumped through the evaporator-superheater, the pre-condenser and the first and the third test sector. They present an uncertainty of ± 0.2% of the full scale.
- An Endress-Hauser volumetric flowmeter, located at the inlet of the test section to report the water flow rate. The declared accuracy is ± 0.2% of the full scale.

Table 3. Experimental transducers inserted in the test rig.

Measurement	Transducer and Location		Channel		Unit
Refrigerant fluid Temperatures (adiabatic sectors)	Upper Thermocouple (A)	Inlet Evaporator	T	1	°C
	Lower Thermocouple (B)		T	2	°C
	Axial Thermocouple (C)		T	3	°C
	Upper Thermocouple (A)	Outlet Evaporator	T	4	°C
	Lower Thermocouple (B)		T	5	°C
	Axial Thermocouple (C)		T	6	°C
	Upper Thermocouple (A)	Inlet Pre-Condenser	T	7	°C
	Lower Thermocouple (B)		T	8	°C
	Axial Thermocouple (C)		T	9	°C
	Upper Thermocouple (A)	Inlet Test Tube	T	10	°C
	Lower Thermocouple (B)		T	11	°C
	Axial Thermocouple (C)		T	12	°C
	Upper Thermocouple (A)	Outlet Test Tube	T	53	°C
	Lower Thermocouple (B)		T	54	°C
	Axial Thermocouple (C)		T	55	°C
Wall Temperatures	Upper Thermocouple +0°	Sector 1 (Pre-Section)	T	13	°C
	Lower Thermocouple +180°		T	14	°C
	Axial Thermocouple -90°		T	15	°C
	Axial Thermocouple +90°		T	16	°C
	Upper Thermocouple +0°	Sector 2 (Middle Section)	T	30	°C
	Lower Thermocouple +180°		T	31	°C
	Axial Thermocouple -90°		T	32	°C
	Axial Thermocouple +90°		T	33	°C
	Upper Thermocouple +45°	Sector 3 (Post-Section)	T	17	°C
	Lower Thermocouple -135°		T	18	°C
	Lower Thermocouple -45°		T	19	°C
	Upper Thermocouple +135°		T	20	°C
Water Temperature Differences	Pre-Condenser Thermopile	Pre-Condenser	ΔT	63	°C
	Thermopile – Section 1	Mixers B-E	ΔT	64	°C
	Thermopile - Section 2	Mixers C-D	ΔT	66	°C
	Thermopile – Section 3	Mixers A-B	ΔT	65	°C
Reference Water Temperatures	Inlet Pre-Condenser	Mixer F	T	59	°C
	Evaporator	Mixer G	T	56	°C
	Inlet Section 3	Mixer A	T	57	°C
	Outlet Section 3	Mixer B	T	21	°C
	Outlet Section 1	Mixer E	T	58	°C
	Inlet Section 2	Mixer C	T	23	°C
	Outlet Section 2	Mixer D	T	22	°C
Refrigerant Mass Flow Rate	Micro Motion Mass Flow Rate	After the Pump	G	41	$kg\ min^{-1}$
Refrigerant Absolute Pressure	Endress-Hauser Pressure Transducer	Inlet Test Section	P	42	bar
Refrigerant Pressure Drop	Differential Pressure Transducer (Endress-Hauser)	Test Tube	ΔP	43	mbar
Refrigerant Gauge Pressure	Gauge Pressure Transducer (Druck)	Inlet Pre-Condenser	P	44	bar
Water Flow Rate	Endress-Hauser Flowmeter	Test Sector	G	45	l/h
Water Flow Rate	Danfoss Flowmeter	Pre-Condenser	G	46	l/h

Water Flow Rate	Danfoss Flowmeter	Superheater	G	47	l/h
Water Flow Rate	Danfoss Flowmeter	Evaporator	G	48	l/h
Water Flow Rate	Danfoss Flowmeter	First and third Test sector	DL	49	l/h
Refrigerant Absolute Pressure	Druck Gauge Pressure Transducer	Inlet Test Section	P	50	bar
Barometric Pressure	Druck Absolute Pressure Transducer	-	P	67	mbar

- An Endress-Hauser pressure transducer, which measures the refrigerant gauge pressure at the inlet of the test section with an accuracy of ± 5 kPa.
- An Endress-Hauser differential pressure transducer, inserted between the inlet and outlet of the test section to measure the refrigerant pressure drop through the test tube. The uncertainty of this instrument is ± 100 Pa.
- The refrigerant gauge pressure is measured in other locations of the plant by means of a different pressure transducers produced by Druck.

1.2.7 Experimental Procedure

Experimental data points are registered under fixed, steady state conditions which are reached through several consecutive equilibrium steps.

Each time, the refrigerant vapour quality, its specific mass flow rate, its saturation pressure and its superheating at the inlet of the pre-condenser are fixed. To obtain these experimental test conditions, all refrigerant and water circuits must be set up beforehand.

The cold water tank temperature is controlled by a PID controller which modulates an electric resistance of 3 kW. Electric resistances of 1.5 and 3 kW of heating power can also be added.

If the cold water temperature has to be set at below 22 °C, the water chiller can be started; otherwise it can be by-passed leaving open only the plate heat exchanger.

The hot water loop is manually controlled and its temperature is set between 85 and 90 °C to superheat the refrigerant vapour by 7-10 °C.

First of all, it is important to start up the hot water pump, to avoid any over pressure or uncontrolled superficial temperature rises of the electric resistances.

As said before, the refrigerant mass flow rate is controlled by an inverter which regulates the rotational velocity of the magnetically coupled gear pump.

Finally, the saturation temperature depends on several different parameters, such as the mass flow rate, the subcooling and the condensation temperature. For this reason, in order to set it at the desired value, i.e. 40 °C, a nitrogen accumulator is used.
The experimental steady state conditions are reached after around 5 hours, necessary to assure the test reliability and repeatability.

1.3 Heat Transfer and Pressure Drop Measurements

1.3.1 Data Reduction

When the test rig parameters reach the desired steady state conditions, the experimental data are recorded and rielaborated to calculate the heat transfer coefficients and the pressure drops. The acquisition system receives all the electric signals from the experimental transducers located in the plant and it permits to set the number of consecutive readings which have to be recorded.

As described before, the acquisition program writes two different files: the first one returns the mean values of the experimental parameters, while their standard deviations are listed in the second.

The average values x, of ten readings x_i, and their standard deviations σ_N, are given by:

$$\overline{x} = \frac{\sum_{i=1}^{10} x_i}{10} \qquad \textbf{Eq. 1}$$

$$\sigma_N = \sqrt{\frac{\sum_{i=1}^{10} \left(x_i - \overline{x}\right)}{9}} \qquad \textbf{Eq. 2}$$

In the following, it is reported the regression analysis of the average experimental values. The data reduction procedure permits to calculate the operating test conditions, such as vapour qualities, the specific refrigerant mass flow rate, saturation temperatures and experimental results: heat transfer coefficients and pressure drops. In the regression analysis, thermophysical properties are calculated using RefProp 7.0, developed by NIST [9].

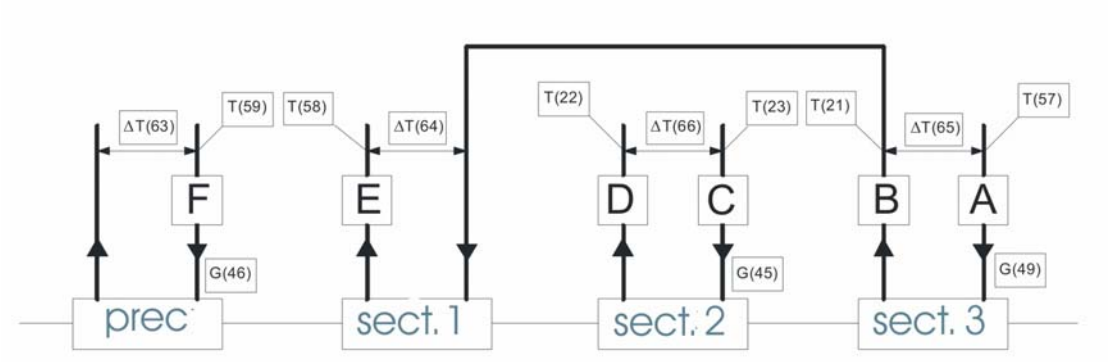

Figure 15. Location of the transducers for water properties measurements: T thermocouple, ΔT thermopile, G Flowmeter. A, B,..., F water mixers.

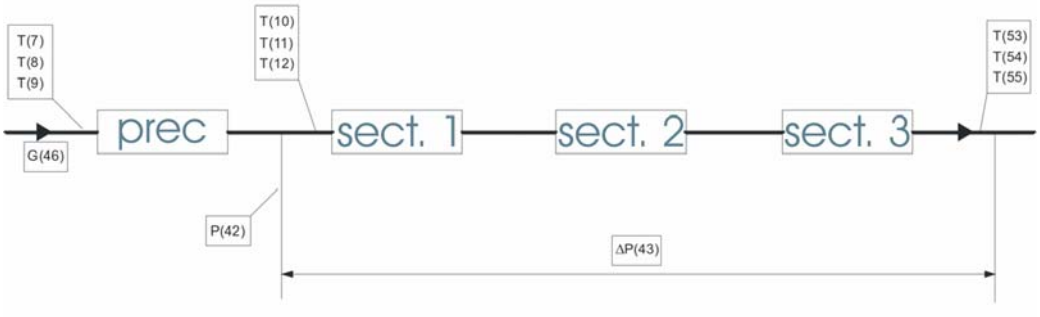

Figure 16. Location of the transducers for refrigerant properties measurements: T thermocouple, G flowmeter, P gauge pressure transducer, ΔP differential pressure transducer.

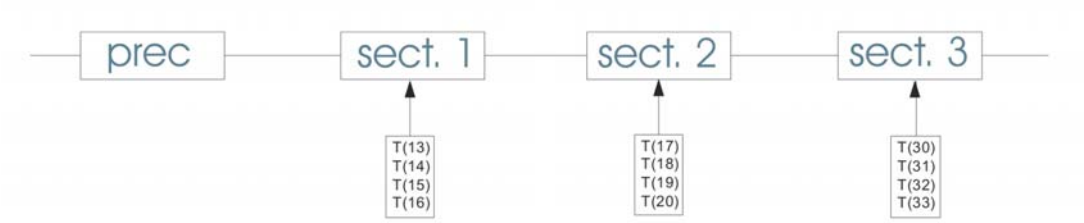

Figure 17. Wall thermocouples locations.

As said before, the test tube has been subdivided into three sectors: a pre-condenser, the test section and a postcondenser.

Figure 15, Figure 16 and Figure 17 report the location of the transducers used to calculate the heat transfer coefficient and the pressure drop during condensation of R410A inside the microfin tube.

The number within the brackets refers to the measure position in the output data file used in the regression analysis.

1.3.1.1 Preliminary Calculation

First of all, with reference to the scheme reported in Figure 15, the average water temperatures in each test sector are calculated as follows:

$$T_{w,1} = T(21) + \frac{\Delta T(64)}{2} \qquad \textbf{Eq. 3}$$

$$T_{w,2} = T(23) + \frac{\Delta T(66)}{2} \qquad \textbf{Eq. 4}$$

$$T_{w,3} = T(57) + \frac{\Delta T(65)}{2} \qquad \textbf{Eq. 5}$$

$$T_{w,prec} = T(59) + \frac{\Delta T(63)}{2} \qquad \textbf{Eq. 6}$$

Where ΔT (xx) is the cold water temperature gain measured by means of a calibrated four junction T-Type thermopile.
The refrigerant absolute pressure at the inlet of the test tube, expressed in Pa, is:

$$p_{ref,in} = P(42) \cdot 10^5 \qquad \textbf{Eq. 7}$$

While the refrigerant pressure at the inlet of the pre-condenser is the sum of the relative pressure measured by the gauge pressure transducer and the barometric value:

$$p_{ref,prec} = \left(P(44) + p_{atm} \right) \cdot 10^5 \qquad \textbf{Eq. 8}$$

The refrigerant pressure at the outlet of the test tube depends on the pressure drop and it is calculated as:

$$p_{ref,out} = p_{ref,in} - \Delta P(43) \qquad \textbf{Eq. 9}$$

Where Δ*P (43)* is the refrigerant two-phase pressure drop inside the microfin test tube.
The refrigerant temperatures at the inlet and outlet of the test tube are measured by means of two different adiabatic sectors equipped with three thermocouples, so that the mean refrigerant temperatures values are given by:

$$T_{ref,in} = \frac{T(10) + T(11) + T(12)}{3} \qquad \textbf{Eq. 10}$$

$$T_{ref,out} = \frac{T(53) + T(54) + T(55)}{3} \qquad \textbf{Eq. 11}$$

The refrigerant specific mass flow rate is calculated with reference to the equivalent cross-sectional area of the smooth tube with inner diameter equal to the fin tip diameter of the microfin tube, A_{cross}. In fact, G expressed in [kg m^{-2} s^{-1}] is:

$$G = \frac{\dot{m}_{ref}}{A_{cross}} \qquad \textbf{Eq. 12}$$

Where $\dot{m}_{ref}$ is G (41) and the cross-sectional area A_{cross} is equal to:

$$A_{cross} = \frac{\pi \cdot D^2}{4} = \frac{\pi \cdot \left(7.69 \cdot 10^{-3}\right)^2}{4} = 4.645 \cdot 10^{-5} \quad \text{m}^2 \qquad \textbf{Eq. 13}$$

The superheated gas temperature is the average value of the measures of the three thermocouples inserted in the adiabatic sector located before the pre-condenser:

$$T_{ref,s} = \frac{T(7) + T(8) + T(9)}{3} \qquad \textbf{Eq. 14}$$

While its pressure is measured by means of an absolute pressure transducer:

$$p_{ref,s} = P(44) \cdot 10^5 \qquad \textbf{Eq. 15}$$

Finally, the average wall temperatures are calculated from the measurements of the four thermocouples embedded in the tube wall in each sector, as follows:

$$T_{wall,1} = \frac{T(13) + T(14) + T(15) + T(16)}{4} \qquad \textbf{Eq. 16}$$

$$T_{wall,2} = \frac{T(17) + T(18) + T(19) + T(20)}{4}$$ **Eq. 17**

$$T_{wall,3} = \frac{T(30) + T(31) + T(32) + T(33)}{4}$$ **Eq. 18**

1.3.1.2 Vapour Quality

The calculated and measured condensation heat transfer coefficient and two-phase pressure drop are both referred to a mean value of vapour quality.

Considering the heat transfer coefficient, the vapour quality change in the actual measuring sector was always kept under the 20%. Therefore, this experimental value can be called "quasi-local".

On the other hand, pressure drop measurements were carried out under adiabatic test conditions, so that no vapour change occured in the test tube and the vapour quality was set by controlling the heat exchanged in the pre-condenser.

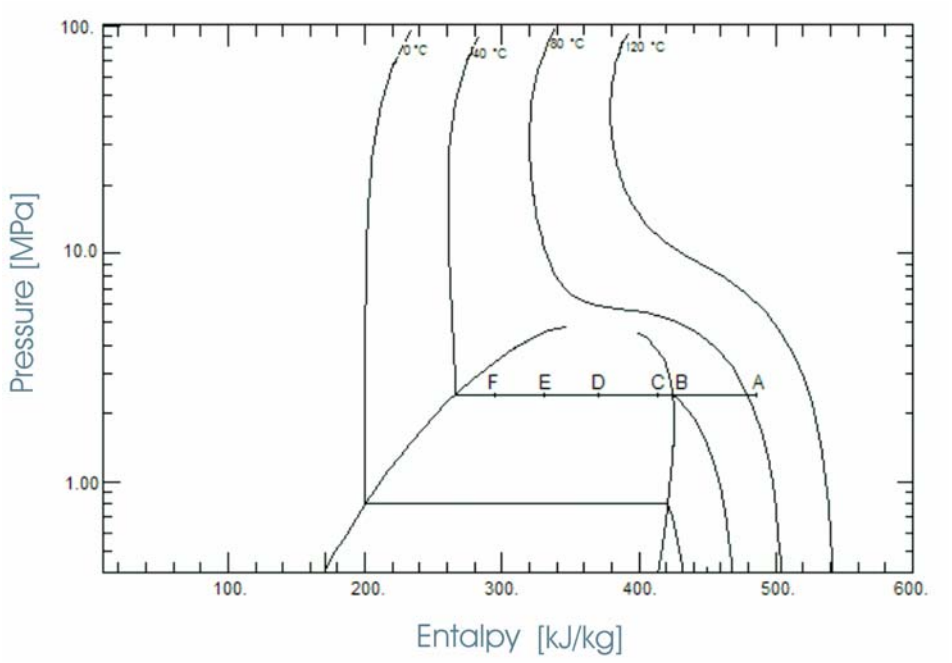

Figure 18. Condensation process plotted in the p-h diagram.

Figure 18 plots the most general test case, where the refrigerant, vaporised and superheated by the hot water, releases its heat to the pre-condenser and in all three sectors of the test tube.
In some cases, depending on the desired operating test conditions, one of the pre-condenser or the first sector can be by-passed.
The heat exchanged by the pre-condenser is equal to:

$$q_{prec} = \dot{m}_w \cdot c_{p,w} \cdot \Delta T_{w,prec} \qquad \textbf{Eq. 19}$$

So, starting from the point A, the vapour is desuperheated and partially condensed by the pre-condenser, reaching the conditions described by the point C.

$$q_{prec} = q_{A-C} = q_{A-B} + q_{B-C} = q_{desup} + q_{cond,prec} \qquad \textbf{Eq. 20}$$

Where q_{desup} is given by:

$$q_{desup} = \dot{m}_{ref} \cdot \left(h_A - h_{vs,B} \right) \qquad \textbf{Eq. 21}$$

And the $q_{cond,prec}$ is obtainable by subtracting these two terms:

$$q_{cond,prec} = q_{prec} - q_{desup} \qquad \textbf{Eq. 22}$$

Therefore, the vapour quality at the inlet of the test tube is:

$$x_{in,ts} = 1 - \frac{q_{cond,prec}}{\dot{m}_{ref} \cdot h_{LG}} \qquad \textbf{Eq. 23}$$

The vapour quality change and the mean vapour quality of each test sector are given by the following equations.
The heat flux exchanged in each test tube part is:

$$q_i = m_{w,i} \cdot c_{pw,i} \cdot \Delta T_{w,i} \qquad \textbf{Eq. 24}$$

$$\Delta x_i = \frac{q_i}{\dot{m}_{ref} \cdot h_{LG}} \qquad \textbf{Eq. 25}$$

Finally, the mean vapour quality is:

$$\overline{x}_i = x_{in,i} - \frac{\Delta x_i}{2} \qquad \textbf{Eq. 26}$$

1.3.1.3 Heat Transfer Coefficient

The tested microfin tube has been equipped with twelve thermocouples, four in each sector, to measure three different heat transfer coefficients during the condensation process.

As described before, paragraph 1.2.5, the lengths of the three sectors are different. The research group has decided to refer the heat transfer coefficient to the second sector, which is 0.2 m long.

The heat transfer coefficient is defined by the following equation:

$$HTC = \frac{q_2}{A \cdot \Delta T_2} \qquad \textbf{Eq. 27}$$

Where A is the heat transfer area of the smooth tube with an inner diameter equal to the fin tip diameter of the microfin tube, corresponding to:

$$A = \pi \cdot D \cdot l = \pi \cdot \left(7.69 \cdot 10^{-3}\right) \cdot 0.2 = 7.248 \cdot 10^{-3} \quad \text{m}^2 \qquad \textbf{Eq. 28}$$

And ΔT_2 is the difference between the saturation and wall temperatures:

$$\Delta T_2 = T_{sat,2} - T_{wall,2} \qquad \textbf{Eq. 29}$$

The saturation temperature is calculated from the saturation pressure, which was fixed at around 2.4 MPa, in the hypothesis that the saturation temperature varies linearly along the test tube. $T_{sat,2}$ is equal to:

$$T_{sat,2} = T_{ref,in} - (T_{ref,in} - T_{ref,out}) \cdot \frac{900}{1400} \quad \textbf{Eq. 30}$$

Where the saturation temperatures at the inlet and outlet of the test tube are calculated from the measured saturation pressures. Experimental measurements were carried out at a saturation temperature of 40 °C.

1.3.1.4 Pressure Drop

During two-phase flow inside the microfin tube, the pressure drops of R410A are directly measured by means of a differential pressure transducer. Generally speaking, the pressure gradient, defined as the ratio of the pressure drop to the reference length of the tube, is the sum of three terms:

$$-\left(\frac{dp}{dz}\right)_{tot} = -\left(\frac{dp}{dz}\right)_{f} - \left(\frac{dp}{dz}\right)_{g} - \left(\frac{dp}{dz}\right)_{a} \quad \textbf{Eq. 31}$$

The subscript *f* refers to the frictional term, *g* to the gravity term and *a* to the acceleration one. Considering the term linked to gravity, it depends on the tube inclination, α and it is:

$$\left(\frac{dp}{dz}\right)_{g} = -\left(\varepsilon \cdot \rho_V + (1-\varepsilon) \cdot \rho_L\right) \cdot g \cdot \sin\alpha \quad \textbf{Eq. 32}$$

Therefore, if the tube is horizontal this term is equal to zero. The acceleration term is:

$$\left(\frac{dp}{dz}\right)_{a} = -G^2 \cdot \frac{d}{dz}\left[\frac{x^2}{\rho_V \cdot \varepsilon} + \frac{(1-x)^2}{\rho_L \cdot (1-\varepsilon)}\right] \quad \textbf{Eq. 33}$$

Hence:

$$-\left(\frac{dp}{dz}\right)_a = G^2 \cdot \left[\left(\frac{x^2}{\varepsilon \cdot \rho_G} + \frac{1-x^2}{(1-\varepsilon)\cdot \rho_L}\right)_{out} - \left(\frac{x^2}{\varepsilon \cdot \rho_G} + \frac{1-x^2}{(1-\varepsilon)\cdot \rho_L}\right)_{in}\right] \cdot \frac{1}{L} \qquad \textbf{Eq. 34}$$

Where L is the total length of the microfin tube, 1.4 m, while the void fraction, ε, is calculated with the equation proposed by Smith [21]:

$$\varepsilon^{-1} = 1 + \frac{(1-x)\cdot \rho_G}{x \cdot \rho_L} \cdot \left[0.4 + 0.6 \cdot \sqrt{\frac{x \cdot \frac{\rho_L}{\rho_G} + 0.4 \cdot (1-x)}{x + 0.4 \cdot (1-x)}}\right] \qquad \textbf{Eq. 35}$$

In particular, if x=0 (total liquid) then ε=0, whilst for x=1 (total vapour) ε=1.
When the gravity and acceleration terms are known, it is possible to estimate the experimental frictional pressure gradient.

1.3.2 Experimental Uncertainty Evaluation

1.3.2.1 Theory Overview

The uncertainty of an experimental value, such as the heat transfer coefficient and the mean vapour quality, which is indirectly obtained from other experimental measures, depends on the operating test procedure and on the intrinsic accuracy of the instruments.

As described before, the experimental procedure foresees to make the mean of ten consecutive readings for each experimental parameter. This implies an additional uncertainty linked to the repeatability of the readings, which can be estimated as follows.

If x is the experimental parameter, its standard deviation is:

$$S(x) = \sqrt{\frac{\sum_{i=1}^{n}(x_i - \bar{x})}{n-1}} \qquad \textbf{Eq. 36}$$

Where $\bar{x}$ is the mean of n readings. The repeatability uncertainty of x depends on the considered statistical distribution:

$$i_A(\bar{x}) = t \cdot \frac{S(x)}{\sqrt{n}} \qquad \textbf{Eq. 37}$$

In this case, the repeatability index, t, is the one read from the Student distribution table for $n\text{-}1$=9 degrees of freedom at 95% confidence level and it is equal to 2.262.

The other term of the uncertainty depends on the accuracy of the instrument used in the measurement of the parameter; this gives another value, i_B, which has to be summed to the repeatability one to obtain the final uncertainty of the parameter, called i_i:

$$i_i = i_A + i_B \qquad \textbf{Eq. 38}$$

When the uncertainty i_i of each parameter is known, the uncertainty of the indirect measure can be calculated. If an indirect measure, y, depends on n independent parameters, as in:

$$y = f(x_1, ..., x_n) \qquad \textbf{Eq. 39}$$

And these independent parameters present an uncertainty i_i:

$$y = f\left(x_1 + i_1, ..., x_n + i_n\right) \qquad \textbf{Eq. 40}$$

Considering the Taylor's series, Eq. 40 can be developed as:

$$f\left(x_1 \pm i_1, ..., x_n \pm i_n\right) = f\left(x_1, ..., x_n\right) \pm \left(\frac{\partial f}{\partial x_1} \cdot i_1 + ... + \frac{\partial f}{\partial x_n} \cdot i_n\right) \pm \pm \frac{1}{2} \cdot \left(\frac{\partial^2 f}{\partial x_1^2} \cdot i_1 + ... + \frac{\partial^2 f}{\partial x_n^2} \cdot i_n\right) + o(i)^2 \qquad \textbf{Eq. 41}$$

And with reference to the first order term, the uncertainty can be written as:

$$i_y \cong \pm \frac{\partial f}{\partial x_1} \cdot i_1 \pm ..... \pm \frac{\partial f}{\partial x_n} \cdot i_n \qquad \textbf{Eq. 42}$$

Where $\frac{\partial f}{\partial x_i}$ are called sensitivity coefficients and they have to be evaluated at x_i. Finally, the overall uncertainty of an in direct measure is given by:

$$i_y = \sqrt{\sum_{i=1}^{n} \left(\frac{\partial f}{\partial x_i} \cdot i_i\right)^2} = \sqrt{\sum_{i=1}^{n} \left(\vartheta_i \cdot i_i\right)^2} \qquad \textbf{Eq. 43}$$

1.3.2.2 Instruments Accuracy

In order to evaluate the uncertainties of the experimental data points, the accuracy of the instruments must be analysed.

Every instrument reports its accuracy in terms of percent of the instant reading or of the full scale (f.s.). As described in paragraph 1.2.6, the experimental test rig is equipped with several different transducers, among which: thermocouples, thermopiles, volumetric flowmeters, mass flowmeter, gauge and absolute pressure transducers, etc. Table 4 reports the accuracy of the instruments used in the test rig.

It is interesting to highlight that all the thermocouples and thermopiles inserted in the test rig were calibrated against a high-precision Pt 100 with an accuracy of ±0.02 K.

Table 4. Accuracy of the instruments installed in the test rig.

Instrument	Measure	Accuracy	Full Scale
T-Type Thermocouple	Temperatures	± 0.05 K	-
4-junction T-Type Thermopile	Temperature Difference	± 0.03 K	-
Endress-Hauser Flowmeter	Water Flow Rate	± 0.2% f.s.	360 l/h
Danfoss Flowmeter	Water Flow Rate	± 0.2% f.s.	300 l/h
Danfoss Flowmeter	Water Flow Rate	± 0.2% f.s.	360 l/h
Micro Motion Flowmeter	Refrigerant Mass Flow Rate	± 0.2% r.	-
Endress-Hauser Absolute Pressure Transducer	Absolute Pressure	± 5 kPa	-
Endress-Hauser Differential Pressure Transducer	Refrigerant Pressure Drop	± 50 Pa	-
Legend: f.s.: full scale; r.: of the reading			

This calibration procedure involves the whole measuring chain, which, for example, for thermocouples consists of the T-Type transducer, the ice point reference and the Voltmeter/data logger.

1.3.2.3 Fluid Properties Uncertainty

As mentioned before, all the fluid properties were estimated using RefProp 7.0 [9], a useful software developed by the National Institute of Standard and Technology (NIST) of the USA. The developer has declared the overall uncertainty of each property; these values are summarised in Table 5.

Table 5. Fluid properties uncertainties. Data by NIST [9].

Property	Uncertainty
Water Density	± 0.0001%
Water Specific Heat	± 0.1%
R410A Density	± 0.2%
R410A Specific Heat	± 2%
R410A Dynamic Viscosity	± 4.81%
R410A Thermal Conductivity	± 3.85%

For the properties not included in Table 5, an uncertainty of 1% was adopted.

1.3.2.4 Pre-condenser and Section 1 Heat Fluxes

The vapour is desuperheated and partially condensed by the cold water pumped through the pre-condenser and the first sector of the test section.

The heat exchanged in these heat exchangers is important in the calculation of the vapour quality; hence, their uncertainties are here evaluated.

Generally speaking, the heat balance at each heat exchanger can be written as:

$$q_i = \dot{m}_{w,i} \cdot c_{p,wi} \cdot \Delta T_{w,i} \qquad \textbf{Eq. 44}$$

And the essential relations for uncertainty calculations are:

$$\frac{\partial q_i}{\partial \dot{m}_{w,i}} = c_{p,wi} \cdot \Delta T_{w,i} = \frac{q_i}{\dot{m}_{w,i}} \qquad \frac{\partial q_i}{\partial c_{p,wi}} = \dot{m}_{w,i} \cdot \Delta T_{w,i} = \frac{q_i}{c_{p,wi}} \qquad \frac{\partial q_i}{\partial \Delta T_{w,i}} = \dot{m}_{w,i} \cdot c_{p,wi} = \frac{q_i}{\Delta T_{w,i}}$$

And finally:

$$i_{qi} = \sqrt{\left(\frac{\partial q_i}{\partial \dot{m}_{w,i}} \cdot i_{mw}\right)^2 + \left(\frac{\partial q_i}{\partial c_{p,wi}} \cdot i_{cp}\right)^2 + \left(\frac{\partial q_i}{\partial \Delta T_i} \cdot i_{\Delta T}\right)^2}$$

Table 6. Experimental pre-condenser heat flux uncertainty.

	q_{PC}	$\dot{m}_w$	ΔT
i_m [%]	1.02	1.18	0.21
i_{max} [%]	3.62	4.65	0.44

Table 7. Experimental section 1 heat flux uncertainty.

	$q_{s,1}$	$\dot{m}_w$	ΔT
i_m [%]	1.16	0.67	0.71
i_{max} [%]	2.61	2.53	1.67

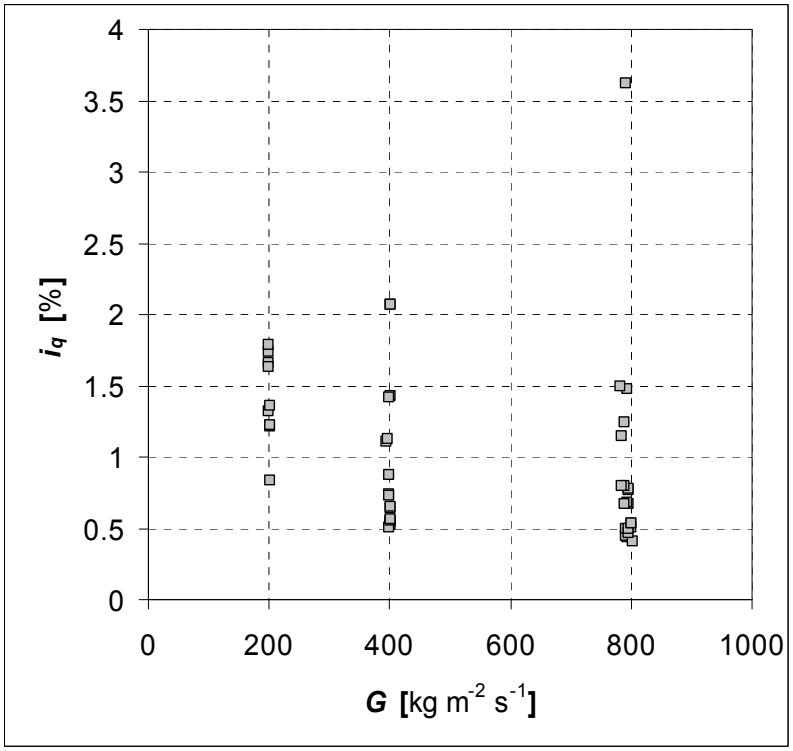

Figure 19. Experimental uncertainty on the pre-condenser heat fluxes plotted against the mass velocity.

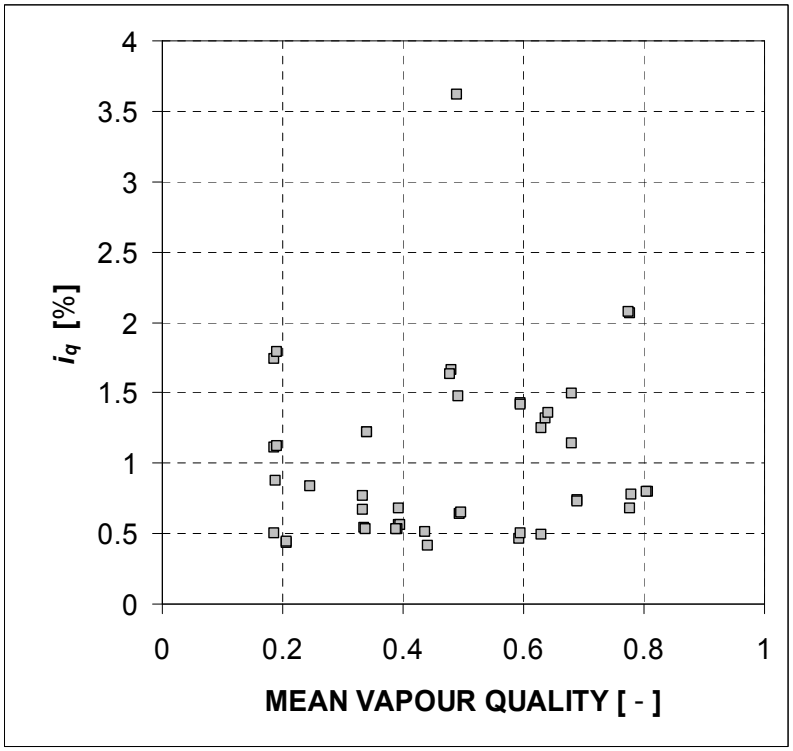

Figure 20. Experimental uncertainty on the pre-condenser heat fluxes plotted against the vapour quality.

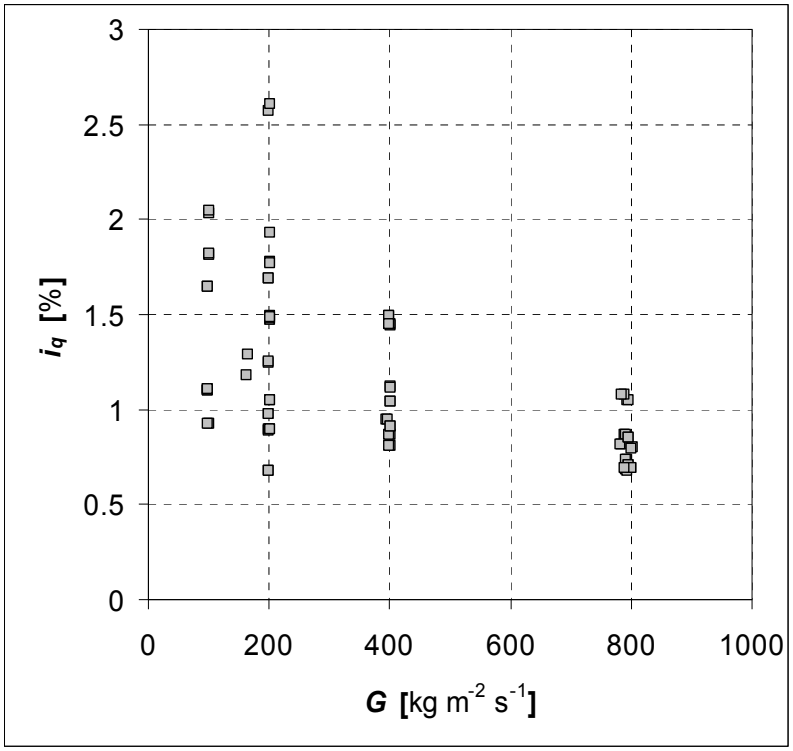

Figure 21. Experimental uncertainty on section 1 heat fluxes plotted against the mass velocity.

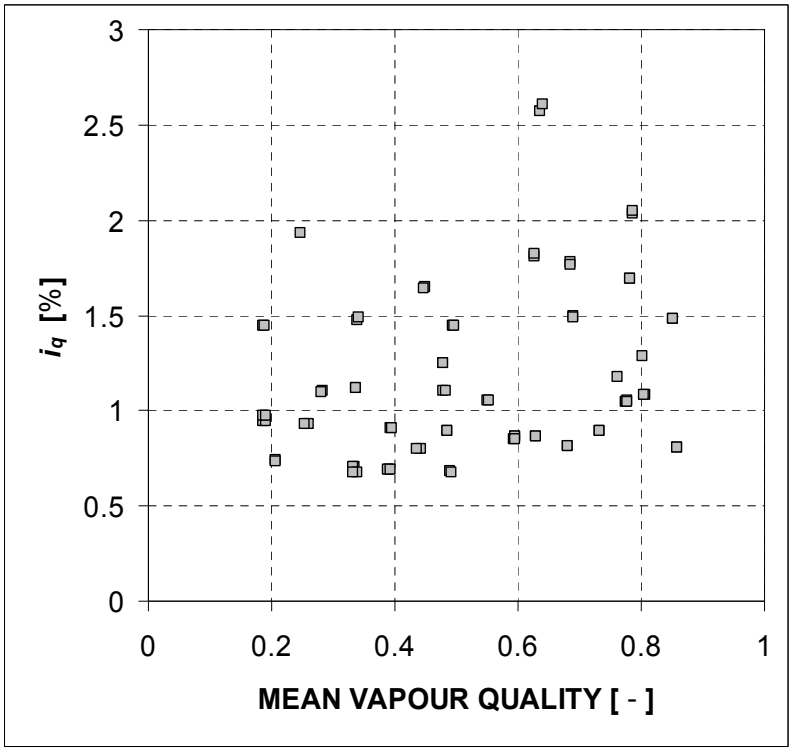

Figure 22. Experimental uncertainty on section 1 heat fluxes plotted against the vapour quality.

Figure 19, Figure 1.Figure 20, Figure 21 and Figure 22 report the experimental uncertainties of the heat fluxes of the pre-condenser and of section 1 plotted against the mass velocity and the vapour quality.

It is interesting to underline that the pre-condenser uncertainty is equally distributed all over the investigated range of mass velocities and vapour qualities, while the same values for the heat fluxes of section 1 decrease as the mass velocity increases and they are quite constant with the vapour quality.

Finally, Table 6 and Table 7 summarize the mean and the maximum values of the experimental uncertainty of the heat fluxes of the pre-condenser and of section 1. Overall, the uncertainties of heat fluxes depend on those of the water flow rates which present the highest values.

1.3.2.5 Inlet Test Sector Enthalpy

The refrigerant enthalpy at the inlet of the test sector can be evaluated using the following equation:

$$h_{ref,in2} = h_{ref,out1} = h_{ref,in1} - \frac{q_1}{\dot{m}_{ref}} \qquad \textbf{Eq. 45}$$

Where $h_{ref,in1}$ is obtained from the heat balance at the pre-condenser. By deriving Eq. 45, the sensitivity coefficients are:

$$\frac{\partial h_{ref,in2}}{\partial h_{ref,in1}} = 1 \qquad \left|\frac{\partial h_{ref,in2}}{\partial q_1}\right| = \frac{1}{\dot{m}_{ref}} \qquad \left|\frac{\partial h_{ref,in2}}{\partial \dot{m}_{ref}}\right| = \frac{q_1}{\dot{m}_{ref}^2}$$

So the derived uncertainty is:

$$i_h = \sqrt{\left(\frac{\partial h_{ref,in2}}{\partial \dot{m}_{ref}} \cdot i_{mref}\right)^2 + \left(\frac{\partial h_{ref,in2}}{\partial h_{hin1}} \cdot i_{hin1}\right)^2 + \left(\frac{\partial h_{ref,in2}}{\partial q_1} \cdot i_{q1}\right)^2}$$

Table 8 reports the calculated average and maximum values of the experimental uncertainty of the different parameters. It appears that the experimental uncertainty of the enthalpy at the inlet test sector strongly depends from that of the enthalpy at the inlet of sector 1.

Table 8. Experimental inlet test sector enthalpy uncertainty.

	$h_{ref,in2}$	$h_{ref,in1}$	q_1
i_m [%]	1.32	1.14	1.16
i_{max} [%]	1.59	1.44	2.61

1.3.2.6 Test Sector Heat Flux

The uncertainty of the heat flux measured in the test sector is one of the most important ones, because the accuracy of the heat transfer coefficients directly depends on this measure. The experimental value of the heat flux exchanged in the test measuring sector is equal to:

$$q_2 = \dot{m}_{w2} \cdot c_{p,w2} \cdot \Delta T_{w,2} \qquad \textbf{Eq. 46}$$

And the essential relations for the sensitivity coefficients used in experimental uncertainty calculations are:

$$\frac{\partial q_2}{\partial \dot{m}_{w,2}} = c_{p,w2} \cdot \Delta T_{w,2} = \frac{q_2}{\dot{m}_{w,2}} \qquad \frac{\partial q_2}{\partial c_{p,w2}} = \dot{m}_{w,2} \cdot \Delta T_{w,2} = \frac{q_2}{c_{p,w2}} \qquad \frac{\partial q_2}{\partial \Delta T_{w,2}} = \dot{m}_{w,2} \cdot c_{p,w2} = \frac{q_2}{\Delta T_{w,2}}$$

And finally:

$$i_{q2} = \sqrt{\left(\frac{\partial q_2}{\partial \dot{m}_{w,2}} \cdot i_{mw}\right)^2 + \left(\frac{\partial q_2}{\partial c_{p,w2}} \cdot i_{cp}\right)^2 + \left(\frac{\partial q_2}{\partial \Delta T_2} \cdot i_{\Delta T}\right)^2}$$

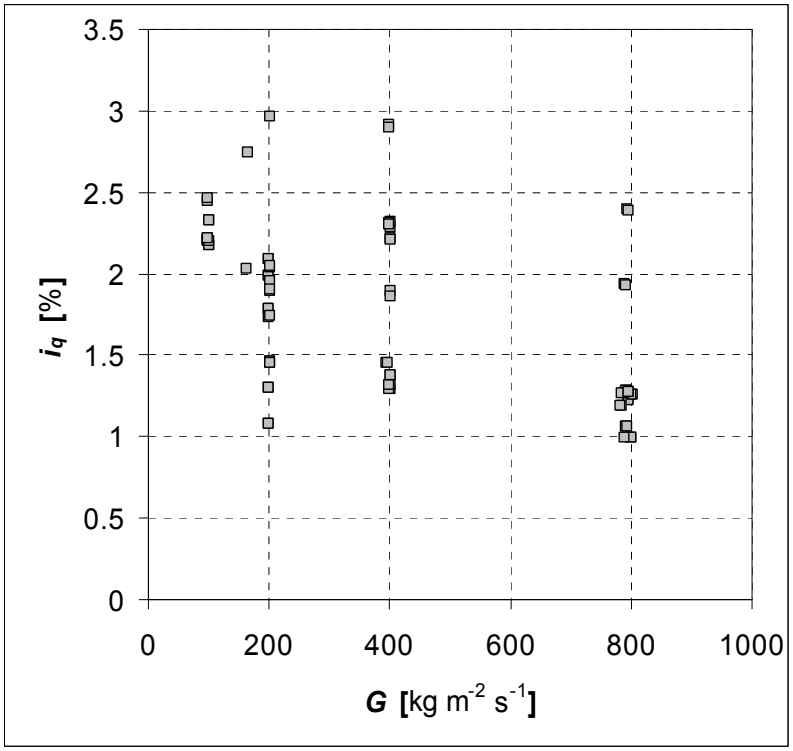

Figure 23. Experimental uncertainty on the test sector heat flux plotted against the mass velocity.

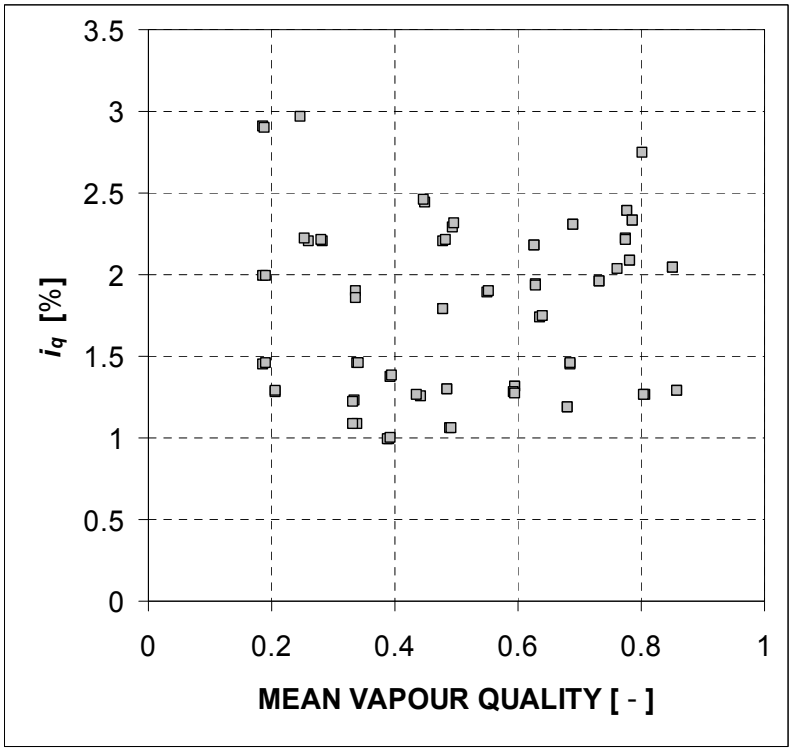

Figure 24. Experimental uncertainty on the test sector heat flux plotted against the vapour quality.

Figure 23 and Figure 24 report the uncertainties calculated for the heat flux exchanged in the measuring sector as a function of mass velocity and vapour quality.

The maximum uncertainty is around 3% at 200 kg m^{-2} s^{-1} at low mean vapour quality. The calculated values are uniformly distributed all over the range of the operating test conditions. Table 9 summarizes the value of the mean and maximum uncertainty values obtained in the calculations. From a deep analysis of the data, it appears that the uncertainty on the heat flux of the test sector depends on that of the water temperature difference.

Table 9. Experimental test sector heat flux uncertainty.

	q_2	$\dot{m}_{w2}$	ΔT_2
i_m **[%]**	1.78	1.60	1.17
i_{max} **[%]**	2.96	10.2	2.89

1.3.2.7 Mean Vapour Quality

The mean vapour quality in the test sector is defined as:

$$\overline{x} = \frac{h_{ref,m} - h_L}{h_{LG}} \qquad \textbf{Eq. 47}$$

As before, the sensitivity coefficients are:

$$\frac{\partial \overline{x}}{\partial h_{ref,m}} = \frac{1}{h_{LG}} \qquad \left|\frac{\partial \overline{x}}{\partial h_L}\right| = \frac{1}{h_{LG}} \qquad \left|\frac{\partial \overline{x}}{\partial h_{LG}}\right| = \frac{h_{ref,m} - h_L}{h_{LG}^2}$$

And finally:

$$i_x = \sqrt{\left(\frac{\partial \overline{x}}{\partial h_{ref,m}} \cdot i_{hm}\right)^2 + \left(\frac{\partial \overline{x}}{\partial h_L} \cdot i_{hL}\right)^2 + \left(\frac{\partial \overline{x}}{\partial h_{LG}} \cdot i_{hLG}\right)^2}$$

Table 10. Vapour quality experimental uncertainty.

	x_m	h_m	h_{LG}
i_m [%]	8.08	1.37	1.41
i_{max} [%]	18.8	1.68	1.41

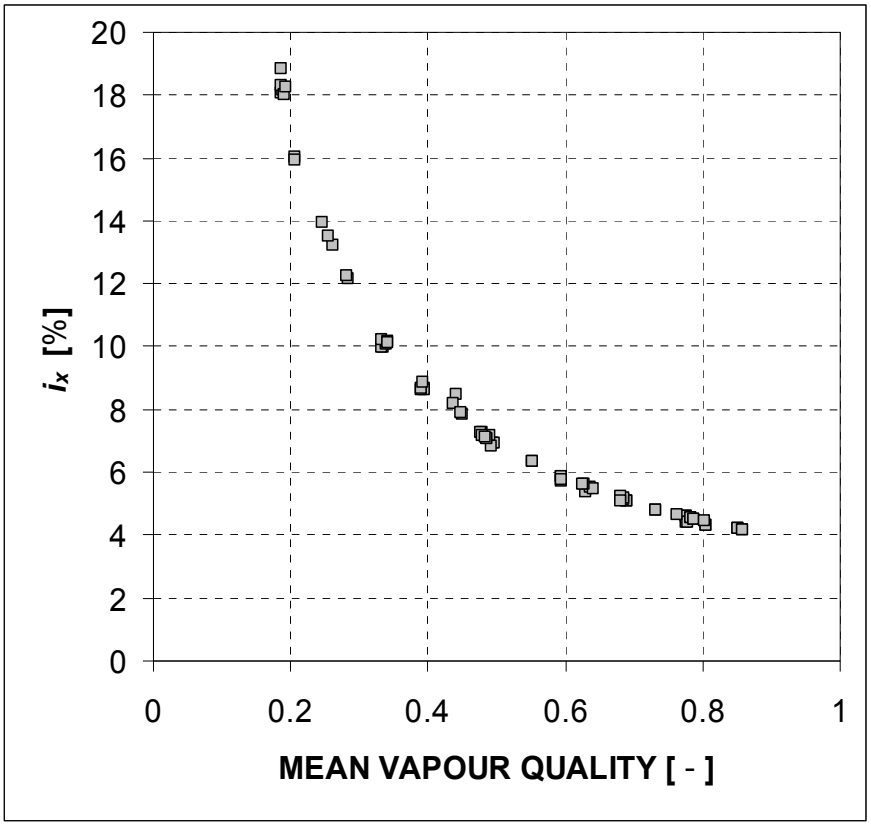

Figure 25. Vapour quality experimental uncertainty plotted against the vapour quality.

The computed statistical parameters of the mean vapour quality uncertainty are reported in Table 10; the mean value is 8.08% with a maximum of 18.8% at low vapour quality. Furthermore, in Figure 25 and Figure 26 the values of the uncertainty are plotted as a function of both the vapour quality and the mass velocity. Since the absolute values of the uncertainty are quite constant, around ± 0.03, the percentage error decreases as the vapour quality increases, while it appears to be independent on the mass velocity.

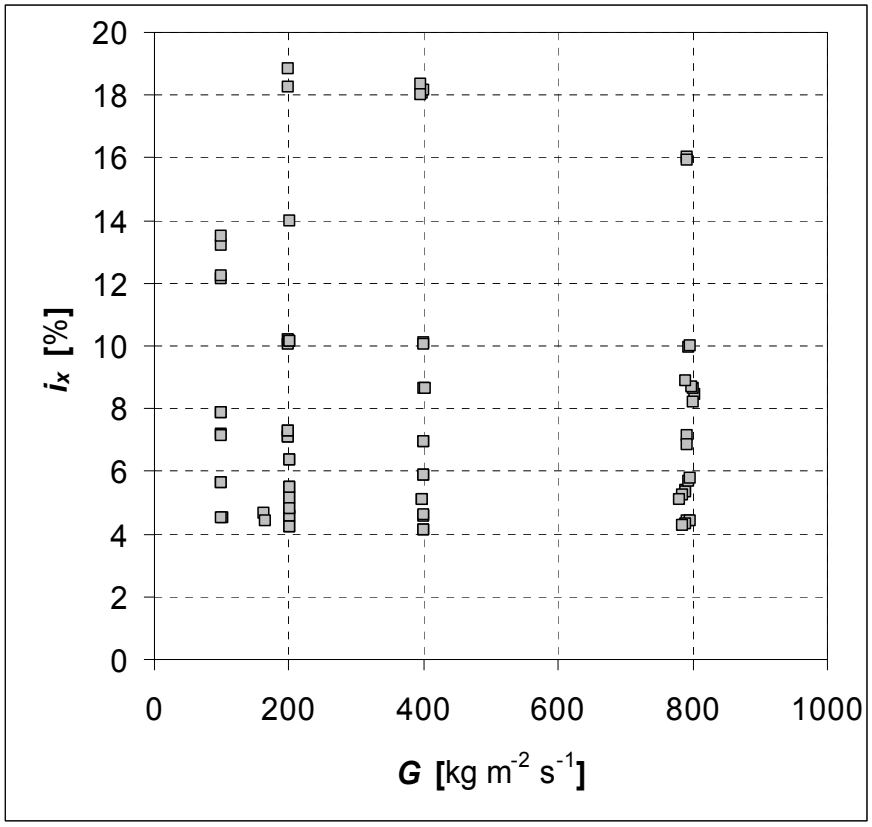

Figure 26. Vapour quality experimental uncertainty plotted against the mass velocity.

1.3.2.8 Heat Transfer Coefficient (HTC)

The heat transfer coefficient defined in paragraph 1.3.1.3 by Eq. 27 is here described as:

$$HTC = \frac{q_2}{A \cdot \left(T_{sat,2} - T_{wall,2} \right)}$$

When this equation is derived, the following sensitivity coefficients can be obtained:

$$\frac{\partial HTC}{\partial q_2} = \frac{1}{A \cdot \left(T_{sat,2} - T_{wall,2} \right)} = \frac{HTC}{q_2} \qquad \frac{\partial HTC}{\partial \Delta T} = \frac{q_2}{A} = \frac{HTC}{\left(T_{sat,2} - T_{wall,2} \right)}$$

And the uncertainty of the heat transfer coefficient is:

$$i_{HTC} = \sqrt{\left(\frac{\partial HTC}{\partial q_2}\cdot i_{q2}\right)^2 + \left(\frac{\partial HTC}{\partial \Delta T}\cdot i_{\Delta T}\right)^2}$$

Table 11 reports the statistical results of the calculation; the maximum value of the heat transfer experimental error is 3.64%, with an average value of around 2.3%.

Table 11. Heat transfer coefficient experimental uncertainty.

	HTC	q_2	ΔT
i_m **[%]**	2.29	1.78	1.38
i_{max} **[%]**	3.64	2.96	2.61

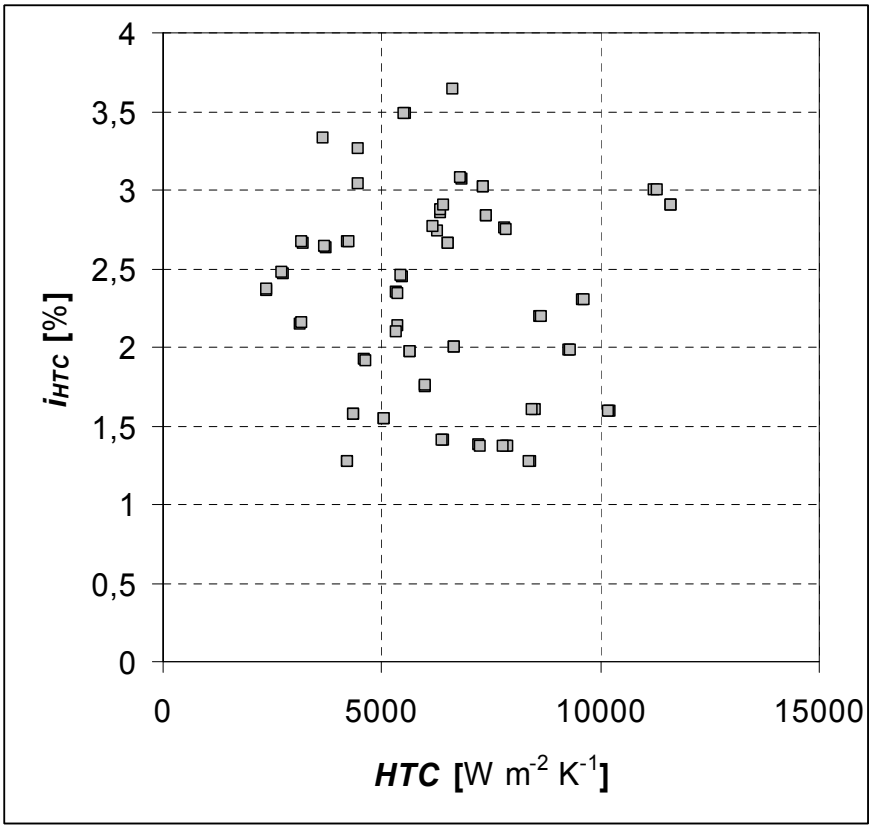

Figure 27. Heat transfer coefficient experimental uncertainty plotted against its value.

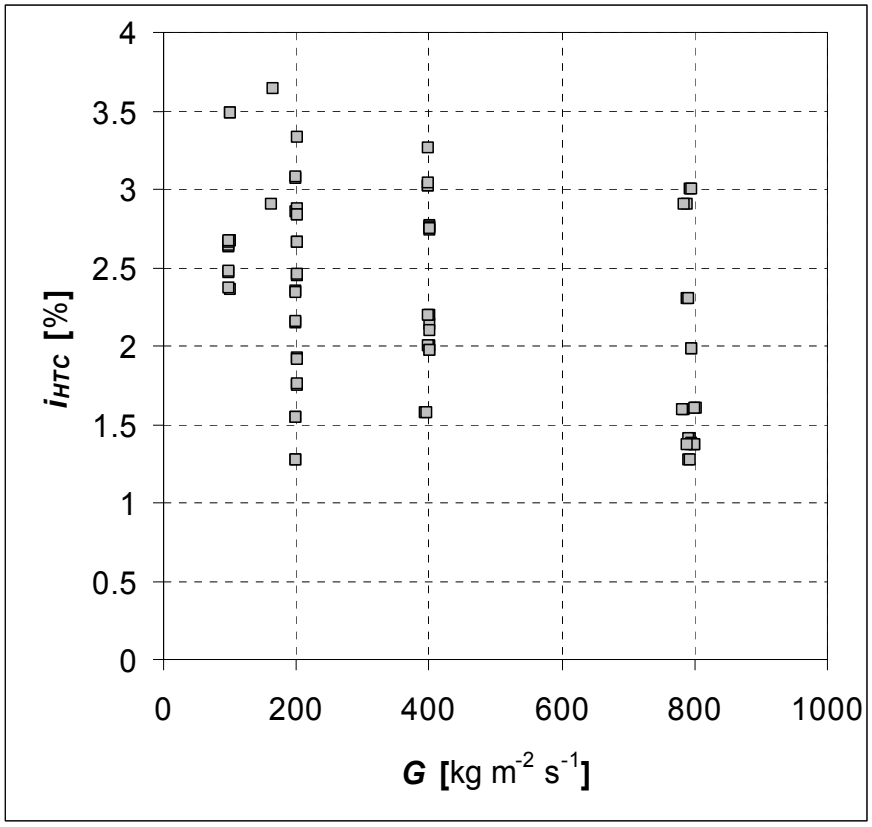

Figure 28. Heat transfer coefficient experimental uncertainty plotted against the mass velocity.

The experimental uncertainty of the heat transfer coefficient is plotted against its value in Figure 27, its values do not exhibit any dependence on the heat transfer coefficient.

Figure 28 and Figure 29 report the heat transfer uncertainty plotted against the most important operating test conditions: the mass velocity and the mean vapour quality. The uncertainty is uniformly distributed over the range of the operating test conditions. Figure 30 and Figure 31 describe the relationships between the uncertainty of the heat transfer coefficient and those of the test section heat flux and temperature difference.

Overall, the heat transfer coefficient uncertainty linearly increases with the uncertainties of both the heat flux and the temperature difference.

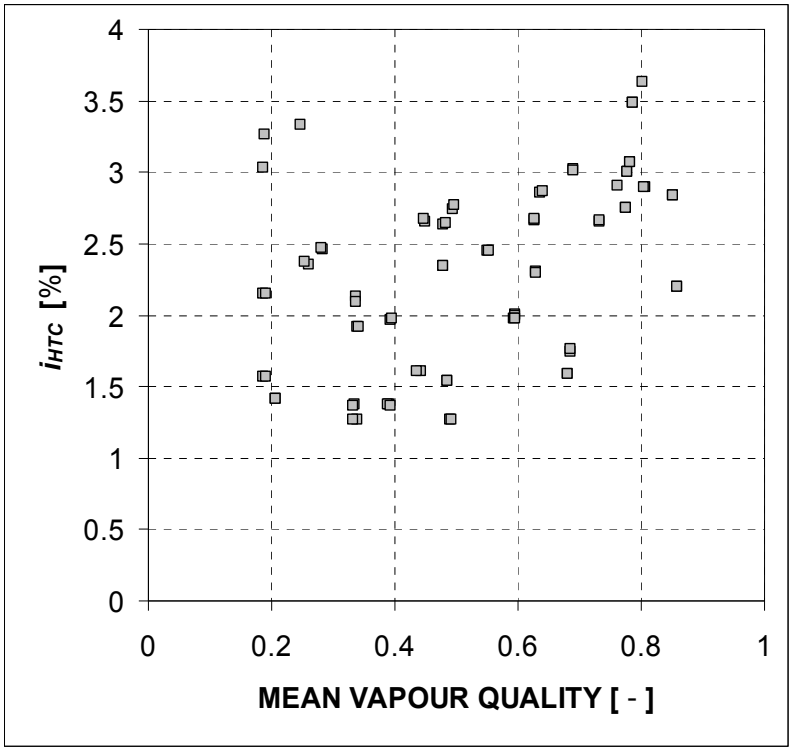

Figure 29. Heat transfer coefficient experimental uncertainty plotted against the mean vapour quality.

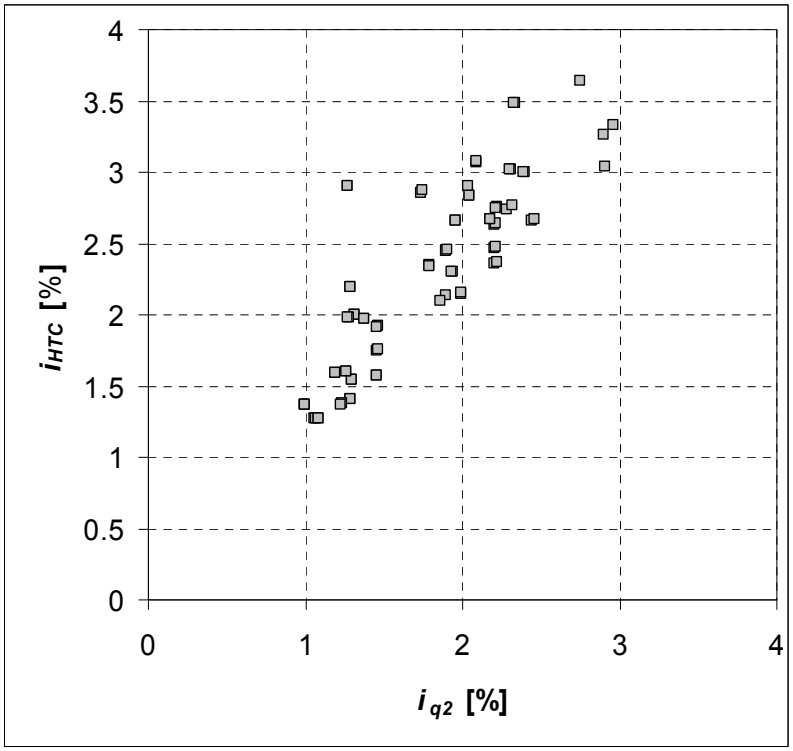

Figure 30. Heat transfer coefficient uncertainty plotted against heat flux uncertainty.

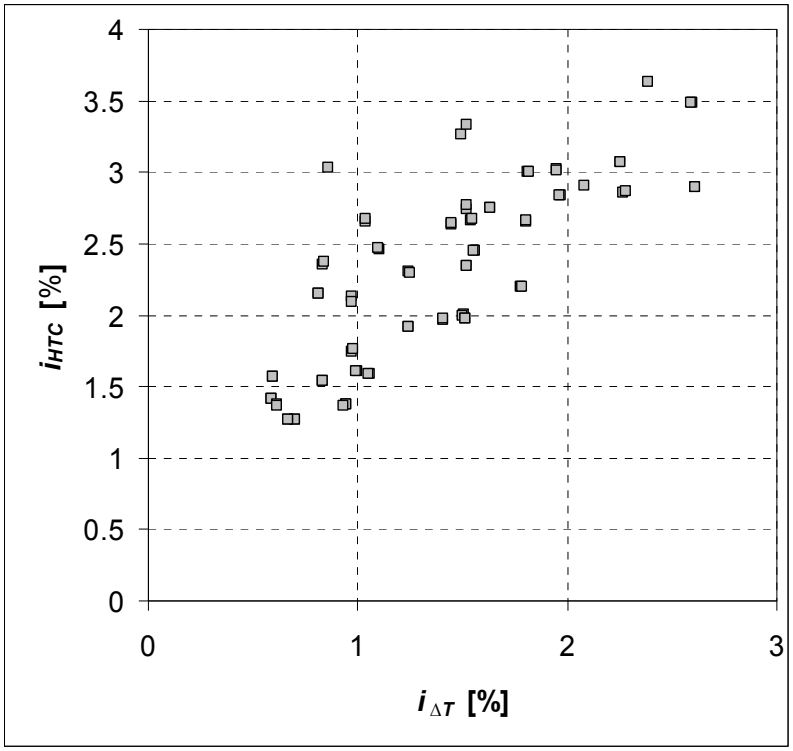

Figure 31. Heat transfer coefficient uncertainty plotted against temperature difference uncertainty.

1.3.2.9 Pressure Drop and Pressure Gradient

The refrigerant pressure drop is a direct measure obtained by means of a differential pressure transducer which has an accuracy of ± 50 Pa.

Figure 32 reports the pressure gradient uncertainty as a function of its experimental value; since the pressure drop accuracy is constant, the error decreases as the pressure gradient increases.

The diagram plots only the uncertainty of the frictional pressure gradient measured under adiabatic test conditions.

Since this fluid is a high pressure refrigerant, it exhibits very low two-phase pressure drops when compared to medium or low pressure refrigerants. This explains the very high experiment uncertainties exhibited at low specific mass flux. In fact these values range between 20% and 5% at 200 kg m^{-2} s^{-1}, while they vary between 3% and 0.2% at 400 and 800 kg m^{-2} s^{-1}.

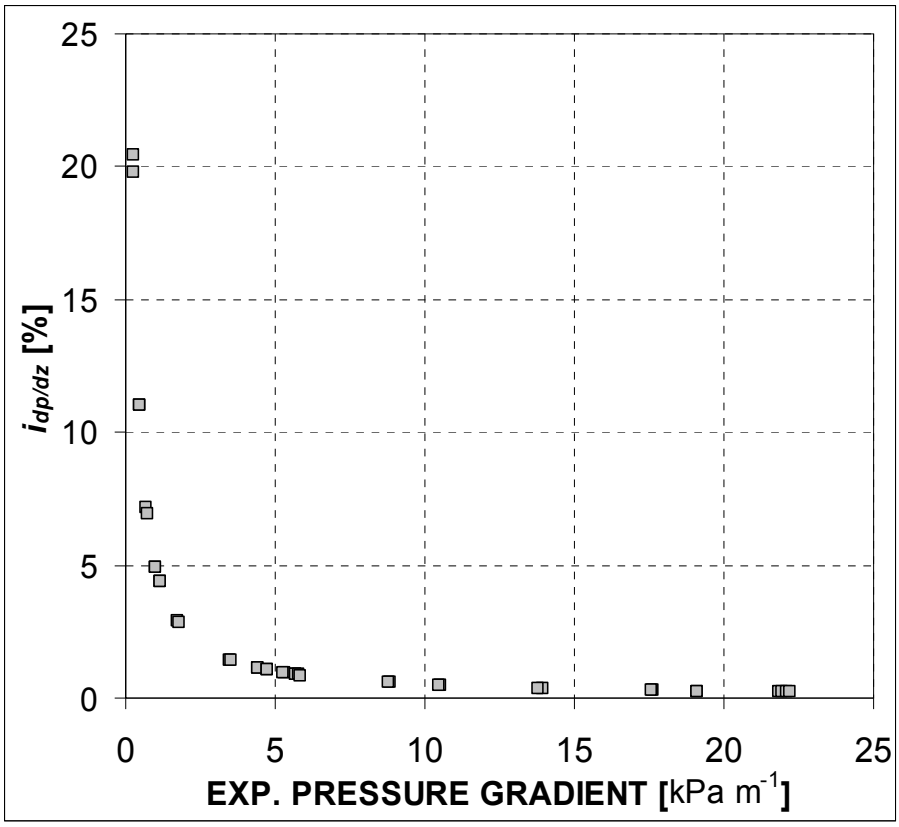

Figure 32. Pressure gradient uncertainty plotted against the experimental frictional pressure gradient.

1.3.3 Experimental Results

1.3.3.1 Operating Test Conditions

The experimental data points were taken during condensation of R410A inside a microfin tube at saturation temperature of around 40 °C. This temperature value represents a reference point for the air conditioning applications.

The refrigerant mass flow rate and the vapour quality were varied in order to investigate a wider range of operating test conditions.

In particular, the mass flow rate was changed between 100 kg m^{-2} s^{-1} and 800 kg m^{-2} s^{-1} and the mean vapour quality was varied from 0.20 to 0.95.

Table 12. Experimental operating test conditions. Within brackets, the experimental data points at each vapour quality.

G [kg m^{-2} s^{-1}]	x, mean vapour quality [-]
Condensation heat transfer measurements at 40 °C of saturation temperature	
100	0.20 (2), 0.22 (2), 0.39 (2), 0.42 (2), 0.57 (2), 0.73 (2)
200	0.19 (2), 0.25 (1), 0.30 (2), 0.34 (2), 0.45 (2), 0.48 (2), 0.52 (2), 0.65 (4), 0.70 (2), 0.75 (2), 0.82 (2)
400	0.19 (4), 0.34 (2), 0.40 (2), 0.50 (2), 0.60 (2), 0.70 (2), 0.78 (2), 0.85 (2)
800	0.21 (2), 0.34 (2), 0.40 (3), 0.44 (2), 0.50 (2), 0.60 (2),0.64 (2), 0.69 (2), 0.79 (2), 0.81 (2)
Condensation pressure drops measurements at 40 °C of saturation temperature	
200	0.42 (2), 0.56 (2), 0.68 (2)
400	0.28 (2), 0.42 (2), 0.46 (2), 0.55 (2), 0.67 (2), 0.74 (2)
800	0.30 (2), 0.43 (2), 0.45 (3), 0.59 (2), 0.64 (2), 0.68 (2), 0.74 (2), 0.82 (2), 0.84 (2)
Adiabatic pressure drops measurements at 40 °C of saturation temperature	
200	0.20 (2), 0.33 (2), 0.48 (2), 0.64 (2), 0.74 (2)
400	0.20 (2), 0.43 (2), 0.57 (2), 0.63 (2), 0.73 (2), 0.83 (2), 0.92 (2)
800	0.27 (2), 0.33 (2), 0.49 (2), 0.64 (2), 0.73 (2), 0.87 (2), 0.96 (2)

Considering the pressure drops measurements, the results are reported in terms of pressure gradient. The data have been subdivided into two categories: the adiabatic measurements and the measurements taken during condensation. When the vapour quality change occurs, the measured pressure drops are less than the ones registered in adiabatic test conditions because of the presence of the acceleration term. The frictional pressure gradients are calculated by subtracting the acceleration terms which are negative during condensation.

Table 12 summarises the operating test conditions concerning heat transfer and pressure drop measurements.

The operating test conditions can be visualised in a flow regime map where the two-phase flow patterns transitions are plotted.

In Figure 33 the condensation heat transfer data are plotted in Doretti et al. [20] flow regime map. As described in paragraph 1.1.4, this map subdivides the plain into two regions: the ΔT-independent sector, where the flow regime is controlled by the shear stress, and the ΔT-dependent sector, where gravity is the controlling force.

As it appears in this diagram, all data points at 100 kg m^{-2} s^{-1} and 800 kg m^{-2} s^{-1} fall into, respectively, the ΔT-dependent and ΔT-independent regions.

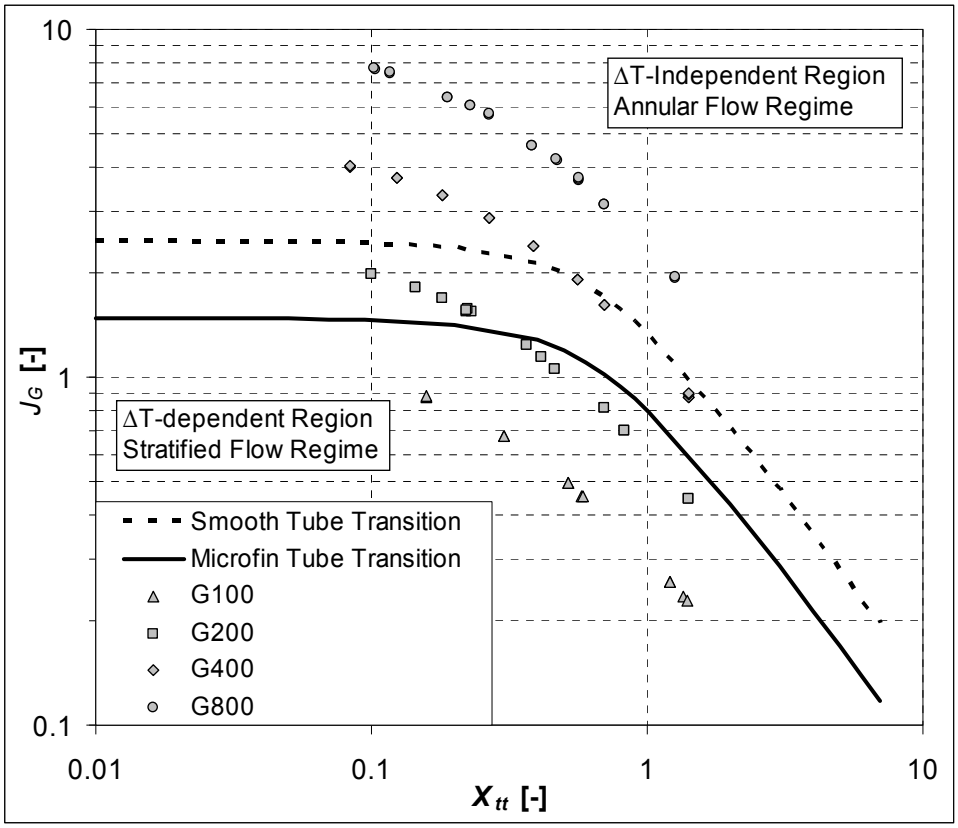

Figure 33. Condensation heat transfer data plotted in Doretti et al. [20] flow regime map G [kg m^{-2} s^{-1}].

Data at 200 kg m^{-2} s^{-1} are over the transition line for microfin tubes. This result confirms the flow pattern visualizations which have demonstrated the effect of the microfin tube geometry on the flow regime transition.

Most of the data at 400 kg m^{-2} s^{-1} are in the ΔT-independent region; few data points, at low vapour quality, are just under the transition line for smooth tubes.

1.3.3.2 Condensation Heat Transfer Coefficient

The experimental heat transfer coefficients were collected during condensation of R410A inside a microfin tube at a saturation temperature of 40 °C.

In Figure 34, the condensation heat transfer coefficient referred to the surface area of a plain tube with an inner diameter of 7.69 mm is plotted against the mean vapour quality.

The trend of the heat transfer coefficient versus the vapour quality is similar to those already measured for R22, R407C and R134a [22, 23]. At high mass velocity, 800 kg m^{-2} s^{-1}, the heat transfer coefficient varies linearly with the vapour quality, while at lower mass velocity, around 200 kg m^{-2} s^{-1}, the heat transfer coefficient increases more than linearly at high vapour quality and decreases more than linearly at low vapour quality.

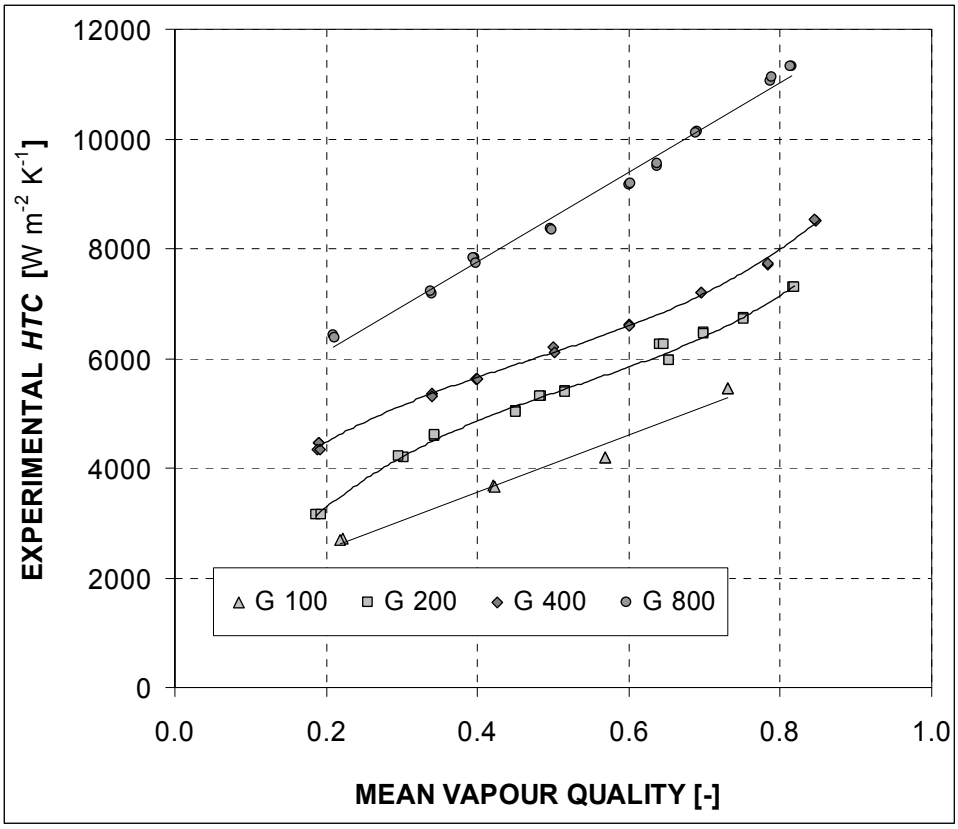

Figure 34. Condensation heat transfer coefficient against the mean vapour quality. Saturation temperature of 40 °C.

In general, the heat transfer coefficient increases as the vapour quality and the mass velocity increase.

The trend exhibited at 200 kg m^{-2} s^{-1} can be explained with reference to Figure 33; in fact, the enhancement of the heat transfer coefficient could be due to the early transition from the wavy stratified flow to the annular flow regime promoted by the spiral micro-fins.

The experimental heat transfer coefficients in the microfin tube can be compared with those calculated for condensation in a smooth tube with an inner diameter equal to the fin tip diameter of the microfin tube at the same operating conditions.

The ratio between these two heat transfer coefficients is called Enhancement Factor (*EF*). The condensation heat transfer coefficient for a smooth tube is calculated using Cavallini et al. [16] model.

This model takes into account a simplified flow regime map, J_G-X_{tt}, where the plain has been subdivided into two parts, a ΔT-independent and a ΔT-dependent region; it was obtained from a best fitting procedure on data measured by the same authors in a smooth tube with a inner diameter of 8 mm [24].

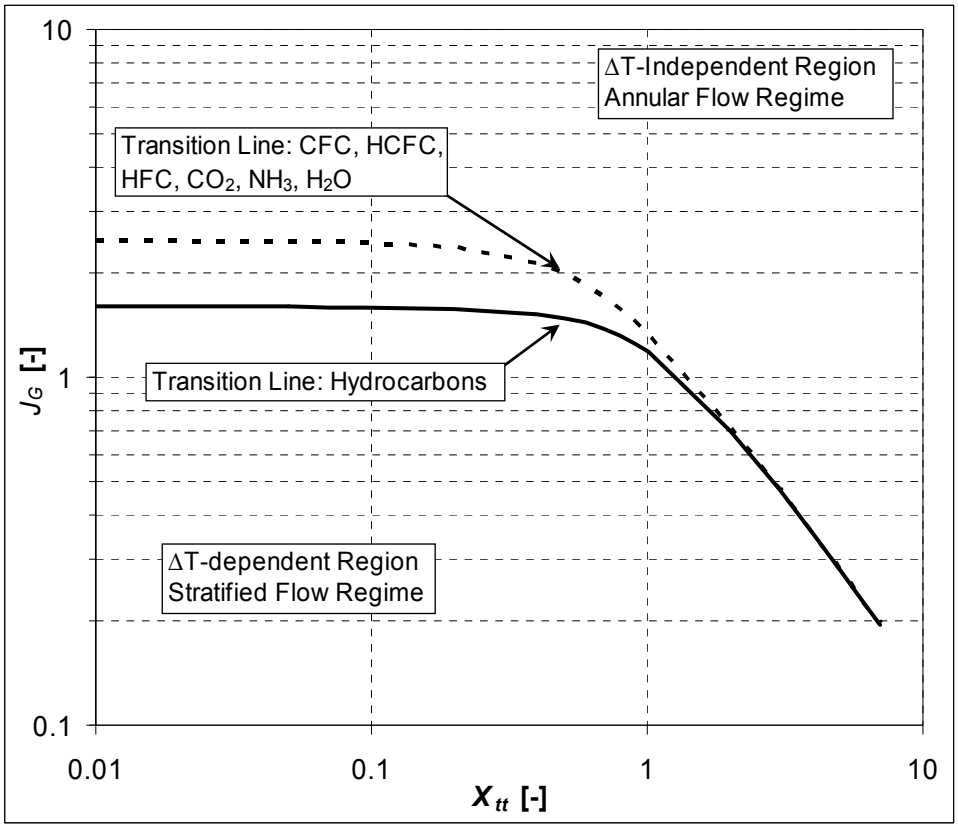

Figure 35. Cavallini et al. [16] flow regime map for the model application for smooth tube.

The transition line, plotted in Figure 35, can be calculated as:

$$J_G^T = \left\{ \left[\frac{7.5}{4.3 \cdot X_{tt}^{1.111} + 1} \right]^{-3} + C_T^{-3} \right\}^{-1/3} \qquad \textbf{Eq. 48}$$

Where C_T is set:

for hydrocarbons: C_T is 1.6
for others refrigerants: C_T is 2.6.

For the ΔT-independent region, $J_G > J_G^T$:

$$HTC_A = HTC_{LO} \cdot \left[1 + 1.128 \cdot x^{0.8170} \cdot \left(\frac{\rho_L}{\rho_G} \right)^{0.3685} \cdot \left(\frac{\mu_L}{\mu_G} \right)^{0.2363} \cdot \left(1 - \frac{\mu_G}{\mu_L} \right)^{2.144} \cdot \mathrm{Pr}_L^{-0.1} \right] \qquad \textbf{Eq. 49}$$

While for the ΔT-dependent region, $J_G < J_G^T$:

$$HTC_D = \left[HTC_A \cdot \left(\frac{J_G^T}{J_G} \right)^{0.8} - HTC_{strat} \right] \cdot \left(\frac{J_G}{J_G^T} \right) + HTC_{strat} \qquad \textbf{Eq. 50}$$

Where:

$$HTC_{LO} = 0.023 \cdot \mathrm{Re}_{LO}^{0.8} \cdot \mathrm{Pr}_L^{0.4} \cdot \frac{\lambda_L}{d_h} \qquad \textbf{Eq. 51}$$

and:

$$HTC_{strat} = \left[\frac{\lambda_L^3 \cdot \rho_L \cdot (\rho_L - \rho_G) \cdot g \cdot h_{LG}}{\mu_L \cdot d_h \cdot \Delta T} \right]^{0.25} \cdot \frac{0.725}{1 + 0.741 \cdot \left[\frac{(1-x)}{x} \right]^{0.3321}} + \left(1 - x^{0.087} \right) \cdot HTC_{LO} \qquad \textbf{Eq. 52}$$

With this value it is possible to calculate the Enhancement Factor as:

$$EF = \frac{HTC_{microfin}}{HTC_{smooth}} \qquad \textbf{Eq. 53}$$

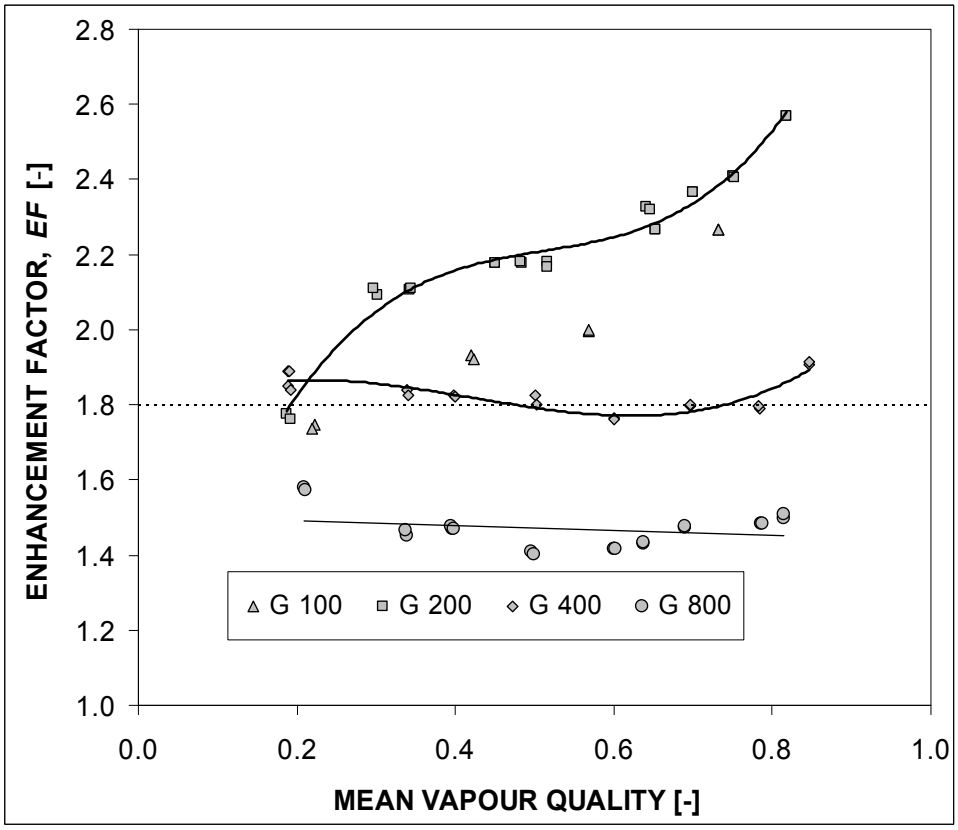

Figure 36. The Enhancement Factor plotted against the mean vapour quality as a function of the mass velocity.

Figure 36 reports the Enhancement Factor plotted against the mean vapour quality as a function of the mass velocity. It is interesting to highlight that at 200 kg m^{-2} s^{-1} the *EF* increases more than linearly at high vapour quality, while it decreases more than linearly at low vapour quality.

At this specific mass flux, the *EF* presents the highest values and, on the whole, it rises with the vapour quality, reaching 2.6 at x=0.8.

Figure 36 also reports the heat transfer area enhancement ($A_{MICROFIN}/A_{SMOOTH}$), which is 1.8; therefore, the enhancement of the heat transfer coefficient is not merely due to the area enhancement.

At low mass velocity, 100 kg m^{-2} s^{-1}, the *EF* increases linearly with the vapour quality, while at high mass velocities, 400 and 800 kg m^{-2} s^{-1}, it appears to be constant with the vapour quality. In particular, at 400 kg m^{-2} s^{-1}, the EF in equal to the heat transfer area enhancement, while at 800 kg m^{-2} s^{-1} the heat transfer coefficient is around 50% higher as compared with the smooth tube, the heat transfer enhancement is lower than the area enhancement. A possible explanation can be found in the increase of the thickness of the liquid film which submerges the micro-fins and penalizes their heat transfer enhancement.

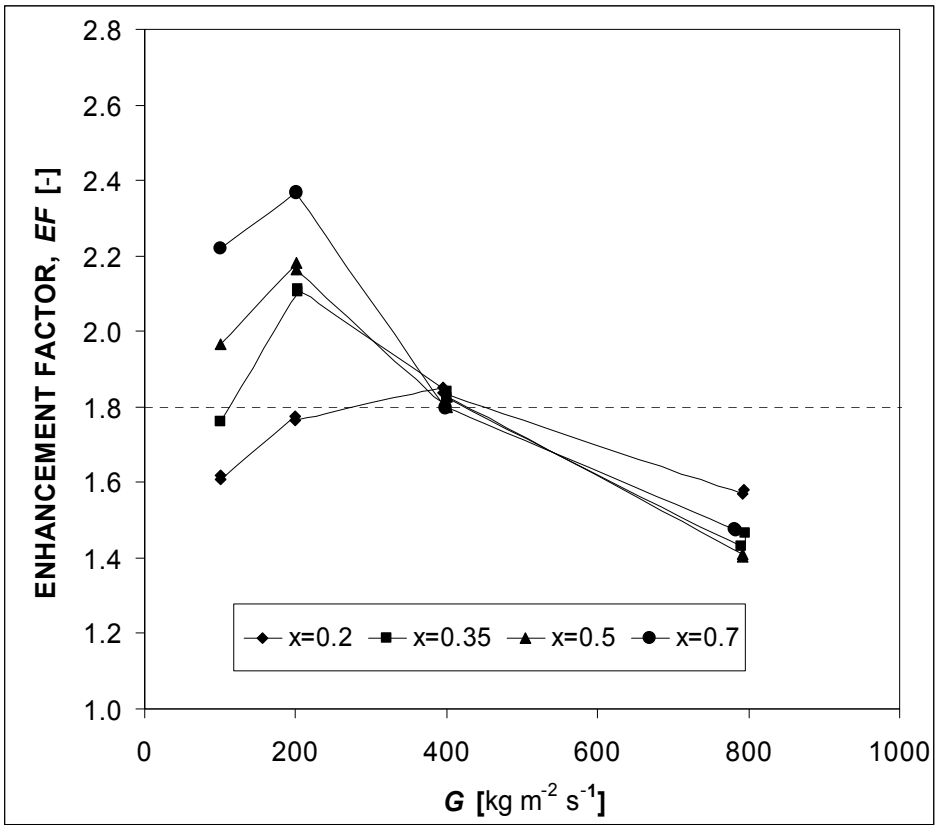

Figure 37. The Enhancement Factor, EF, plotted against the mass velocity as a function of the vapour quality.

Figure 37 plots the *EF* against the mass velocity as a function of the mean vapour quality and it shows that there is an optimal value of the mass velocity with respect to the heat transfer performance of a microfin tube. This is due to the flow pattern in the tube, as shown by Doretti et al. [20] and Cavallini et al. [7]. In fact, at low values of specific mass flux, micro-fins promote the annular flow pattern, leading to the maximum enhancement at a certain value of mass velocity.

1.3.3.3 Two-Phase Pressure Drop

During the experimental tests on condensation, two-phase pressure drops were also measured. Pressure drops are measured in the whole 1.4 m microfin test section, which is made of three diabatic parts. A differential pressure transducer is used in the tests. The total measured pressure drop is the sum of frictional and acceleration components. All data points were measured under saturated conditions all along the test section, with vapour quality changes ranging between 0.2 and 0.6. The frictional pressure gradient, reported in Figure 38, is obtained from the total pressure drop by subtracting the acceleration component, which is negative during the condensation process, Eq. 34. As said before, the void fraction model by Smith [21], Eq. 35, is used in the computation of the acceleration pressure change. The frictional pressure gradient was also measured under adiabatic test conditions in order to compare the different experimental procedures.

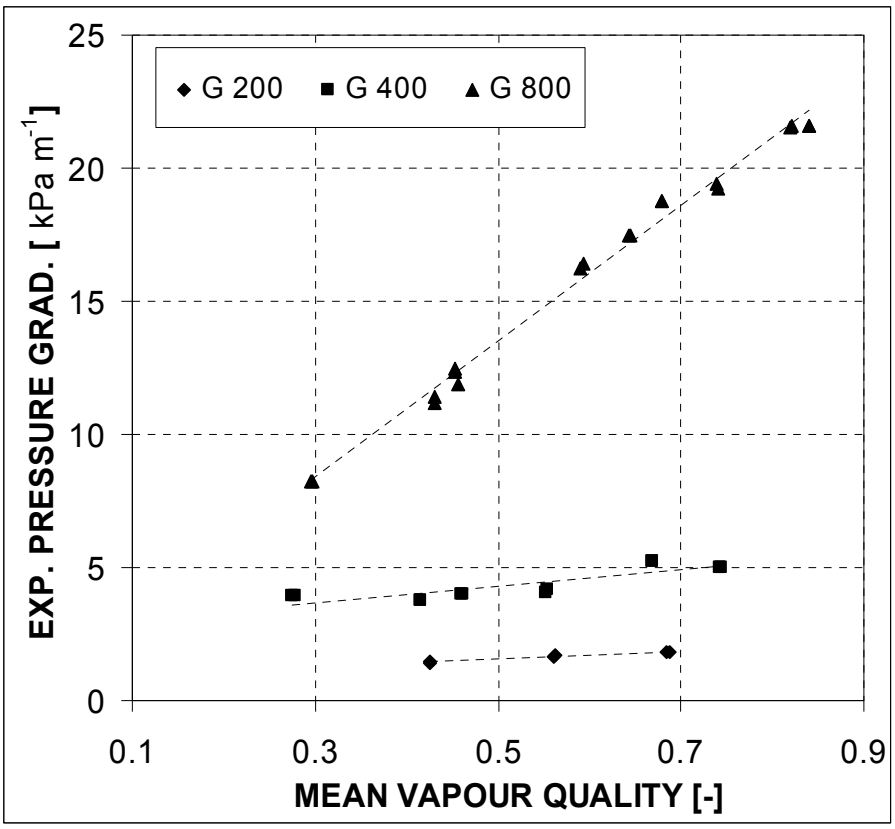

Figure 38. Frictional pressure gradient plotted against the vapour quality as a function of the specific mass flux. Diabatic tests.

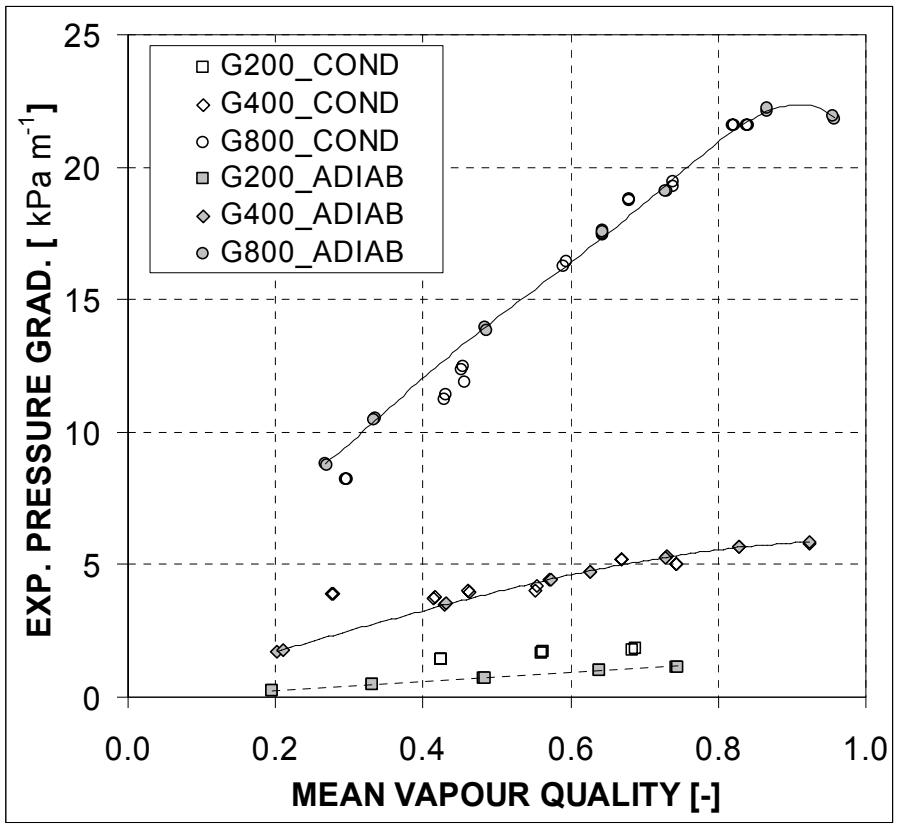

Figure 38 and Figure 39 report the described results; in particular, Figure 38 plots the frictional pressure gradients obtained from the condensation measurements against the mean vapour quality, while Figure 39 those measured in the adiabatic tests.

The frictional pressure gradient increases linearly with the average vapour quality and the increment appears to be higher at high mass velocity.

With respect to Figure 39, the two experimental procedures are in quite good agreement. Only at 200 kg m^{-2} s^{-1}, the frictional pressure gradients obtained from the condensation measurements are higher than those measured in the adiabatic tests.

Furthermore, at 800 kg m^{-2} s^{-1}, the frictional pressure gradient exhibits a maximum at x=0.86: the same qualitative results were found by Cavallini et al. [22 ,23] during tests with R134a and R22.

In fact, the frictional pressure gradient increases with the vapour quality, but at x=1 it must be equal to the gas one.

Figure 39. Frictional pressure gradient plotted against the vapour quality as a function of the specific mass flux. Adiabatic tests.

At the same operating conditions, the pressure gradient in a microfin tube can be compared to the pressure gradient in a smooth tube with an equivalent internal diameter. This ratio indicates that during condensation of R410A the pressure drops are about 2.5 times higher in the microfin tube than in the smooth one at mass velocities of 400 and 800 kg m^{-2} s^{-1}. The ratio of the pressure gradient in a microfin tube to that in a plain tube is above three at a mass velocity of 200 kg m^{-2} s^{-1}.

Table 13. Experimental and calculated pressure gradients.

G	x_{in}	x_{out}	Δx	$\bar{x}$	ε_{in}	ε_{out}	$-\left(\frac{dp}{dz}\right)_{tot}$	$-\left(\frac{dp}{dz}\right)_{a}$	$-\left(\frac{dp}{dz}\right)_{f}$	$\frac{-\left(\frac{dp}{dz}\right)_{f}}{-\left(\frac{dp}{dz}\right)_{tot}}$
[kg m^{-2} s^{-1}]	-	-	-	-	-	-	[Pa/m]	[Pa/m]	[Pa/m]	-
200	0.80	0.29	0.51	0.54	0.95	0.65	1526.8	-127.9	1654.7	1.08
200	0.80	0.29	0.51	0.55	0.95	0.66	1560.8	-127.9	1688.7	1.08
201	0.82	0.51	0.31	0.66	0.95	0.82	1709.4	-86.8	1796.2	1.05
201	0.82	0.51	0.31	0.67	0.96	0.83	1718.5	-86.3	1804.8	1.05
202	0.67	0.15	0.52	0.41	0.90	0.47	1329.2	-114.8	1444.0	1.09
202	0.67	0.15	0.52	0.41	0.90	0.47	1319.4	-114.8	1434.2	1.09
398	0.88	0.59	0.30	0.74	0.97	0.87	4681	-343.5	5024.5	1.07
399	0.89	0.59	0.30	0.74	0.97	0.87	4683.9	-343.6	5027.5	1.07
399	0.52	0.04	0.48	0.28	0.83	0.19	3559.8	-360.5	3920.3	1.10
399	0.52	0.04	0.47	0.28	0.83	0.21	3563.4	-359.0	3922.5	1.10
401	0.71	0.39	0.33	0.55	0.92	0.74	3859.8	-325.5	4185.3	1.08
401	0.71	0.38	0.33	0.55	0.92	0.74	3717.4	-328.0	4045.4	1.09
401	0.63	0.18	0.45	0.41	0.89	0.52	3356.6	-397.2	3753.7	1.12
401	0.63	0.18	0.45	0.41	0.89	0.52	3395.5	-397.6	3793.1	1.12
401	1.00	0.65	0.35	0.83	1.00	0.90	5986.1	-435.9	6422.1	1.07
790	0.81	0.53	0.28	0.67	0.95	0.84	17577	-1198.3	18775.3	1.07
791	0.81	0.53	0.28	0.67	0.95	0.84	17551.7	-1203.2	18754.9	1.07
792	0.87	0.30	0.56	0.58	0.97	0.67	13969.9	-2299.3	16269.2	1.17
792	0.54	0.05	0.50	0.29	0.85	0.23	6744.6	-1490.2	8234.8	1.22
793	0.87	0.31	0.56	0.59	0.97	0.68	14139	-2307.1	16446.2	1.16
793	0.54	0.04	0.50	0.29	0.85	0.22	6741	-1493.5	8234.5	1.22
793	0.92	0.70	0.22	0.81	0.98	0.92	20473.7	-1066.6	21540.3	1.05
795	0.69	0.16	0.54	0.43	0.91	0.49	9574.3	-1874.8	11449.1	1.20
796	0.69	0.16	0.54	0.43	0.91	0.49	9362.3	-1875.2	11237.5	1.20
797	0.92	0.70	0.22	0.81	0.98	0.92	20481.2	-1070.2	21551.4	1.05

Table 13 summarizes the pressure drop data reduction reporting the experimental friction pressure gradients, the acceleration terms and the ratio between the friction value and the measured total pressure gradient.

Moreover, the acceleration contribute varies between 4% and 18% with respect to the frictional one and it depends from the vapour quality change occurred during experimental measures.

In Table 13 are also reported: the mass velocity, the vapour qualities at the inlet and outlet of the test tube, the mean vapour quality and its variations, the void fractions at the inlet and outlet of the test tube calculated by Smith's equation [16].

The ratio between the friction and the total pressure gradient is listed in the last column. Since the acceleration term is negative, this ratio is always bigger than 1.

1.4 Prediction Models

1.4.1 Pressure Gradient: Introduction

In the previous paragraph, the experimental pressure drops measured during two-phase flow of R410A inside a microfin tube at a saturation temperature of 40 °C have been reported in terms of pressure gradients. An accurate estimation of the pressure gradient for different tube geometries, fluids and operating test conditions appears to be an important challenge for the researcher because of its relevance in the design of efficient heat exchangers. The pressure gradient is usually regarded as the sum of three components, namely the accelerational, gravitational, and frictional pressure gradients.

Here, we will categorize the models that are commonly used for predicting these system variables as follows.

1.4.2 Homogeneous Model

Here, the phases are assumed to be intimately mixed such that the mixture can be assigned a density corresponding to the total mass rate of flow divided by the total volume rate of flow.

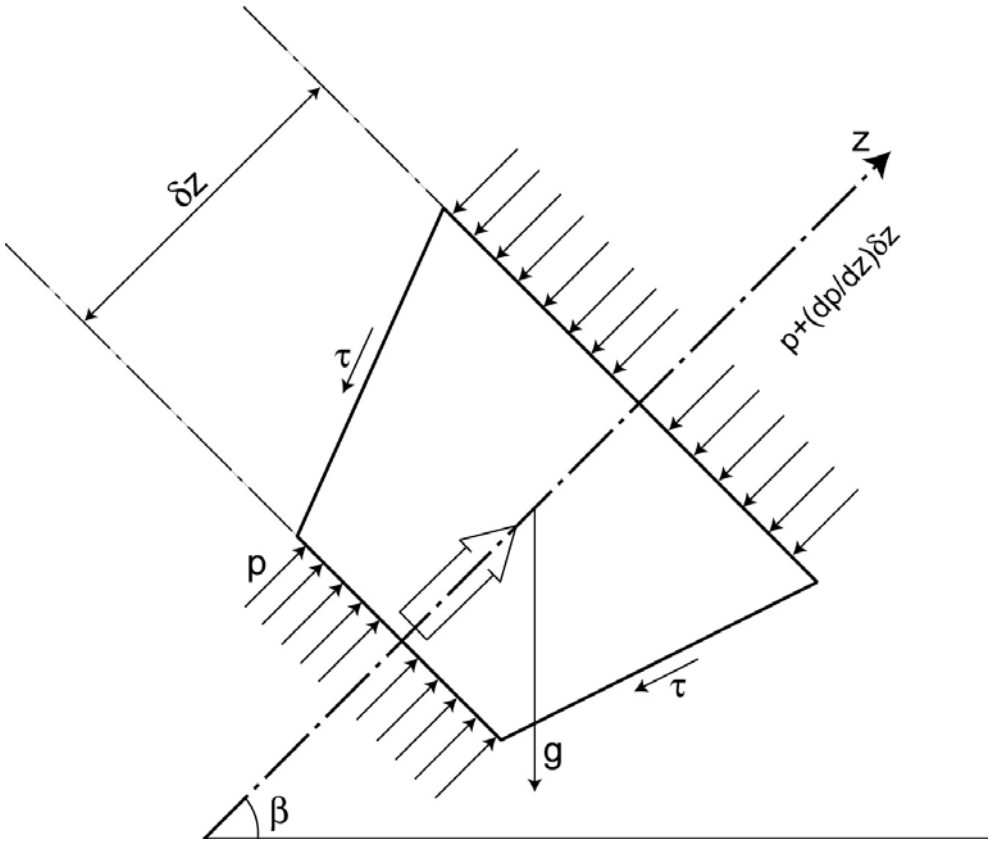

Figure 40. Schematic duct element for homogeneous model.

The velocity of the two phases is considered to be equal, and the flow can be treated by analogy with the single-phase flow. The acceleration and gravitational components of pressure drop can be calculated directly from the independent variables, and a correlation is required only for the friction term. Often, this term is calculated on the basis of single-phase flow correlations using an appropriate mean viscosity.
With respect to Figure 40, the homogeneous model considers the two-phase system as a homogeneous mixture where the liquid and vapour phases flow with the same velocity:

$$u_G = u_L \qquad u_G = \frac{G \cdot x}{\varepsilon \cdot \rho_G} \qquad u_L = \frac{G \cdot (1-x)}{\varepsilon \cdot \rho_L} \qquad \textbf{Eq. 54}$$

By substituting the liquid and vapour velocities in Eq. 54, it is possible to calculate the homogeneous expression of the void fraction (ε):

$$\varepsilon = \frac{\dfrac{x}{\rho_G}}{\dfrac{x}{\rho_G} + \dfrac{1-x}{\rho_L}} = \left[1 + \frac{(1-x)\cdot \rho_G}{x \cdot \rho_L}\right]^{-1} \qquad \textbf{Eq. 55}$$

When the ρ_L/ρ_G ratio increases, the homogeneous void fraction rises quickly from the vapour quality and it is equal to the vapour quality value at the critical point because $\rho_L=\rho_G$.
Considering the expression of the void fraction, the homogeneous density can be written as:

$$\rho_M = \varepsilon \cdot \rho_G + (1-\varepsilon)\cdot \rho_L = \left(\frac{x}{\rho_G} + \frac{1-x}{\rho_L}\right)^{-1} = \rho_{ho} \qquad \textbf{Eq. 56}$$

By applying the momentum change conservation to the duct element, represented in Figure 40, the following equation can be obtained:

$$-\left(\frac{dp}{dz}\right)\cdot A \cdot \delta z - \tau \cdot P \cdot \delta z - \rho_{ho} \cdot g \cdot \sin\beta \cdot A \cdot \delta z = \left(\frac{d(m \cdot u)}{dz}\right)\cdot \delta z \qquad \textbf{Eq. 57}$$

Where τ is the shear stress and u is the mixture velocity, which can be written as:

$$u = \frac{m}{\rho_{ho} \cdot A} \qquad \textbf{Eq. 58}$$

Finally, if the duct cross-sectional area is constant, Eq. 57 can be rearranged as:

$$-\left(\frac{dp}{dz}\right)_{TOT} =$$

$$= \frac{\tau \cdot P}{A} + \rho_{ho} \cdot g \cdot \sin\beta + G^2 \cdot \left(\frac{d\left(\frac{1}{\rho_{ho}}\right)}{dz} \right) = \left[-\left(\frac{dp}{dz}\right)_f \right] + \left[-\left(\frac{dp}{dz}\right)_g \right] + \left[-\left(\frac{dp}{dz}\right)_a \right] \qquad \textbf{Eq. 59}$$

In paragraph 1.3.1.4, a similar expression for the total pressure gradient was found; as said before, the subscripts *f*, *g* and *a* indicate the frictional, gravity and acceleration terms of the pressure gradient.

In general, the homogeneous model gives a poor representation of data for pressure gradient and void fraction in two-phase flows. As might have been expected, the closest fit to homogeneous model is obtained when the densities of the two phases begin to approach each other at high pressure.

1.4.3 Separated Flow Model

Here, the two phases are considered to be flowing in separate regions and with different velocities. However, the equations describing the flow (continuity, momentum and energy) are in combined form. To solve for the accelerational and gravitational pressure gradients, a correlation is required for void fraction, and for the frictional pressure gradient a separate correlation is required. Thus, while the method is usually more accurate than the homogeneous model, more empirical correlations are needed.

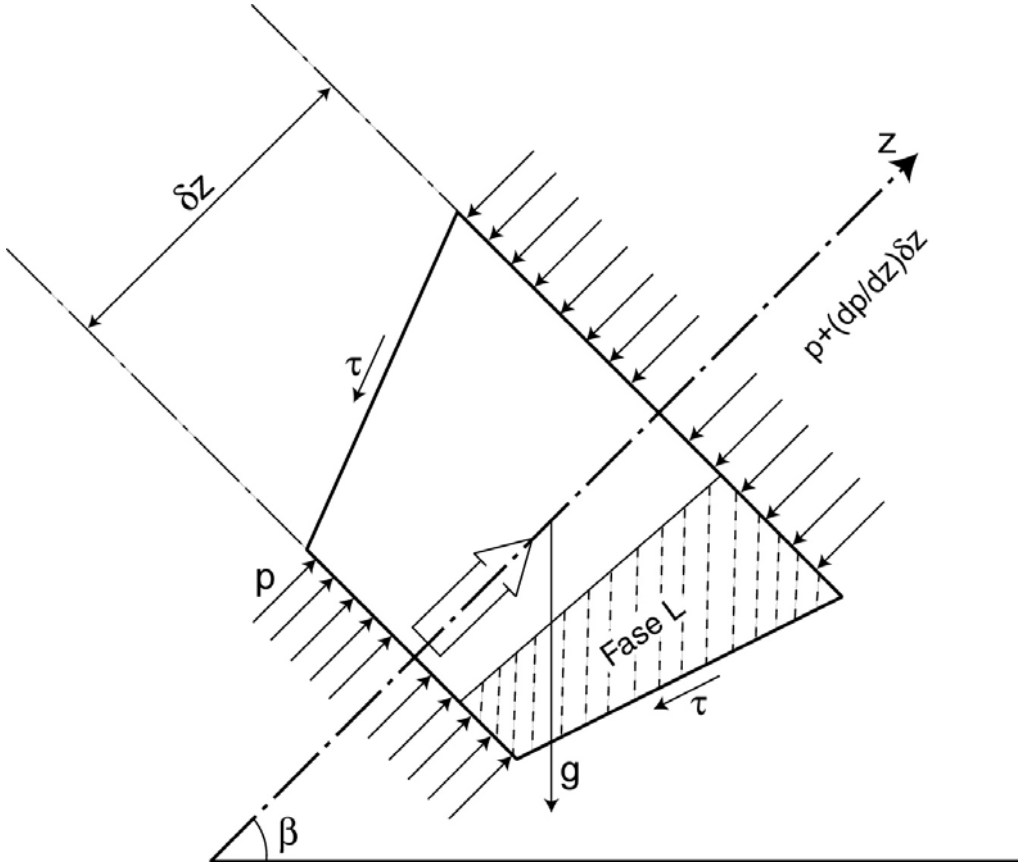

Figure 41. Schematic duct element for separated phases model.

As described in Figure 41, the two phases flow separated in two distinct regions with different velocities, one for the liquid phase and the other for the vapour one.
By analysing the duct element, it is possible to write the momentum change conservation principle, which can be explicated as follows:

$$-\left(\frac{dp}{dz}\right)\cdot A\cdot \delta z-\tau\cdot P\cdot \delta z-\rho_M\cdot g\cdot \sin\beta\cdot A\cdot \delta z=\left(\frac{d\left(m_G\cdot u_G+m_L\cdot u_L\right)}{dz}\right)\cdot \delta z \qquad \textbf{Eq. 60}$$

The mixture density and the two velocities are defined as:

$$\rho_M=\varepsilon\cdot\rho_G+(1-\varepsilon)\cdot\rho_L \qquad u_G=\frac{G\cdot x}{\varepsilon\cdot\rho_G} \qquad u_L=\frac{G\cdot(1-x)}{\varepsilon\cdot\rho_L} \qquad \textbf{Eq. 61}$$

If the cross-sectional area can be considered constant along the duct, the following expression can be obtained for the total pressure gradient:

$$-\left(\frac{dp}{dz}\right)=\frac{\tau\cdot P}{A}+\rho_M=\left(\varepsilon\cdot\rho_G+(1-\varepsilon)\cdot\rho_L\right)\cdot g\cdot\sin\beta+G^2\cdot\frac{d}{dz}\left(\frac{x^2}{\varepsilon\cdot\rho_G}+\frac{(1-x)^2}{(1-\varepsilon)\cdot\rho_L}\right)=$$
$$=\left[-\left(\frac{dp}{dz}\right)_f\right]+\left[-\left(\frac{dp}{dz}\right)_g\right]+\left[-\left(\frac{dp}{dz}\right)_a\right] \qquad \textbf{Eq. 62}$$

Again, the total pressure gradient can be expressed as the sum of three independent terms: the frictional, the gravitational and the accelerational pressure gradients.

Since the test microfin test is horizontal, the term linked to gravity is equal to zero, while the acceleration term has to be subtracted from the total measured pressure gradient.

For the separated flow model, correlations are required for both the frictional pressure gradient and the void fraction which influences both the accelerational and gravitational terms.

Therefore, in order to evaluate the acceleration pressure gradient, an accurate void fraction model has to be chosen. Three of the most important correlations are reported in the following.

Zivi's equation [26]:

$$\varepsilon=\frac{x}{\left[x+(1-x)\cdot\left(\frac{\rho_G}{\rho_L}\right)^{0.66}\right]} \qquad \textbf{Eq. 63}$$

Smith's correlation [21]:

$$\varepsilon^{-1}=1+\frac{(1-x)\cdot\rho_G}{x\cdot\rho_L}\cdot\left[0.4+0.6\cdot\sqrt{\frac{x\cdot\frac{\rho_L}{\rho_G}+0.4\cdot(1-x)}{x+0.4\cdot(1-x)}}\right] \qquad \textbf{Eq. 64}$$

Baroczy's correlation [27]:

$$\varepsilon = \left[1 + \left(\frac{1-x}{x} \right)^{0.74} \cdot \left(\frac{\rho_G}{\rho_L} \right)^{0.65} \cdot \left(\frac{\mu_L}{\mu_G} \right)^{0.13} \right]^{-1} \qquad \textbf{Eq. 65}$$

Considering the two-phase frictional pressure gradient, this can be linked to the one of the single-phase flow, which is more simply defined.

Thus, the two-phase multipliers are defined as the ratio between the two-phase frictional pressure gradients and the single-phase ones:

$$\Phi_L^2 = \frac{-\left(\frac{dp}{dz} \right)_f}{-\left(\frac{dp}{dz} \right)_{f,L}} \qquad \textbf{Eq. 66}$$

$$\left(\frac{dp}{dz} \right)_{f,L} = 2 \cdot f_L \cdot \frac{G^2 \cdot (1-x)^2}{d_h \cdot \rho_L} \qquad \textbf{Eq. 67}$$

.

$$\Phi_G^2 = \frac{-\left(\frac{dp}{dz} \right)_f}{-\left(\frac{dp}{dz} \right)_{f,G}} \qquad \textbf{Eq. 68}$$

$$\left(\frac{dp}{dz} \right)_{f,G} = 2 \cdot f_G \cdot \frac{G^2 \cdot x^2}{d_h \cdot \rho_G} \qquad \textbf{Eq. 69}$$

.

$$\Phi_{LO}^2 = \frac{-\left(\frac{dp}{dz} \right)_f}{-\left(\frac{dp}{dz} \right)_{f,LO}} \qquad \textbf{Eq. 70}$$

$$\left(\frac{dp}{dz} \right)_{f,LO} = 2 \cdot f_{LO} \cdot \frac{G^2}{d_h \cdot \rho_L} \qquad \textbf{Eq. 71}$$

$$\Phi_{GO}^2 = \frac{-\left(\frac{dp}{dz} \right)_f}{-\left(\frac{dp}{dz} \right)_{f,GO}} \qquad \textbf{Eq. 72}$$

$$\left(\frac{dp}{dz} \right)_{f,GO} = 2 \cdot f_{VO} \cdot \frac{G^2}{d_h \cdot \rho_G} \qquad \textbf{Eq. 73}$$

The single-phase friction factors, recalled in the previous equations, are calculated in relation to the flow pattern with the following equations:

for laminar flow regime:

$$f = \frac{16}{\mathrm{Re}} \qquad \textbf{Eq. 74} \qquad \mathrm{Re} < 2000$$

for turbolent flow regime:

$$f = 0.046 \cdot \mathrm{Re}^{-0.2} \qquad \textbf{Eq. 75} \qquad \mathrm{Re} > 2000$$

or:

$$f = 0.079 \cdot \mathrm{Re}^{-0.25} \qquad \textbf{Eq. 76} \qquad \mathrm{Re} > 2000$$

The friction factors f_L, f_G, f_{LO} and f_{GO} are estimated using the Reynolds number defined as follows:

$$\mathrm{Re}_L = \frac{G \cdot (1-x) \cdot d_h}{\mu_L} \qquad \textbf{Eq. 77}$$

$$\mathrm{Re}_G = \frac{G \cdot x \cdot d_h}{\mu_G} \qquad \textbf{Eq. 78}$$

$$\mathrm{Re}_{LO} = \frac{G \cdot d_h}{\mu_L} \qquad \textbf{Eq. 79}$$

$$\mathrm{Re}_{GO} = \frac{G \cdot d_h}{\mu_G} \qquad \textbf{Eq. 80}$$

Several of the different semi-empirical correlations for the evaluation of the frictional pressure drop proposed in the open literature are presented here and applied to the experimental test conditions. The results will be compared with the experimental pressure drops in order to analyse the accuracy of the predictions.

1.4.3.1 Haraguchi et al. Model [28]

Haraguchi et al. [28] proposed a correlation based on their measured pressure drop data for condensation in a microfin tube with R123, R134a and R22.

The pressure gradient is expressed by:

$$-\left(\frac{dp}{dz}\right)_f = \Phi_G^2\left[-\left(\frac{dp}{dz}\right)_{f,G}\right] = \Phi_G^2 \ \frac{2 f_{G,e}\left(G\,x\right)^2}{d_{eq}\ \rho_G} \qquad \textbf{Eq. 81}$$

Where:

$$\Phi_G = 1.1 + 1.3\left(Fr_{eq}\ X_{tt}\right)^{0.35} \qquad \textbf{Eq. 82}$$

and:

$$Fr_{eq} = \frac{G}{\sqrt{\rho_G\left(\rho_L - \rho_G\right) g\, d_{eq}}} \qquad \textbf{Eq. 83}$$

$$f_{G,eq} = 0.046\, Re_{G,eq}^{-0.2} \qquad \textbf{Eq. 84}$$

$$Re_{G,eq} = \frac{G\ x\ d_{eq}}{\mu_G} \qquad \textbf{Eq. 85}$$

X_{tt} is the Martinelli parameter defined **by** Eq. 2 while the equivalent diameter is calculated with Eq. 86, where A_{eff} is the actual flow area:

$$d_{eq} = \sqrt{\frac{4A_{eff}}{\pi}} \qquad \textbf{Eq. 86}$$

Finally, the void fraction is calculated with Smith equation [21].

1.4.3.2 Kedzierski and Goncalves Model [29]

Kedzierski and Goncalves [29] tested the condensation of four refrigerants (R134a, R410A, R125 and R32) inside a microfin tube. They proposed a modified Pierre [30] correlation (originally proposed for flow boiling pressure drop in horizontal smooth tubes) in which the hydraulic diameter was used and a friction factor was developed to account for the fin effect on flow.

The acceleration and the frictional pressure gradients can be expressed by the following equations, respectively:

$$\left(-\frac{\Delta p}{L}\right)_a = \frac{G^2}{L}\left(\frac{1}{\rho_{ho,out}} - \frac{1}{\rho_{ho,in}}\right) \qquad \textbf{Eq. 87}$$

$$\left(-\frac{\Delta p}{L}\right)_f = \frac{f_{tp}\, G^2}{d_h}\left(\frac{1}{\rho_{ho,out}} + \frac{1}{\rho_{ho,in}}\right) \qquad \textbf{Eq. 88}$$

So, the total pressure gradient for a horizontal microfin tube is:

$$\left(-\frac{\Delta p}{L}\right) = \left(-\frac{\Delta p}{L}\right)_f + \left(-\frac{\Delta p}{L}\right)_a == G^2\left[\frac{f_{tp}}{d_h}\left(\frac{1}{\rho_{ho,out}} + \frac{1}{\rho_{ho,in}}\right) + \frac{1}{L}\left(\frac{1}{\rho_{ho,out}} - \frac{1}{\rho_{ho,in}}\right)\right] \qquad \textbf{Eq. 89}$$

Where the two-phase friction factor can be regressed by the following correlation:

$$f_{tp} = \left(0.002275 + 0.00933\, e^{\frac{-h}{0.003\, d_{eq}}}\right) Re_{LO,h}^{\frac{-1}{4.16+532h/d_{eq}}}\ \Phi^{0.211} \qquad \textbf{Eq. 90}$$

with:

$$\Phi = \frac{\left(x_{in} - x_{out}\right) h_{LG}}{L\, g} \qquad \textbf{Eq. 91}$$

The hydraulic diameter used in the Reynolds number calculation is defined as:

$$d_h = \frac{4 A_{eff} \cos\beta}{\pi \, d_b \, E_a} \qquad \textbf{Eq. 92}$$

Where E_a is the surface area enhancement as compared with a smooth tube with the fin root diameter d_b. And the related liquid-only Reynolds number is:

$$Re_{LO,h} = \frac{G \, d_h}{\mu_L} \qquad \textbf{Eq. 93}$$

1.4.3.3 Cavallini et al. Model [31]

Cavallini et al. [31] proposed a correlation derived from Friedel [32] correlation (originally suggested for adiabatic two-phase flow pressure drop in vertical and horizontal smooth tubes) and based on a variety of experimental data, in which an equivalent roughness was used to account for the effect of the micro-fins and the Mickley et al. [33] correction term was incorporated to consider the mass transport effects at the interface.

The adiabatic frictional pressure gradient is given by:

$$-\left(\frac{dp}{dz}\right)_{f,adiab} = \Phi_{LO}^2 \left[-\left(\frac{dp}{dz}\right)_{LO}\right] = \Phi_{LO}^2 \, \frac{2 f_{LO} G^2}{D \, \rho_L} \qquad \textbf{Eq. 94}$$

Where the two-phase multiplier is:

$$\Phi_{LO}{}^2 = E + \frac{3.24 \, F \, H}{Fr^{0.045} \, We^{0.035}} \qquad \textbf{Eq. 95}$$

Using the following terms:

$$E = (1-x)^2 + x^2 \left(\frac{\rho_L}{\rho_G}\right)\left(\frac{f_{GO}}{f_{LO}}\right) \qquad \textbf{Eq. 96}$$

$$F = x^{0.78} (1-x)^{0.224} \qquad \textbf{Eq. 97}$$

$$H = \left(\frac{\rho_L}{\rho_G}\right)^{0.91} \left(\frac{\mu_G}{\mu_L}\right)^{0.19} \left(1 - \frac{\mu_G}{\mu_L}\right)^{0.7} \quad \textbf{Eq. 98}$$

The Froude and Weber numbers are defined as:

$$Fr = \frac{G^2}{g\ D\ \rho_{ho}^2} \quad \textbf{Eq. 99}$$

$$We = \frac{G^2\ D}{\rho_{ho}\ \sigma} \quad \textbf{Eq. 100}$$

Where ρ_{ho} is the homogeneous density calculated with Eq. 56, while the liquid-only friction factor can be evaluated with the following algorithm:

$$f_{LO} = max\left(f_{LO1}, f_{LO2}\right), \qquad f_{GO} = max\left(f_{GO1}, f_{GO2}\right) \quad \textbf{Eq. 101}$$

Where f_{LO1} and f_{GO1} are:

$$f_{LO1} = \begin{cases} 0.079\, Re_{LO}^{-0.25} & \text{turbulent flow} \\ 16\, Re_{LO}^{-1} & \text{laminar flow} \end{cases}; \quad \textbf{Eq. 102}$$

and:

$$f_{GO1} = \begin{cases} 0.079\, Re_{GO}^{-0.25} & \text{turbulent flow} \\ 16\, Re_{GO}^{-1} & \text{laminar flow} \end{cases} \quad \textbf{Eq. 103}$$

The Reynolds numbers are calculated with Eq. 79 and Eq. 80 while f_{LO2} and f_{GO2} are given by:

$$f_{LO2} = f_{GO2} = \frac{1}{4}\ \left[1.74 - 2\ log_{10}\left(2k\right)\right]^{-2} \quad \textbf{Eq. 104}$$

In Eq. 104, k represents an equivalent roughness for the microfin tube and it is defined by:

$$k = 0.18\ \frac{h}{D} \cdot \frac{1}{0.1 + cos\,\beta} \qquad \textbf{Eq. 105}$$

Finally, the condensation frictional pressure gradient is obtained by introducing the Mickley correction term, θ:

$$-\left(\frac{dp}{dz}\right)_{f,cond} = -\left(\frac{dp}{dz}\right)_{f,adiab} \Theta \qquad \textbf{Eq. 106}$$

Where:

$$\Theta = \psi\left(e^{\psi} - 1\right)^{-1} \qquad \textbf{Eq. 107}$$

$$\psi = -\frac{G_{co}\ u_G}{\tau_i} \qquad \textbf{Eq. 108}$$

with:

$$G_{co} = \frac{G\ D}{4}\frac{dx}{dz} \qquad \textbf{Eq. 109} \qquad \tau_i = \left(\frac{dp}{dz}\right)_{f,adiab}\frac{D}{4} \qquad \textbf{Eq. 110} \qquad u_G = \frac{G\ x}{\rho_G\ \varepsilon} \qquad \textbf{Eq. 111}$$

The void fraction, ε, must be calculated using the Rouhani [34] model described by Eq. 112, Eq. 113 and Eq. 114:

$$\varepsilon = \frac{x\,\rho_L}{C_0\left[x\ \rho_L + (1-x)\,\rho_G\right] + \left(\rho_L\ \rho_G\, u_{gj}\right)/G} \qquad \textbf{Eq. 112}$$

$$C_0 = \begin{cases} 1 + 0.2(1-x)\left[\left(g\ D\ \rho_L{}^2\right)/G^2\right]^{0.25} & \text{per} \quad \varepsilon > 0.1 \\ 0 \quad \text{per} \quad \varepsilon \to 0 \end{cases} \qquad \textbf{Eq. 113}$$

$$u_{gj} = 1.18(1-x)\left[\sigma g\left(\rho_L - \rho_G\right)/\rho_L^{\,2}\right]^{0.25} \qquad \textbf{Eq. 114}$$

1.4.3.4 Goto et al. Model [35]

Goto et al. [35] developed two correlations based on pressure drops measured during condensation and evaporation of R22 and R410A inside a helical microfin tube and a herringbone microfin tube. Here, these correlations are presented and then applied.

Goto et al. model A:

$$-\left(\frac{dP}{dz}\right)_{f,(A)} = \Phi_G^2 \frac{2\, f_G \left(G\, x\right)^2}{\rho_G\, d_{eq}} \qquad \textbf{Eq. 115}$$

with:

$$\Phi_G^2 = \left(1 + 1.64\, X_{tt}^{0.79}\right)^2 \qquad \textbf{Eq. 116}$$

Goto et al. model B:

$$-\left(\frac{dP}{dz}\right)_{f,(B)} = \Phi_L^2 \frac{2\, f_L \left[G(1-x)\right]^2}{\rho_L\, d_{eq}} \qquad \textbf{Eq. 117}$$

with:

$$\Phi_L^2 = 1 + 7.61\, X_{tt}^{-1.70} \qquad \textbf{Eq. 118}$$

Where:

$$f = \begin{cases} 16/Re_{eq} & \text{per } Re_{eq} \le 2000 \\ 1.47\cdot 10^{-4}\, Re_{eq}^{0.53} & \text{per } 2000 < Re_{eq} \le 2600 \\ 0.046\, Re_{eq}^{-0.2} & \text{per } 2600 < Re_{eq} \le 6500 \\ 1.23\cdot 10^{-3}\, Re_{eq}^{0.21} & \text{per } 6500 < Re_{eq} \le 12700 \\ 9.20\cdot 10^{-3} & \text{per } Re_{eq} > 12700 \end{cases} \qquad \textbf{Eq. 119}$$

The Reynolds number is based on the effective flow cross-sectional area:

$$Re_{G,eq} = \frac{G\, x\, d_{eq}}{\mu_G} \qquad \textbf{Eq. 120}$$

$$Re_{L,eq} = \frac{G\,(1-x)\, d_{eq}}{\mu_L} \qquad \textbf{Eq. 121}$$

1.4.3.5 Choi et al. Model [36]

Choi et al. [36] proposed a pressure drop correlation taking the form of Pierre [30] model. Their model is based on the experimental data of a microfin tube for condensation of R32, R125, R134a, and R410A and evaporation of R32, R125, R134a, R410A, R22, R407C. They suggested that their correlation could be applicable to evaporation and condensation in smooth and microfin tubes of lubricant-free refrigerants and refrigerant/lubricant mixtures.

$$\left(-\frac{\Delta p}{L}\right)_f = \frac{f_{tp}\, G^2}{d_h}\left(\frac{1}{\rho_{om,us}} + \frac{1}{\rho_{om,in}}\right) \qquad \textbf{Eq. 122}$$

$$f_{tp} = 0.00506\ Re_{LO,h}^{-0.0951}\left[\frac{(x_{in} - x_{out})\, h_{LG}}{L\, g}\right] \qquad \textbf{Eq. 123}$$

The Reynolds number and the hydraulic diameter are the same defined by Kedzierski and Goncalves [29] in Eq. 93 and Eq. 92.

1.4.4 Condensation Heat Transfer Coefficient Models

Since the 80's, several models of condensation heat transfer coefficient calculations have been proposed in the open literature. In the following, seven of them have been chosen to compare the experimental data points with the calculations results.

1.4.4.1 Cavallini et al. Model [37]

Cavallini et al. presented a model for condensation inside low-fin and micro-fin tubes based on the Cavallini-Zecchin [38] equation originally designed only for smooth tubes. The correlation introduces two parameters which account for the geometrical effect *Rx* and the ratio of vapour shear to surface tension forces by introducing the product of Froude and Bond numbers.

The *Rx* factor is equal to the ratio between the exchange area enhancement factor for axially microfinned tubes and the cosine function of the helix angle, and accounts for the effect of the heat transfer area increase. [39, 40]

As highlighted before, the heat transfer coefficient is defined with reference to the cylindrical envelope surface area of the finned surface at the fin tip.

The fin tip diameter is used as a reference for all calculated non-dimensional parameters.

This model, originally developed for pure refrigerants, can be applied to mixtures using the Silver [41] and Bell and Ghaly [42] correction to account for mass transport thermal resistance. For zeotropic mixtures used in refrigeration, with a maximum total isobaric temperature glide around 6-8 K, the correction factor can be considered constant and equal to:

$$\frac{\delta q_{SV}}{\delta q_{TOT}} \approx x \cdot c_{pG} \cdot \frac{\Delta T}{h_{LG}} \qquad \textbf{Eq. 124}$$

Where ΔT is the isobaric temperature glide of the mixture and h_{LG} is the latent heat of condensation.

The Cavallini et al. [37] correlation is:

$$Nu = \frac{HTC\ D}{\lambda_L} = 0.05\ \ Re_{eq}^{\ 0.8}\ Pr_L^{\ 1/3}\ Rx^s \left(Bo \cdot Fr\right)^t \qquad \textbf{Eq. 125}$$

Where the geometrical enhancement factor is defined by:

$$Rx = \left[\frac{2\ h\ n_g \left(1 - sin\left(\gamma / 2\right)\right)}{\pi\ D cos\left(\gamma / 2\right)} + 1 \right] \cdot \frac{1}{cos\ \beta} \qquad \textbf{Eq. 126}$$

While the non-dimensional parameters are:

$$Re_{eq} = 4\ \dot{m}_f\ \frac{\left(1-x\right) + x\left(\rho_L / \rho_G\right)^{1/2}}{\pi\ D\ \mu_L} \qquad \textbf{Eq. 127}$$

$$Pr_L = \frac{\mu_L\ c_{pL}}{\lambda_L} \qquad \textbf{Eq. 128} \qquad Fr = \frac{u_{GO}^{\ 2}}{g\ D} \qquad \textbf{Eq. 129} \qquad Bo = \frac{g\ \rho_L\ h\ \pi\ D}{8\ \sigma\ n_g} \qquad \textbf{Eq. 130}$$

The vapour velocity u_{GO} must be evaluated with reference to the total two-phase mass flow rate and the properties of the vapour phase:

$$u_{GO} = \frac{G}{\rho_G} \qquad \textbf{Eq. 131}$$

This correlation has to be applied when Re_{eq} is greater than 15000, $0.2<p_R<0.8$, $7°<\beta<30°$ and $0.3<Bo\ Fr<508$.

The exponents *s* and *t* of Eq. 125 are the following:

for low-fins: s = 1.40 ; t = -0.08

for micro-fins : s = 2.00 ; t = -0.26

for cross-grooved : s = 2.10 ; t = -0.26

1.4.4.2 Yu and Koyama Model [43]

Yu and Koyama correlation [43] consists of two terms which apply to the forced convection condensation regime and the gravity drained condensation regime, respectively. It derives from Haraguchi et al. [44] condensation model for smooth tubes, extended to microfinned tubes.

$$Nu = \frac{HTC_e \; d_M}{\lambda_L} = \left({Nu_F}^2 + {Nu_B}^2 \right)^{0.5}$$ **Eq. 132**

For the forced convection condensation regime, the geometrical effect is accounted for by referring the heat transfer coefficient to the actual surface area. For the gravity drained condensation regime, the Nusselt [45] type condensation is assumed, along with a correction term for stratified condensate. A weaker dependence on the surface area increase than on the forced convection condensation regime is assumed. Finally, the void fraction is calculated by Smith [21] equation, and the reference diameter is the average tube diameter:

$$d_M = D + h$$ **Eq. 133**

The forced convection condensation term is given by:

$$Nu_F = 0.152 \left(\frac{\Phi_G}{X_{tt}} \right) {Re_L}^{0.68} \left(0.3 + 0.1 \, {Pr_L}^{1.1} \right)$$ **Eq. 134**

Where:

$$\Phi_G = 1.1 + 1.3 \frac{G^{0.35} {X_{tt}}^{0.35}}{\left[g \; d_M \; \rho_G \left(\rho_L - \rho_G \right) \right]^{0.175}}$$ **Eq. 135**

The gravity-driven condensation term is given by:

$$Nu_B = 0.725 \;\; H\left(\varepsilon \right) \left(\frac{Ga \cdot Pr_L}{Ph_L \cdot \eta_a} \right)^{0.25}$$ **Eq. 136**

The surface area enhancement η_a is defined by:

$$\eta_a = \varepsilon_a \frac{D}{d_M}$$ **Eq. 137**

Where ε_a is the surface area enhancement referred to the smooth tube with the inner diameter equal to the fin tip diameter of the microfin tube, and the void fraction function, is:

$$H(\varepsilon) = \varepsilon + \left[10\left(1-\varepsilon\right)^{0.1} - 8.0\right] \cdot \varepsilon^{0.5} \cdot \left(1-\varepsilon^{0.5}\right) \quad \textbf{Eq. 138}$$

Finally, the non-dimensional numbers are:

$$Ga = \frac{g\ \rho_L^{\ 2}\ d_M^{\ 3}}{\mu_L^{\ 2}} \quad \textbf{Eq. 139} \qquad Ph_L = \frac{c_{pL}\left(T_{sat} - T_{wall}\right)}{h_{LG}} \quad \textbf{Eq. 140} \qquad Re_L = \frac{G\left(1-x\right)d_M}{\mu_L} \quad \textbf{Eq. 141}$$

1.4.4.3 Kedzierski and Goncalves Model [46]

The Kedzierski and Goncalves model [46] derives from a complete regression analysis based on their experimental database for condensation of R134a, R410A, R125 and R32 inside a microfin tube.

In their correlation, the geometrical effect is accounted for by using the hydraulic diameter as the length scale and referring the heat transfer coefficient to the actual surface area.

The Authors neglect the surface tension effect as they refer the heat transfer enhancement to the turbulence induced in the liquid films by the micro-fins.

The correlation accounts for the reduced pressure effect on the condensation heat transfer:

$$Nu = \frac{HTC_e\ d_h}{\lambda_L} = 2.256\ Re^{0.303}\ Ph_L^{\ A}\ Pr_L^{\ 0.393}\ p_R^{\ B}\left(-log_{10}\ p_R\right)^C\ Sv^D \quad \textbf{Eq. 142}$$

Where the exponents are:

$$A = -0.232\ x \qquad B = -0.578\ x^2 \qquad C = -0.474\ x^2 \qquad D = 2.531\ x$$

The reduced pressure p_R and the Reynolds number are respectively:

$$p_R = \frac{p}{p_{cr}} \quad \textbf{Eq. 143} \qquad Re = \frac{G\ d_h}{\mu_L} \quad \textbf{Eq. 144}$$

While the non-dimensional specific volume is given by:

$$Sv = \frac{\left(\rho_L / \rho_G\right) - 1}{x\left(\rho_L / \rho_G\right) + 1 - x} \qquad \textbf{Eq. 145}$$

Finally, the hydraulic diameter is defined by considering the effective flow cross-sectional area:

$$d_h = \frac{4\, A_{eff}\, \cos\beta}{\pi\, d_b\, E_a} \qquad \textbf{Eq. 146}$$

Where E_a is the surface area enhancement as compared with a smooth tube with the fin root diameter d_b. The other non-dimensional numbers are the ones previously defined.

1.4.4.4 Chamra et al. Models [47, 48]

In 2004, Chamra et al. [47] proposed a new correlation for condensation heat transfer of pure refrigerants in microfin tubes.This model was based on a theoretical analysis of turbulent film condensation inside smooth tubes. Several modifications were implemented in the original smooth-tube model to account for the heat transfer enhancement due to the presence of micro-fins on the internal wall surface. The model was compared against a set of 400 experimental data points and takes the following form:

$$HTC = \frac{P_1\, \rho_L\, c_{pL} \left(\frac{\tau_w}{\rho_L}\right)^{P_2}}{T^+} \cdot Rx^{P_3} \qquad \textbf{Eq. 147}$$

Where Rx is the parameter defined by Cavallini et al. [37] and it is given by Eq. 126, while the constants are: P_1=0.208, P_2=0.224, P_3=1.321. The wall shear stress and the non-dimensional temperature are defined by the following equations:

$$\tau_w = -\left(\frac{dp}{dz}\right)_f \frac{D}{4} \qquad \textbf{Eq. 148}$$

And:

$$T^+ = \begin{cases} \delta^+ \cdot Pr_L & \text{per} \quad \delta^+ \le 5 \\ 5\left\{ Pr_L + ln\left[1 + Pr_L \left(\frac{\delta^+}{5} - 1 \right) \right] \right\} & \text{per} \quad 5 < \delta^+ \le 30 \\ 5\left\{ Pr_L + ln\left(1 + 5\,Pr_L\right) + 0.5\,ln\left(\frac{\delta^+ - 2.5}{27.5} \right) \right\} & \text{per} \quad \delta^+ > 30 \end{cases} \qquad \textbf{Eq. 149}$$

Where δ^+, the non-dimensional liquid film thickness, is equal to:

$$\delta^+ = \begin{cases} 0.866\ Re_L^{0.5} & \text{for} \quad Re_L \le 1600 \\ 0.051\ Re_L^{0.87} & \text{for} \quad Re_L > 1600 \end{cases} \qquad \textbf{Eq. 150}$$

With the liquid Reynolds number defined by Eq. 77 using the fin tip diameter as a reference length scale. The Authors suggested to use the Cavallini et al. [31] model for calculating two-phase pressure gradient.

The model proposed by Chamra and Mago [48] in 2006 has been developed for condensation of refrigerant mixtures inside microfin tubes. This model is based on the previous correlation for pure refrigerants where the correction of Silver [41] and Bell and Ghaly [42] was introduced and all the exponents were recalculated. Therefore, it is possible to consider this equation as another model from Chamra et al. [47] correlation. The new correlation is:

$$HTC = \left[\frac{1}{\dfrac{M_1\ \rho_L\ c_{pL} \left(\dfrac{\tau_w}{\rho_L} \right)^{M_2}}{T^+} \cdot Rx^{M_3}} + \left(\frac{\delta q_{SV}}{\delta q_{TOT}} \right) HTC_G^{-1} \right]^{-1} \qquad \textbf{Eq. 151}$$

The constants are: M_1 = 0.31, M_2 = 0.314, M_3 = 0.993, while the other parameters must be estimated as in Chamra et al. [46] model.

HTC_G, the heat transfer coefficient of the vapour phase, is calculated using the fomous Dittus-Boelter [49] correlation:

$$HTC_G = 0.023 \cdot \frac{\lambda_G}{D}\left(\frac{G\,x\,D}{\mu_G}\right)^{0.8}\left(\frac{c_{pG}\,\mu_G}{\lambda_G}\right)^{0.3} \qquad \textbf{Eq. 152}$$

1.4.4.5 Han and Lee Model [50]

Han and Lee [50] studied both experimentally and theoretically the condensation of R134a, R22 and R410A in four microfin tubes. Experimental results were proposed in terms of the enhancement factor and penalty factors.

They developed a correlation for condensation heat transfer coefficient in an annular flow regime based on the experimental data and the heat-momentum analogy.

The heat transfer correlation was developed for annular flow regimes; it is assumed that the liquid film thickness is uniform around the tube periphery because of the greater influence of the shear force. Since the vapour core is highly turbulent, radial temperature gradients and the temperature in the vapour core are neglected. Temperatures in the vapour core and at the liquid-vapour interface are assumed to be equal to the saturation temperature. In these hypotheses the model has been developed as:

$$HTC_b = \frac{\rho_L\; c_{pL}\; u_t}{0.904\left(e^+\right)^{0.592}\; Pr_L^{\;0.729} + 2.1335\; ln\dfrac{\delta}{h}} \qquad \textbf{Eq. 153}$$

The heat transfer coefficient is referred to the surface area of the enveloped cylinder with the root fin diameter, while u_t is the frictional turbulent velocity and δ is the film thickness evaluated by:

$$u_t = \left\{\frac{d_b}{4\rho_L}\left(\frac{\partial p}{\partial z}\right)_f\right\}^{0.5} \qquad \textbf{Eq. 154}$$

$$e^+ = \frac{h\,u_t\;\rho_L}{\mu_L} \qquad \textbf{Eq. 155}$$

$$\delta = \frac{\left(1-\varepsilon\right)d_b}{4} \qquad \textbf{Eq. 156}$$

The void fraction is calculated with Smith [21] equation, while the pressure gradient is given by the application of their own model.

The frictional pressure gradient is:

$$-\left(\frac{dp}{dz}\right)_f = \Phi_L^2 \ \frac{f_L\left[G(1-x)\right]^2}{2\ d_b\ \rho_L} \qquad \textbf{Eq. 157}$$

Where the liquid friction factor and the liquid two-phase multiplier are obtained from the following equations:

$$f_L = 0.193\left[\frac{G(1-x)d_b}{\mu_L}\right]^{-0.024}\left(\frac{p_g}{h_g}\right)^{-0.539} \qquad \textbf{Eq. 158}$$

$$\Phi_L^2 = 2.684\ X_{tt}^{-1.946} \qquad \textbf{Eq. 159}$$

X_{tt} is the Martinelli parameter while p_g is the axial fin pitch, defined by the following relation:

$$p_g = \frac{\pi\ d_b}{n_g\ \tan\beta} \qquad \textbf{Eq. 160}$$

1.4.4.6 Koyama and Yonemoto Model [51]

In the work of these Authors, the heat transfer correlation proposed by Yu and Koyama [43] is modified using some correlations, developed for microfin tubes, for the void fraction and the friction coefficient. To propose these correlations, experimental data obtained by the Authors, Haraguchi [53] and Miyara [52] are used.

Looking at Eq. 132, the heat transfer coefficient correlation proposed by Yu and Koyama [43] is expressed by the combination of forced and natural convection condensation terms. The void fraction and the frictional pressure gradient were calculated using correlations developed for smooth tubes. Koyama and Yonemoto [51] suggested the use of the following correlation.

$$Nu = \left(Nu_F^2 + Nu_N^2\right)^{0.5} \qquad \textbf{Eq. 161}$$

Where the forced convection term is:

$$Nu_F = 2.12\sqrt{f_G}\Phi_G\left(\frac{\rho_L}{\rho_G}\right)^{0.1}\left(\frac{x}{1-x}\right)Re_L^{0.5}\,Pr_L^{0.5} \qquad \textbf{Eq. 162}$$

Where f_G is the friction factor estimated by Carnavos [54] correlation, while Φ_G is calculated as:

$$\Phi_G = 1+1.2Fr^{0.05}X_{tt}^{0.5} \qquad \textbf{Eq. 163}$$

Where Froude number is defined as:

$$Fr = \frac{G}{\sqrt{gd_M\rho_G\left(\rho_L-\rho_G\right)}} \qquad \textbf{Eq. 164}$$

Carnavos [54] suggested to calculate the frictional factor as follows:

$$f_G = \frac{0.046}{Re_G^{0.2}\,F^*} \qquad \textbf{Eq. 165}$$

with F* depending on the geometrical characteristics of the microfin tube:

$$F^* = \left(\frac{A_{eff}}{A_{root}}\right)^{0.5} sec\,\beta \qquad \textbf{Eq. 166}$$

A_{eff} is the actual free flow area, while A_{root} is the nominal flow area on the tube internal diameter as if the fin structures were not present.
The Nusselt number for natural convection condensation is then defined by:

$$Nu_N = 1.98\frac{H\left(\varepsilon\right)}{\eta_A^{0.5}Bo^{0.1}}\left(\frac{Ga\,Pr_L}{Ph_L}\right)^{0.25} \qquad \textbf{Eq. 167}$$

Where η_A is the area enlargement whilst Bond, Galileo and phase change numbers are defined as:

$$Bo = \frac{(P-t)\, d_M\, g\,(\rho_L - \rho_G)}{\sigma} \quad \textbf{Eq. 168} \qquad Ga = \frac{g\,\rho_L^2\, d_M^3}{\mu_L^2} \quad \textbf{Eq. 169} \qquad Ph_L = \frac{c_{pL}\,\Delta T_{sat}}{h_{LG}} \quad \textbf{Eq. 170}$$

Where d_M is the average inner diameter of the microfin tube, while P and t are the fins pitch and the width of the fin tip, respectively.
$H(\varepsilon)$ is the function expressing the effect of the thick liquid film flowing at the bottom of the tube and its value is obtainable by applying the following equation:

$$H(\varepsilon) = \varepsilon + \left[10(1-\varepsilon)^{0.1} - 8.9\right]\sqrt{\varepsilon}\left(1-\sqrt{\varepsilon}\right) \quad \textbf{Eq. 171}$$

This function depends on the void fraction value calculated by:

$$\varepsilon = 0.81\varepsilon_{Smith} + 0.19 x^{100(\rho_V/\rho_L)^{0.8}} \varepsilon_{ho} \quad \textbf{Eq. 172}$$

As it appears from Eq. 172, the void fraction function proposed by Koyama and Yonemoto is a linear combination of Smith [21] and Homogeneous void fractions, Eq. 64 and Eq. 55.

1.4.4.7 Wang et al. Model [55]

More recently, Wang et al. [55] suggested a new model for condensation heat transfer coefficient in microfin tubes. The correlation has been evaluated against a large database of around 440 experimental data points covering five refrigerants (R11, R123, R134a, R22 and R410A) and seven microfin tubes. The mass velocity ranges from 90 kg m^{-2} s^{-1} to 460 kg m^{-2} s^{-1}.
Therefore, the correlation to calculate the condensation Nusselt number is:

$$Nu = a_1 \left[\frac{g\,(\rho_L - \rho_G)\, h_{LG}\, d_b^{\,3}}{\mu_L \lambda_L \Delta T_{sat}}\right]^{0.25} Re_{L}^{n1}\, Pr_L^{n2} \left(\frac{A}{A_C}\right)^{n3} \varepsilon_{A}^{n4} \left(sec\,\beta\right)^{n5} \Phi_G^{n6}\, X_{tt}^{n7}\, Bo^{n8} \quad \textbf{Eq. 173}$$

Table 14. Experimental fitting values.

a1	0.0089
n1	0.25
n2	0.3333
n3	5.6
n4	-0.4
n5	11.4
n6	0.75
n7	-0.5
n8	-0.2

(A/A_C) is the ratio between the cross-sectional area based on the inner fin root diameter and the core cross-sectional area based on the fin tip diameter, ε_A is the surface area enhancement ratio as compared to the smooth tube with fin root diameter, d_b.
The Bond number is defined as:

$$Bo = \frac{d_b hg\left(\rho_L - \rho_G\right)}{8 n_g \sigma} \qquad \textbf{Eq. 174}$$

While the two-phase multiplier Φ_G is calculated with the following equation:

$$\Phi_G = \left[1 + \left(1 + \frac{10}{Fr}\right)^{-0.5} \left(25 X_{tt} + 1.6 X_{tt}^2\right)\right]^{0.5} \qquad \textbf{Eq. 175}$$

Once again, X_{tt} is Lockhart Martinelli parameter, while Froude number is here defined with reference to the fin root diameter, d_b:

$$Fr = \frac{Gx}{\sqrt{\rho_G\left(\rho_L - \rho_G\right) g d_b}} \qquad \textbf{Eq. 176}$$

1.5 Comparison with Prediction Models

1.5.1 Introduction

Several different prediction models for condensation heat transfer and pressure drop calculations have been summarized above. The estimations obtained from the application of these correlations are reported graphically and numerically in the following paragraphs.

In order to make a homogeneous comparison between the semi-empirical correlations, the relative deviation e_R, the absolute deviation e_A and the standard deviation σ_N must be defined.

Relative deviation, e_R:

$$e_R = \frac{\sum e_P}{N} \quad [\%] \qquad \textbf{Eq. 177}$$

Absolute deviation, e_A:

$$e_A = \frac{\sum |e_P|}{N} \quad [\%] \qquad \textbf{Eq. 178}$$

Standard deviation, σ_N:

$$\sigma_N = \sqrt{\frac{\sum (e_P - e_R)^2}{N-1}} \quad [\%] \qquad \textbf{Eq. 179}$$

Where N is the number of experimental data points. The experimental deviation e_P is given by:

$$e_P = \frac{z_{CALC} - z_{EXP}}{z_{EXP}} \cdot 100 \quad [\%] \qquad \textbf{Eq. 180}$$

These statistical values are listed in a table under each applied model. A positive value of the average deviation indicates overprediction of data, while a negative value implies underprediction.

1.5.2 Pressure Drop Comparisons: Model by Haraguchi et al. [28]

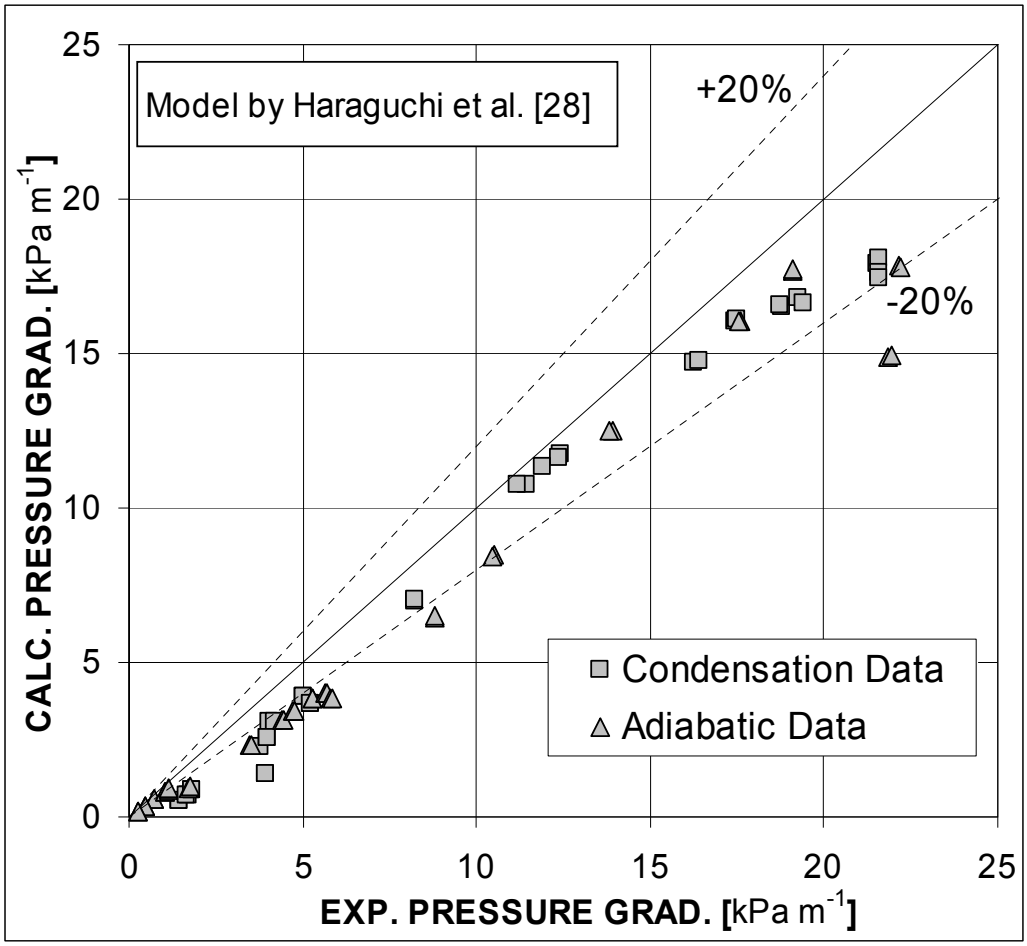

Figure 42. Calculated vs. experimental pressure gradient data: model by Haraguchi et al. [28].

Table 15. Deviations from the experimental values of Haraguchi et al. [28] model.

	e_R [%]	e_A [%]	σ_N [%]
Haraguchi et al. [28]	-23.8	23.8	9.30

1.5.3 Pressure Drop Comparisons: Model by Kedzierski and Goncalves [29]

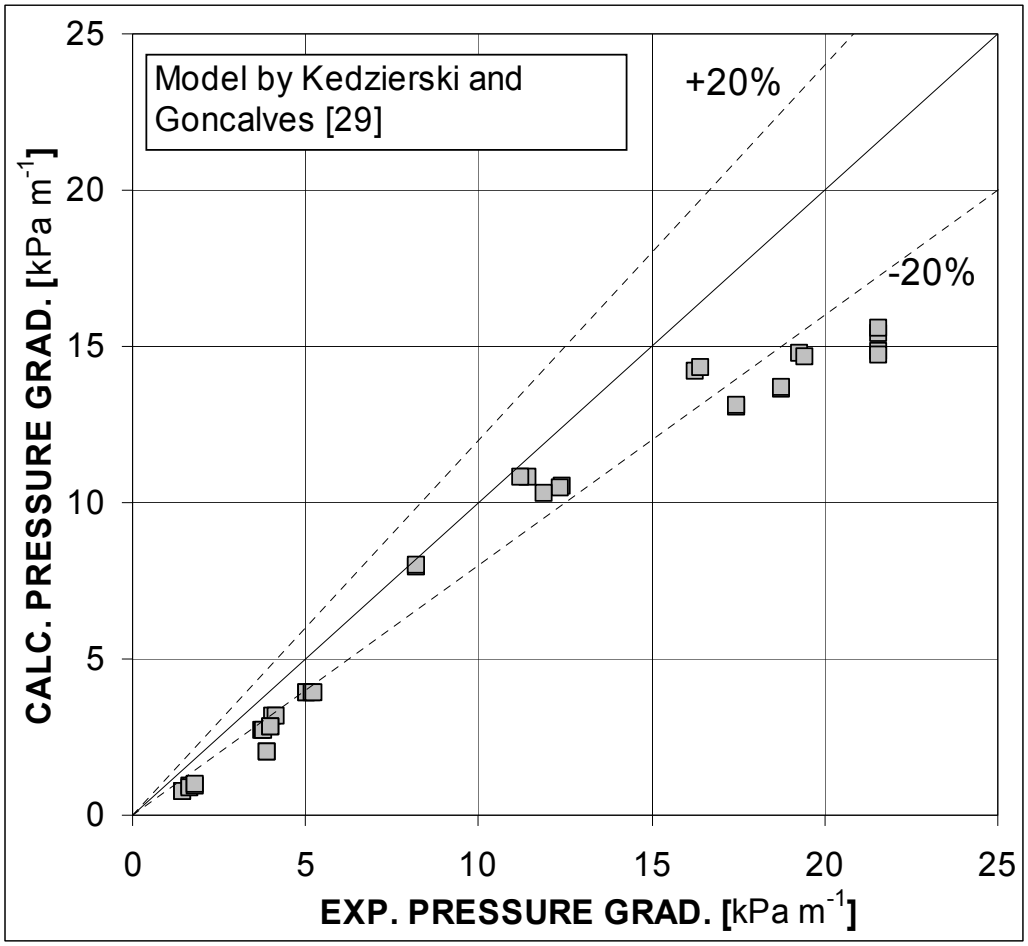

Figure 43. Calculated vs. experimental pressure gradient data: model by Kedzierski and Goncalves [29].

Table 16. Deviations from the experimental values of Kedzierski and Goncalves [29] model.

	e_R [%]	e_A [%]	σ_N [%]
Kedzierski and Goncalves [29]	-27.0	27.0	13.7

1.5.4 Pressure Drop Comparisons: Model by Cavallini et al. [31]

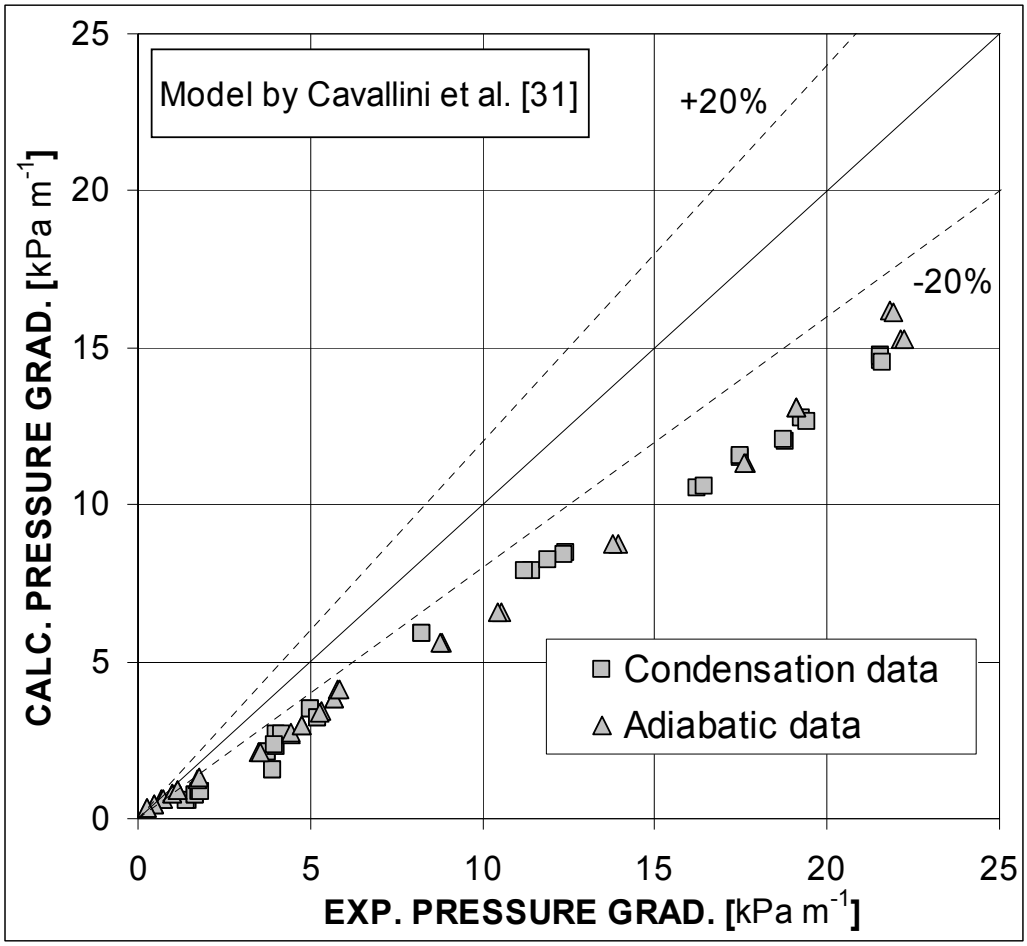

Figure 44. Calculated vs. experimental pressure gradient data: model by Cavallini et al. [31].

Table 17. Deviations from the experimental values of Cavallini et al. [31] model.

	e_R [%]	e_A [%]	σ_N [%]
Cavallini et al. [31]	-32.1	34.4	16.6

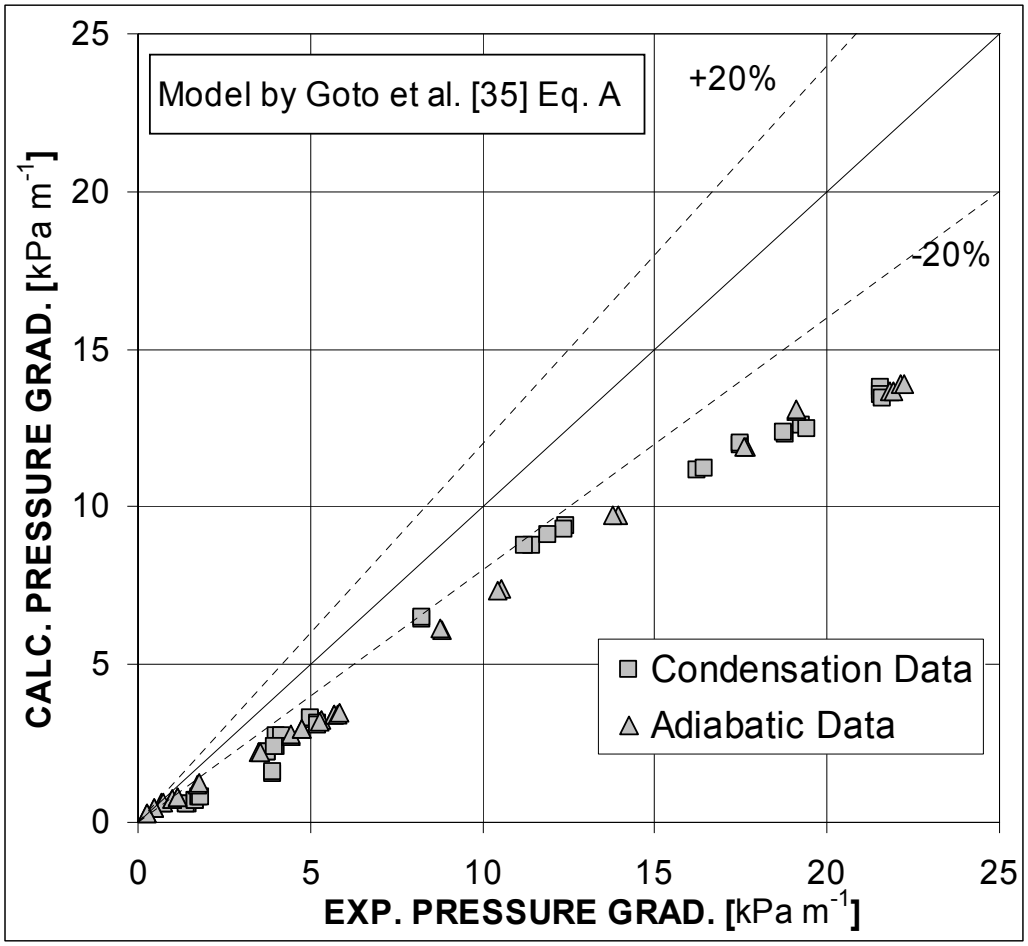

1.5.5 Pressure Drop Comparisons: Model by Goto et al. [35], Equation A

Figure 45. Calculated vs. experimental pressure gradient data: model by Goto et al. [35], equation A.

Table 18. Deviations from the experimental values of Goto et al. [35] model, equation A.

	e_R [%]	e_A [%]	σ_N [%]
Goto et al. [35], Equation A	-33.2	34.4	14.7

1.5.6 Pressure Drop Comparisons: Model by Goto et al. [35], Equation B

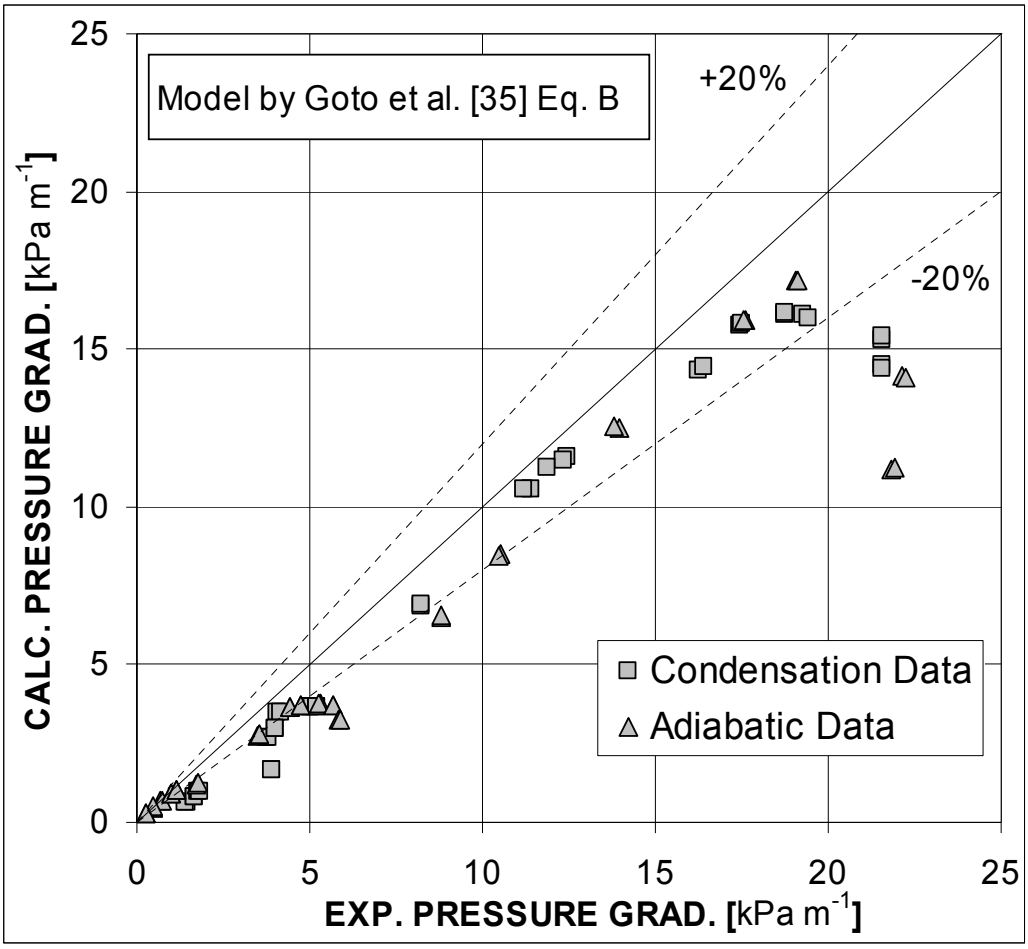

Figure 46. Calculated vs. experimental pressure gradient data: model by Goto et al. [35], equation B.

Table 19. Deviations from the experimental values of Goto et al. [35] model, equation B.

	e_R [%]	e_A [%]	σ_N [%]
Goto et al. [35], Equation B	-22.7	23.7	16.7

1.5.7 Pressure Drop Comparisons: Model by Choi et al. [36]

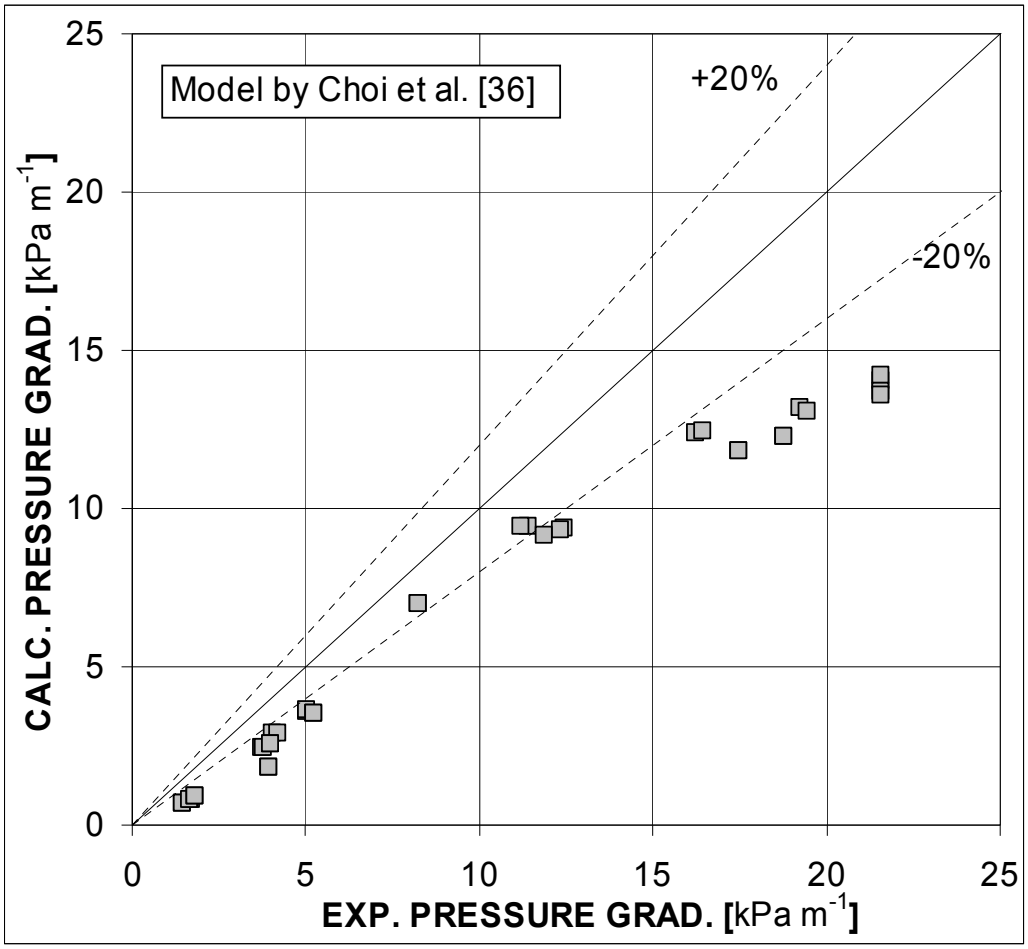

Figure 47. Calculated vs. experimental pressure gradient data: model by Choi et al. [36].

Table 20. Deviations from the experimental values of Choi et al. [36] model.

	e_R [%]	e_A [%]	σ_N [%]
Choi et al. [36]	-34.2	34.2	11.3

1.5.8 Pressure Drop Comparisons

The experimental pressure gradient data were compared against some correlations, available in the open literature, for the prediction of two-phase frictional pressure drop in enhanced tubes: Haraguchi et al. [28], Kedzierski and Goncalves [29], Cavallini et al. [31], Goto et al. [35] Equations A and B by Choi et al. [36].

As one can see from Figure 42 to Figure 47, all the tested models tend to underestimate the experimental values. The best agreement is found using the correlation by Haraguchi et al. [28] and Equation B of Goto et al. [36] model: most of the experimental data are within a range of ±20%.

This trend is confirmed by the statistical deviations summarized in Table 21; it is interesting to point out that all tested models present a low standard deviation.

The worst agreement with the experimental data points is exhibited by the model proposed by Choi et al. [36].

Table 21. Deviations from the experimental values of the models.

Model	e_R **[%]**	e_A **[%]**	σ_N **[%]**
Haraguchi et al. [28]	-23.8	23.8	9.30
Kedzierski and Goncalves [29]	-27.0	27.0	13.7
Cavallini et al. [31]	-32.1	34.4	16.6
Goto et al. [35], equation A	-33.2	34.4	14.7
Goto et al. [35], equation B	-22.7	23.7	16.7
Choi et al. [36]	-34.2	34.2	11.3

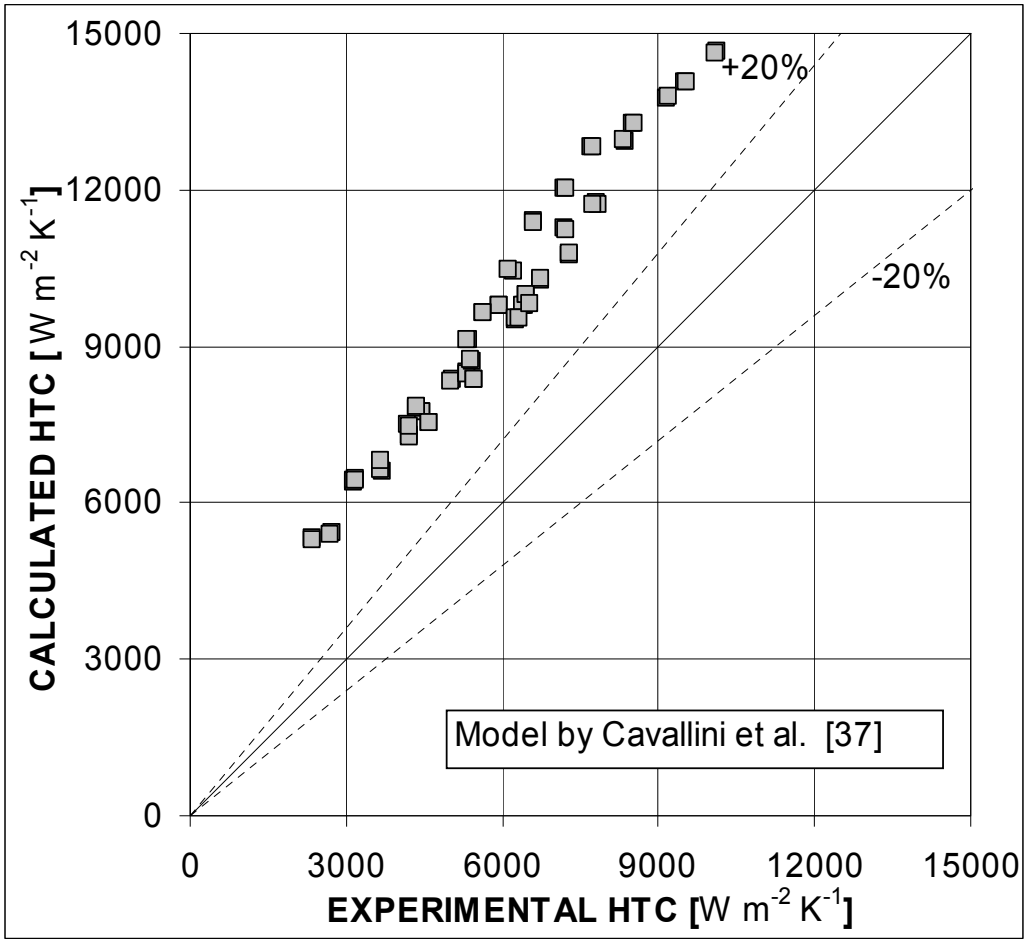

1.5.9 Condensation Heat Transfer Coefficient Comparisons: Model by Cavallini et al. [37]

Figure 48. Calculated vs. experimental condensation heat transfer coefficients: model by Cavallini et al. [37].

Table 22. Deviations from the experimental values of Cavallini et al. [37] model.

	e_R [%]	e_A [%]	σ_N [%]
Cavallini et al. [37]	65.4	65.4	18.8

1.5.10 Condensation Heat Transfer Coefficient Comparisons: Model by Yu and Koyama [43]

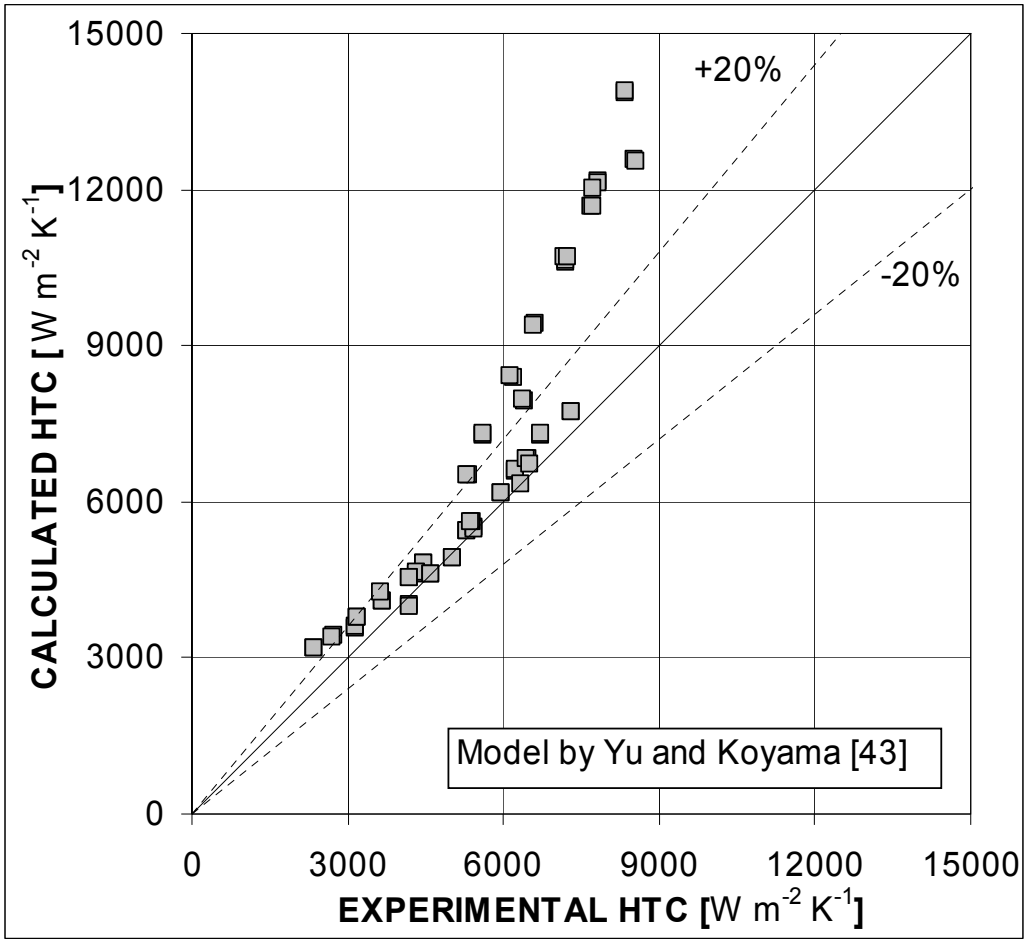

Figure 49. Calculated vs. experimental condensation heat transfer coefficients: model by Yu and Koyama [43].

Table 23. Deviations from the experimental values of Yu and Koyama [43] model.

	e_R [%]	e_A [%]	σ_N [%]
Yu and Koyama [43]	28.8	29.1	27.6

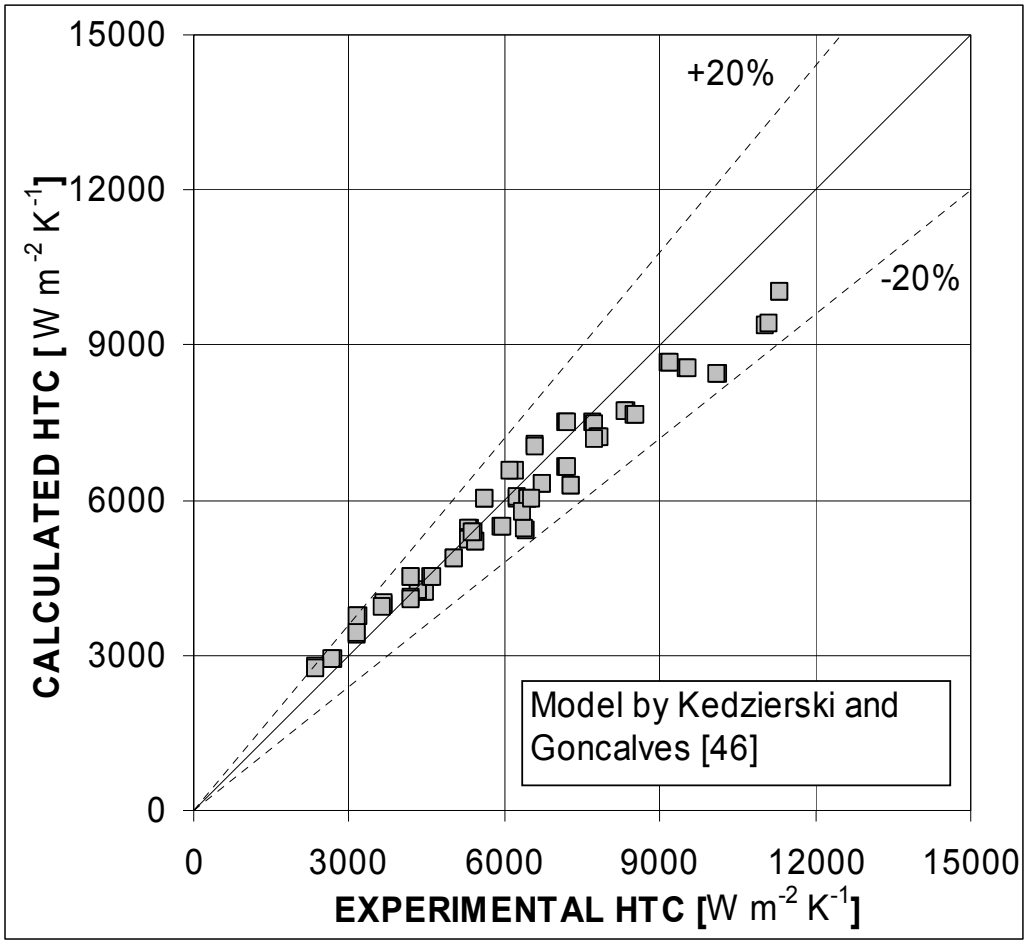

1.5.11 Condensation Heat Transfer Coefficient Comparisons: Model by Kedzierski and Goncalves [46]

Figure 50. Calculated vs. experimental condensation heat transfer coefficients: model by Kedzierski and Goncalves [46].

Table 24. Deviations from the experimental values of Kedzierski and Goncalves [46] model.

	e_R [%]	e_A [%]	σ_N [%]
Kedzierski and Goncalves [46]	-2.34	7.63	8.63

1.5.12 Condensation Heat Transfer Coefficient Comparisons: Model by Chamra and Mago [48]

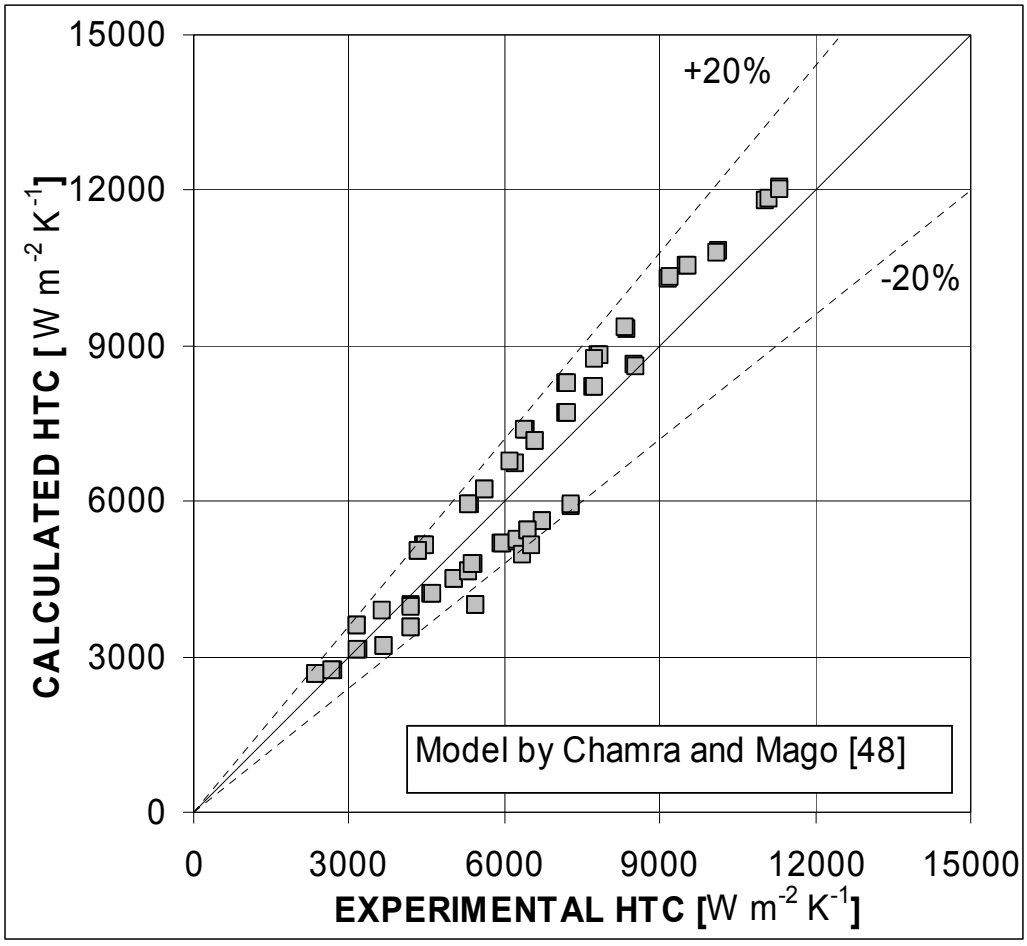

Figure 51. Calculated vs. experimental condensation heat transfer coefficients: model by Chamra and Mago [48].

Table 25. Deviations from the experimental values of Chamra and Mago [48] model.

	e_R [%]	e_A [%]	σ_N [%]
Chamra and Mago [48]	0.34	11.5	12.8

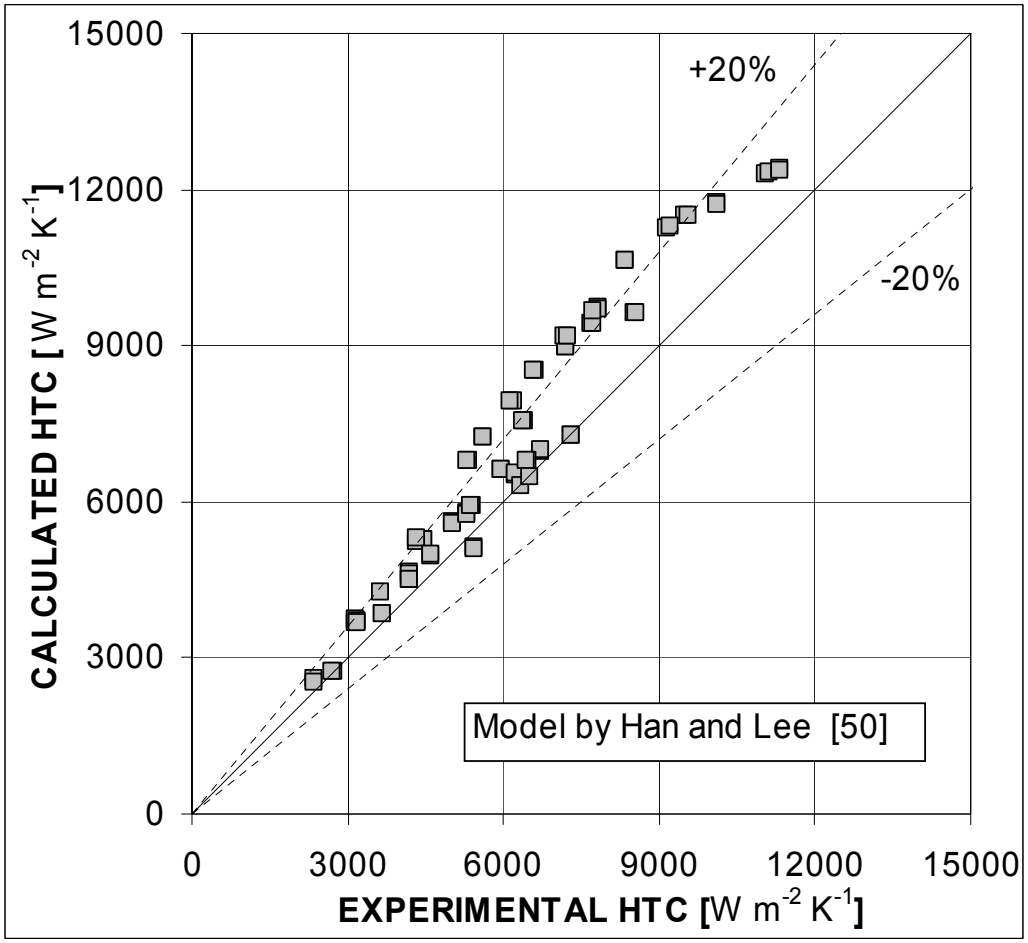

1.5.13 Condensation Heat Transfer Coefficient Comparisons: Model by Han and Lee [50]

Figure 52. Calculated vs. experimental condensation heat transfer coefficients: model by Han and Lee [50].

Table 26. Deviations from the experimental values of Han and Lee [50] model.

	e_R [%]	e_A [%]	σ_N [%]
Han and Lee [50]	14.4	14.8	9.58

1.5.14 Condensation Heat Transfer Coefficient Comparisons: Model by Koyama and Yonemoto [51]

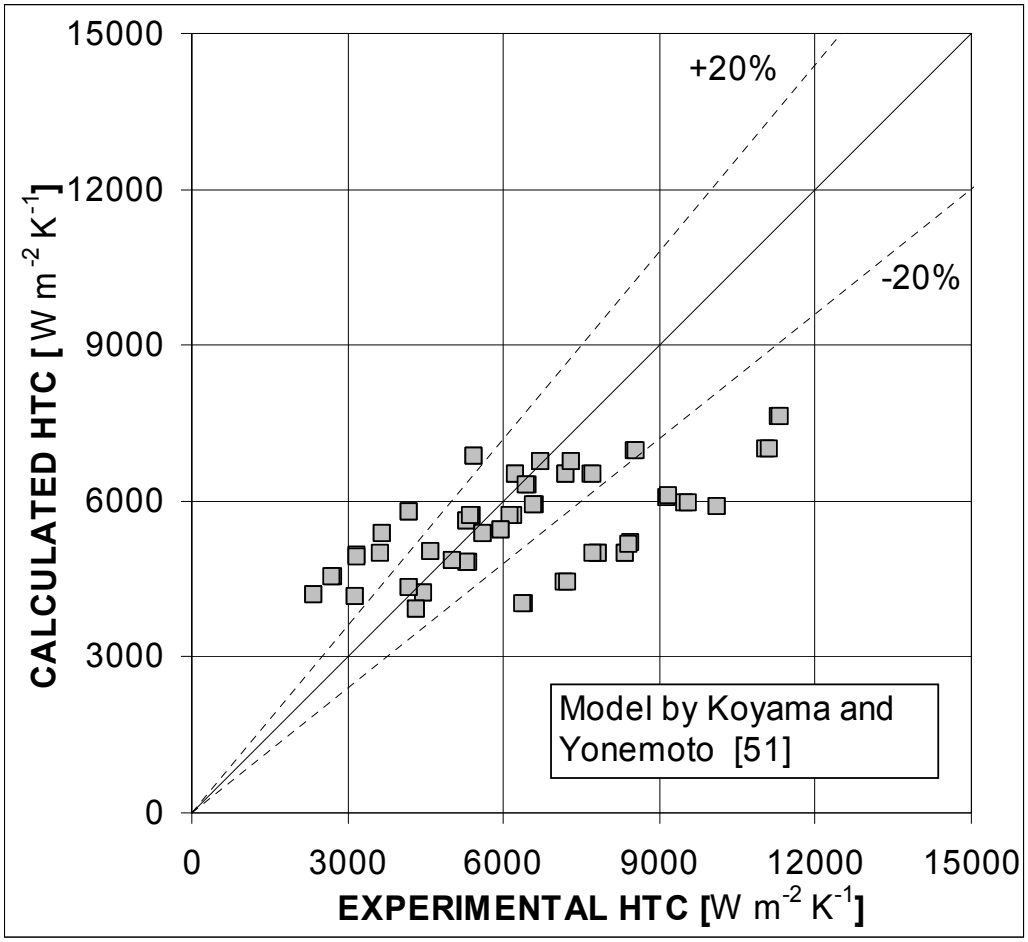

Figure 53. Calculated vs. experimental condensation heat transfer coefficients: model by Koyama and Yonemoto [51].

Table 27. Deviations from the experimental values of Koyama and Yonemoto [51] model.

	e_R [%]	e_A [%]	σ_N [%]
Koyama and Yonemoto [51]	3.03	24.1	31.1

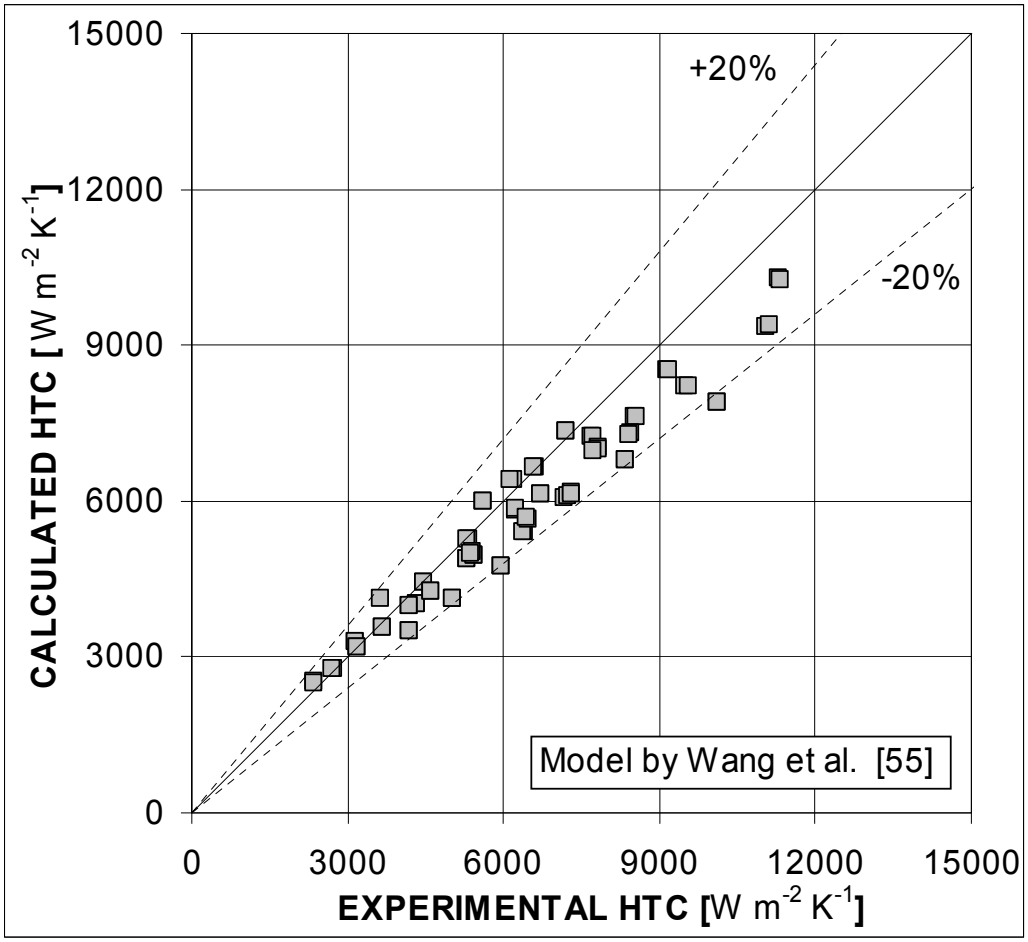

1.5.15 Condensation Heat Transfer Coefficient Comparisons: Model by Wang et al. [55]

Figure 54. Calculated vs. experimental condensation heat transfer coefficients: model by Wang et al. [55].

Table 28. Deviations from the experimental values of Wang et al. [55] model.

	e_R [%]	e_A [%]	σ_N [%]
Wang et al. [55]	-7.50	9.30	8.08

1.5.16 Condensation Heat Transfer Coefficient Comparisons

The experimental values of the heat transfer coefficient were compared against the predictive procedures proposed by Cavallini et al. [37], Yu and Koyama [43], Kedzierski and Goncalves [46], Han and Lee [50], Chamra and Mago [48], Koyama and Yonemoto [51] and Wang et al. [55]. These comparisons are shown in Figure 48 to Figure 54. Average mean and standard deviations between data and models are reported in Table 29.

The model by Cavallini et al. [37], which was developed by independent research databases, overpredicts the experimental heat transfer coefficients; this is probably due to the fact that the range of operating conditions of the data bank used for the development of the model is not sufficiently extended.

The correlation by Yu and Koyama shows the ability to predict the experimental heat transfer coefficients only at low mass velocity. The latest correlation proposed by Koyama and Yonemoto [51], which modifies Yu and Koyama [43] equation, does not fit the R410A experimental heat transfer database.

Han and Lee [50] model tends to overestimate experimental condensation heat transfer coefficients. Among the other three models, the correlations by Kedzierski and Goncalves [46] and by Wang et al. [55] show the best agreement with experimental data.

On the whole, the model by Kedzierski and Goncalves [46] appears to be better than that by Wang et al. [55]: the correlation, which was obtained by regression of their own data, is able to capture the experimental trend of the heat transfer coefficient versus vapour quality. The predicted and experimental trends versus mass velocity do not perfectly match.

Table 29. Deviations from the experimental values of the tested models.

Model	e_R **[%]**	e_A **[%]**	σ_N **[%]**
Cavallini et al. [37]	65.4	65.4	18.8
Yu and Koyama [43]	28.8	29.1	27.6
Kedzierski and Goncalves [46]	-2.34	7.63	8.63
Chamra and Mago [48]	0.34	11.5	12.8
Han and Lee [50]	14.4	14.8	9.58
Koyama and Yonemoto [51]	3.03	24.1	31.1
Wang et al. [55]	-7.50	9.30	8.08

1.6 A New Condensation Heat Transfer Model

1.6.1 Introduction

In the last decades, several Authors have experimentally studied condensation inside microfin tubes measuring the heat transfer coefficient and the pressure gradient of different natural and synthetic refrigerants.

Cavallini et al. [8, 56] have collected more than 4000 experimental measures of mean, quasi-local and local condensation heat transfer coefficients in order to critically review the models available in the open literature and to develop a new computational procedure for heat transfer prediction.

As described before, in recent years many researchers such as Cavallini et al. [37], Yu and Koyama [43], Kedzierski and Goncalves [46], Chamra et al. [47, 48], Koyama and Yonemoto [51] and Wang et al. [55] have suggested different simple semi-empirical models for the calculation of the heat transfer coefficient during condensation in horizontal helical microfin tubes.

In the following, the predictions from the above models will be compared with experimental data, showing that no model seems to have general validity, even if some correlations provide more accurate predictions than others.

A new original computational procedure to calculate the heat transfer coefficients of halogenated and natural refrigerants, pure fluids or nearly-azeotropic mixtures condensing in helical microfin tubes is then presented. This model takes into account the fluid physical properties, the geometrical characteristics of the tube and a simplified flow regime classification.

This modelling procedure combines the accuracy of a two-phase flow based correlation and the simplicity of an empirical equation.

1.6.2 Experimental Database

During the last ten years, the Two-phase Research Group of the University of Padova has generated a database of around 4000 experimental mean, quasi-local and local heat transfer coefficients collected from several independent laboratories.

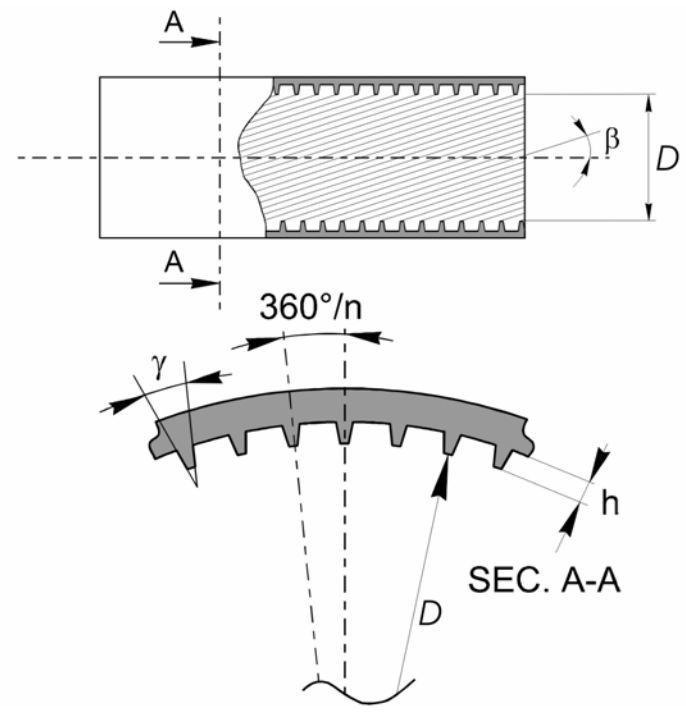

Figure 55. Characteristic geometrical parameters of microfin tubes.

Table 30 summarizes the operating test conditions of all the available experimental test runs. In particular, Table 30 reports: number of the test runs N_p, saturation temperature t_{sat}, mean vapour mass quality x, mass flux G. Several fluids are included in this database and the reduced pressure varies between 0.05 and 0.67. The mean vapour quality ranges between 0.0 and 1.0, the mass flux from 80 to around 900 kg m^{-2} s^{-1}.

Considering the nomenclature shown in Figure 55, Table 31 reports the geometrical characteristics of the tubes measured in the transversal cross-section: inner fin tip diameter of the tube D, number of fins n_g, fin height h, apex fin angle γ and helix angle β.

Inner tube surface geometries are characterized by the following parameters: 6mm<D<14mm, 2l<n_g<82, 0.12 mm<h<0.35 mm, 25°<γ<64°, 0°<β<30°.

Although different Authors may use different definitions of the heat transfer coefficient, all values in the data bank have been recalculated and referred to the same heat transfer area, the

heat transfer area of the smooth tube with a diameter equal to the fin tip diameter of the microfin tube.

Table 30. Intube condensation data: operating test conditions.

Reference	*Np*	Fluid	t_{sat} [°C]	*x* [-]	*G* [kg m^{-2}s^{-1}]	ΔT [K]
Tatsumi et al. [57]	8	22	36	0.00 - 1.00	100-300	/
Shinohara and Tobe [58]	8	22	36	0.00 - 1.00	100-300	/
Yasuda et al. [59]	14	22	40	0.00 - 1.00	120-326	/
Hori and Shinohara [60]	7	22	40	0.00 - 1.00	250	/
Schlager et al. [61]	13	22	39-43	0.15 - 0.90	133-487	/
Schlager et al. [62]	15	22	40.5	0.15 - 0.85	205-550	/
Eckels and Pate [63]	28	12, 134a	30-50	0.14 - 0.88	142-448	/
Eckels et al. [64]	4	134a	40	0.15 - 0.90	141-390	/
Eckels et al. [65]	61	12, 134a	38-41	0.10-0.90	90-384	1.5 – 5.4
Eckels and Tesene [66]	610	22, 134a, 410A	39-53	0.10-0.90	135-650	0.8 – 12.4
Torikoshi et al. [67,68]	23	22, 32, 134a, 32/134a	50	0.00 - 1.00	143-569	/
Arosio et al. [69]	14	22	35	0.20 - 0.80	96-436	2.5 – 7.5
EPRI [70]	44	22, 134a, 404A, 407C, 502, 507	51-53	0.00 - 1.00	163-868	1.2 – 8.0
Webb et al. [71]	22	22	23.8	0.20 - 0.80	80-320	/
Kedzierski and Goncalves [72]	1489	32, 125, 134a, 410A	22-51	0.00- 1.00	85-500	0.8 – 12.6
Tang [73]	228	22, 134a, 410A	35-41	0.00 - 0.90	277-890	/
Kwon and Kim [74]	42	22, 410A	31	0.85-0.05	97-202	/
Thors and Bogart [75]	26	22, 134a, 410A	40.6	0.20-0.80	224-910	/
Nozu and Honda [76]	52	11	29-50	0.05-0.951	134-516	0.8 – 10.7
Miyara et al. [77]	64	410	40	0.05-1.00	109-435	0.8 – 12.3
M.-H. Kim et al. [78]	43	22, 410A	45	0.10-0.85	292	1.0 – 3.2
Cavallini et al. [3, 22, 23]	323	22, 134a, 410A	30-60	0.20-0.85	100-800	3.8 – 16.7
Haraguchi [52]	190	22, 123,134a	48-70	0.10-0.95	107-319	0.8 – 11.3
Zilli et al. [79]	25	744	-15 -25	0.10-0.90	220-440	3.0 – 6.0
Colombo et al. [80]	46	134a	35	0.15-0.8	94-468	2.7 – 18.1
Uchida et al. [81]	28	22	41	0.10-0.90	141-446	0.8 – 4.3

The experimental data used for the validation of the model include CO_2, pure halogenated refrigerants and near azeotropic mixtures. Only the data presenting ΔT>0.8 K have been considered. The data sets for which ΔT is not available are considered only for dimensionless gas velocity J_G larger than 2.5 imposing ΔT=5 K.

While most data are quasi-local, the data by Arosio et al. [69], Eckels and Pate [63], Eckels et al. [64], Eckels et al. [65], EPRI [70], Schlager et al. [62], Thors and Bogarts [75] exhibit medium or large quality variation in the test tube (Δx=0.6-1.0). In this case the computed value has been calculated at the mean vapour quality.

It has been pointed out that only 171 data points by Tang [73] are relative to condensation in axial microfin tubes, β=0°; for these data the temperature difference ΔT is not available: the comparisons have been carried out for J_G=2.5.

Table 31. Intube condensation data: geometrical characteristics.

Reference	D [mm]	n_g [-]	h [mm]	γ [°]	β [°]
Tatsumi et al. [57]	8.32-8.52	65	0.15-0.25	45	7-25
Shinohara and Tobe [58]	8.52-8.68	60-65	0.12-0.20	25-80	7-25
Yasuda et al. [59]	6.94-8.52	50-60	0.20-0.25	40	18-30
Hori and Shinohara [60]	5.95-6.21	30-60	0.15-0.20	33-60	8-18
Schlager et al. [61]	7.75-8.32	21-60	0.20-0.38	0-50	18-30
Schlager et al. [62]	8.52-8.62	60	0.15-0.20	50	15-25
Eckels and Pate [63]	8.32	60	0.20	50	17
Eckels et al. [64]	8.52	60	0.20	50	17
Eckels et al. [65]	8.52-11.5	60	0.2	50	17
Eckels and Tesene [66]	8.51	60	0.203	51	18
Torikoshi et al. [67,68]	6.14	50	0.18	40	18
Arosio et al. [69]	8.52	60-65	0.15-0.20	53-90	18-25
EPRI [70]	8.52	60	0.20	53	18
Webb et al. [71]	14.18	74-80	0.35	30	15-27
Kedzierski and Goncalves [72]	8.51	60	0.2	50	18
Tang [73]	8.52	60-72	0.2	40-15	18
Kwon and Kim [74]	8.52	60	0.2	53	18
Thors and Bogart [75]	8.51	60	0.2	50	18
Nozu and Honda [76]	7.96	47	0.24	64.2	20
Miyara et al. [77]	6.08-6.11	50-60	0.21-0.19	40.9-26.2	18
M.-H. Kim et al. [78]	8.52-8.47-8.53	60-65-54	0.2-0.25-0.195	53-40-25	18-22-15.5
Cavallini et al. [3, 22, 23]	7.69	60	0.23	43	13
Haraguchi [52]	8.16	60	0.16	41.7	18
Zilli et al. [79]	5.97	54	0.15	45	18
Colombo et al. [80]	8.53-8.25	54-82	0.195-0.185	40	18
Uchida et al. [81]	6.06	50	0.22	25.4	12

1.6.3 Comparisons among Different Models

1.6.3.1 Model by Cavallini et al. [37]

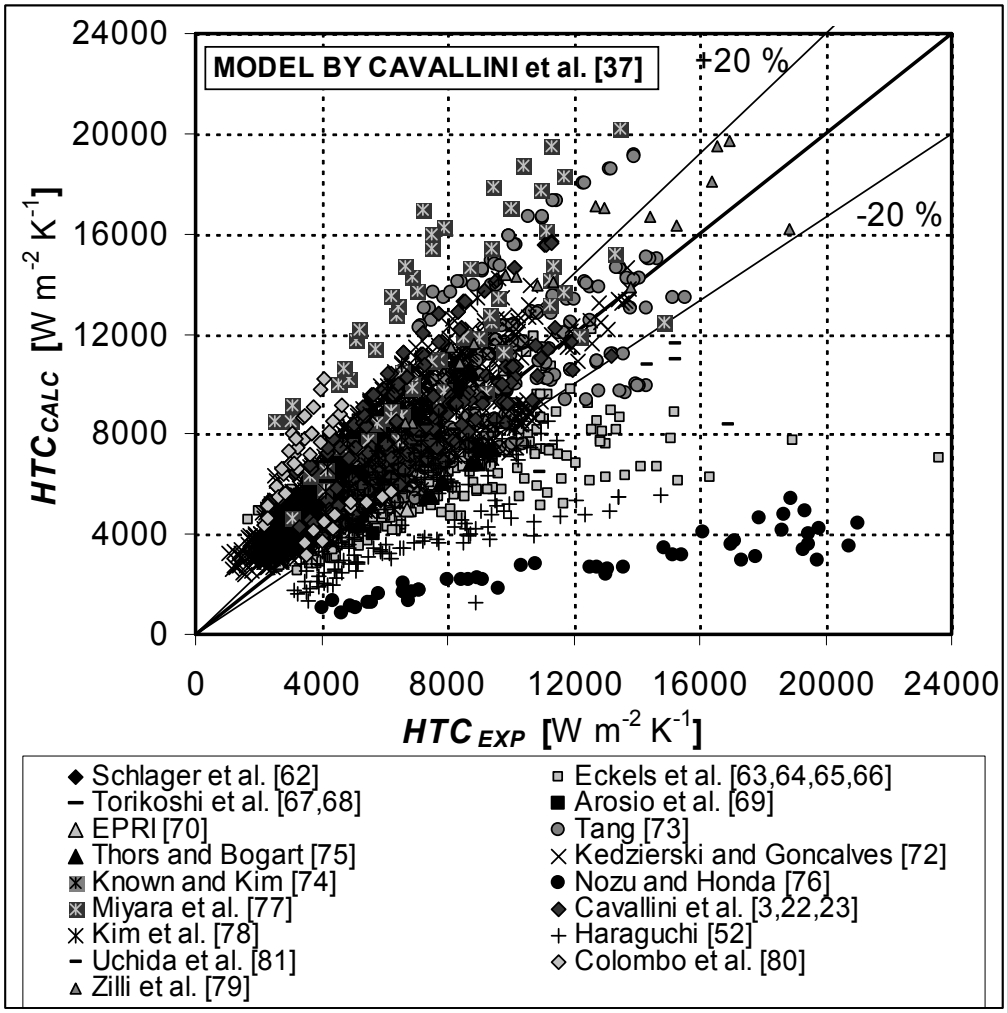

Figure 56. Calculated vs. experimental condensation heat transfer coefficients: model by Cavallini et al. [37].

Table 32. Deviations for Cavallini et al. [37] correlation (expressed in %).

Data set	Cavallini et al. [37]		
	e_R	e_A	σ_N
High Pressure Refrigerants: R32, R125, R404A, R410A and R744 (Np=266)	52	52	33
Low and Medium Refrigerants: R22, R123 and R134a (Np=694)	-0.54	22	35
Data by Cavallini et al. [3,22,23]: R22, R134a and R410A (Np=253)	25	27	30
Data by Eckels et al. [66]: R22, R134a, R410A, R507A (Np=687)	9.0	26	32
Data by Kedzierski and Goncalves [72]: R32, R125, R410A and R134a (Np=1389)	34	35	29
CFC data by Honda and Nozu [76]: R11 (Np=79)	-50	54	35
All database 3115 data points	**20**	**32**	**38**

1.6.3.2 Model by Yu and Koyama [43]

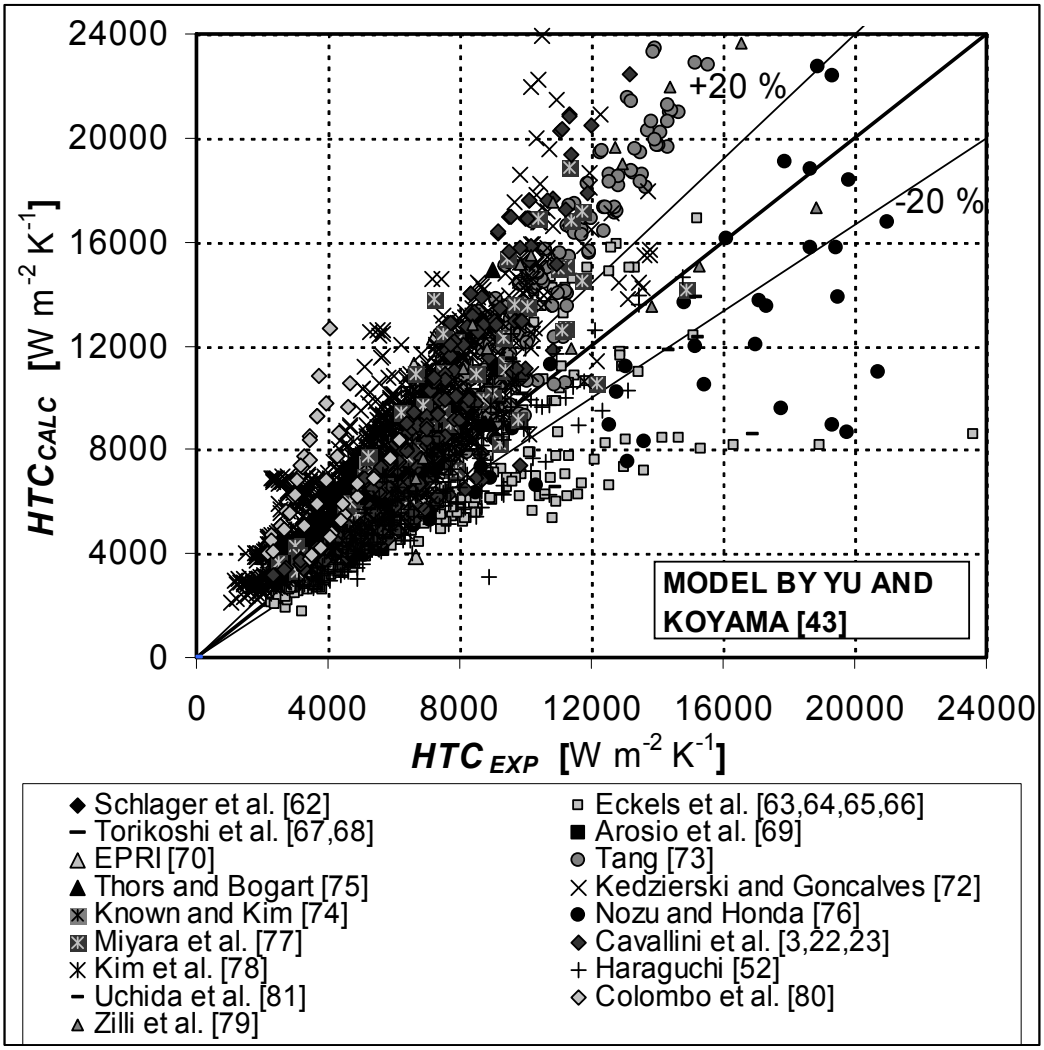

Figure 57. Calculated vs. experimental condensation heat transfer coefficients: model by Yu and Koyama [43].

Table 33. Deviations for Yu and Koyama [43] correlation (expressed in %).

Data set	Yu and Koyama [38]		
	e_R	e_A	σ_N
High Pressure Refrigerants: R32, R125, R404A, R410A and R744 (Np=266)	29	31	25
Low and Medium Refrigerants: R22, R123 and R134a (Np=694)	15	25	33
Data by Cavallini et al. [3,22,23]: R22, R134a and R410A (Np=253)	20	25	27
Data by Eckels et al. [66]: R22, R134a, R410A, R507A (Np=687)	6.7	24	30
Data by Kedzierski and Goncalves [72]: R32, R125, R410A and R134a (Np=1389)	42	42	31
CFC data by Honda and Nozu [76]: R11 (Np=79)	-9.6	19	21
All database 3115 data points	**26**	**33**	**35**

1.6.3.3 Model by Kedzierski and Goncalves [46]

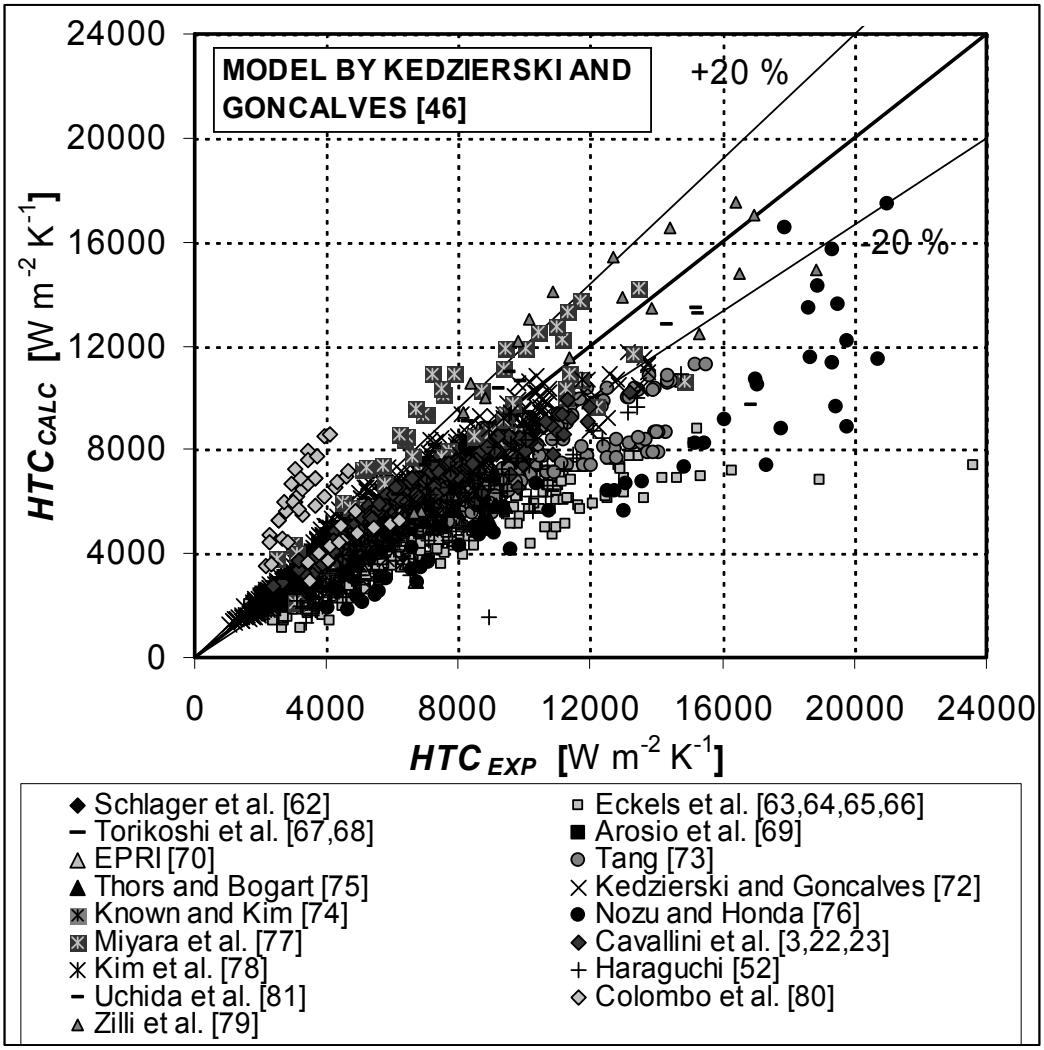

Figure 58. Calculated vs. experimental condensation heat transfer coefficients: model by Kedzierski and Goncalves [46].

Table 34. Deviations for Kedzierski and Goncalves [46] correlation (expressed in %).

Data set	Kedzierski and Goncalves [46]		
	e_R	e_A	σ_N
High Pressure Refrigerants: R32, R125, R404A, R410A and R744 (Np=266)	-7.2	16	19
Low and Medium Refrigerants: R22, R123 and R134a (Np=694)	-14	23	28
Data by Cavallini et al. [3,22,23]: R22, R134a and R410A (Np=253)	-7.4	10	9.7
Data by Eckels et al. [66]: R22, R134a, R410A, R507A (Np=687)	-28	29	15
Data by Kedzierski and Goncalves [72]: R32, R125, R410A and R134a (Np=1389)	-4.7	10	11
CFC data by Honda and Nozu [76]: R11 (Np=79)	-36	36	15
All database 3115 data points	**-13**	**19**	**20**

1.6.3.4 Model by Chamra et al. [47, 48]

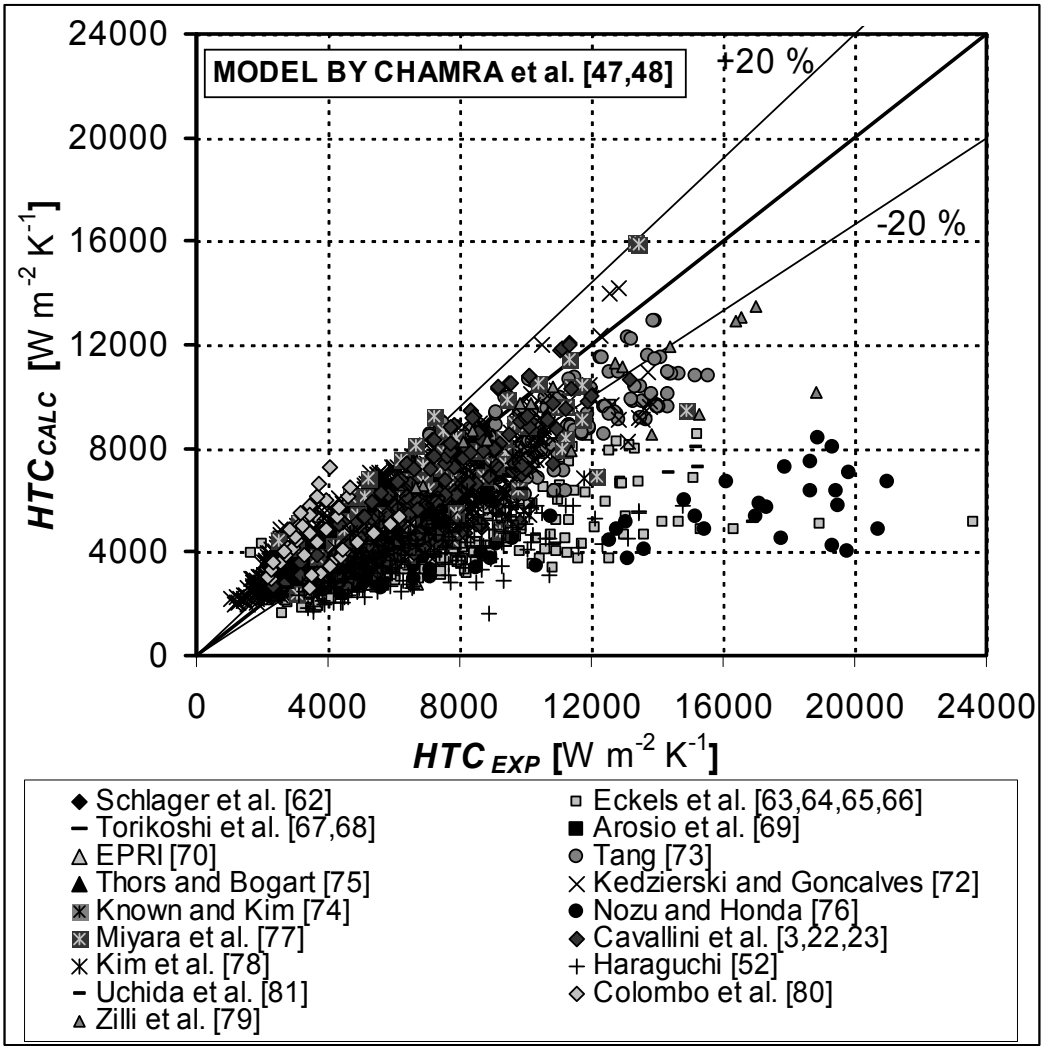

Figure 59. Calculated vs. experimental condensation heat transfer coefficients: model by Chamra et al. [47,48].

Table 35. Deviations for Chamra et al. [47,48] correlation (expressed in %).

Data set	Chamra and Mago [47,48]		
	e_R	e_A	σ_N
High Pressure Refrigerants: R32, R125, R404A, R410A and R744 (Np=266)	-4.4	13	17
Low and Medium Refrigerants: R22, R123 and R134a (Np=694)	-24	29	23
Data by Cavallini et al. [3,22,23]: R22, R134a and R410A (Np=253)	-13	17	16
Data by Eckels et al. [66]: R22, R134a, R410A, R507A (Np=687)	-17	25	25
Data by Kedzierski and Goncalves [72]: R32, R125, R410A and R134a (Np=1389)	1.7	18	23
CFC data by Honda and Nozu [76]: R11 (Np=79)	-46	46	20
All database 3115 data points	**-9.9**	**22**	**26**

1.6.3.5 Model by Han and Lee [50]

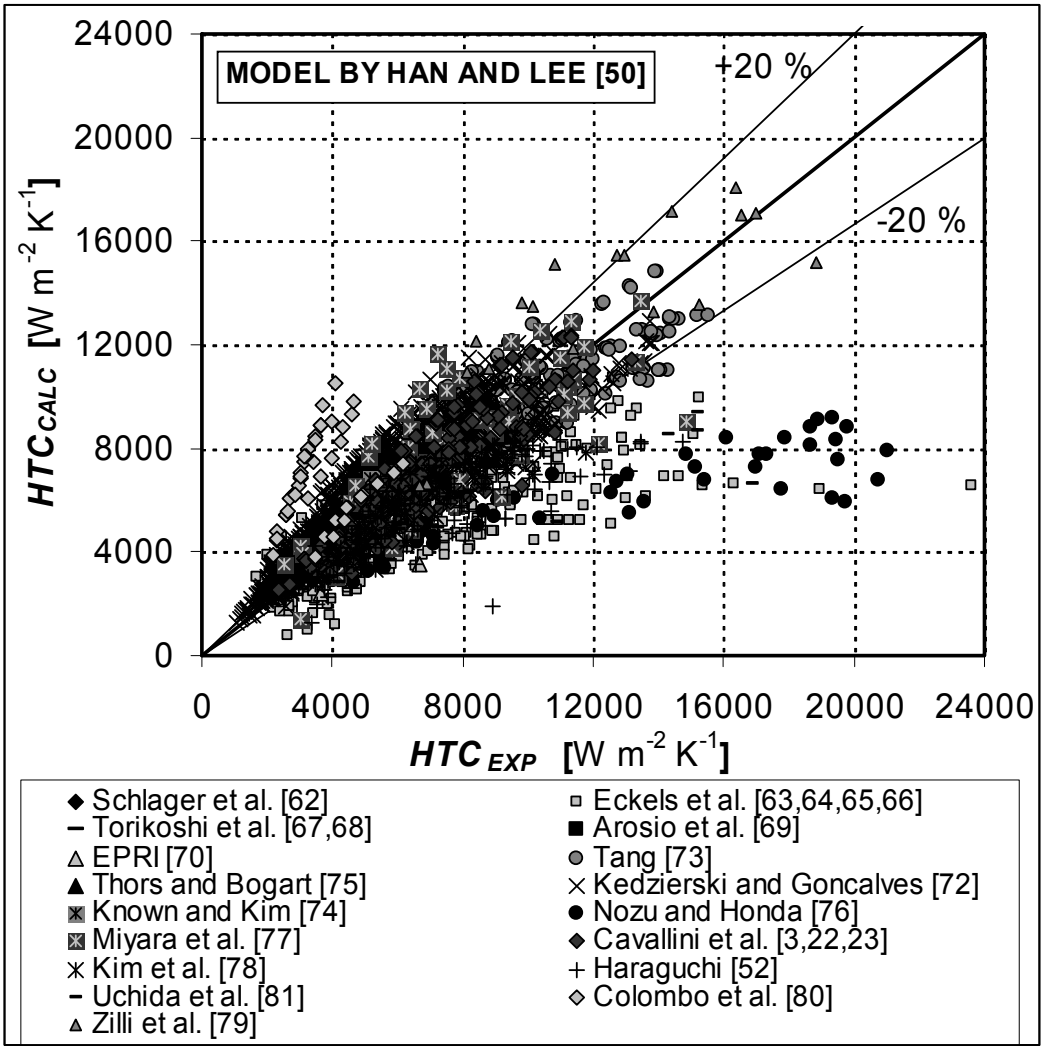

Figure 60. Calculated vs. experimental condensation heat transfer coefficients: model by Han and Lee [50]
.

Table 36. Deviations for Han and Lee [50] correlation (expressed in %).

Data set	Han and Lee [50]		
	e_R	e_A	σ_N
High Pressure Refrigerants: R32, R125, R404A, R410A and R744 (Np=266)	11	16	17
Low and Medium Refrigerants: R22, R123 and R134a (Np=694)	0.11	19	32
Data by Cavallini et al. [3,22,23]: R22, R134a and R410A (Np=253)	3.2	11	13
Data by Eckels et al. [66]: R22, R134a, R410A, R507A (Np=687)	-5.4	21	26
Data by Kedzierski and Goncalves [72]: R32, R125, R410A and R134a (Np=1389)	18	22	19
CFC data by Honda and Nozu [76]: R11 (Np=79)	-31	34	24
All database 3115 data points	**7.1**	**21**	**27**

1.6.3.6 Model by Koyama and Yonemoto [51]

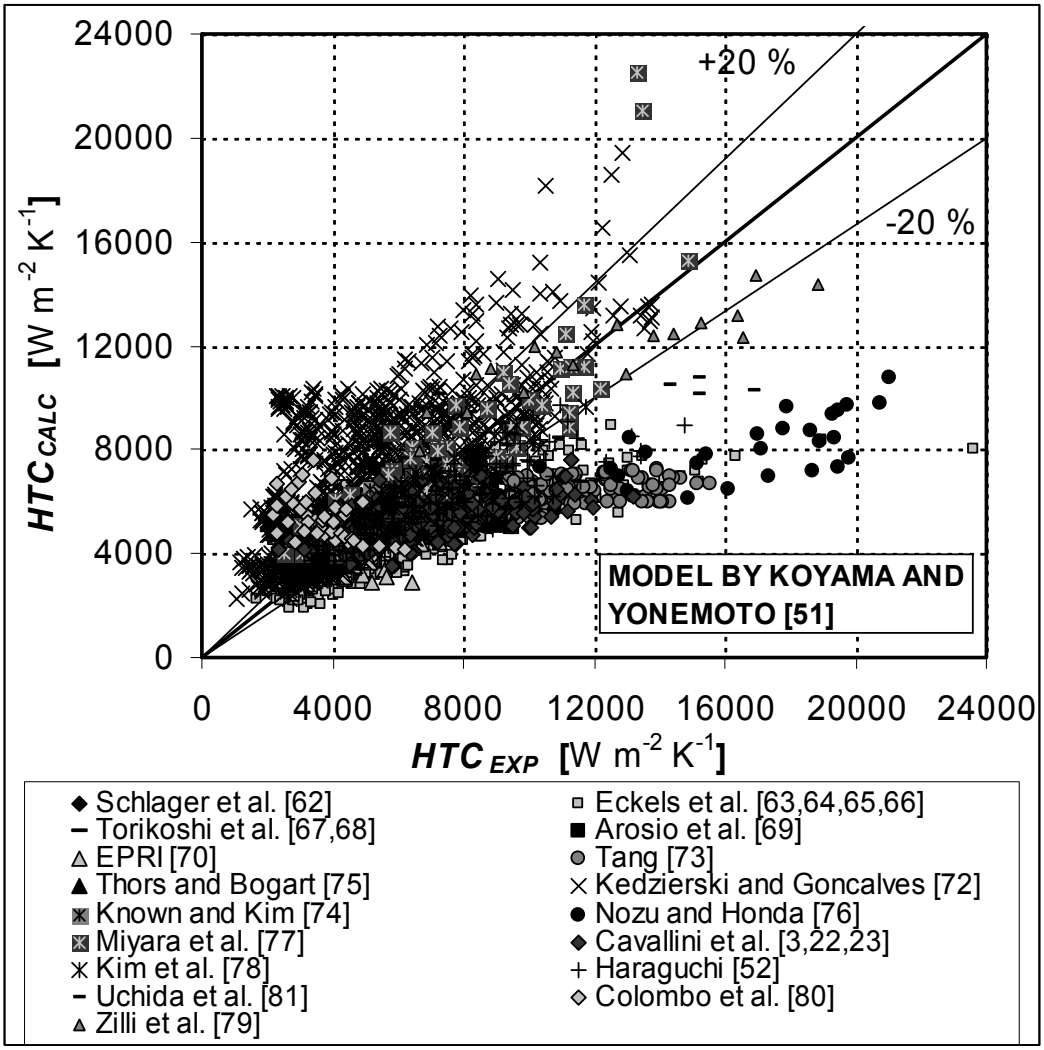

Figure 61. Calculated vs. experimental condensation heat transfer coefficients: model by Koyama and Yonemoto [51].

Table 37. Deviations for Koyama and Yonemoto [51] correlation (expressed in %).

Data set	Koyama and Yonemoto [51]		
	e_R	e_A	σ_N
High Pressure Refrigerants: R32, R125, R404A, R410A and R744 (Np=266)	-8.8	23	27
Low and Medium Refrigerants: R22, R123 and R134a (Np=694)	-13	27	32
Data by Cavallini et al. [3,22,23]: R22, R134a and R410A (Np=253)	-15	25	25
Data by Eckels et al. [66]: R22, R134a, R410A, R507A (Np=687)	-16	24	25
Data by Kedzierski and Goncalves [72]: R32, R125, R410A and R134a (Np=1389)	38	45	59
CFC data by Honda and Nozu [76]: R11 (Np=79)	-23	29	26
All database 3115 data points	**9.4**	**34**	**52**

1.6.3.7 Model by Wang et al. [55]

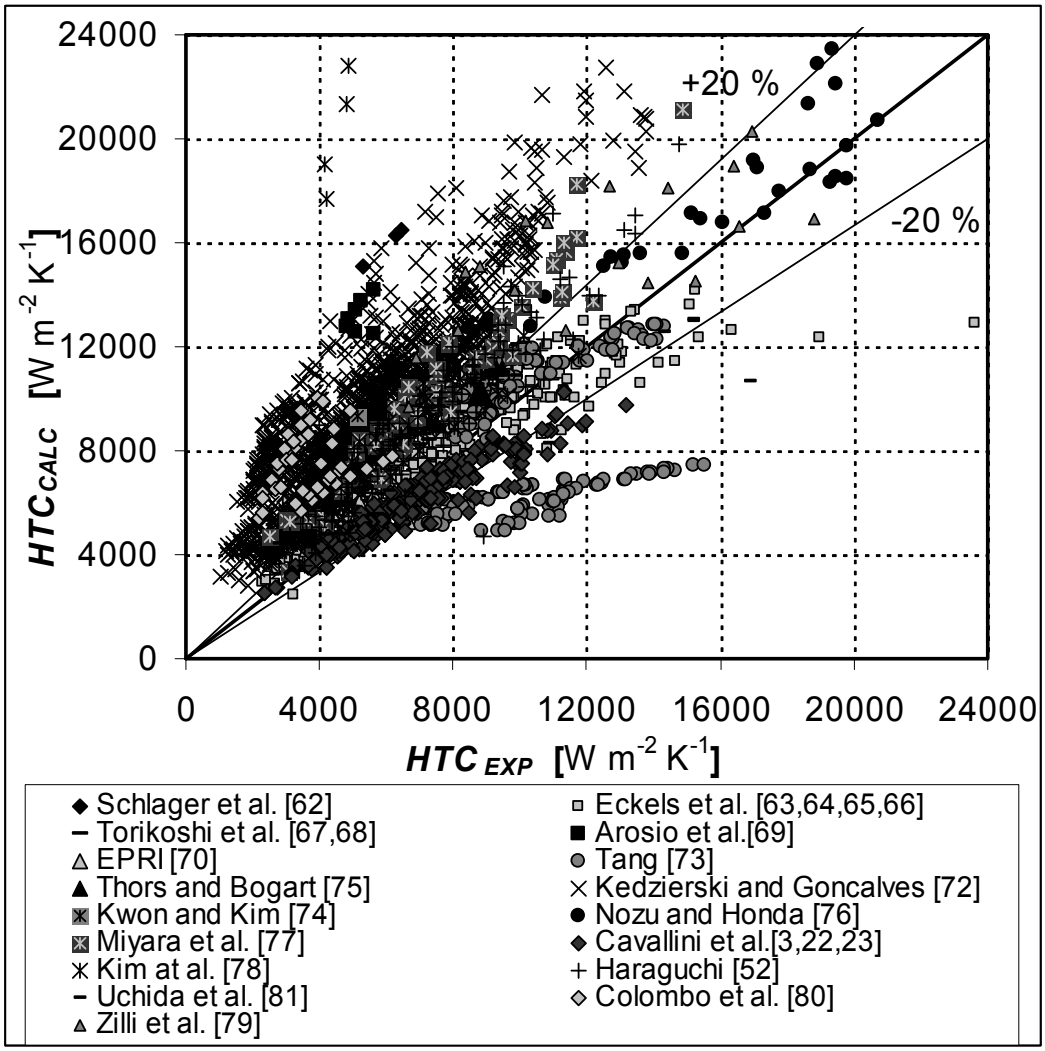

Figure 62. Calculated vs. experimental condensation heat transfer coefficients: model by Wang et al. [55].

Table 38. Deviations for Wang et al. [55] correlation (expressed in %).

Data set	Model by Wang et al. [55]		
	e_R	e_A	σ_N
High Pressure Refrigerants: R32, R125, R404A, R410A and R744 (Np=266)	17	32	54
Low and Medium Refrigerants: R22, R123 and R134a (Np=694)	22	36	51
Data by Cavallini et al. [3,22,23]: R22, R134a and R410A (Np=253)	-9.3	11	8.9
Data by Eckels et al. [66]: R22, R134a, R410A, R507A (Np=687)	28	30	23
Data by Kedzierski and Goncalves [72]: R32, R125, R410A and R134a (Np=1389)	90	90	54
CFC data by Honda and Nozu [76]: R11 (Np=79)	29	30	20
All database 3115 data points	**53**	**58**	**57**

1.6.3.8 Summary

In this paragraph, the experimental database is compared to the prediction of the models previously described.

The experimental points in the data bank (including the data by Honda and Nozu [26]) are compared against prediction of different models and results are reported in Table 39, in terms of relative deviation (e_R), average absolute deviation (e_A) and standard deviation (σ_N).

In order to give a clear overview of the behaviour of each model, the database has been subdivided in different data sets and the statistical parameters have been calculated and reported in a table located under each diagram.

It has to be pointed out that the selected models have been developed considering databases with different tube geometries, operating refrigerants and test conditions. The aim of the comparisons is to validate the proposed models also outside of their regression database in order to present some additional information about their capacity to predict heat transfer coefficients in different applications.

When comparing the experimental heat transfer coefficients with predictions from correlations, both are reduced to the same reference area.

Table 39. Deviations evaluated all over the database, for the tested correlations (expressed in %).

Model	e_R	e_A	σ_N
Cavallini et al. [37]	20	32	38
Yu and Koyama [43]	26	33	35
Kedzierski and Goncalves [46]	-13	19	20
Chamra et al. [47,48]	-9.9	22	26
Han and Lee [50]	7.1	21	27
Koyama and Yonemoto [51]	9.4	34	52
Wang et al. [55]	53	58	57

With reference to Table 35, the equation proposed by Chamra and Mago [47,48] shows a good agreement with the high pressure refrigerant data points. For low and medium refrigerant categories, all selected models appear to be quite scattered.

Equations by Kedzierski and Goncalves [46], Han and Lee [51], Wang et al. [55] display a very good behaviour when compared to the condensation heat transfer coefficients measured by Cavallini et al. [3,22,23].

All applied models tend to underestimate the data points measured by Eckels and Tesene [66]. The equation proposed by Kedzierski and Goncalves [22] is the most accurate when applied to its original database.

The data by Honda and Nozu [26] for R11 at reduced pressure p_R = 0.028 are underestimated by almost all the applied models.

Finally, when all data points are considered, the models by Kedzierski and Goncalves [46], Chamra and Mago [47,48] and Han and Lee [51] present the most accurate predictions.

These comparisons show that no model seems to have general validity, though some correlations provide more accurate predictions than others.

Therefore, a new original computational procedure to calculate the heat transfer coefficient of halogenated and natural refrigerants, pure fluids and nearly azeotropic mixtures condensing in helical microfin tubes has been developed.

1.6.4 Development of a New Correlation

In the following there will be presented a new computational procedure to predict the heat transfer coefficient of halogenated and natural refrigerants, pure fluids or nearly azeotropic mixtures condensing in helical microfin tubes. This model takes into account the physical properties of the fluid, the geometrical characteristics of the tube and a simplified flow regime classification. This modeling procedure combines the accuracy of a two-phase flow based correlation and the simplicity of an empirical equation. The most important issues of the new correlation are explained in what follows.

1.6.4.1 Simplified Flow Regime Map

As highlighted before, this new computational procedure is based on a simplified flow regime map which descends from its homologue for condensation inside smooth tubes.

Cavallini et al. [16] presented a model for the heat transfer coefficient during condensation in a smooth tube based on a simple flow regime subdivision. They only considered two flow regimes: the ΔT independent regime associated to high vapour shear forces and annular flow and the ΔT dependent flow regime associated to wavy and stratified flows. This simple flow regime map is described also in paragraph 1.1.4. Figure 63 shows the Cavallini et al. [16] transition for smooth tubes in the J_G-X_{tt} chart, described by the following equation:

$$J_G^T = \left\{ \left[\frac{7.5}{4.3X_{tt}^{1.111} + 1} \right]^{-3} + C_T^{-3} \right\}^{-0.3333} \qquad \textbf{Eq. 181}$$

Where C_T is set:

for hydrocarbons C_T is1.6
for other refrigerants C_T is 2.6

In a microfin tube the liquid formed at the wall is drained into the spiral groove by combined surface tension, centrifugal and gravity forces, while vapour shear forces drive the condensate in the downstream direction.

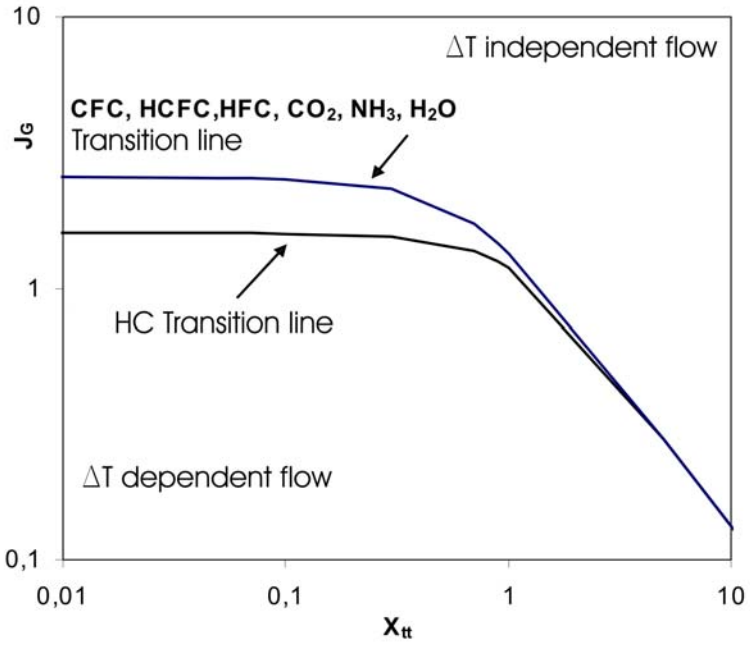

Figure 63. Cavallini et al. [15, 16] simplified flow regime map for smooth tubes.

Doretti et al. [20] observed flow patterns during condensation of refrigerants R410A, R134a, R236ea, flowing inside a smooth tube and a helical microfin tube. They plotted their visual observations on the Cavallini et al. [15, 16] map and found a good correspondence for the smooth tube, while they had to shift the annular-wavy stratified transition to lower values of the dimensionless gas velocity J_G for the helical microfin tube. Figure 64 shows the Doretti et al. [20] transition for the microfin tube, which can be interpolated with the following equation:

$$J_G^* = 0.6 \cdot \left\{ \left[\frac{7.5}{4.3 X_{tt}^{1.111} + 1} \right]^{-3} + 2.5^{-3} \right\}^{-0.3333} \qquad \textbf{Eq. 182}$$

Also visualization studies with air-water by Shedd and Newell [82] indicate that helical grooves tend to redistribute the liquid film, while the mean liquid film is thinner in tubes with 18° helical grooves as compared to 9° helical, axial grooved and smooth tubes.
From these studies it can be concluded that helical grooves promote and extend the range of annular flow.

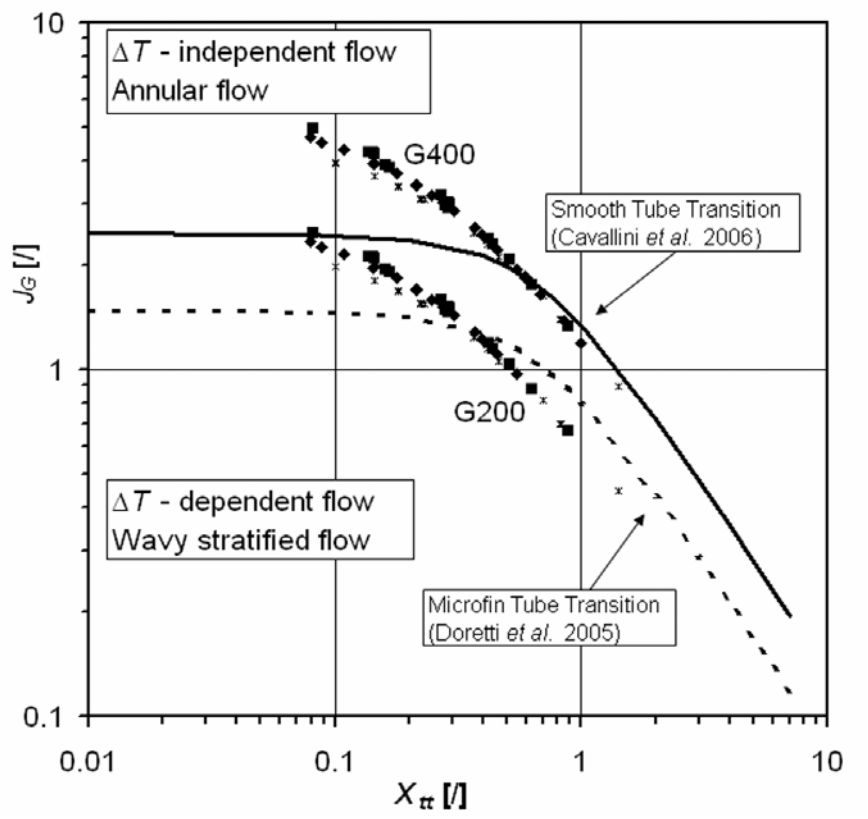

Figure 64. Transition for smooth and helical microfin tubes. The data points for G=200 kg m^{-2} s^{-1} and 400 kg m^{-2} s^{-1} are also plotted.

Cavallini et al. [3, 22, 23] measured heat transfer coefficients during condensation of R22, R134a, R410A inside a microfin tube. Their experimental data show that at high dimensionless gas velocities the heat transfer coefficient does not depend on the temperature difference ΔT while it does at low J_G. As explained in Figure 65, at intermediate values of J_G and exactly at values of dimensionless gas velocities falling in the region between the smooth tube and the microfin tube transitions, ($J_G^T < J_G < J_G$*), Cavallini et al. [3, 22, 23] heat transfer coefficients depend on temperature difference; in this region, even if annular flow is present, the heat transfer coefficient shows to be higher at lower ΔT. In Figure 64, the experimental data for R22, R134a, R410A at saturation temperature around 40°C and mass velocity G=200 kg m^{-2} s^{-1} and G=400 kg m^{-2} s^{-1} are also plotted on the J_G-X_{tt} map.

Cavallini et al. [3, 22, 23] also showed that the experimental heat transfer coefficient increases with vapour quality and mass velocity. Furthermore, it increases when lowering reduced pressure and it is influenced by surface geometry.

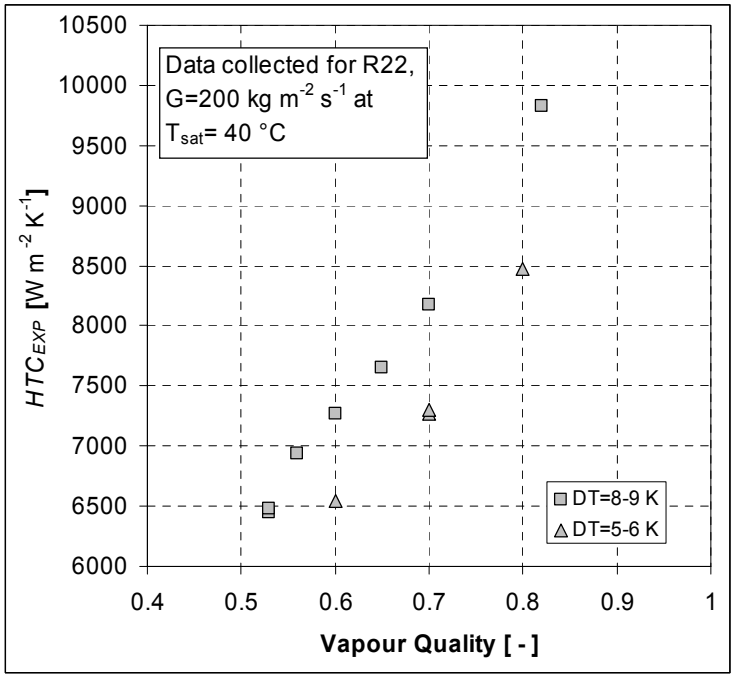

Figure 65. Condensation heat transfer coefficient vs. vapour quality as a function of saturation to wall temperature difference.

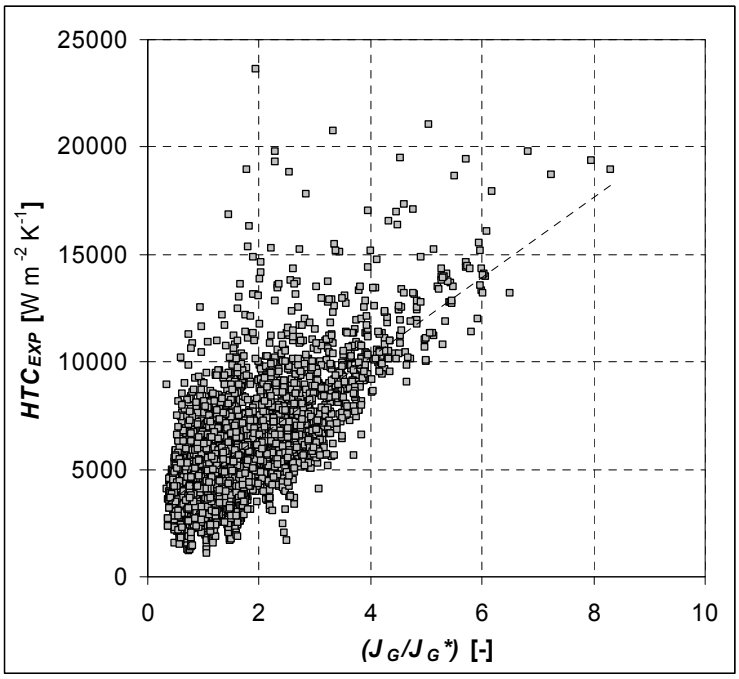

Figure 66. Relationship between non-dimensional gas velocity ratio and heat transfer coefficient.

Figure 66 plots the heat transfer coefficient as a function of non-dimensional gas velocity ratio. Generally speaking, the condensation heat transfer coefficient increases as the ratio increases.

1.6.4.2 Geometrical Characteristics of Microfin Tubes

Apex angle, helix angle, inner diameter, number of grooves, groove depth are the main geometrical parameters that influence condensation.

Tsuchida et al. [83], Hori and Shinohara [60] and Houfuku et al. [39] experimentally studied the influence of the geometrical characteristics of microfin tubes on condensation heat transfer.

In particular, they analysed the influence of fin height and of number of fins on condensation heat transfer coefficients.

Number of fins

Tsuchida et al. [83] and Hori and Shinohara [60] demonstrated that there is an optimum value for the number of fins with respect to both evaporation and condensation.

In particular, as highlighted by Figure 67, considering mass velocities around 200 kg m^{-2} s^{-1}, there is an optimal number of grooves which maximizes the condensation performance and this number increases with tube diameter.

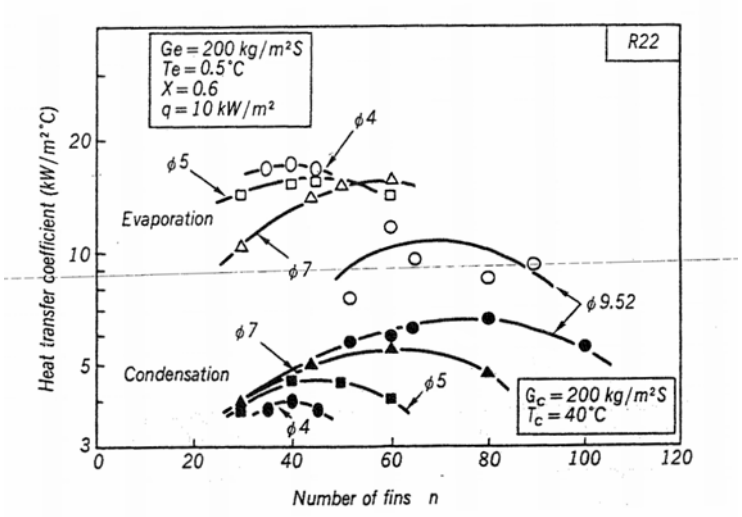

Figure 67. Relationship between number of fins and the heat transfer coefficient (Tsuchida et al. [83]).

With a number of grooves higher than the optimal value, the cross-sectional total liquid flow area in the grooves becomes smaller and the liquid film on the inner surface thickens as suggested by Yasuda et al. [59]. The condensation heat transfer coefficient seems to increase with the helix angle (Bukasa et al.) [84], while there seems to be an optimal fin height.

Fin height

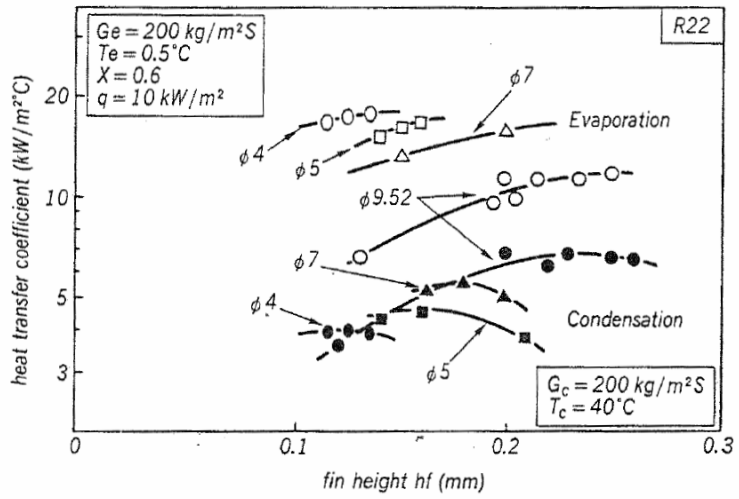

Figure 68. Relationship between fin height and the heat transfer coefficient (Tsuchida et al.) [83].

This is confirmed by the experimental results found by Tsuchida et al. [83], as reported in Figure 68. It appears that the condensation heat transfer coefficient presents a maximum as a function of fin height. Hence, an optimum value of fin height exists which appears to increase with tube diameter.

Colombo et al. [80] measured the condensation heat transfer coefficient inside two microfin tubes with different numbers of fins: 82 and 54.
All the heat transfer models tested before overestimate the data for the 82 fins microfin tube because they only consider the mere increase of the heat transfer area.
Starting from this consideration and from the results described by Tsuchida et al. [83], a parameter which takes into account the optimum value of the number of fins is proposed.
The optimum number of fins is given by:

$$n_{opt} = 4064.4 \cdot D + 23.257 \qquad D[\mathrm{m}]$$

$$\begin{aligned} C &= 1 && if\ \left(n_{opt}/n_g\right) \geq 0.8 \\ C &= \left(n_{opt}/n_g\right)^a && if\ \left(n_{opt}/n_g\right) < 0.8 \end{aligned} \qquad \textbf{Eq. 183}$$

Where the term C is a constant that will be inserted in the final equation to introduce a correction with reference to the optimum fin number.
Naturally, optimization is here intended only related to the heat transfer coefficient, with no consideration of the associated frictional pressure drop.
The heat transfer area enhancement due to the presence of fins is taken into account by the following parameter:

$$Rx = \left\{ \frac{2h \cdot n_g \left[1 - \sin(\gamma/2)\right]}{\pi D \cos(\gamma/2)} + 1 \right\} \frac{1}{\cos\beta} \qquad \textbf{Eq. 184}$$

The geometry enhancement factor *Rx* is a function of the ratio of the inside surface area of the microfin tube divided by the inside area of the smooth tube with the fin tip diameter.

1.6.4.3 Development of the Model Equations

As described before, the heat transfer coefficient is defined with reference to the heat transfer area of the smooth tube with diameter *D* equal to the fin tip diameter of the microfin tube:

$$HTC = \frac{q}{\pi DL} \frac{1}{\Delta T} \qquad \textbf{Eq. 185}$$

The heat transfer coefficient is calculated as the combination of two terms: the heat transfer coefficient for the ΔT independent zone HTC_A and the heat transfer coefficient for the ΔT dependent zone HTC_D .

$$HTC = \left[HTC_A^3 + HTC_D^3 \right]^{0.333} \qquad \textbf{Eq. 186}$$

The forced convective condensation term HTC_A is obtained as the product of the convective heat transfer coefficient for the smooth tube HTC_{AS}, given by Cavallini et al. [16], by a function (term *A*) of the geometry enhancement factor *Rx* and the Froude number Fr. The term *C* (Eq. 183) acts to lower the heat transfer coefficient when the fin number n_g is greater than the optimal value n_{opt} for the given diameter *D*.

$$HTC_A = HTC_{AS} \cdot A \cdot C$$ **Eq. 187**

$$HTC_{AS} = HTC_{LO}\left\{1 + x^{0.8170}\left[1.128\left(\frac{\rho_L}{\rho_G}\right)^{0.3685}\left(\frac{\mu_L}{\mu_G}\right)^{0.2363}\left(1-\frac{\mu_G}{\mu_L}\right)^{2.144}\mathrm{Pr}_L^{-0.100}\right]\right\}$$ **Eq. 188**

Where:

$$HTC_{LO} = 0.023\frac{\lambda_L}{D}\cdot \mathrm{Re}_{LO}^{0.8}\cdot \mathrm{Pr}_L^{0.4} = 0.023\frac{\lambda_L}{D}\cdot\left(\frac{GD}{\mu_L}\right)^{0.8}\cdot \mathrm{Pr}_L^{0.4}$$ **Eq. 189**

and the two constants *A* and *C* are given by:

$$A = 1+1.119\cdot Fr^{-0.3821}\cdot (Rx\text{-}1)^{0.3586}$$ **Eq. 190**

$$\begin{aligned} &C = 1 && if\left(n_{opt}/n_g\right) \geq 0.8 \\ &C = \left(n_{opt}/n_g\right)^{1.904} && if\left(n_{opt}/n_g\right) < 0.8 \\ &n_{opt} = 4064.4\cdot D + 23.257 && D[\mathrm{m}] \end{aligned}$$ **Eq. 191**

The heat transfer coefficient for the ΔT dependent zone HTC_D is expressed as the function of the term *C*, the geometry enhancement factor *Rx* and the (ΔT dependent) coefficient $HTC_{D,S}$ for smooth tubes (Cavallini et al. [16]). If the dimensionless gas velocity is lower than the transition gas velocity J_G* ($J_G < J_G$*) the heat transfer coefficient is reduced through the constant C_1.

$$HTC_D = C\cdot[2.4\,x^{0.1206}\cdot(Rx\text{-}1)^{1.466}\cdot C_1^{0.6875}+1]\cdot HTC_{D,S} + C\cdot(1\text{-}x^{0.087})\cdot Rx\cdot HTC_{LO}$$ **Eq. 192**

$$HTC_{D,S} = 0.725\left\{1+0.741\left[\frac{1-x}{x}\right]^{0.3321}\right\}^{-1}\left[\frac{\lambda_L^3\cdot\rho_L\left(\rho_L-\rho_G\right)g\cdot h_{LG}}{\mu_L\cdot D\cdot\Delta T}\right]^{0.25}$$ **Eq. 193**

$$C = 1 \qquad \text{if } J_G \geq J_G^*$$
$$C = \left(\frac{J_G}{J_G^*} \right) \qquad \text{if } J_G \geq J_G^* \qquad \textbf{Eq. 194}$$

Where J_G* is calculated with Eq. 182 while Re_{LO}, Fr and Pr_L are calculated with:

$$Re_{LO} = \frac{GD}{\mu_L} \qquad \textbf{Eq. 195} \qquad Fr = \frac{G^2}{gD(\rho_L - \rho_G)^2} \qquad \textbf{Eq. 196} \qquad Pr_L = \frac{\mu_L c_{pL}}{\lambda_L} \qquad \textbf{Eq. 197}$$

The model is valid for tubes with helical fins having fin height to diameter ratio h/D less than 0.04. This model should be applied to halogenated refrigerants and carbon dioxide with reduced pressure $0.1<p_R<0.67$, vapour quality $0<x<1$ and mass velocity ranging between $90<G<900$ kg m^{-2} s^{-1}.

The empirical constants in Eq. 190, Eq. 191 and Eq. 192 are obtained reducing 558 experimental data points, selected with low experimental uncertainty, available temperature difference, different tube geometries and operative fluids.

Precisely, with reference to Table 30 and Table 31, the following data sets are used in the best fitting procedure:

186 points by Cavallini et al. [3,22,23] for R22, R134a and R410A;
96 by Haraguchi [52] for R134a and R123;
106 by Kedzierski and Goncalves [72] for R32;
10 by Arosio et al. [69] for R22;
52 by Miyara et al. [77] for R410A;
39 by Kim et al. [78] for R22 and R410A;
20 by Zilli et al. [79] for CO_2;
32 by Colombo et al. [80] for R134a;
17 by Uchida et al. [81] for R22.

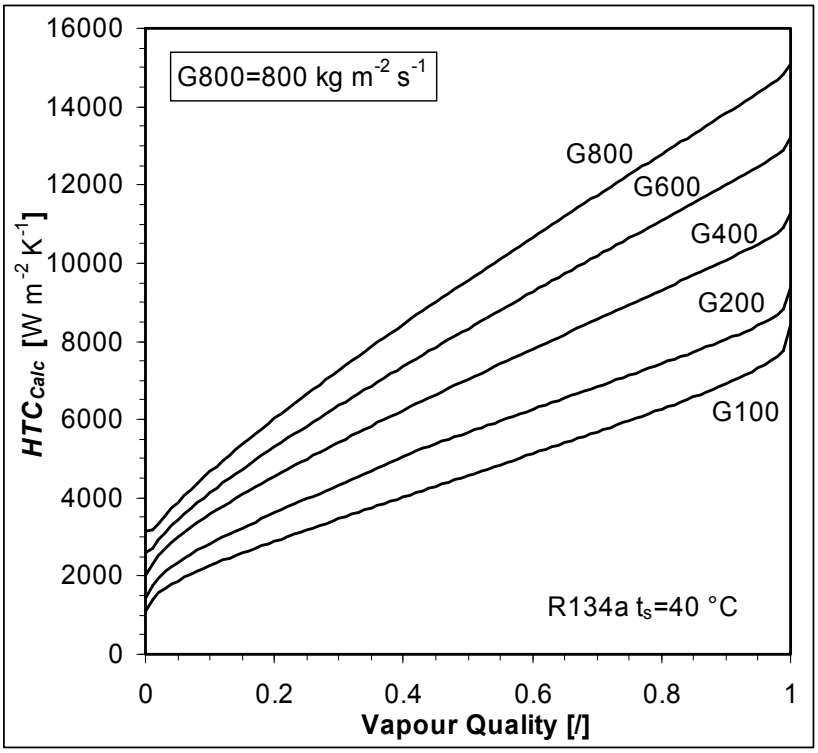

Figure 69. Prediction of the heat transfer coefficient at constant mass velocity, G.

The present model provides a smooth trend for the heat transfer coefficient when the condensation proceeds, as shown in Figure 2: the predicted heat transfer coefficient for R134a condensing inside a microfin tube (inside fin tip diameter D= 7.69 mm, number of grooves n_g=60 , fin height h = 0.23 mm, apex angle γ= 43° and spiral angle β= 13°) at 40 °C saturation temperature is plotted versus vapour quality in Figure 69, covering mass velocities in the range of 100–800 kg m^{-2} s^{-1}. Saturation to wall temperature difference is kept constant (5 K).

1.6.5 Comparisons Against Experimental Data

The predictions from the proposed model have been compared against 3115 experimental data points, collected from several independent laboratories and listed in Table 30 and Table 31. This model should be applied with reference to the following constraints: 6mm<D<14mm, 2l<n_g<82, 0.12 mm<h<0.35 mm, 25°<γ<64°, 0°<β<30°. The experimental data used for the validation of the model include CO_2, pure halogenated refrigerants and near azeotropic mixtures. Only data which present ΔT>0.8 K have been considered. The data sets for which ΔT is not available are considered only for dimensionless gas velocity J_G larger than 2.5 imposing ΔT=5 K. In fact, for J_G >2.5 the calculated annular component HTC_A (Eq. 187)

accounts for more than 90-95% of the total calculated heat transfer coefficient *HTC* (Eq. 186), as shown in Figure 70.

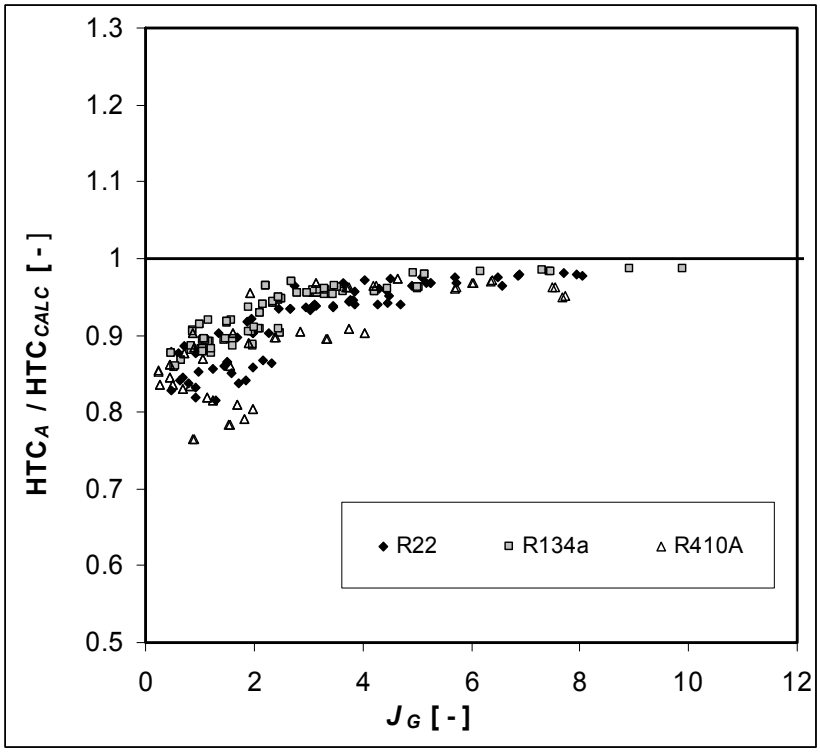

Figure 70. Calculated annular component HTC_A divided by total calculated heat transfer coefficient vs. J_G .

Experimental and calculated heat transfer coefficients, obtained by means of the present model, are compared in the following diagrams. Figure 71 shows the results relative to R22, R134a and R410A experimental data by Cavallini et al. [2, 22, 23].

The model shows a very good agreement with the experimental data points; the average deviation e_R is -2.15% while the absolute deviation is e_A= 6.20% with a standard deviation σ_N= 8.16%.

Figure 72 and Figure 73 show the results relative to CO_2 and to HCFC and HFC pure fluids and near azeotropic mixtures. Although some data sets relative to low pressure refrigerants are quite scattered, there is a good agreement between the model and the experimental data, especially for the high pressure refrigerants. Only data by Haraguchi [29] are underestimated more than 20%, the other data points are predicted within ±20%.

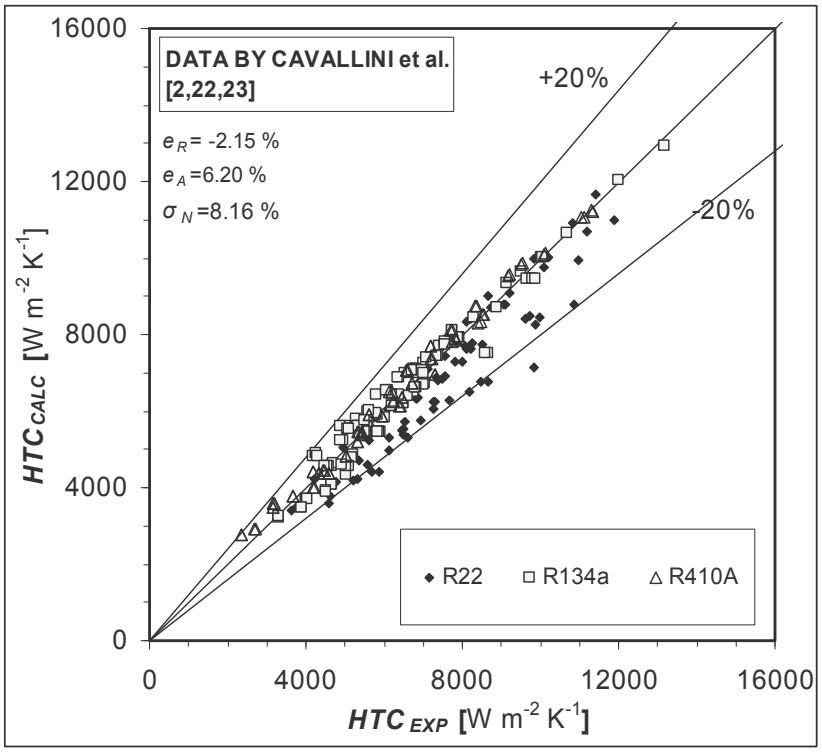

Figure 71. Application of the model to Cavallini et al. [2, 22, 23] data.

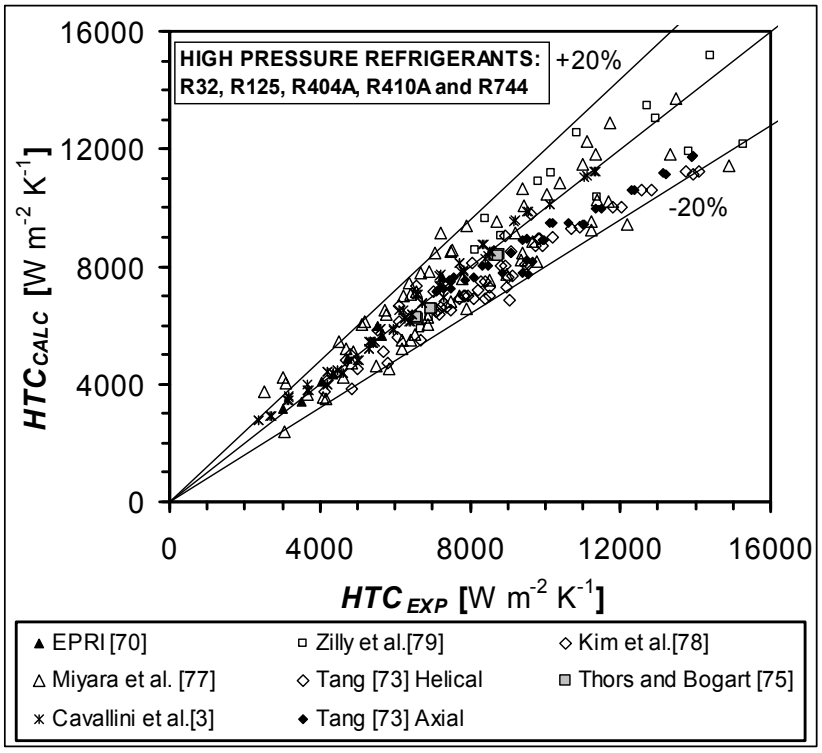

Figure 72. Application of the model to high pressure refrigerant data.

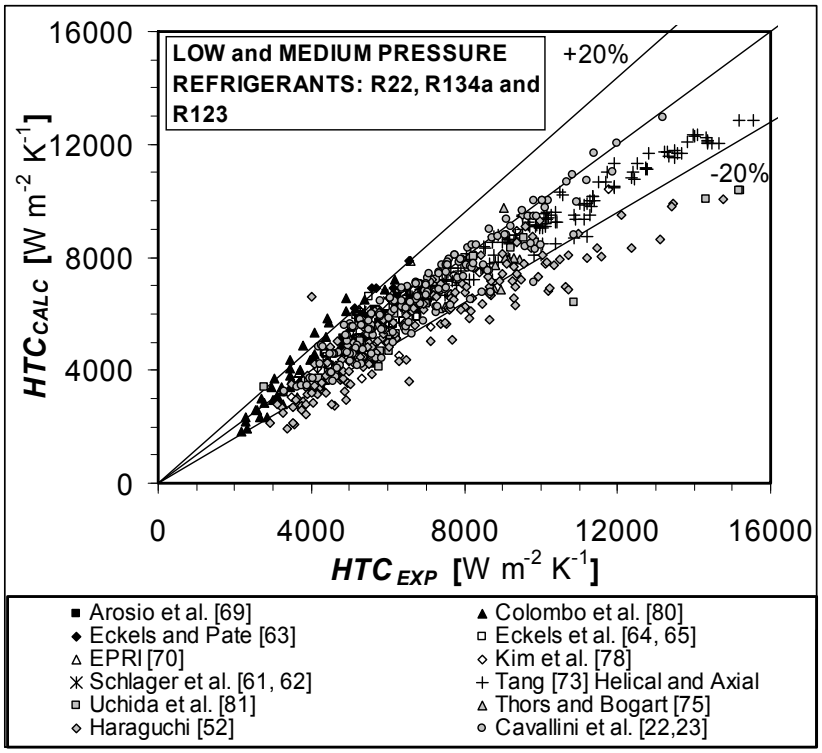

Figure 73. Application of the model to low and medium refrigerant data.

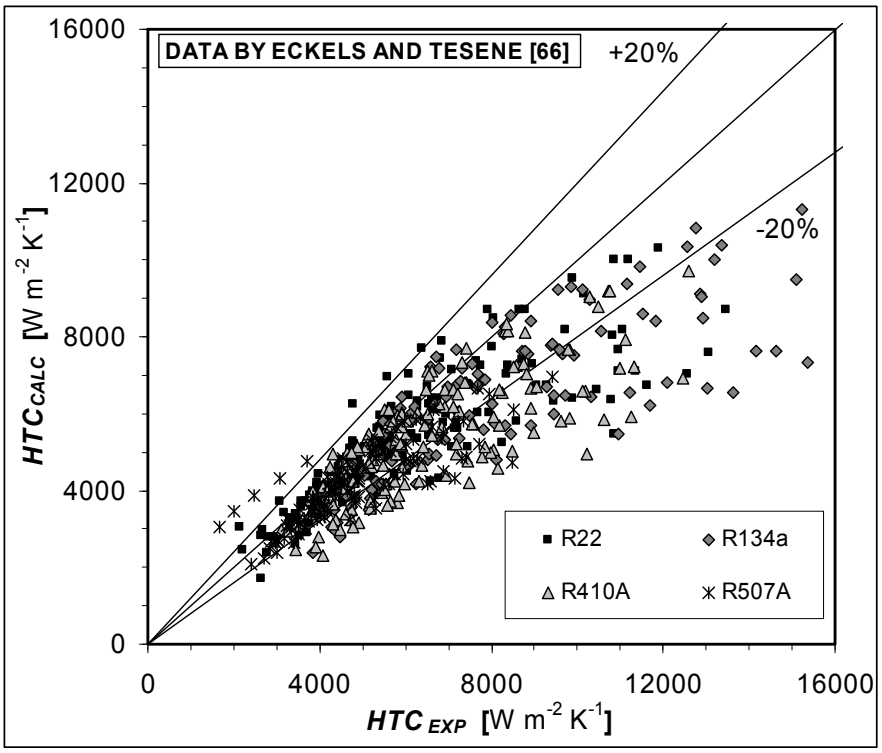

Figure 74. Application of the model to Eckels and Tesene [66] data.

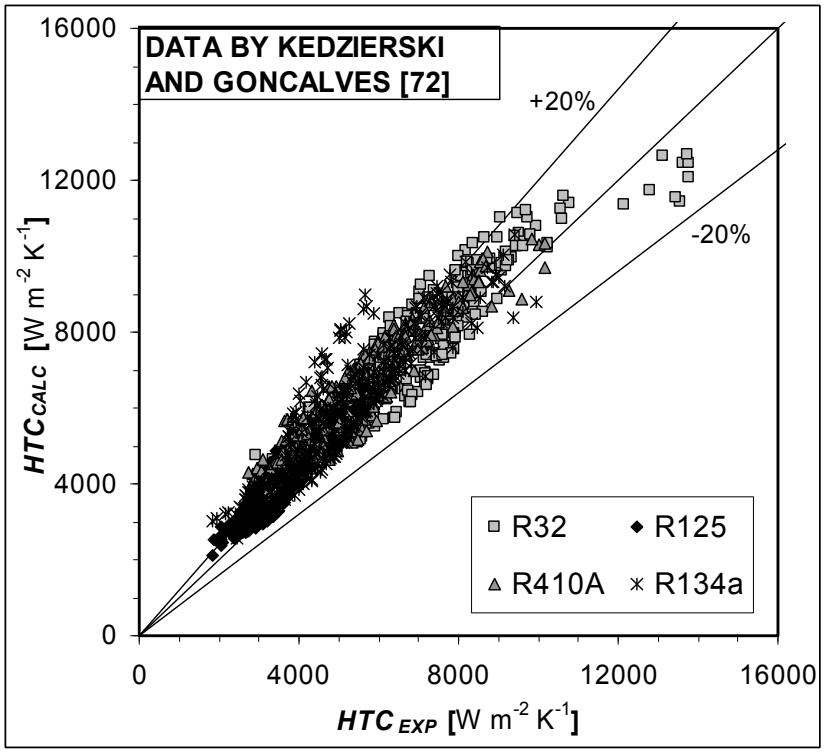

Figure 75. Application of the model to Kedzierski and Goncalves [72] data.

It has to be pointed out that only 171 data points by Tang [73] are relative to condensation in axial microfin tubes (β=0°). For this data the temperature difference ΔT is not available and comparisons have been carried out for J_G>2.5.

The comparison with Eckels and Tesene [66] data is reported in a separated graph (Figure 74); the results appear quite scattered but the experimental data also present a high declared uncertainty.

The comparison with Kedzierski and Goncalves [72] data, having a declared experimental uncertainty lower than ± 30%, is also reported in Figure 75. The model tends to slightly overestimate the experimental heat transfer coefficient and most of the data are calculated within ±20%.

The ratio of calculated to experimental heat transfer coefficients for all high pressure and low pressure refrigerant data is plotted against the dimensionless gas velocity J_G in Figure 76 and against the geometry enhancement factor Rx in Figure 77. Deviations do not show dependence on these parameters.

On the whole, most of the data are within ±20% and the prediction capacity increases as the non-dimensional gas velocity rises. Plotted against the area enhancement factor, the same ratio does not show any dependence.

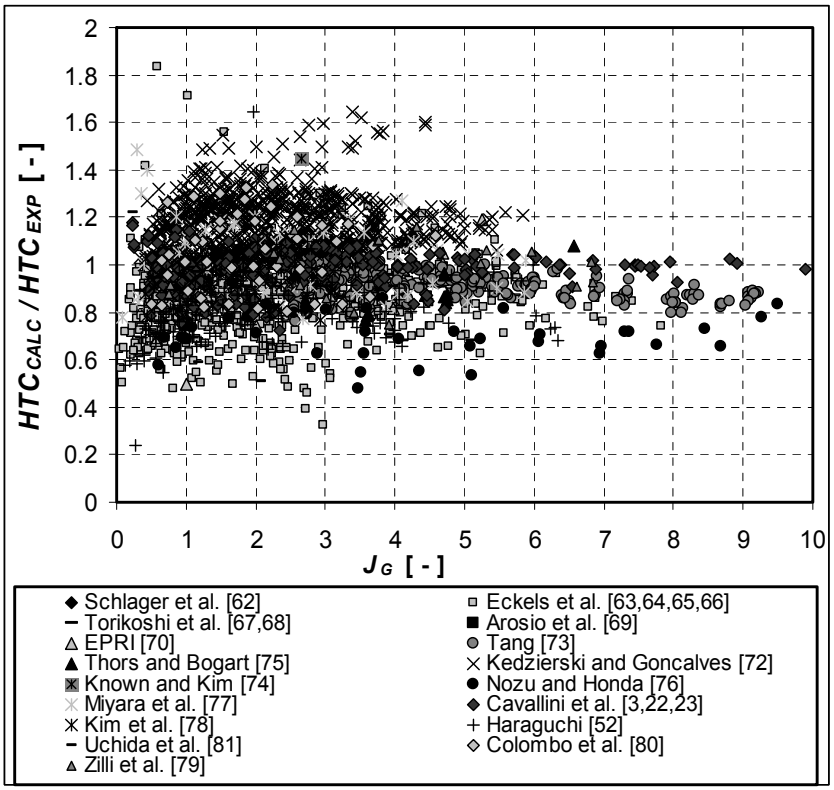

Figure 76. Ratio of calculated to experimental heat transfer coefficient vs. J_G.

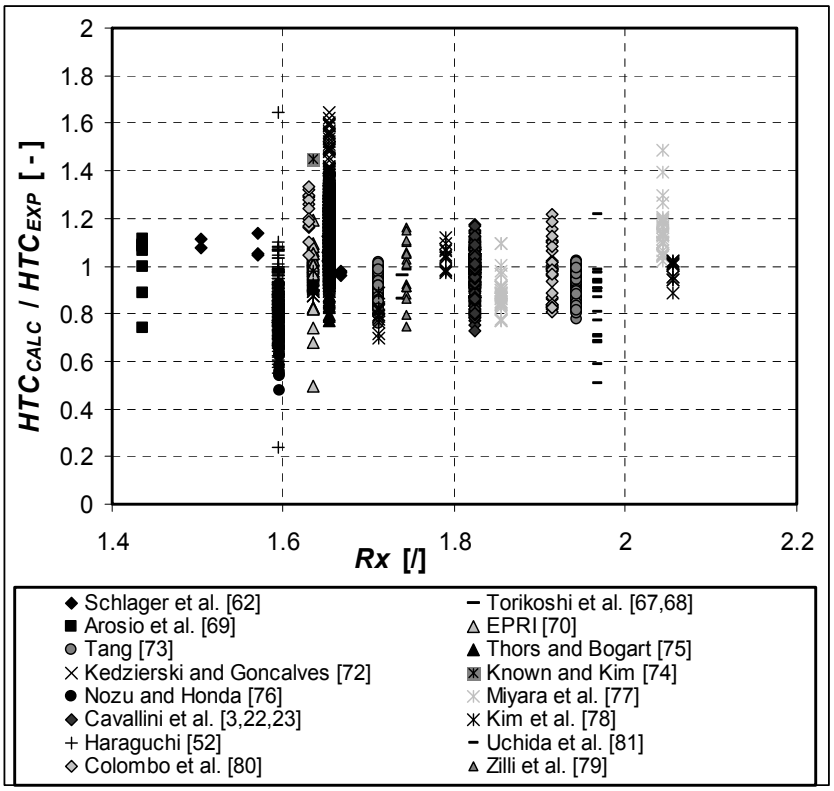

Figure 77. Ratio of calculated to experimental heat transfer coefficient vs. Rx.

When considering all the 3115 data points the average deviation e_R comes to be 3.2% with e_A = 16.5% and σ_N = 21.9%. In Table 40 average, absolute and standard deviations are summarized by subdividing the database into different data sets.

Only data by Kedzierski and Goncalves appear to be overestimated (e_R =20.0%, e_A = 20.0%, σ_N =19.0 %), while the data by Nozu and Honda [76] for R11 at lower reduced pressure p_R = 0.028 are underestimated (e_R =-27.6%, e_A = 27.6%, σ_N = 9.8%).

For the other data sets, the new procedure presents the most accurate predictions when compared to the models in the open literature.

No data for hydrocarbons are included in the database. The model should not be applied to water and ammonia, as both fluids have high surface tension.

Table 40. Deviations for the new correlation (expressed in %).

Data set	**Present model by Cavallini et al.**		
	e_R	e_A	σ_N
High Pressure Refrigerants: R32, R125, R404A, R410A and R744 (Np=266)	-3.8	9.1	11
Low and Medium Refrigerants: R22, R123 and R134a (Np=694)	-8.0	12	13
Data by Cavallini et al. [3,22,23]: R22, R134a and R410A (Np=253)	-2.2	6.2	8.2
Data by Eckels et al. [66]: R22, R134a, R410A, R507A (Np=687)	-13	16	16
Data by Kedzierski and Goncalves [72]: R32, R125, R410A and R134a (Np=1389)	20	20	19
CFC data by Honda and Nozu [76]: R11 (Np=79)	-28	28	9.8
All database 3115 data points	**3.2**	**17**	**22**

1.7 Conclusions

Microfin tubes are widely used in air and water cooled heat exchangers for heat pump and refrigeration applications during condensation or evaporation of refrigerants. In condensation, microfin tubes show a heat transfer enhancement, compared to equivalent smooth tubes under the same operating conditions.

In this thesis, experimental convective condensation measurements for R410A inside a microfin tube were presented. Both heat transfer and pressure drop measurements were provided. Test runs were carried out in the two-phase laboratory at the Dipartimento di Fisica Tecnica of Padova University.

In general, the value of the condensation heat transfer coefficient increases with increasing vapour quality and mass velocity. At 200 kg m^{-2} s^{-1} the condensation heat transfer coefficient for R410A follows the qualitative trend found by Cavallini et al. [22, 23] for R22 and R134a. in fact, the heat transfer coefficient rises more than linearly at high vapour quality, while it decreases more than linearly at low vapour quality.

The results are the same when the enhancement factor (*EF*) is considered.

The enhancement factor *EF* is defined as the ratio between the heat transfer coefficient in the microfin tube and the heat transfer coefficient in an equivalent ID smooth tube at the same operating conditions (the internal diameter ID at the fin tip is taken as a reference in the microfin tube and the condensation heat transfer coefficient for smooth tubes is calculated with Cavallini et al. [16] model).

The heat transfer enhancement factor depends on mass velocity and vapour quality. Again, at 200 kg m^{-2} s^{-1}, the *EF* rises more than linearly at high vapour quality, while it decreases more than linearly at low vapour quality. Moreover, at this mass velocity the *EF* reaches its maximum value of 2.6 at around x=0.8. At higher mass velocities, the *EF* appears to be quite constant with vapour quality. At 400 kg m^{-2} s^{-1}, the *EF* is equal to the effective area enhancement while at 800 kg m^{-2} s^{-1} the heat transfer coefficient is only around 50% higher than in the smooth tube.

This behaviour can be explained considering the flow pattern inside the microfin tube; in fact, the micro-fins promote the annular flow pattern, leading to the maximum enhancement at a certain value of mass velocity, as reported in Cavallini et al. [7].

Several different heat transfer correlations suggested in the open literature were chosen to evaluate the R410A condensation heat transfer coefficient.

The most accurate predictions are given by Kedzierski and Goncalves [46], Han and Lee [50] and Chamra et al. [47,48] models.

Two-phase pressure drops both during condensation and under adiabatic operating conditions were also measured. The frictional pressure gradient increases with increasing vapour quality and mass velocity and a good agreement between condensation and adiabatic values was found.

Experimental pressure gradients were compared against correlations available in the open literature for the prediction of the two-phase frictional pressure gradient.

The best agreement was found using the correlation by Haraguchi et al. [28] and Equation B of the model by Goto et al. [35]: most data points were predicted within ±20%.

Furthermore, analytical work was carried out to suggest a new heat transfer correlation for the estimation of the condensation heat transfer coefficient.

A new predictive procedure to compute the heat transfer coefficient during condensation inside horizontal microfin tubes with h/D<0.04 and a helix angle between 0 and 30° was developed.

This simple and easy-to-use model is suitable for condenser design and modeling applications, it includes a simple and objective criterion for the definition of the transition between two different flow categories: annular and wavy-stratified flow.

The model has been developed from an extensive analysis of 3115 experimental heat transfer data points including different inner tube surface geometries, characterized by the following parameters: 6mm<D<14mm, 2l<n_g<82, 0.12 mm<h<0.35 mm, 25°<γ<64°, 0°<β<30°.

Its structure allows to clearly point out the influence of the various parameters, as it accounts for the geometrical characteristics of the microfin tube, the fluid thermodynamic and thermophysical properties and, finally, the two-phase flow pattern.

For validation the model was compared against a total of 3115 data points relative to HCFCs, HFCs (pure fluids or near azeotropic mixtures) and carbon dioxide from several independent laboratories all over the world, obtaining an average deviation e_R = 3.2%, an absolute mean deviation e_A = 16.5%, and a standard deviation σ_N = 21.9%. The model can be applied when 0.1< p_R <0.67.

Other models have been compared against the available database. On average, the equations by Kedzierski and Gongalves [46], Han and Lee [50] and Chamra and Mago [47, 48] exhibit

pretty good agreement with the experimental data points. On the other hand, in some cases, they appear to be more scattered than the new computational procedure.

Finally, in this first part of the Ph. D. thesis, a comprehensive study of the condensation of halogenated and natural refrigerants inside enhanced tubes was presented, in particular, R410A condensation heat transfer coefficients and pressure drops inside a microfin tube were measured and compared with different correlations suggested in the open literature.
Moreover, a large experimental database was completed and a new computational procedure for calculating the condensation heat transfer coefficient was developed and tested, giving very good results when compared with other models proposed in the open literature.
A possible extension of this work would be to develop a new correlation for frictional pressure gradient calculation based on an extended database including the most recent experimental measurements from the open literature.

1.8 Nomenclature

A_{cross}	cross-sectional area of the smooth tube referred to the fin tip diameter [m^2]
A_{eff}	effective free-flow cross sectional area [m^2]
c_p	specific heat capacity [J kg^{-1} K^{-1}]
D	fin tip diameter [m]
d_b	fin root diameter [m]
d_h	hydraulic diameter [m]
(dp/dz)	pressure gradient [Pa m^{-1}]
e_P	deviation [%]
e_A	mean absolute deviation [%]
e_R	mean relative deviation [%]
f	friction factor
g	gravitational acceleration [m s^{-1}]
G	mass flux or mass velocity [kg m^{-2} s^{-1}]
h	fin height [m] or specific enthalpy [J kg^{-1}]
h_{LG}	latent heat [J kg^{-1}]
HTC	heat transfer coefficient [W m^{-2} K^{-1}] *referred to the fin tip diameter*
HTC_b	heat transfer coefficient [W m^{-2} K^{-1}] *referred to the fin root diameter*
HTC_e	heat transfer coefficient [W m^{-2} K^{-1}] *referred to the total heat transfer area*
i	uncertainty [%]
L, l	tube length [m]
$\dot{m}$	mass flow rate [kg s^{-1}]
N_p	number of experimental data points
n_g	number of grooves, number of fins

p	pressure [Pa]
p_{cr}	critical pressure [Pa]
P	perimeter [m]
Δp	pressure difference [Pa]
q	heat flow rate [W]
t	temperature [K]
ΔT	temperature difference [K]
u	velocity [m s^{-1}]
x	vapour quality
Δx	vapour quality change

Non-dimensional Number

Pr	Prandtl number
Re	Reynolds number
Bo	Bond number
Ph	Phase change number
Ga	Galileo number
Fr	Froude number
We	Weber number
J_G	non-dimensional gas velocity
p_R	reduced pressure [-]
Rx	geometric enhancement factor
X_{tt}	Lockhart-Martinelli parameter

Greek Symbols

β	spiral angle [rad]
γ	apex angle [rad]
ε	void fraction
λ	thermal conductivity [W m^{-1} K^{-1}]
μ	dynamic viscosity [kg m^{-1} s^{-1}]
ρ	density [kg m^{-3}]
σ_N	standard deviation
τ	shear stress [Pa]

Subscripts

A	ΔT-independent flow regime
CALC	calculated
D	ΔT-dependent flow regime
EXP	experimental
eq	equivalent
G	gas phase
GO	gas only
ho	homogeneous
in	inlet
L	liquid phase
LO	liquid only

out	outlet
ref	refrigerant
sat	saturation
strat	stratified
w	water

1.9 References

[1] Stephan K., Heat Transfer in Condensation and Boiling, Springer-Verlag, Berlin, 1992.

[2] Incropera F.P., De Witt D.P., Fundamentals of heat and mass transfer, 3rd edition, Wiley, 1990.

[3] Cavallini A., In-tube condensation performance of refrigerants, Invited lecture at 11th *Proc. of Int. Refrigeration and Air Conditioning Conf. at Purdue*, July 17-20, 2006.

[4] Fujie K., Itoh N., Kimura H., Nakayama N., Yanugidi T., Heat transfer pipe, US Patent 4044797, assigned to Hitachi LTD, 1977.

[5] Han D., Lee K-J, Experimental study on condensation heat transfer enhancement and pressure drop penalty factors in four microfin tubes*, Int. J. of Heat and Mass Transfer*, 48 (2005): 3804-3816.

[6] Cavallini A., Del Col D., Doretti L., Longo G.A., Rossetto L., Heat transfer and pressure drop during condensation of refrigerants inside horizontal enhanced tubes, *Int. J. of Refrigeration*, 23 (2000): 4-25.

[7] Cavallini A., Del Col D., Doretti L., Mancin S., Rossetto L., Zilio C., Visualization of the heat transfer enhancement during condensation in a microfin tube, *Proc. of FEDSM2006,* July 17-20, Miami, F.

[8] Cavallini A, Del Col D., Mancin S., Rossetto L., An updated model for condensation of halogenated refrigerants inside enhanced tubes, *Proc. of Int. Congress of Refrigeration* 2007, Beijing.

[9] NIST, RefProp 7.0.

[10] Collier J. G., Thome J.R., Convective Boiling and Condensation, 3rd edition, Oxford University Press, Oxford, 1994.

[11] Cavallini A., Censi G., Del Col D., Doretti L., Longo G.A., Rossetto L., In-tube Condensation of Halogenated Refrigerants, *ASHRAE Trans.* 2002, Paper 4507

[12] Taitel Y., Dukler A.E., A model for predicting flow regime transitions in horizontal tubes, *AIChE J.*, 22 (1976): 47-55.

[13] Breber G., Palen J., Taborek J., Prediction of horizontal tube-side condensation of pure components using flow regime criteria, *J. of Heat Transfer*, 102 (1980): 471-476.

[14] Tandon T.N., Varma H.K., Gupta C.P., A new flow regime map for condensation inside horizontal tubes, *ASME J. Heat Transfer,* 104 (1982): 763-768.

[15] Cavallini A., Censi G., Del Col D., Doretti L., Matkovic M., Rossetto L., Zilio C., Condensation of refrigerant in smooth tube: a new heat transfer model for heat exchanger design, *3rd Int. Conf. on Heat Transfer, Fluid Mechanics and Thermodynamics,* Cape Town, South Africa, Paper CA1.

[16] Cavallini A., Censi G., Del Col D., Doretti L., Matkovic M., Rossetto L., Zilio C., Condensation in Horizontal Smooth Tube: A New Heat Transfer Model for Heat Exchanger Design, *Heat Transfer Engineering*, 27 (8) (2006): 31-38.

[17] Nozu S., Katayama H., Nakata H., Honda H., Condensation of a refrigerant CFC11 in horizontal microfin tubes (Proposal of a correlation equation for frictional pressure gradient), *Exp. Thermal and Fluid Science*, 18 (1998): 82-96.

[18] Yu M-H, Lin T-K., Tseng C-C, Heat transfer and flow pattern during two-phase flow boiling of R134a in horizontal smooth and microfin tubes, *Int. J. of Refrigeration*, 25 (2002): 789-798.

[19] Censi G., Doretti L., Rossetto L., Zilio C., Flow pattern visualization during condensation of R134a inside horizontal microfin and smooth tubes, *Proc. of Int. Congress of Refrigeration*, Washington, D.C., 2003.

[20] Doretti L., Fantin F., Zilio C., Flow Pattern During Condensation Of Three Refrigerants: Microfin vs. Smooth tube, *Proc. of IIR International Conference*, 31 Aug-2 Sept, Vicenza, Italy, 2005.

[21] Smith S.L., Void fraction in two-phase flow: a correlation based on equal velocity head model, *Heat and Fluid Flow*, 1 (1) (1971):22-39.

[22] Cavallini A., Censi G., Del Col D., Doretti L., Longo G.A., Rossetto L., Zilio C., Experimental heat transfer coefficient and pressure drop during condensation of R22 and R407C inside a horizontal microfin tube, *Proc. of Int. Heat Transfer Conf.*, Grenoble, August 18-23, 2002.

[23] Cavallini A., Del Col D., Doretti L., Longo G.A., Rossetto L., Heat Transfer Coefficients of HFC refrigerants during condensation at high temperature inside an enhanced tube, *Proc. of Int. Refrig. Conf. at Purdue*, July 16-19, 2002.

[24] Cavallini A., Censi G., Del Col D., Doretti L., Longo G.A., Rossetto L., Experimental investiugation on condensation heat transfer and pressure drop of new HFC refrigerants (R134a, R125, R32, R410A, R236ea) in a horizontal smooth tube, *Int. Journal of Refrigeration*, 24(1) (2001):74-88.

[25] Kandlikar S.G., Masahiro S., Vijav K.D., Handbook of PHASE CHANGE. Boiling and Condensation, Ed. Taylor and Francis (1999) Chap. 8.

[26] Zivi, S.M., Estimation of Steady State Void Fraction by Means of Minimum Entropy Production. *J. of Heat Transfer,* 86 (1964):247-252.

[27] Baroczy C. J., Correlation of liquid fraction in two-phase flow with applications to liquid methods, *Chemical Engineering Progress Symposium Series*, 61 (1965):179-191.

[28] Haraguchi H., Koyama S., Esaki J., Fujii T., Condensation heat transfer of refrigerants HCFC134a, HCFC123 and HCFC22 in a horizontal smooth tube and a horizontal microfin tube. *Proc. of the 30th National Symposium of Japan*, Yokohama, 1993, 343-345

[29] Kedzierski M.A., Goncalves J.M., Horizontal Convective Condensation of Alternative Refrigerants Within a Micro-Fin Tube, *Enhanced Heat Transfer*, 6 (1999):161-178.

[30] Pierre B., Flow resistance with boiling refrigerants, part I, *ASHRAE Journal* 6 (9) (1964):58-65.

[31] Cavallini A., Del Col D., Doretti L., Longo G.A., Rossetto L., Pressure drop during condensation and vaporisation refrigerants inside enhanced tubes. *Heat and Technology* 15 (1) (1997):3-10.

[32] Friedel L., Improved frictional pressure drop correlations for horizontal and vertical two-phase pipe flow. *European Two Phase Flow Group Meeting*, Ispra, Italy, 1979, paper E2

[33] Mickley H.S., Ross R.C., Squyers A.L., Stewart W.E., Mass and momentum transfer flow over a flat plate with bowing or suction. *Rep. no. NACA-TN-3208*, 1954.

[34] Rouhani Z., Axelsson E., Calculation of volume void fraction in the subcooled and quality region. *Int. J. Heat Mass Transfer*, 13 (1970):383-393

[35] Goto M., Inoue N., Ishiwatari N., Condensation and evaporation heat transfer of R410A inside internally grooved horizontal tubes. *Int. J. of Refrigeration* 24 (2001):628-638.

[36] Choi J.Y., Kedzierski M.A., Domanski P.A., Generalized pressure drop correlation for evaporation and condensation in smooth and microfin tubes. *Proc. of IIF-IIR,* Commision B1, Paderborn, Germany, vol. B4, 2001:9-1.

[37] Cavallini A., Doretti L., Klammsteiner N., Longo G.A., Rossetto L., Condensation of new refrigerants inside smooth and enhanced tubes. *Proc. of 19th International Congress of Refrigeration, The Hague, Chemical Engineering Progress*, IVa, 1995, 105-114.

[38] Cavallini A., Zecchin R., High velocity condensation of organic refrigerants inside tubes. *Proc. of the 8th International Congress of Refrigeration*, Washington D.C., 1971.

[39] Houfuku M., Suzuki Y., Inui K., High-performance, Lightweight "THERMOFIN" Tubes for Air Conditioners Using Alternative Refrigerants, *Hitachi Cable Review*, 20 (2001):97-100.

[40] Del Col D., Experimental and theoretical analysis of refrigerant two-phase heat transfer inside enhanced tubes, Ph.D. Thesis, University of Padova, 1998.

[41] Silver L., Gas cooling with aqueous condensation. *Trans. Inst. Chem. Eng*., 25 (1947):30-42.

[42] Bell K.J., Ghaly M.A., An approximate generalized design method for multicomponent / partial condenser. *AICHE Symp. Ser.*, 69 (1973): 72-79.

[43] Yu J., Koyama S., Condensation heat transfer of pure refrigerants in microfin tubes. *Proc. of the International Refrigeration Conference at Purdue*, 1998, 325-330.

[44] Haraguchi, H., Koyama, S., Fujii, T., Condensation of refrigerants HCFC 22, HFC 134a and HCFC 123 in a horizontal smooth tube (2nd report, proposal of empirical expressions for local heat transfer coefficient). *Trans. JSME*, 60 (1994): .245-252 n.574.

[45] Nusselt W., Die Oberflächenkondensation des Wasserdampfes. *Zeit Ver Deut Ing* (VDI) 60 (1919):82-96.

[46] Kedzierski M.A., Goncalves J.M., Horizontal convective condensation of alternative refrigerants within a micro-fin tube. NISTIR 6095, Gaithersburg (MD USA). National Institute of Standard and Technology (NIST), 1997. Also in: *J. of Enhanced Heat Transfer,* 6 (1999):161-178

[47] Chamra L.M., Mago P.J., Tan M.O., Kung C.C., Modelling of condensation heat transfer of pure refrigerants in micro-fin tubes. *Exp. Thermal and Fluid Science*, 28 (2004):617-628.

[48] Chamra L.M., Mago P.J. Modeling of condensation heat transfer of refrigerant mixture in micro-fin tubes. *Int. J. of Heat and Mass Transfer*, 49 (2006):1915-1921.

[49] Dittus F.W., Boelter L.M.K., University of California at Berkeley Publications On Engineering, 2 (1930):443.

[50] Han D., Lee K.J., Experimental study on condensation heat transfer enhancement and pressure drop penalty factors in four microfin tubes. *Int. J. of Heat and Mass Transfer* 48 (2005):3804-3816.

[51] Koyama S, Yonemoto R., Experimental Study of Pure Refrigerants in Horizontal Micro-Fin Tube –Proposal of Correlation for Heat Transfer Coefficient and Fictional Pressure Drop- *Int. Refrigeration and Air Conditioning Conference at Purdue*, July 17-20, 2006 West Lafayette, Indiana USA, paper R133

[52] Haraguchi H, Doctor Thesis, Condensation of pure refrigerants in horizontal smooth and microfin tubes, Kyushu University.

[53] Miyara A., Nonaka K., Taniguchi M., Condensation heat transfer and fluid pattern inside a herringbone-type micro-fin tube, *Int. J. of Refrigeration*, 23 (2000):141-152.

[54] Carnavos T.C., Heat Transfer Performance of Internally Finned Tubes in Turbulent Flow, *Heat Transfer Engineering*, 1(4) (1980):32-37.

[55] Wang H.S., Wei J.J., Honda H., Rose J.W., Condensation of refrigerants in horizontal microfin tubes: a new correlation, *Proc. of Int. Congress of Refrigeration*, Beijing, 2007, 658.

[56] Cavallini A., Del Col D., Mancin S., Rossetto L., Condensation of pure and near-zeotropic refrigerants in microfin tubes: A new computational procedure, *Int. J. of Refrigeration,* 32 (1) (2009):162-174.

[57] Tatsumi A., Oizumi K., Hayashi M., Ito M., Application of inner groove tubes to air conditioners, *Hitachi Cable Review,* 1 (1982):55-60.

[58] Shinohara Y, Tobe M. Development of an improved 'THERMOFIN TUBE'. *Hitachi Cable Review*, 4 (1985):47-50.

[59] Yasuda K., Ohizumi K., Hori M., Kawamata O., Development of condensing "THERMOFIN-HEX-C TUBE", *Hitachi Cable Review,* 9 (1990):27-30.

[60] Hori M., Shinohara Y., Internal heat transfer characteristics of small-diameter Thermofin tubes, *Hitachi Cable Review,* 10 (1991):85-90.

[61] Schlager L.M., Pate M.B., Bergles A.E., Heat transfer and pressure drop during evaporation and condensation of R22 in horizontal micro-fin tubes, *Int. J. of Refrigeration* 12 (1989):6-14.

[62] Schlager L.M., Pate M.B., Bergles A.E., Effect of oil on heat transfer and pressure drop inside augmented tubes during condensation and evaporation of refrigerants, (RP-469) Final Report, College of Eng. Iowa State Univ, 1989, 332p.

[63] Eckels S. J.,. Pate M. B, An experimental comparison of evaporation and condensation heat transfer coefficients for HFC-134 and CFC-12, *Int. J. of Refrigeration* 14 (1991):70-77.

[64] Eckels S.J., Doerr T.M., Pate M.B., In-tube heat transfer and pressure drop of 134a and ester lubricant mixtures in a smooth tube and a micro-fin tube: part II - condensation, *ASHRAE Trans*., 100 (1994):547-557.

[65] Eckels S.J., Doerr T.M., Pate M.B., Heat transfer and pressure drop during condensation and evaporation of R-134a/Oil mixtures in smooth and micro-fin tubes, ERI-94402 Final Report RP-630, 1993, 357 p.

[66] Eckels S.J., Tesene B.A., A comparison of R22, R134a, R410A and R407C condensation performance in smooth and enhanced tubes: Part I, Heat Transfer, *ASHRAE Trans*., 105 (1999):428-441.

[67] Torikoshi K., Ebisu T., Heat transfer and pressure drop characteristics of R134a, R32, and a mixture of R32/R134a inside a horizontal tube. *ASHRAE Trans.,* 99 (1993):90-96.

[68] Torikoshi K., Ebisu T., In-tube heat transfer characteristics of refrigerant mixtures of R32/R134a and HFC32/125/ 134a. *Proc. of Int. Refrigeration Conf. Purdue*, 1994, 293-298

[69] Arosio S., Muzzio A., Niro A., Evaporation and condensation heat transfer and pressure drop of R22 inside micro-fin tubes, *Proc. of the 14th UIT Nat. Heat Transfer Conf. at Rome*, 1996, 227-233.

[70] EPRI, Heat transfer characteristics of alternate refrigerants. Vol.2 Condenser inside tube, 1996, Project 3412-51.

[71] Webb R.L., Chamra L.M., Randlett M.R., Advanced microfin tubes for condensation, *Int. J. Heat Mass Transfer,* 39 (1996):1839-1846.

[72] Kedzierski M.A., Goncalves J.M., Horizontal convective condensation of alternative refrigerants within a micro-fin tube, 1997, NISTIR 6095, U.S. Dept. Commerce, 74 p.

[73] Tang L., Empirical study of new refrigerant flow condensation inside horizontal smooth and micro-fin tubes, 1997, University of Maryland at College Park, PhD Thesis, 251 p.

[74] Kwon J.T., Kim M.H., Enhanced condensation heat transfer of an alternative refrigerant in a microfin tube. *Proc. of 3rd Int. Conf. Multiphase Flow*, ICMF'98, Lyon, France, 1998.

[75] Thors P., Bogart J., Personal communication to Professor Cavallini, 1998.

[76] Nozu S., Honda H., Condensation of refrigerants in horizontal, spirally grooved microfin tubes: Numerical Analysis of heat transfer in annular flow regime, *ASME J. Heat Transfer,* 122 (2000):80-91.

[77] Miyara A., Personal communication from Huasheng Wang to A. Cavallini, 2002.

[78] Kim M-H, Shin J-S, Lim B-H, Condensation heat transfer of R22 and R410A in horizontal smooth and microfin tubes, *Zero Leakage-Minimum Charge, IIR-IIF Section B and E*, 2002, Stockholm, pp. 253-261.

[79] Zilli J., Jang J., Hrnjak P. S., Condensation of CO_2 at low temperature inside horizontal microfinned tubes, ACRC CR-49, 2003, University of Illinois at Urbana-Champaign, 61p.

[80] Colombo L., Lucchini A., Muzzio A., Niro A., Heat transfer and pressure drop during evaporation and condensation of R134a inside two microfin tubes of new design, *Proc. of International Heat Transfer Conference at Sidney*, Australia, 2006, 13-18 August, MPH-10.

[81] Uchida M., Itoh M., Shikazono N., Hatada T., Ohtani T., Development of high performance microfin tubes (2nd report: experimental study), *Proc. of 31th Air Cond. and Refrig. Eng. Joint Conference*, 1997, Tokyo, Japan, pp. 81-84.

[82] Shedd T.A., Newell T.A., Observations of the influence of helical microgrooves on the behaviour of annular two-phase flow, *Zero leakage-Minimum Charge, IIR/IIF*, 2002, Stockholm, Sweden, 213-220.

[83] Tsuchida T., Yasuda K., Hori M., Otani T., Internal heat transfer characteristics and workability of narrow "THERMOFEIN" tubes, *Hitachi Cable Review*, 12 (1993):59-64.

[84] Bukasa J.P., Liebenberg L., Meyer J.P., Influence of spiral angle on heat transfer during condensation inside spiralled micro-fin tubes, *HEFAT 2003*, Victoria Falls, Zambia, 1-20.

2

Part 2:

Single-Phase Enhanced Heat Transfer

2.1 Introduction

With the trend towards further miniaturization of electronic packages, the thermal design problem is recognized as one of the factors limiting the achievement of higher packaging densities. The reliability of machines is, therefore, becoming more critically dependent on the accuracy of heat transfer analysis, which traces the heat flow from the chip to the air. High power dissipation may require new cooling techniques but, where possible, direct air cooling still remains an attractive method because of its mechanical simplicity [1].

Microelectronic devices, which include a variety of applications such as PCs, servers, laser diodes, electronic packaging for aeronautical and aerospace crafts are constantly pushing the heat transfer flux density requirements to higher levels [2]. Efficient heat spreaders and dissipators and compact heat exchangers are in great demand for various applications.

Even if the specific heat fluxes in electronic applications are continuously growing, the chip operating wall temperature must be kept lower than 70 °C. In the last years, also novel cooling techniques, such as single and multiple impinging air jets [3-6], ionic wind [7] or miniature heat pipes [8], thermoelectric coolers, liquid cooling (liquid heat sinks and direct immersion cooling) [9, 10] and two-phase flow heat sinks [11, 12], have been proposed to take electronics to the densities and speeds which next generation application demands.

On the other hand, it is clear that air represents the safest and cheapest operating natural fluid for these applications. It is therefore important to find some new technological solutions permitting to increase its heat transfer capabilities.

In the past decades, many technologies, such as plain and louvered fins, pin fins, offset strip fins and wire screens, have been developed to increase the heat transfer area density of heat sinks without loosing the necessary compactness [13-17].

The problem is that conventional air cooling techniques are no longer adequate, since Saini and Webb have demonstrated that there is an upper heat rejection limit for traditional air cooling systems [18]. However, novel structures, such as metal honeycombs, cellular structures materials both stochastic and periodic, have recently been proposed as possible substitutes for the traditional ones.

Cellular materials exhibit two predominant topologies: stochastic (foamed) and periodic [19]. Metal foams present random microstructures consisting of randomly oriented open cells, which are mostly homogeneous in size and shape. Most commercially available metal foams are based on aluminum, copper, nickel and metal alloys [20]. Very interesting stochastic

porous materials are carbon foams, which are receiving special attention for their potential applications in several areas of thermal management [21].

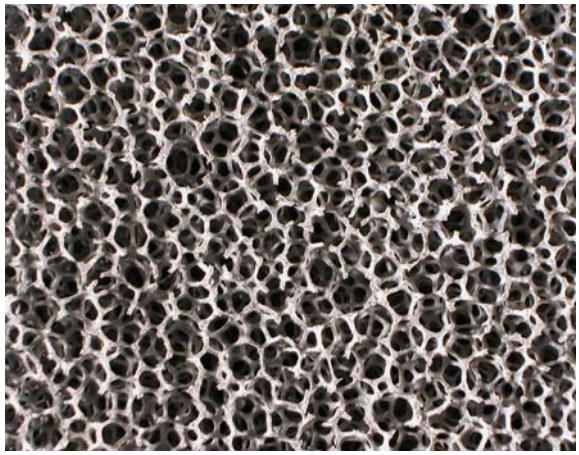

Figure 78. Aluminum metal foam (photography).

Periodic cellular structures include lattice-frame materials (LFM), consisting of a 3D network of rods, and prismatic materials, which are 2D periodic channels. LFM are extremely stiff and strong, qualities that make them the ideal candidates for multifunctional structures requiring both heat dissipation and mechanical load carrying capabilities [22].

Several relevant studies concerning single-phase heat transfer characteristics of cellular structure materials are reported in the open literature. Kim et al. [22] have experimentally studied the heat dissipation of aluminum lattice-frame materials. Tian et al. [19] have investigated the heat transfer behaviour of cellular copper structures. Wen et al. [23] have tested different copper and stainless steel honeycombs during forced-air convection. Lu [24] has studied the thermal efficiency of metal honeycombs.

Figure 79. Example of copper honeycomb (left) and 2D copper structure (right) (photo by Tian et al. [19]).

Experimental measurements of single-phase heat transfer and pressure drops across aluminum foams have been done by Calmidi and Mahajan [25], Hsieh et al. [26], Kim et al. [27], Hwang et al. [28].

Kim et al. [29] have experimentally characterized the thermal performances of FeCrAlY metal foam.

Though several research works have been performed all over the word, more experimental measurements are needed to fully characterize the thermal fluid-dynamic behaviour of these new enhanced surfaces.

In this work, a new experimental set-up has been designed, developed, built and started up in order to make heat transfer and pressure drop measurements during single-phase air flow through different enhanced surfaces, such as traditional plain and louvered finned surfaces, offset pin fins, cellular structure materials both stochastic and periodic and microgeometries.

This project has been supported by the University of Padova within the framework of a program called “Progetti di Ricerca di Ateneo”.

In the following, the development of the new experimental test rig considering all innovative implemented solutions, the design process and the test rig validation will be presented.

Then, in a separated chapter, the experimental heat transfer and pressure drop measurements of air forced convection through five different aluminum metal foams will be reported.

All collected experimental data will be used to test available semi-empirical correlations and, when necessary, to develop new ones for the prediction of the heat transfer coefficients and pressure drops for air flow on different geometries which can be applied in compact heat exchanger design.

2.2 Development of New Test Equipment

2.2.1 Outlines

In the following, the work done to design, develop and build the new test facility at the laboratory of the "Dipartimento di Fisica Tecnica" of the University of Padova will be explained.

Since these new enhanced surfaces display different fluid-dynamic behaviours as compared to the traditional finned surfaces for electronic cooling applications, a complete literature review has been carried out. This work has allowed to understand the experimental constraints and difficulties which we would have found during the design of the test facility.

Thanks to this review, a new test equipment has been designed. It is able to measure heat transfer coefficients and pressure drops during air forced convection through different enhanced surfaces under a wide range of operating conditions.

Therefore, this chapter starts with a brief summary of the most important results of the literature review done initially. Then the design, development or selection of the different parts of the test rig will be deeply discussed, in order to highlight the innovative technical solutions, the possibilities and the limits of this new test facility.

2.2.2 State of the Art

In the last decade, several research groups all over the world have focused their attention on new enhanced surfaces, called cellular structure materials, which have been proposed as possible substitutes of traditional finned surfaces.

This new class of heat transfer surfaces will be described in the next chapters, where the experimental test campaigns will be reported in terms of heat transfer coefficient and pressure drop measurements.

As already mentioned, cellular materials exhibit two predominant topologies: stochastic (foamed) and periodic [19]. Metal foams have random microstructures consisting of open cells which are randomly oriented and mostly homogeneous in size and shape, while periodic cellular structures include lattice-frame materials (LFM) consisting of a 3D network of rods and prismatic materials which are 2D periodic channels (honeycombs).

Starting from the works concerning the stochastic cellular structure material, Calmidi and Mahajan [25] characterized the heat transfer behaviour of different aluminum foams which were inserted in a wind tunnel. The measurements were conducted by heating the base of the

foam and using air as the coolant. Calmidi and Mahajan [25] studied 7 tested aluminum foams which presented a variable number of pores per inch (PPI): 5 to 40 PPI, with variable porosity between 0.89 and 0.97. A schematic of the test facility built by Calmidi and Mahajan [25] is drawn in Figure 80.

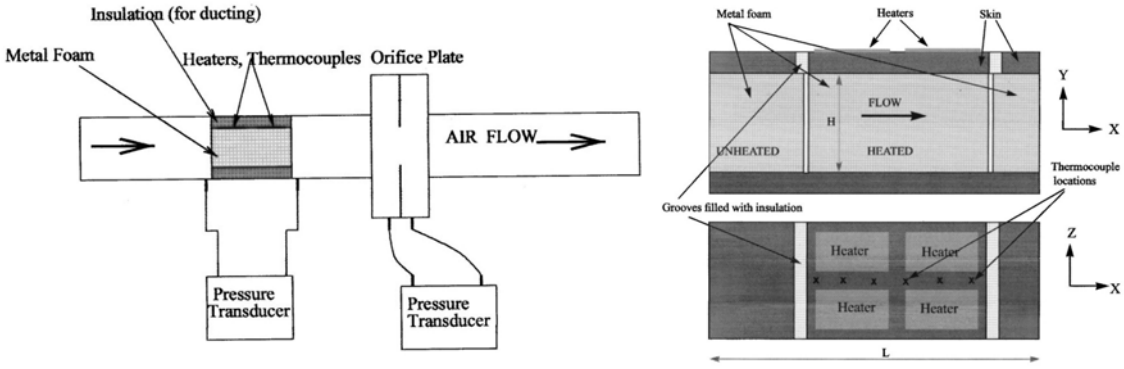

Figure 80. Schematic of the test rig used by Calmidi and Mahajan [25] (left); a particular of the heating part of the test section (right).

The Authors [25] tested samples measuring 63 mm height, 45 mm depth and 196 mm length. The test facility was a wind tunnel where air was supplied by connecting the plexiglass tube to a fan/motor assembly downstream of the test sample. The test section was the main working area of the wind tunnel. Very low conductivity Styrofoam was used to block the space around the sample to fully prevent flow bypass. As it appears from the scheme, the air flow rate was measured by means of a volumetric flowmeter, consisting of an orifice plate located between two flanges connected to a differential pressure transducer. The air flow rate was obtained according to ISO-5167-1:1991.

Four electrical pads were used to heat the samples, thirty six thermocouples were located along the center line to measure the wall temperatures. Finally, the heat power was supplied by the upper plate of the specimen.

The power input to the patch heaters was set between 15 and 35 W. The temperature at the inlet of the test section was measured, but no temperature transducers were located at the outlet of the sample.

Thus, the heat balance between the electrical power and the air was not being controlled, and the heat transfer coefficient was referred to the inlet temperature, not to the logarithmic mean temperature difference. Finally, the base area was used to calculate the heat transfer coefficient.

Pressure drops were measured by drilling pressure taps into the aluminum plate at various axial locations of the metal foam. Axial locations were chosen after allowing for a conservative flow developing length of around 75 mm.

They found that the experimental Nusselt number rises with the Reynolds number. In addition, at constant number of pores per inch (PPI), the Nusselt number appears to be higher at higher porosity values.

Uncertainties of ±4.3% and ±4.1% were reported for heat transfer coefficients and pressure drops, respectively.

Hsieh et al. [26] carried out an experimental study to characterize the heat transfer characteristics of several heat sinks made of aluminum metal foams with different porosities (0.87-0.96) and PPI (10-40).

Hsieh et al. [26] also experimentally analyzed the effect of porosity in heat transfer. They measured the heat transfer performance of four samples with 20 PPI and different porosity.

The experimental test rig consists of a vertical wind tunnel in which a cylindrical heat sink is located in the base and the air flows from the top side to the bottom side. The heater is a copper plate heated by an electrical pad. The foam base temperature is measured by means of a set of thermocouples.

The Nusselt number increases with the increasing of porosity. At constant porosity, they found that the heat transfer performance is better at higher PPI levels.

Kim et al. [27] experimentally studied the heat transfer in forced convection of air through aluminum foams. Figure 81 shows a schematic of the test rig. Instead of a fan, the Authors used a compressor to pump the air through the test channel. A different boundary condition was imposed in the experiments: a constant temperature of the top side of the sample was maintained by means of a hot bath located over the upper wall of the channel. The maximum wall temperature obtainable with this technical solution was 50 °C.

The two channel walls (bath and test section) were fastened together using six C-shaped clamps to reduce the thermal contact resistance between the wall bath and the specimen. As the compression loading was increased, convective heat transfer rate approached an asymptotic value which was considered as a condition for minimal contact resistance. Five thermocouples were vertically distributed at 5 mm downstream of the test section to measure the bulk temperature of the air at the exit. The heat transfer coefficient was referred to the logarithmic mean temperature difference between air and channel walls.

The Authors tested three foams which presented 10, 20 and 40 PPI with a constant porosity of 0.92. The samples were inserted into a plexiglass rectangular channel imposing a constant wall temperature as a boundary condition. The Authors found that at constant Reynolds number the heat transfer performance was improved by varying the number of pores per inch from 10 to 40. On the other hand, the 40 PPI aluminum foam presented the highest pressure drop during single-phase air heat transfer. The uncertainty of the heat transfer coefficient was estimated to be less than ±12.3%. For the pressure drop measurements, an inclined manometer was used, but uncertainty was not mentioned in the paper.

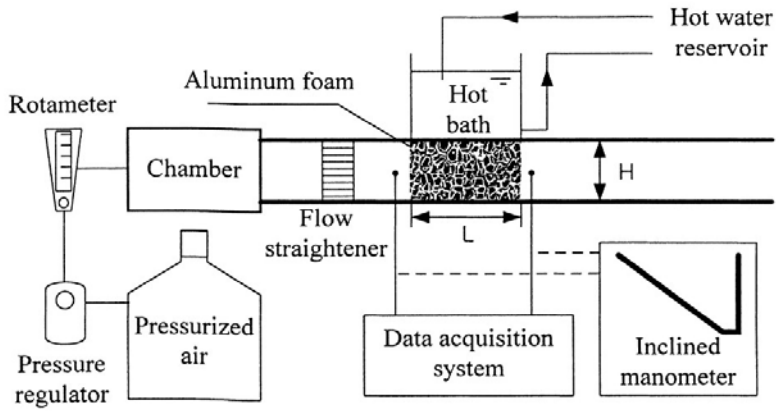

Figure 81. Schematic of the test rig used by Kim et al. [27].

Kim et al. [28] analyzed the heat transfer characteristics of different FeCrAlY foams in the test rig shown in Figure 82. The experimental apparatus consisted of four main sections: coolant supply, test section, test model and data acquisition system. Air at ambient condition was used as the coolant and it was drawn through the channel by an air suction device. A honeycomb and a wire screen were inserted in the channel before the contraction. Then, the coolant passed through a 9:1 contraction and a parallel section, in which the ratio of section length to channel height was 20, before it reached the test section. A flow rate regulator was located between the exit of the test section and the suction device. A silicon rubber etched foil heater produced by Watlow Inc. was used to heat the sample.

Uncertainty in the heat transfer measurements was reported to be less than ±5.0%. The pressure drops across the FeCrAlY foams were measured with a differential pressure transducer with an accuracy of ±5.0% connected to four static pressure drop taps placed on the top substrate along the flow direction. Two T-Type thermocouples were positioned separately at the inlet and outlet of the test section at mid-height of the channel to measure the

air temperature gain. The Authors defined a volumetric heat transfer coefficient. The thermal performance of these metal foams was penalized by their low thermal conductivity.

Kim et al. [22] analyzed the behaviour of aluminum lattice-frame materials during single-phase heat transfer using air as the coolant. The data were collected in the test rig described in Figure 82., already mentioned. The samples were inserted into a rectangular channel and heated by an electric pad.

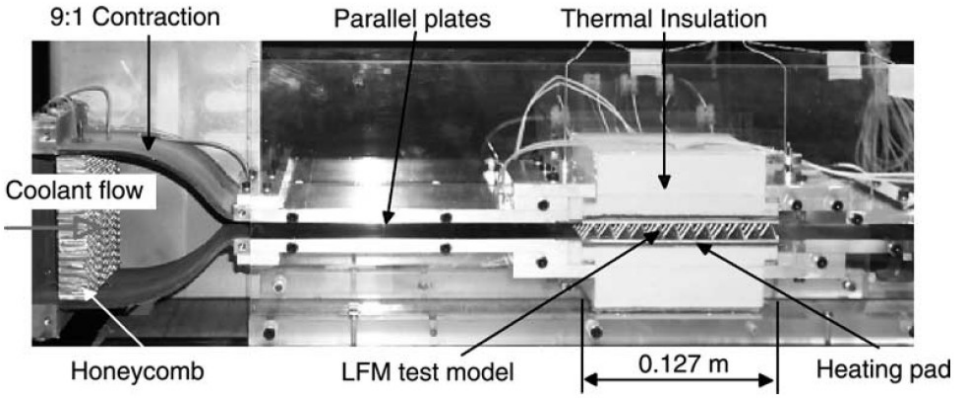

Figure 82. Schematic of the test rig used by Kim et al. [22, 28] and Wen et al. [23].

The pressure drops across the lattice-frame materials were measured by means of a differential transducer connected to two pressure taps at the inlet and outlet of the heated section. Uncertainties were estimated to be less than ±5.0% for both heat transfer coefficients and pressure drops.

Tian et al. [19] performed heat transfer and pressure drop measurements during single-phase heat transfer across different cellular copper structures heated by an electric pad located at the bottom face sheet of the test specimen. The Authors used the test rig shown in Figure 82. The samples were inserted into an open-circuit suction-type wind tunnel with rectangular cross shaped section. The heat transfer coefficient was referred to the bulk inlet temperature. The Authors declared uncertainties of ±5.0% and ±5.3% for pressure drops and heat transfer coefficients, respectively.

Recently, stainless and copper honeycomb structures were experimentally characterized by Wen et al. [23], who measured heat transfer coefficients and pressure drops during single-phase air heat transfer.

Metal honeycomb heat sinks were inserted into an open circuit type wind tunnel like that of Figure 82 and heated by electrical pads. The heat transfer coefficient was referred to the base area using the inlet temperature of the air.

Wen et al. [23] studied several topologies of metal honeycombs with different hydraulic diameters and channel shapes. They also investigated the influence of materials in the heat transfer behaviour by testing both stainless steel and copper honeycomb structures. Uncertainties of ±6.4% and ±2.83% were reported for heat transfer coefficients and pressure drops, respectively.

Del Col et al. [30], and successively Cavallini et al. [31], collected different sets of experimental data points measured by several research groups in order to understand the effective heat transfer capabilities of these new enhanced surfaces. In these works, a possible method for comparing different enhanced surfaces for electronic cooling systems was proposed.

Not all of the experimental heat transfer coefficients were defined in the same way. A complete revision of the different data sets has been carried out in order to build a homogeneous database.

Table 41. Major morphological characteristics and principal test conditions.

Author	*Topology*	*Material*	*Porosity, ε***	*PPI****	*U [m/s]*
Kim et al. [22]	P.S.	Aluminum	0.94	/	2.0-26.0
Tian et al [19]	P.S.	Copper	0.68-0.80	/	1.0-14.0
Wen et al. [23]	P.S.	Copper	0.68-0.86	/	2.0-26.0
Calmidi and Mahajan [25]	Foam	Aluminum	0.90-0.97	5-40	0.0-5.0
Hsieh et al. [26]	Foam	Aluminum	0.87-0.96	10-40	0.5-4.0
Kim et al. [27]	Foam	Aluminum	0.92	10-40	1.0-5.0
Kim et al. [28]	Foam	FeCrAlY	0.82-0.92	10-60	2.2-16.0

Some interesting suggestions for the design of a new test rig were inferred from this brief literature review. First of all, only one study reported a constant wall temperature as a boundary condition (Kim et al.) [27], all other Authors imposed a heat flux at the top or bottom of the samples.

Secondly, since nobody measured the outlet air temperature, with the exception of Kim et al. [28], the heat balance between the input electrical power and the air was not performed, and the heat transfer coefficient was almost referred to the inlet air temperature.

This is a critical point for all these experimental works since, if the heat balance between the supplied electrical power and air heat flow rate is within ± 5%, the accuracy of the measurements can be assured.

The aim of the new experimental test rig designed during this Ph.D. work is to measure the heat transfer behaviour of different new enhanced surfaces and microgeometries in a range of operating conditions as wide as possible.

When a fan is used to supply the desired air flow rate, the pressure drops across the test rig control the amount of air moved. Hence, the experimental pressure gradients measured by the Authors listed in Table 41 were studied.

Figure 83, Figure 84, Figure 85 and Figure 86 report the experimental pressure gradients measured during air forced convection through cellular structure materials: the first two figures refer to periodic materials, the second two refer to stochastic materials.

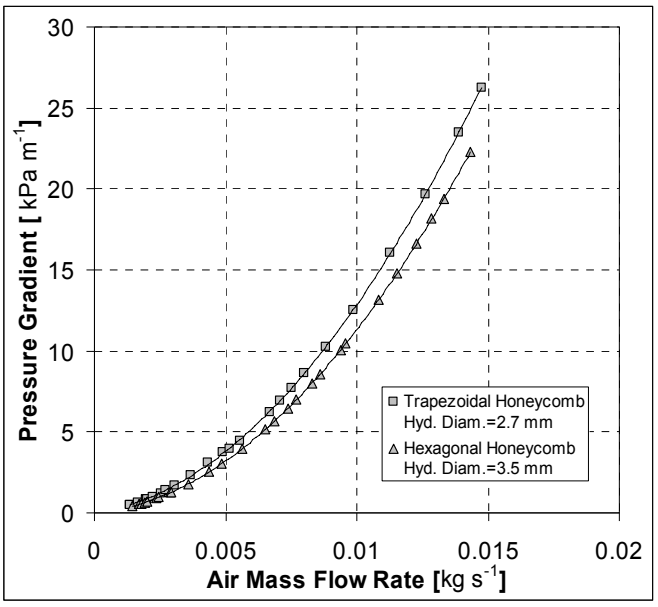

Figure 83. Pressure gradient of two different honeycomb structures tested by Wen et al. [23].

This new enhanced surfaces present high pressure drops as compared with the traditional finned surfaces used in electronic cooling applications.

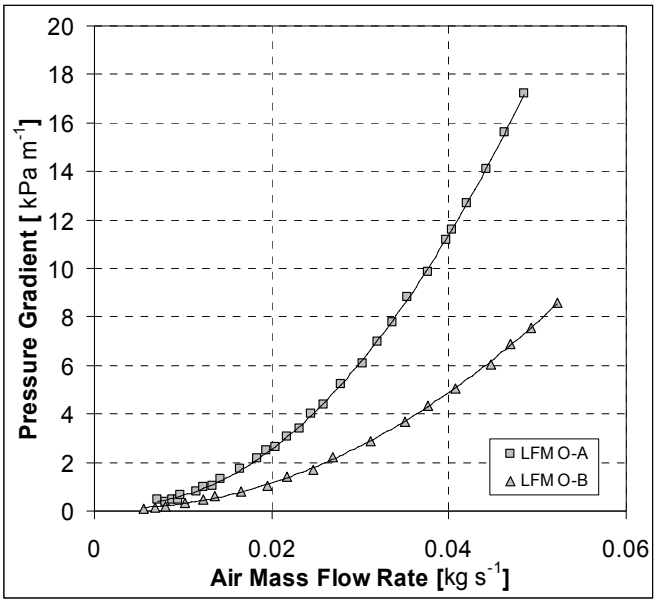

Figure 84. Pressure gradient of two different honeycomb structures tested by Wen et al. [23].

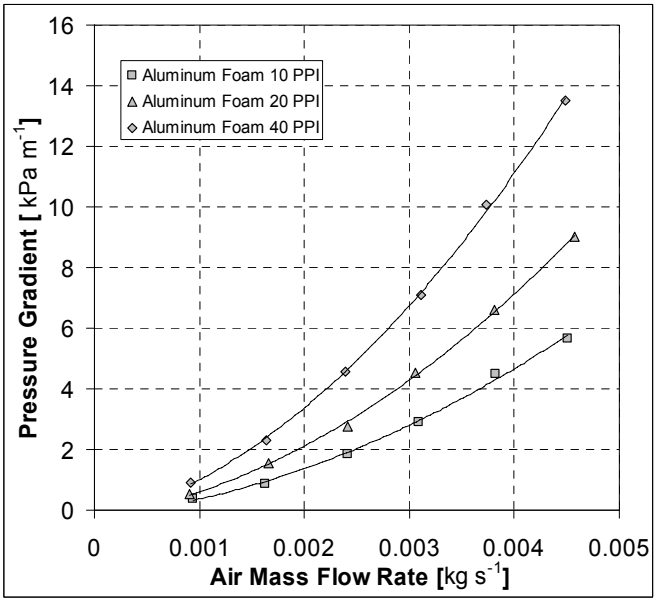

Figure 85. Pressure gradient of three different aluminum foams tested by Kim et al. [27].

As it appears from Figure 86, a 60 PPI FeCrAlY at 0.01 kg s^{-1} presents a pressure gradient of over 120 kPa m^{-1}.

As one can see in Figure 87, at the same operating conditions the stochastic cellular structure materials (foams) exhibit higher pressure gradients than the periodic structures.

In fact, at around 0.004 kg s^{-1} the honeycomb structures present a pressure gradient of 4 kPa m^{-1} while that of metal foam is of 14 kPa m^{-1}.

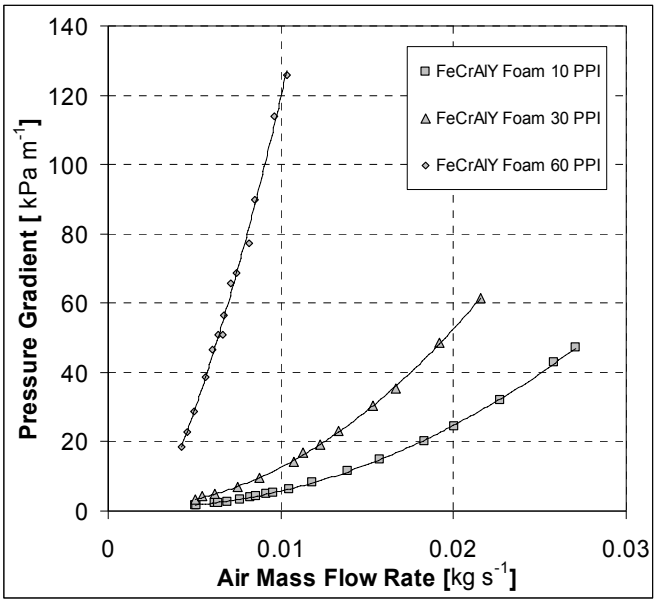

Figure 86. Pressure gradient of three different aluminum foams tested by Kim et al. [28].

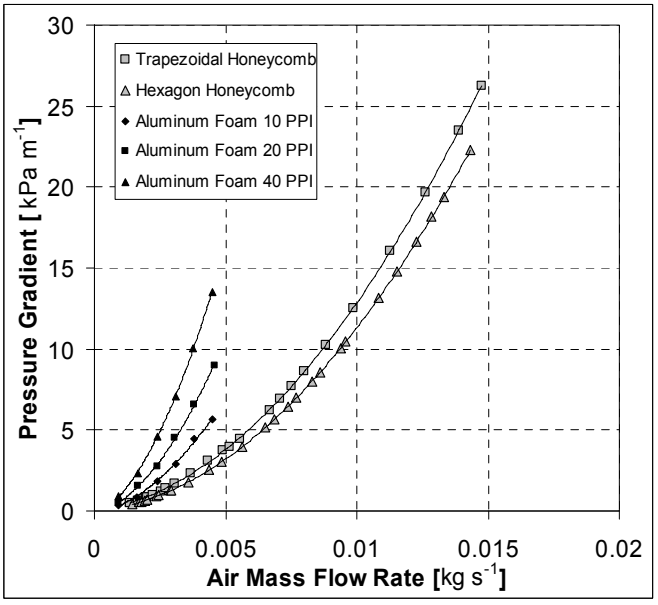

Figure 87. Comparison between periodic and stochastic cellular structure materials (data by Wen et al. [23], Kim et al. [27]).

In this brief literature review, only pressure drops and measurement techniques were deeply analysed, in order to find the most useful design solutions.

The heat transfer behaviour of cellular structure materials was analysed in Del Col et al. [30] and in Cavallini et al. [31], where different enhanced surfaces have been compared against a traditional finned surface for electronics cooling applications which was optimised by Saini and Webb [18].

2.2.3 Components Development, Design or Selection

In this paragraph, the development, the design or the selection of the most important components of the test facility will be completely analysed. First of all, a brief overview of the test facility will be given, then the designed or selected components will be illustrated. Finally, the test facility components will be discussed.

2.2.3.1 Overview

This overview of the new experimental set-up begins with Figure 88, which describes the meaning of the three most important words in this work: *development*, *design* and *building*.

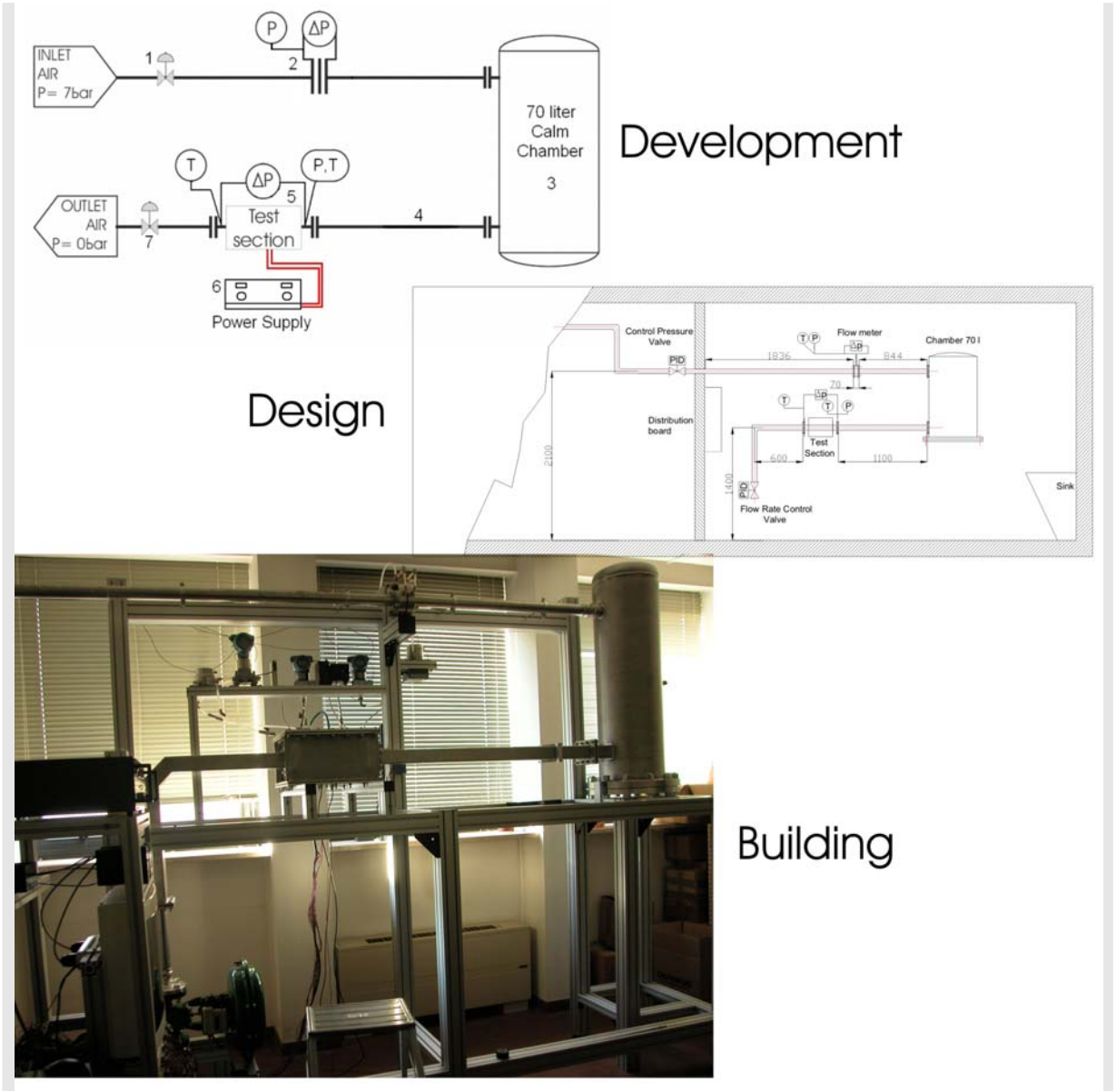

Figure 88. The development, the design and the building of the new experimental set-up.

The scheme illustrated in Figure 88 has been adopted in the development, design and building of the new test rig. This approach reveals to be very useful as it synthesizes and gathers the most important technical information.

As it results from the analysis of Figure 88, the *idea* first takes the form of a simple flowchart in which the most important components (valves, flowmeter, power supply and chamber), parameters (temperatures, gauge or differential pressures) which will be measured and technical solutions (chamber, components locations, etc.) are inserted and highlighted.

This first flowchart permits to select or design the components which can entail new constraints in the test rig design. For instance, the pressure control valve position (1) implies that the connection channel between the valve and the flowmeter has to be longer than a fixed length.

The second step, summarized by the word *design*, permits to draw the possible layout of the test rig. This operating layout takes into account all the distance or volume constraints linked to components selection. The layout gives the first operating idea of the possible shape of the test rig and its work area as compared to the total volume of the room.

If the technical solutions obtained from the development (flowchart) do not match the operating layout (i.e., the work area is bigger than the room) (design), new constraints have to be considered in the selection or design of the different components.

Finally, the result of this procedure is reported in the last part of the figure: it is the effective test rig.

Considering the literature review, an open-circuit type wind tunnel with a rectangular cross section was selected as test facility typology.

The second step was to decide what kind of air supplier achieved the best compromise between the constraints highlighted by the different enhanced surfaces (pressure drops) and the operating test conditions.

Therefore, since the pressure drops of these cellular structure materials are orders of magnitude higher than those of traditional finned surfaces, and in order to ensure the most open operating test conditions for all the possible test samples, a compressor was chosen as air supplier.

The experimental set-up can be subdivided into two parts: the first one consists in an Air Compressor Workplace, while the second is the true experimental test part.

Figure 89 shows a schematic of the Air Compressor Workplace, where it is possible to find: (1) the compressor, (2) a R134a drier, (3) a set of filters and (4) a 500 L air receiver.

The compressor is an air cooled GA 7 VSD workplace full feature produced by Atlas Copco. The screw compressor is able to provide a variable volumetric air mass flow ranging between 0 and 90 m^3h^{-1} at a constant gauge pressure of 7 bar.

The humid and oiled compressed air is dehydrated by a R134a drier to the dew point temperature of 3°C and then filtered by a set of filters, in order to remove water, oil and particulate materials.

Figure 89. Air Compressor Workplace: scheme and photos.

As shown in Figure 89, an additional active carbon filter is located before the 500 L air receiver to eliminate the residual oil up to 3 ppm.
The whole test facility is made of stainless steel AISI 316 L, with the exception of the 500 L air receiver, which is made of zinc coated steel.
In order to limit pressure drops through the channels connecting the different components of the test facility, the inner diameter was set to 51 mm, with a circular cross-sectional area.
In Figure 90 are shown a schematic and some photos of the second part of the test facility. This is the effective experimental test sector, and includes: pressure and mass flow control valves, the volumetric flowmeter, the test section with the power supply and the data acquisition system.
Compressed air at 7 bar is drawn from the air receiver to the test part. As plotted in Figure 90, the inlet air is elaborated by a pressure control valve designed to reduce the pressure between 7 bar and atmospheric condition. After that, according to EN ISO 5167-1:1997/A1:2000 [32], a volumetric orifice flowmeter, equipped with a high-precision differential pressure transducer, measures its flow rate.
Afterwards the air flows in a 70 L calm chamber, then through the inlet tube to the test section and finally it arrives to the flow rate control valve and is discharged to the atmosphere.
The connection tube from the chamber to the test section is 1.1 m long, with a rectangular cross section with a width of 100 mm and a height of 60 mm. It was designed to permit the full development of the air flow. The discharge tube is 0.6 m long and it has a rectangular cross section with the same geometrical characteristics of the inlet duct.

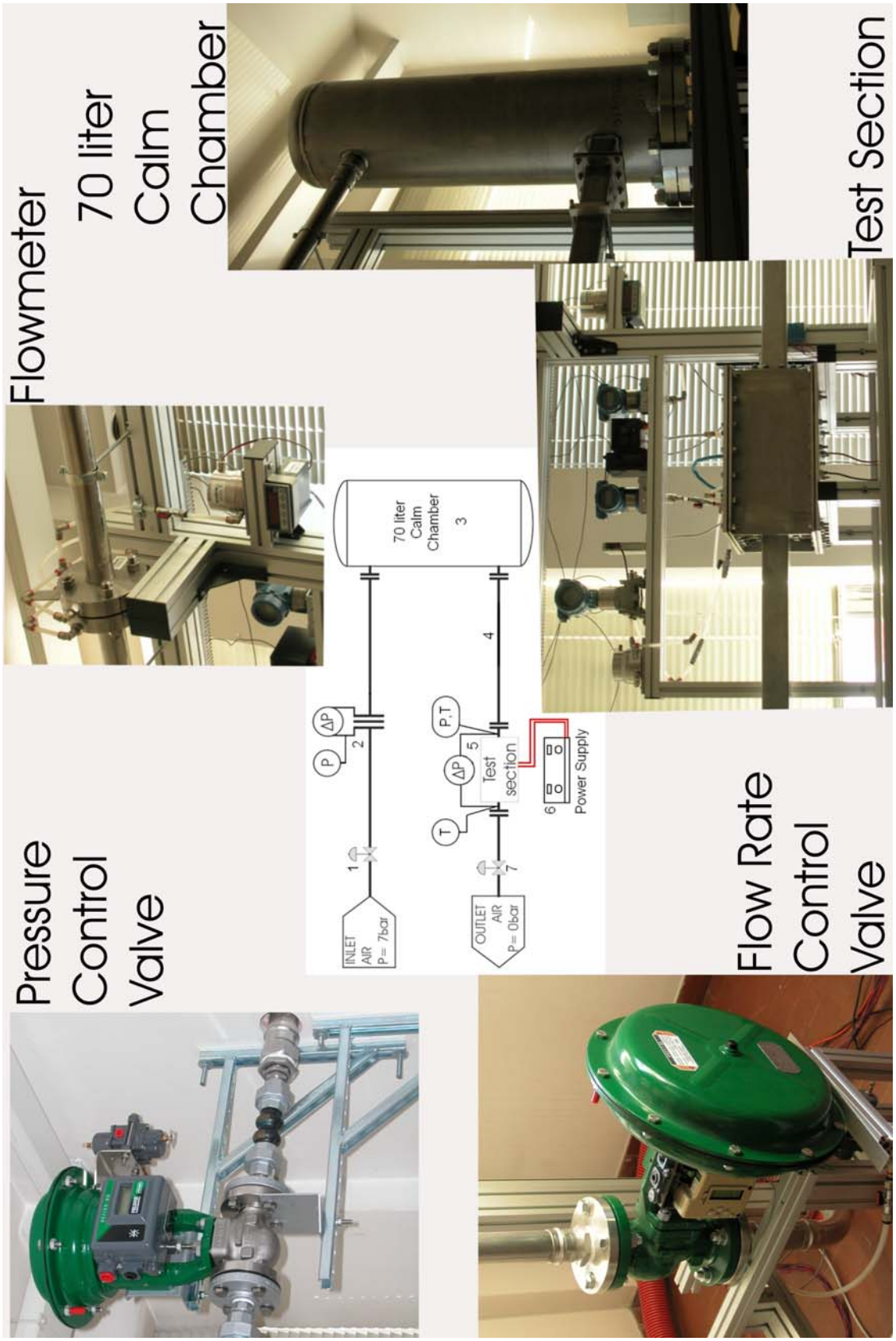

Figure 90. Experimental test part: scheme and photos.

Figure 91 reports the experimental test section, made of stainless steel AISI316L and with a width of 300 mm, a length of 300 mm and a height of 200 mm, fitted with a suitable Bakelite channel.

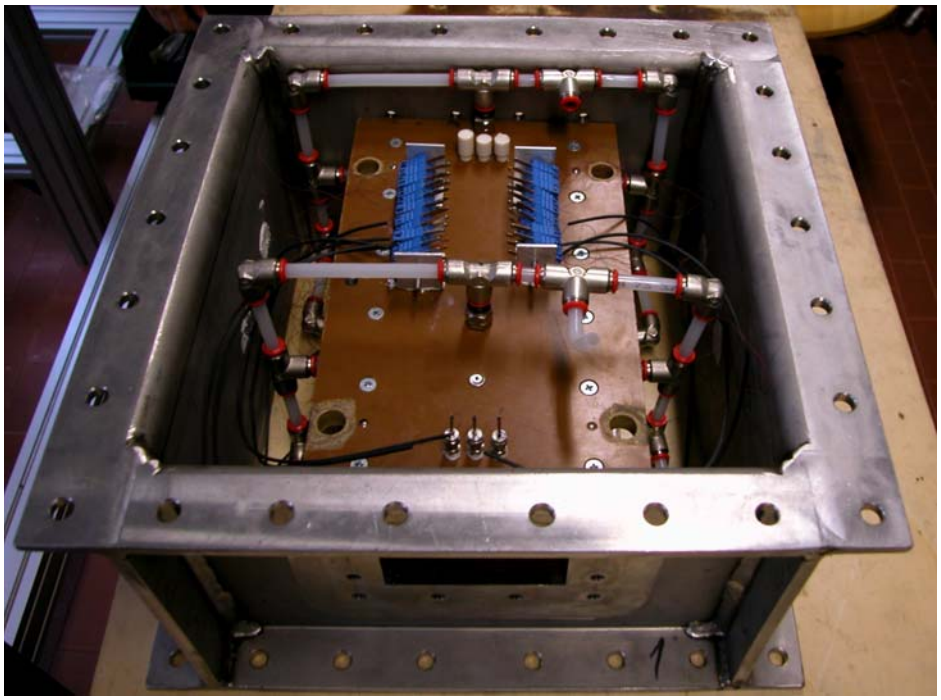

Figure 91. Photo of the test section fitted with a suitable bakelite channel.

The test sample is located inside the stainless steel test section and it is heated from the bottom by means of a copper plate machined to allow the passage of an electrical wire resistance powered by a 900 W DC power generator.

Temperatures at the inlet and outlet of the specimen are measured by means of two grids equipped with T-Type thermocouples. As shown in Figure 90, the absolute pressure is measured in two places by means of two transducers: one is located on the inlet flange of the volumetric flowmeter, the other one before the test section. In addition, two differential pressure transducers are used to measure pressure drops across both the calibrated orifice flowmeter and the test sample.

Finally, all the data are recorded by an acquisition system consisting in an Agilent HP34970A digital multimeter and elaborated by a visual data program developed in LabView 6.0 ambient.

2.2.3.2 Air Compressor Workplace

As described before, the compressor workplace consists of a screw compressor, a R134a drier, a set of filters and a 500 L air receiver. These components are illustrated in Figure 92.

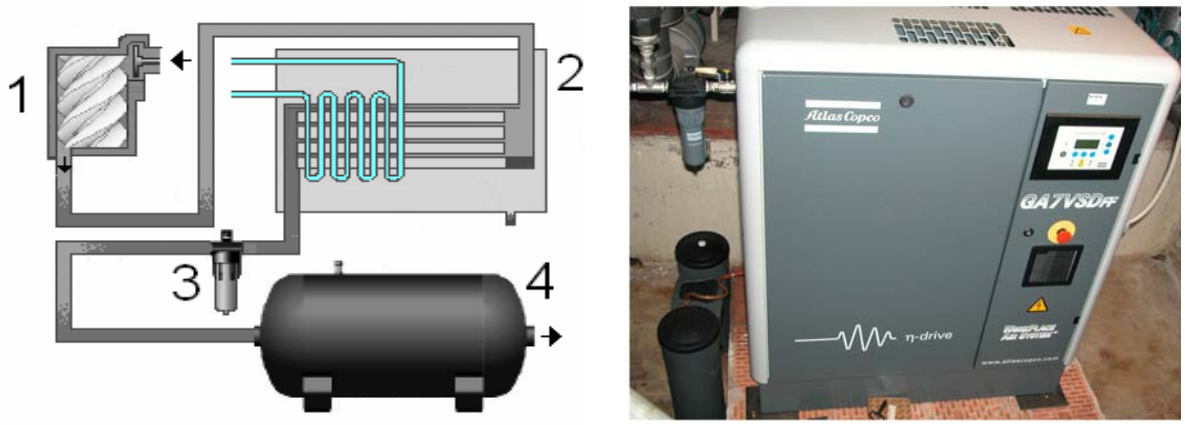

Figure 92. Schematic (left) and photo (right) of the air compressor workplace components.

The air compressor (1) is a single stage, oil injected screw compressor driven by an electric motor with inverter driver. The inverter controls the rotational speed of the compressor, which can vary between 1500 rpm and around 3000 rpm, pumping a variable air flow rate from 0 to 90 $m^3\ h^{-1}$ at a constant pressure of 7 bar.

After the compression stage, the air flows through the R134a drier (2), inside which the vapour contained in the air condenses over the cold surface of the evaporator. The drier is an air cooled R134a refrigeration system consisting of an evaporator embedded in a box which cooles and dehumidifies the compressed air to a dew point temperature of 3 °C. The circuit is completed by a compressor and an air cooled condenser.

The compressed air at the exit of the evaporator can be considered as dry air because the contained water vapour is negligible. In fact, the humidity ratio (defined as the ratio between actual mass of water vapour present in air to the mass of dry air) of air at the absolute pressure of 8 bar and at the dew-point temperature of 3 °C is 0.6 10^{-3} kg of vapour for each kg of dry air. Therefore, the effect of humidity ratio on air enthalpy is negligible and, also considering that it does not vary during the sensible heat transfer process, its value has not been measured.

A set of filters (3) are inserted to eliminate the residual oil and particle materials; then the compressed air reaches the 500 L air receiver (4).

2.2.3.3 Volumetric Air Flowmeter

The air flow rate coming from the pressure control valve is measured by means of a calibrated orifice flowmeter. As already mentioned, after careful consideration of the merits of nozzles and orifices, an orifice flowmeter was selected as the more reliable under the operating conditions and for the particular application.

To use an orifice is the most convenient method of measuring air flow, since it is simple in construction (nowadays it can be made with high accuracy at any good workshop) and its size can readily be changed by sliding in new orifice plates.

The volumetric air flowmeter has been designed according to EN ISO 5167-1:1997/A1:2000 [32]. It measures the air flow rate using a high accuracy differential pressure transducer which measures the air pressure drop across a calibrated orifice.

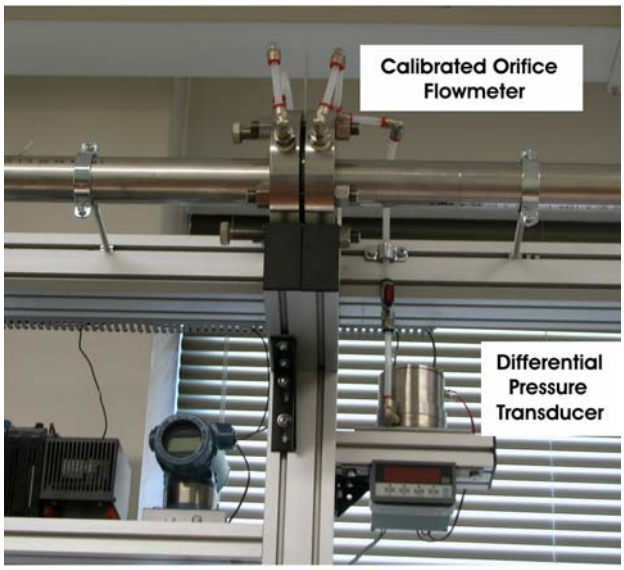

Figure 93. Photo of the calibrated orifice flowmeter.

In order to obtain the best accuracy in the air flow rate measurement, a high-precision difference pressure transducer LPX 9381, produced by Druck, has been chosen and connected to 4 flange taps. This pressure transducer has a declared accuracy of ±0.1% of full scale (F.S.= 20 mbar), but according to the calibration certificate it has a better performance. Fluid properties are estimated from the temperature and pressure measurements made at the inlet of the flowmeter.

In Figure 94, the uncertainties of the calibrated orifice flowmeter calculated according to the reference norm UNI EN ISO [32] are plotted against the ratio between the calibrated orifice

diameter and the inlet tube diameter, β. Uncertainties include the differential pressure transducer accuracy. It is interesting to point out that uncertainty in flow rate measurement is always less than 0.8%.

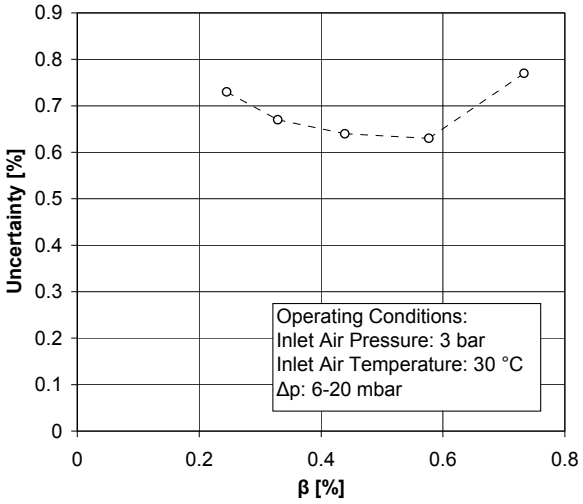

Figure 94. Uncertainty of the calibrated orifice flowmeter, calculated according to EN ISO 5167-1:1997/A1:2000 [32] as a function of the diameters ratio, β.

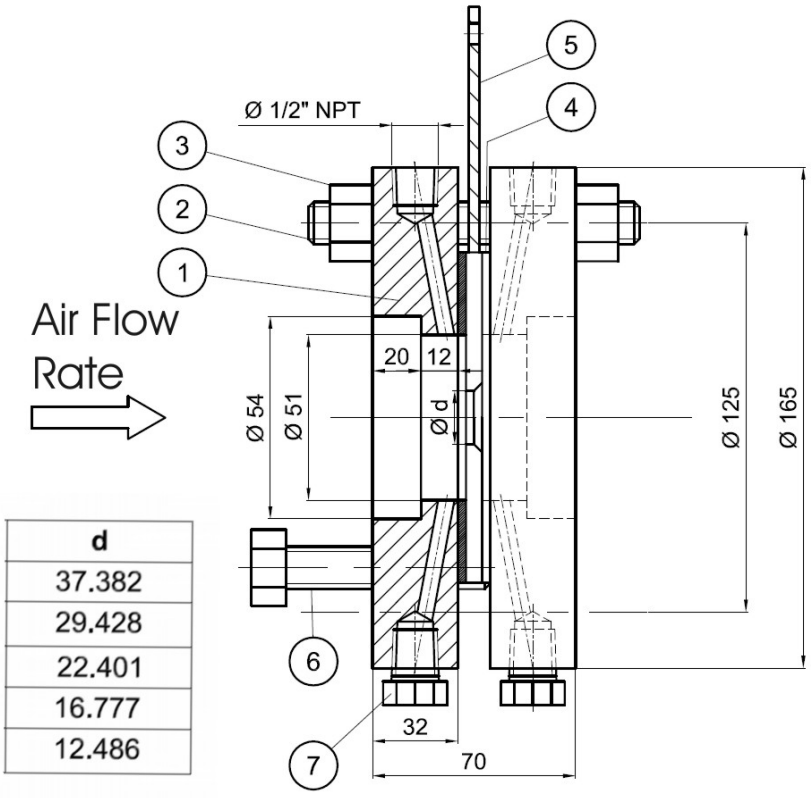

Figure 95. Drawing of the orifice volumetric flowmeter.

Figure 95 shows a drawing of the orifice flowmeter. This consists of two flanges containing orifice plates. The orifice plates were designed to measure different air flow rates with a constant pressure drop range: 6 to 20 mbar. In this way, the experimental uncertainty in the flow rate measurement is maintained as low as possible.

According to the different orifice diameters reported in Figure 95, the values of the ratio β are reported in Table 42. This ratio varies between 0.245 and 0.733.

Table 42. Values of the diameter ratio, β.

Duct Diameter, D [mm]	Orifice Diameter, d [mm]	β [-]
51	37.382	0.73298
	29.428	0.57702
	22.401	0.43923
	16.777	0.32896
	12.486	0.24482

Figure 96 shows the simulation of the range of the measurements of the different orifice plates: it appears that each orifice plate measures a part of the total air flow range without leaving dead zones.

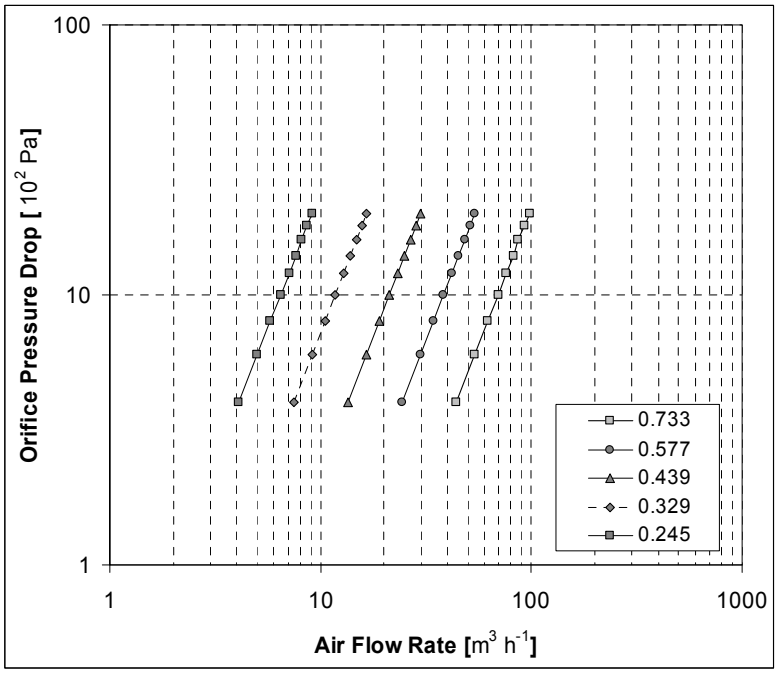

Figure 96. Orifice pressure drop against the related air flow rate as a function of the different ratios of the characteristic diameters, β.

Though it cannot be automatic, this measurement technique permits the measurement of a wide range of air flow rates with high accuracy and relatively low economic investment as compared with different typologies of flowmeters (like Coriolis effect or thermal effect mass flowmeters).

EN ISO standard 5167-1:1997/A1:2000 [32] suggests a calculation procedure for evaluation of the air flow rate. The inputs of this algorithm are: the orifice pressure drop, the temperature and the pressure of the air at the inlet of the calibrated flanges and the diameters ratio, β.

Humid air is a mixture of vapour and dry air; therefore, in order to define its thermodynamic state, three thermodynamic coordinates are needed. In our case, since the drier reduces the amount of the vapour in the air to a value which can be neglected, the humidity ratio has been considered equal to 0.6 10^{-3} kg_v kg_{da}^{-1}.

The other two thermodynamic coordinates, air temperature and pressure, are measured at the inlet of the calibrated orifice flowmeter. Hence, the density and the dynamic viscosity of the air at the inlet of the flowmeter are estimated as follows:

$$\rho = \frac{1}{\left[0.2871 \cdot \left(t_{in} + 273.15\right) \cdot \left(1 + 1.6078 \cdot x\right) \cdot \frac{1000}{p_a}\right]} \qquad \textbf{Eq. 198}$$

$$\mu = \left(0.0455 \cdot t_{in} + 17.055\right) \cdot \frac{1}{1000} \qquad \textbf{Eq. 199}$$

The air mass flow rate can be calculated using the following equation:

$$\dot{m}_{air} = \frac{C}{\sqrt{1-\beta^4}} \cdot \varepsilon \cdot \left(3.1415 \cdot \frac{d^2}{4}\right) \cdot \left(2 \cdot \Delta p \cdot 100 \cdot \rho\right)^{0.5} \qquad \textbf{Eq. 200}$$

Where Δp is the orifice pressure drop, while C and ε are the coefficient of discharge and the gas expansion factor, respectively.

These are evaluated with the next equations:

$$C = 0.5961 + 0.0261 \cdot \beta^2 - 0.216 \cdot \beta^8 + 0.000521 \cdot \left(10^6 \cdot \frac{\beta}{\mathrm{Re}}\right)^{0.7}$$
$$+ \left[0.0188 + 0.0063 \cdot \left(19000 \cdot \frac{\beta}{\mathrm{Re}}\right)^{0.8}\right] \cdot \beta^{3.5} \cdot \left(\frac{10^6}{\mathrm{Re}}\right)^{0.3} + \left(0.043 + 0.08 \cdot e^{-10 \cdot L_1} - 0.123 \cdot e^{-7 \cdot L_2}\right) \cdot \quad \textbf{Eq. 201}$$
$$\cdot \left[1 - 0.11 \cdot \left(19000 \cdot \frac{\beta}{\mathrm{Re}}\right)^{0.8}\right] \cdot \frac{\beta^4}{1-\beta^4} - 0.031 \cdot \left[2 \cdot \frac{L_2}{1-\beta} - 0.8 \cdot \left(\frac{2 \cdot L_1}{1-\beta}\right)^{1.1}\right] \cdot \beta^{1.3}$$

And:

$$\varepsilon = 1 - \left(0.351 + 0.256 \cdot \beta^4 + 0.93 \cdot \beta^8\right) \cdot \left[1 - \left(\frac{p_a - \Delta p}{p_a}\right)^{\frac{1}{k}}\right] \quad \textbf{Eq. 202}$$

Where k is the ratio of specific heats, equal to 1.4.

As it appears, the coefficient of discharge C depends on different parameters, the ratio of the characteristic diameters β and the Reynolds number, and two geometrical characteristics, L_1 and L_2, which are linked to the internal duct diameter:

$$L_1 = L_2 = \frac{25.4}{D \cdot 1000} \quad \textbf{Eq. 203}$$

While the Reynolds number is defined by:

$$\mathrm{Re} = \frac{4 \cdot \dot{m}_{air}}{\pi \cdot \mathrm{D} \cdot \mu} \quad \textbf{Eq. 204}$$

Considering the gas expansion factor ε, again it depends on the ratio of the characteristic diameters β, and also on the orifice pressure drop and on the inlet air pressure.

This computational procedure results to be iterative, because at the first step the Reynolds number called in the coefficient of discharge calculation is not longer known. Therefore, its

value is initialized to a default value of 20000 and then it is recalculated with the output air mass flow rate.

The iterative procedure ends when the difference between the last two Reynolds numbers results to be less than a predefined threshold which has been fixed at 0.00001.

2.2.3.4 Stainless Steel Components: 70 Liter Chamber, Test Section and Channels

The whole test rig was designed to resist a maximum operating pressure of 7 bar. As already mentioned, all components are made of stainless steel AISI 316 L. This paragraph reports the executive drawings of the most important components. Considering again Figure 97, these components, from the calm chamber to the discharge valve, are listed and discussed, describing only the stainless steel ones.

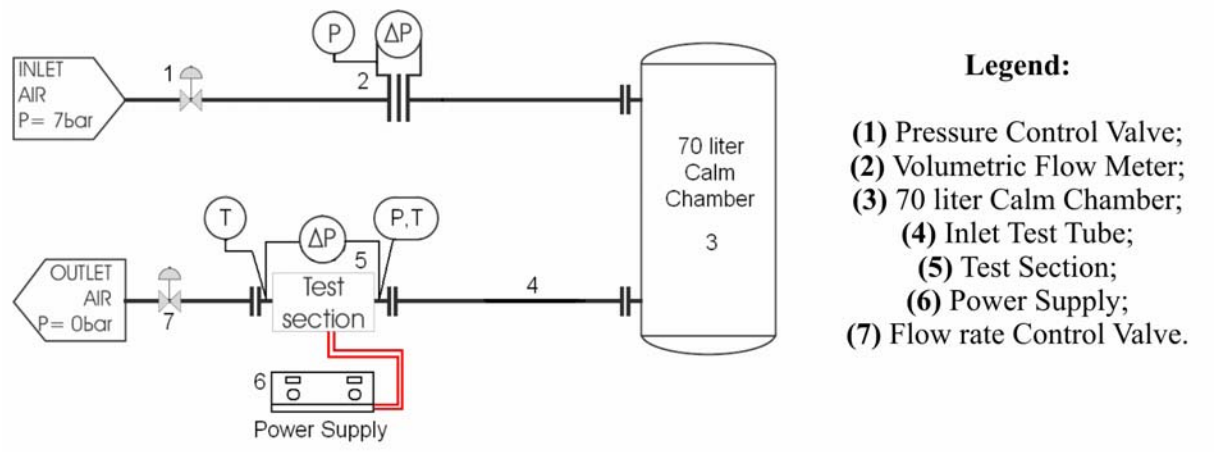

Figure 97. Schematic of the experimental test facility.

70 Liter Calm chamber

This "strategic" component permits to change the cross-sectional area of the test tube, passing from a circular one to a rectangular one, as reported in Figure 98. This technical solution permits to get rid of the design of such a complicated interconnection manifold. Furthermore, it allows to reduce the total length of the inlet test tube.

Figure 98 also shows the executive technical drawing of the calm chamber, which is 1064 mm high, with an internal diameter of 317 mm and a thickness of 5 mm. The wall thickness was designed for 10 bar working pressure with a safety coefficient of 2.

The top side of this air receiver is blind, while a DN 300 flange is soldered on the other side to allow inspection and maintenance operations. Finally, a ½" connector was included to screw a safety valve set at a pressure of 5 bar.

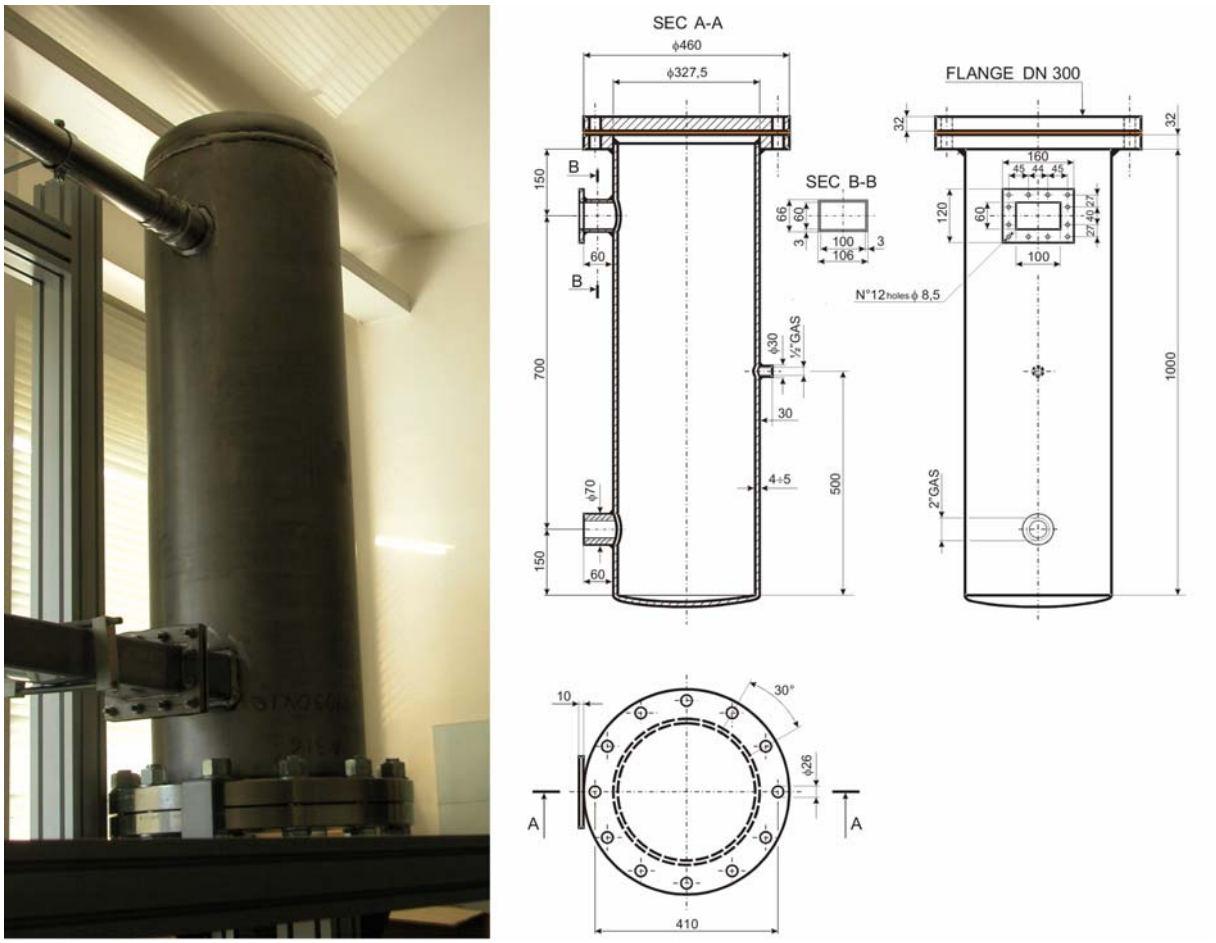

Figure 98. Photo and executive technical drawing of the 70 liter calm chamber.

Inlet Test Tube

The inlet test tube has a rectangular cross-sectional area which is 100 mm wide and 60 mm high. Figure 99 reports its executive technical drawing. The total length of this channel is 1.1 m; it was designed to ensure the full development of the air flow before it reaches the test section .

In fact, the hydrodynamic entrance length is defined as the duct length required to achieve a maximum duct cross section velocity as 99% of that of a fully developed flow when the entering fluid velocity profile is uniform.

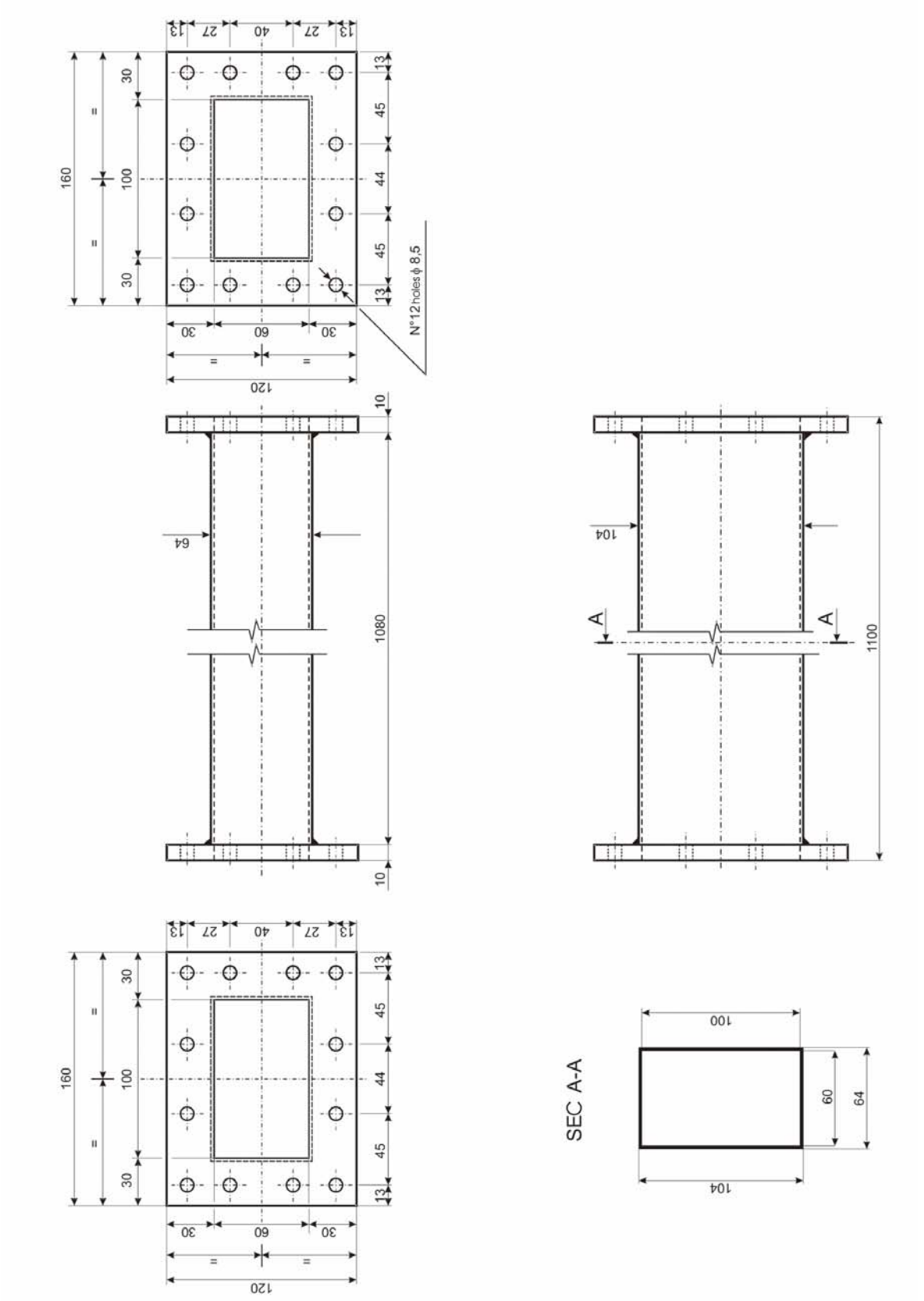

Figure 99. Executive technical drawing of the inlet test tube.

Test Section

The stainless steel test section is 300 mm long, 300 mm wide and 200 mm high; it can hold any kind of test sample with the following maximum size: 100 mm width, 60 mm height and 200 mm length (Figure 100). It consists of 3 parts: the top and bottom plates, which are bolted to allow inspections and maintenance operations, and the core where the test sample is inserted.

The executive technical drawing of the cover plates is reported in Figure 101.

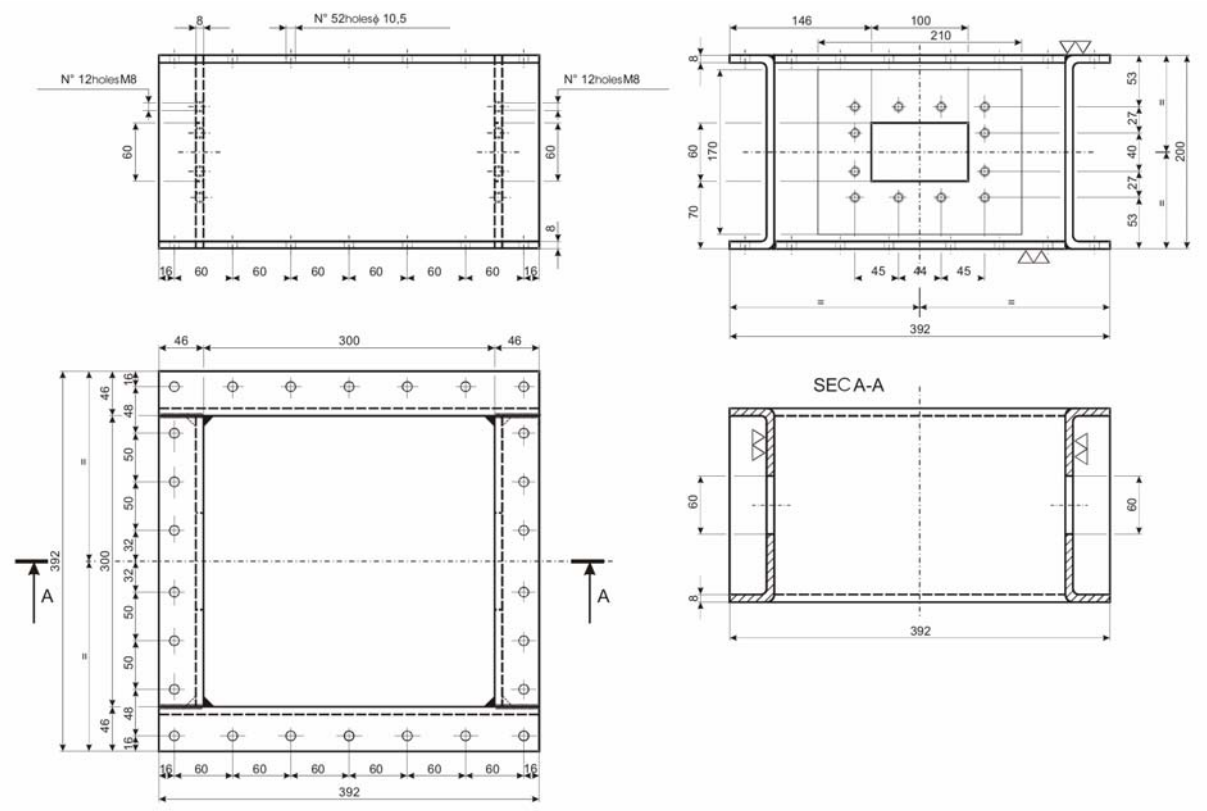

Figure 100. Executive technical drawing of the test section.

Six holes were successively drilled in the two cover plates: three in the top one and three in the bottom one. Considering the top plate, its three holes permit the passage of the thermocouples wires connecting the transducers to the ice point reference and the connection of the two pressure transducers to the static pressure taps. The three holes in the bottom plate are used to acquire the electrical difference potential of the wire resistance and to connect the DC generator to the heater.

All these connections are pressure resistant because special insulated connectors have been used.

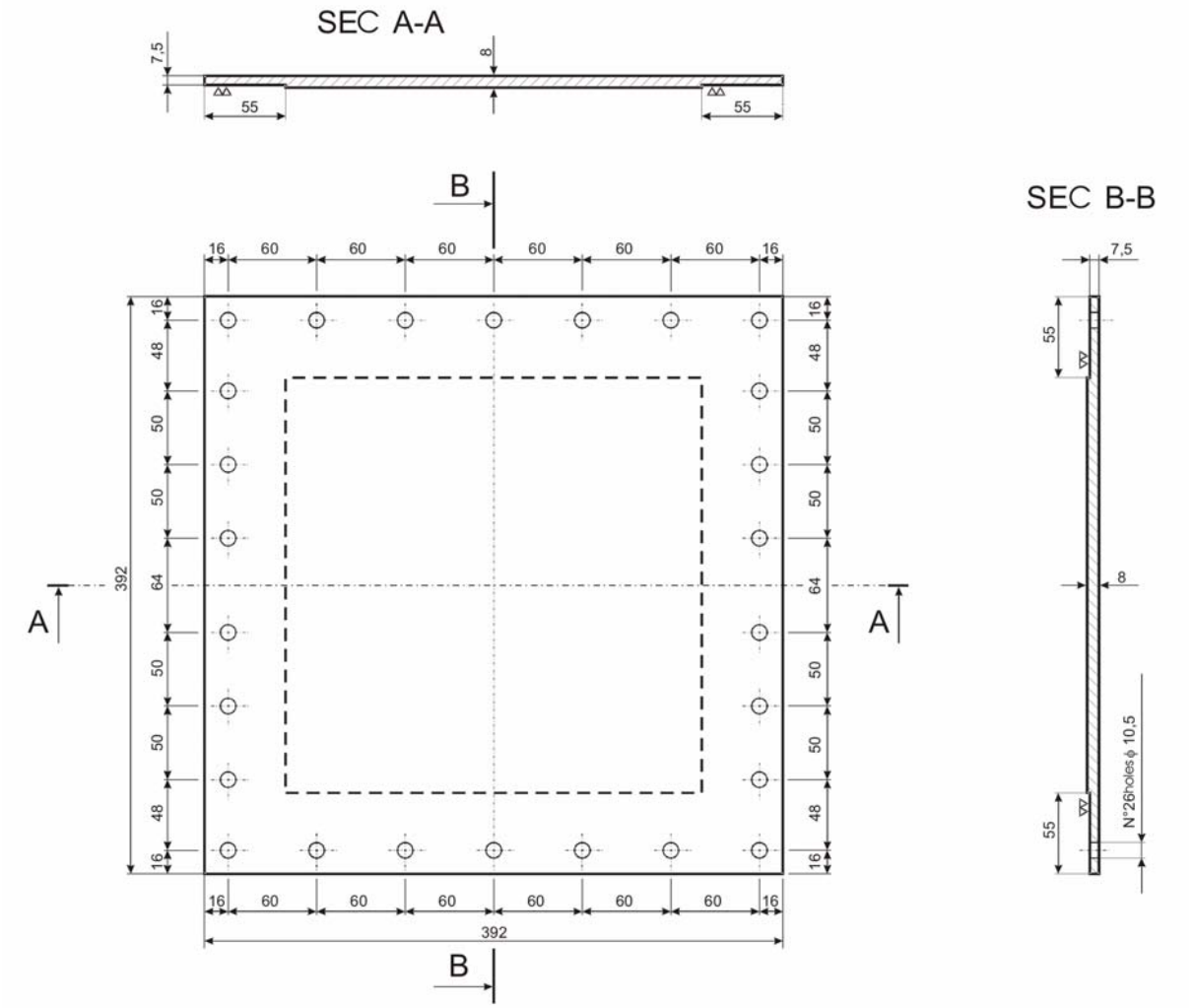

Figure 101. Executive technical drawing of the two plates.

Discharge Tube

The test section is connected to the flow rate control valve by two different tubes: the first one, the effective discharge tube, has a rectangular cross-sectional area, while the other is a 2" ID circular tube.

As it appears from the executive technical drawing of Figure 102, the discharge tube is an L-shaped duct 600 mm long.

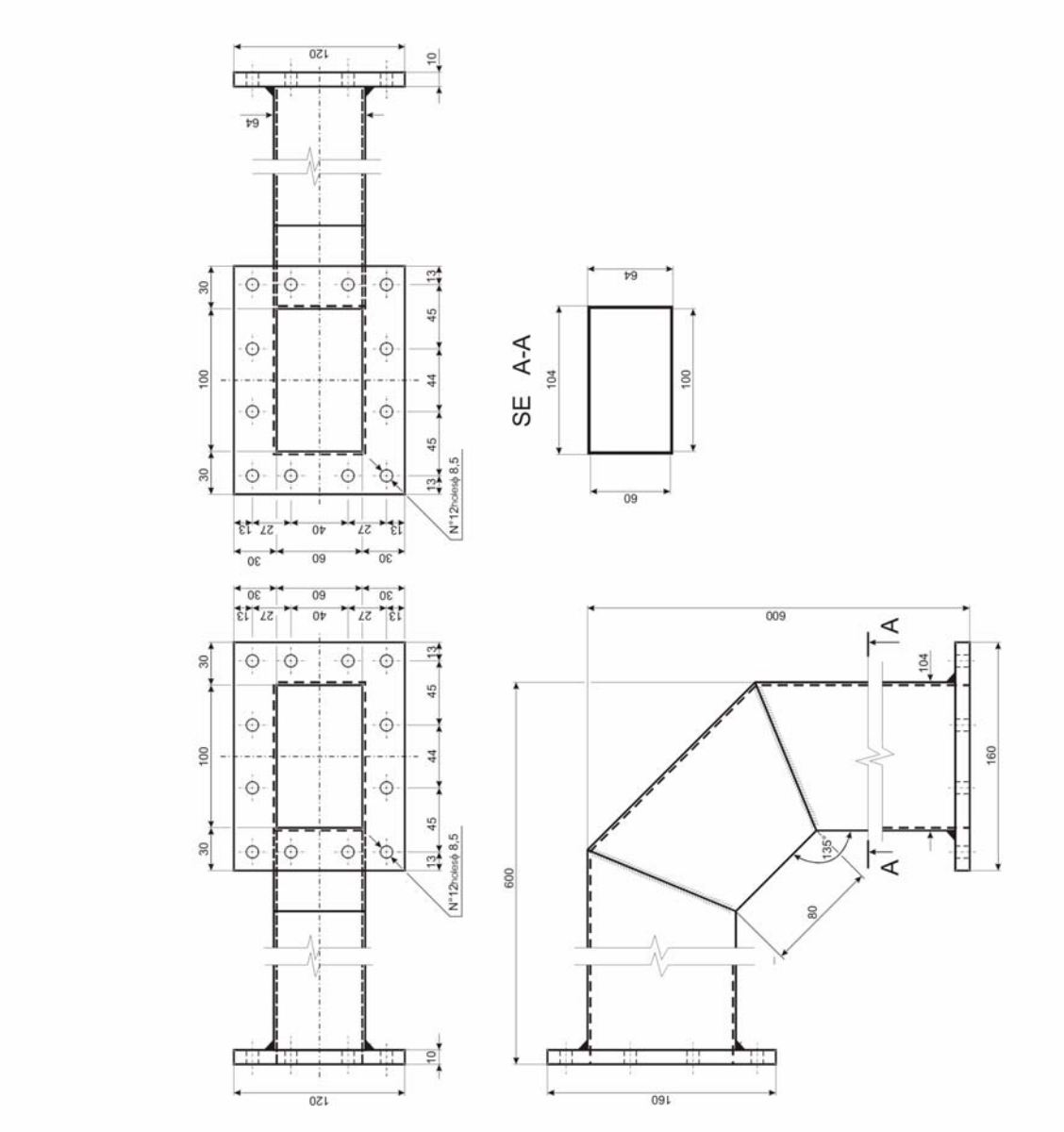

Figure 102. Executive technical drawing of the discharge tube.

2.2.3.5 Pressure and Air Flow Rate Valves

The Fisher Design GX is a compact, state-of-the-art control valve and actuator system, designed to control a wide range of process gases, vapours and fluids.

Two of these control valves were selected to permit the control of both the operating pressure and the air flow rate independently one from the other. Figure 103 reports a scheme of the designed pressure and mass flow rate control system implemented in the test rig in order to control the pressure and the flow rate independently one from the other.

As one can see, the compressed air gets to the pressure reducer at 7 bar and leaves the valve at 0-3 bar, values which have been chosen as the design pressure range of the calibrated orifice flow meter used to measure the volumetric flow rate.

The pressure control system consists of a GX DVC2000 DN25 valve with a digital actuator produced by Fisher and an external PID commanding the actuator.

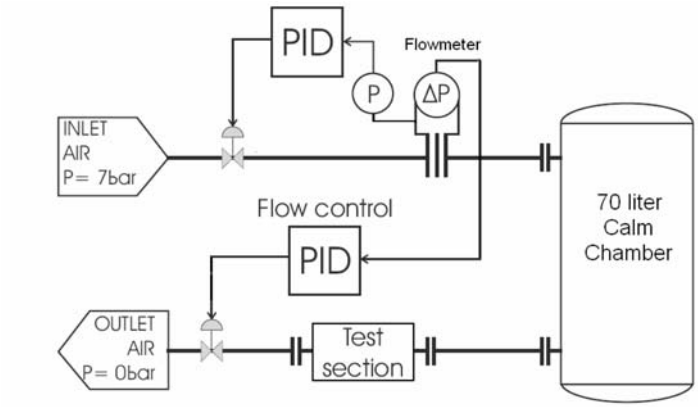

Figure 103. Simplified scheme of the designed pressure and mass flow rate control system.

The compressor permits to have a constant incoming air at 7 bar and the reduction is commanded by the effective pressure measured by a Rosemount pressure transducer at the inlet of the calibrated flowmeter. The feedback signal from the pressure transducer is elaborated by the PID which performs the best approach to the set point.

A second loop is inserted in the test rig for the flow rate control in the apparatus. It is an independent system consisting of a GX DVC2000 DN50 valve with a digital actuator produced by Fisher and an external PID controlling the movements of the actuator.

The analogic feedback signal coming from the flowmeter is analysed by the digital PID controller which drives the actuator of the valve. In order to control the pressure and the flow

rate independently, the two sets of time constants (proportional, integrative and derivative) of the PIDs must be precisely tuned.

The experimental rig itself behaves as a complex fluid-dynamic system, so that it is extremely difficult to describe the exact model for achieving an accurate control performance. In general, it is possible to propose a simplified bilinear system model. It is well known that this situation can cause an unstable behaviour because of the interaction of system components with control loops under continuously changing flow conditions.

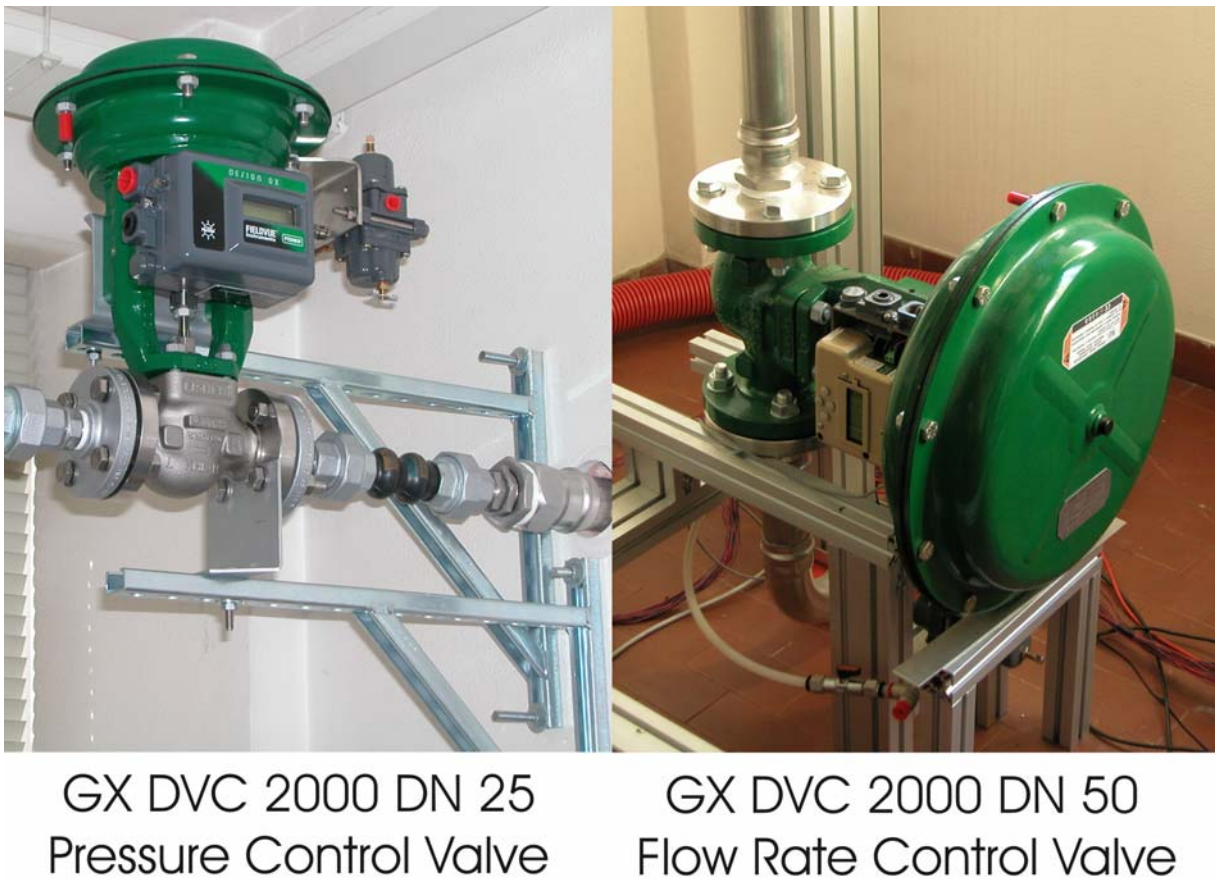

Figure 104. Photos of the designed pressure and mass flow rate control systems.

Although this complicate system has been fully implemented in the test rig, the experimental campaign that will be presented in this thesis did not use it. PID controls have been by-passed using manual controls, simpler and sufficiently accurate and repeatable.

In fact, the compressor was set to run at fixed velocity (rpm) and the inertia of the 500 L tank was sufficient to obtain fixed mass flow rate once that the position of the valves was selected manually.

2.2.3.6 Test Section

Here we describe the core of the experimental set-up: the test section. The stainless steel box where the bakelite channel is inserted has been presented previously. It is important to highlight that the test section consists of both the bakelite channel and the stainless steel box.

In this part of the experimental wind tunnel, the heat transfer coefficients and the pressure drops of different enhanced surfaces during single-phase air flow are measured. (Figure 81) shows a photo of the complete test section, and Figure 105 a photo of the test section during start-up works.

In Figure 105, some important components of the test section are evident. Among them we can mention the bakelite channel with the Teflon base plate, the heating copper plate, the mixer, some thermocouple connectors and part of the pressure connectors.

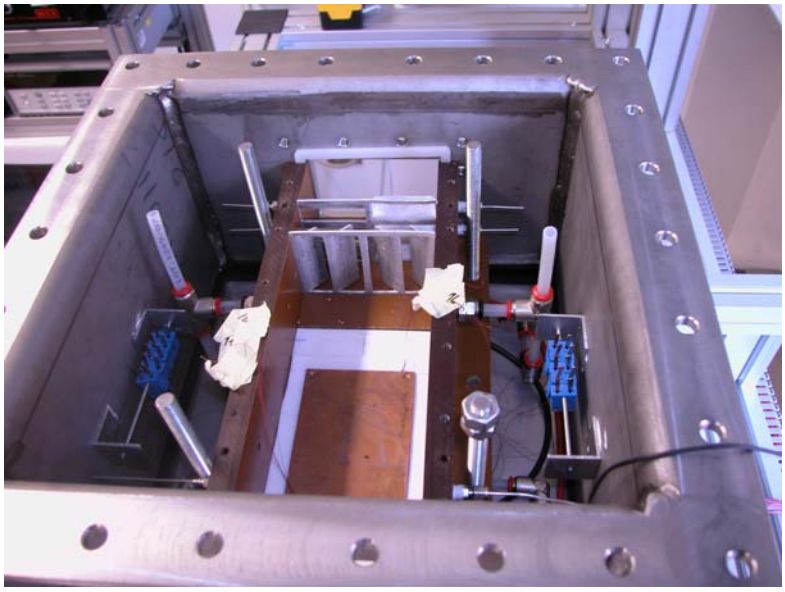

Figure 105. Photo of the test section during the set-up process.

As highlighted by the cross section of the bakelite channel drawn in Figure 106, a 15 mm thick plate of Teflon is machined to obtain a location for the copper heater where the sample is tightened. This Teflon plate is blocked within two bakelite walls which are located over two guides milled in a bakelite base. Then the rectangular channel is completed with a bakelite ceiling. It is also possible to supply the heat from both the upper and bottom surfaces of the test sample; in this way, both symmetrical and asymmetrical heating can be investigated.

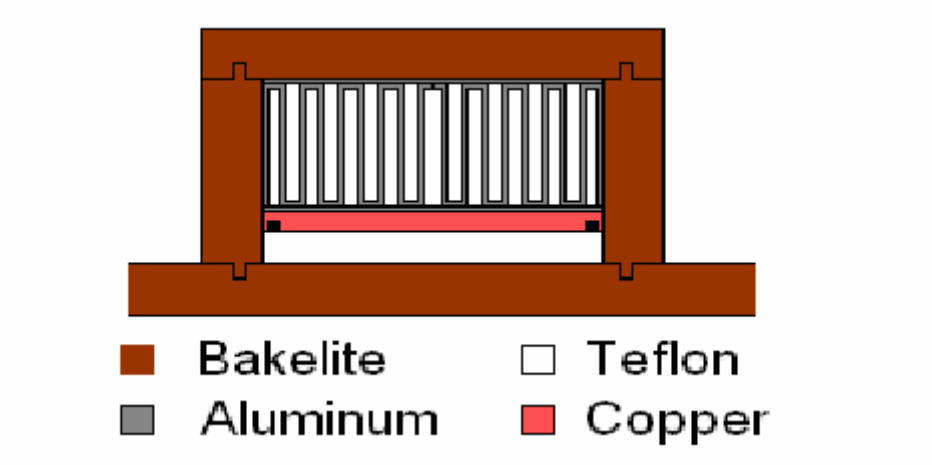

Figure 106. Drawing of a cross section of the bakelite channel.

As described before, the bakelite channel has been equipped with pressure and temperature transducers, a copper heater and electrical potential difference measuring wires. As shown in Figure 107, the test specimen is located within a rectangular duct made of Teflon and bakelite.

When the air reaches the test section, its temperature is measured by means on nine calibrated T-Type thermocouples (3). Since the inlet test tube is 1.1 m long, the fully development of the air flow is assured. The air absolute pressure is also measured by means of an absolute pressure transducer which is connected to four static pressure taps (1). More details of the pressure measurements will be given in the following.

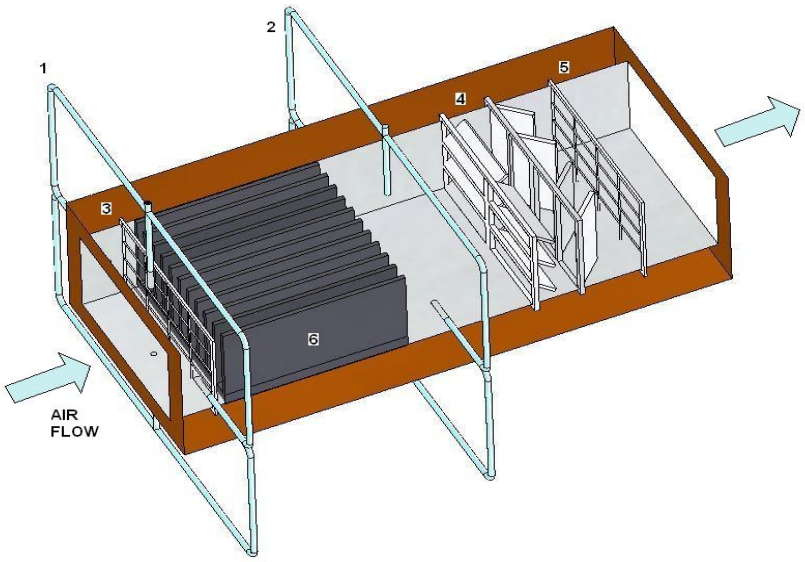

Figure 107. Schematic of the bakelite channel arrangement: (1) inlet pressure taps, (2) outlet pressure taps, (3) nine inlet thermocouples, (4) mixer, (5) nine outlet thermocouples, (6) tested heat sink.

Then the air arrives to the heat sink (6) which is heated by the copper heater. After the test sample, other four static pressure taps are drilled to measure the pressure drops of the air by means of a differential pressure transducer connected to the inlet and outlet pressure tubes, (1) and (2).

At the exit of the test sample the air temperature profile is stratified. A mixer has therefore been designed to eliminate temperature non-uniformities, allowing to measure the mean air temperature by means of nine calibrated T-Type thermocouples.

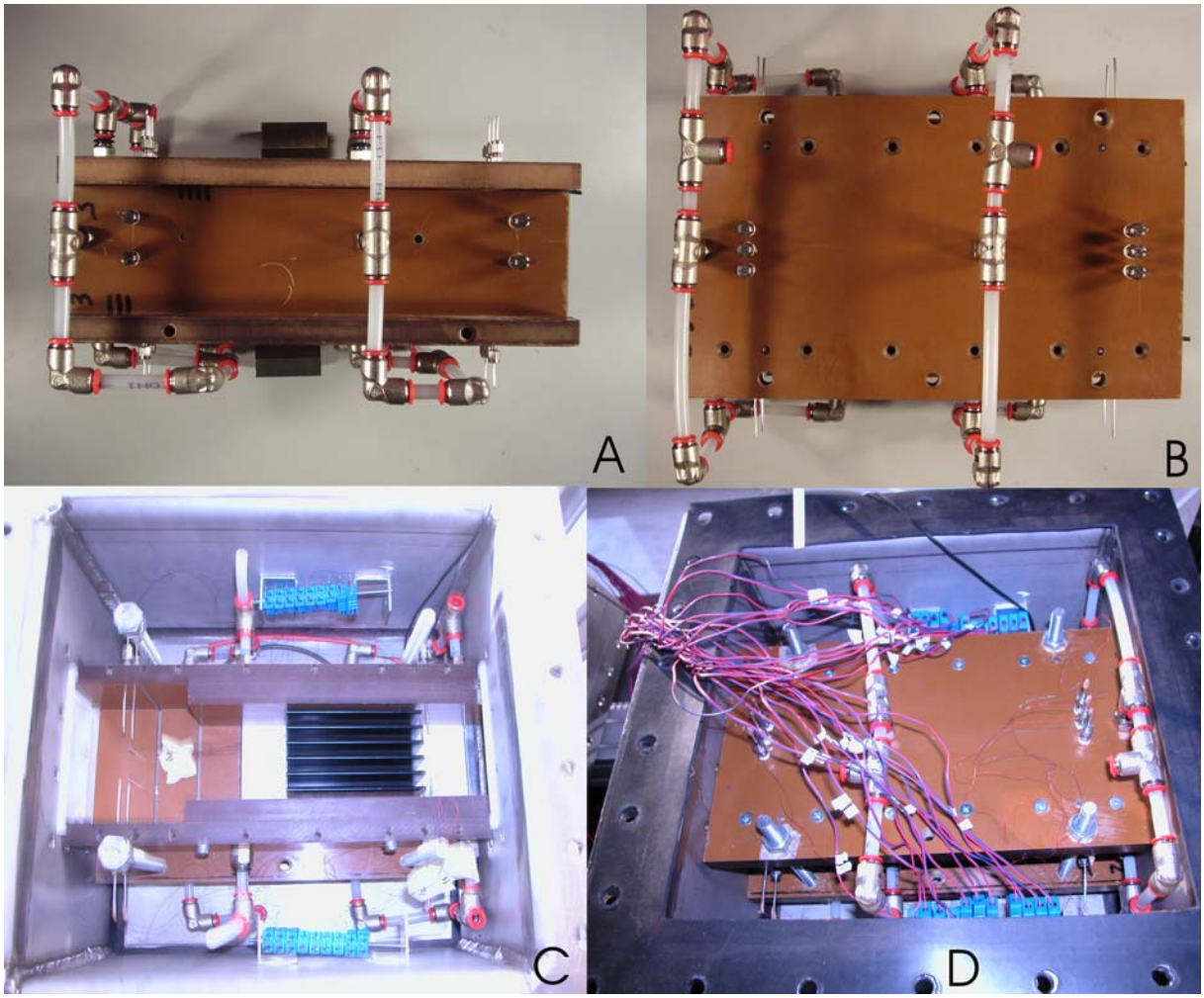

Figure 108. Four photos of the experimental test section: (A) side view, (B) top view, (C) finned surface arrangement, (D) full instrumented test section.

The photos of Figure 108 show the test bakelite channel. Photo A shows a side view of the test section: the side pressure taps and the thermocouples connector are evident. Photo B shows a top view of the bakelite channel: as in photo A, the pressure taps and the thermocouples at the inlet and outlet of the test section are apparent.

Photos C and D illustrate the construction of the test section. It is interesting to highlight that in photo C the finned surface and the additional side walls used to reduce the frontal area are evident, while photo D is a close-up of the instrumented test section.

2.2.3.7 Acquisition System

The acquisition system permits to acquire and elaborate the most important parameters which control the test rig evolution during the experimental test runs.

It consists of a HP34970A digital multimeter which is connected to both the transducers and the computer. It acquires the analogical signals following a defined time schedule. The recorded signals are then elaborated by a computer interface program developed in LabView 6.0.

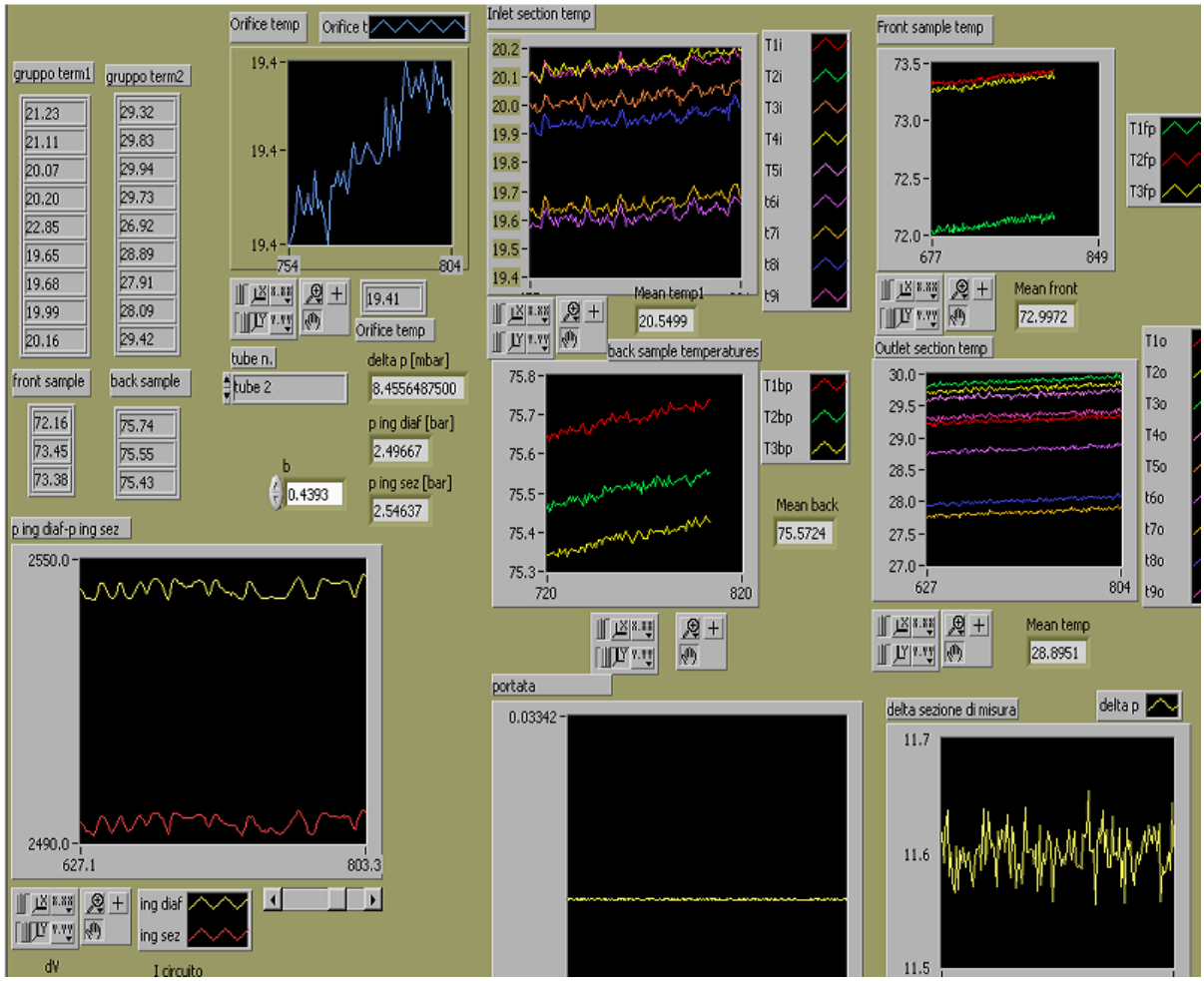

Figure 109. Part of the visual interface of the acquisition system developed in LabView 6.0 ambient.

Table 43. List of recorded transducers.

Channel	***Description***	***Unit***
101	Orifice flowmeter inlet air temperature	°C
102	Test section inlet air temperature	°C
103	Test section inlet air temperature	°C
104	Test section inlet air temperature	°C
105	Test section inlet air temperature	°C
106	Test section inlet air temperature	°C
107	Test section inlet air temperature	°C
108	Test section inlet air temperature	°C
109	Test section inlet air temperature	°C
110	Test section inlet air temperature	°C
111	Frontal test sample wall temperature	°C
112	Frontal test sample wall temperature	°C
113	Frontal test sample wall temperature	°C
114	Back test sample wall temperature	°C
115	Back test sample wall temperature	°C
116	Back test sample wall temperature	°C
117	Test section outlet air temperature	°C
118	Test section outlet air temperature	°C
119	Test section outlet air temperature	°C
120	Test section outlet air temperature	°C
201	Test section outlet air temperature	°C
202	Test section outlet air temperature	°C
203	Test section outlet air temperature	°C
204	Test section outlet air temperature	°C
205	Test section outlet air temperature	°C
311	Orifice flowmeter air pressure drop	mbar
312	Orifice flowmeter inlet absolute air pressure	bar
313	Test section inlet absolute air pressure	bar
314	Test sample air pressure drop	Pa
315	Circuit current	A
316	Electric differential potential of the wire resistance	V

Table 43 reports the main acquired transducers. It is important to underline that each different enhanced surface needs its dedicated channels set up and acquisition system.

Figure 109 shows an example of part of the visual interface of the acquisition system. It is clear that the acquisition system allows to understand the actual working regime of the experimental set-up: each diagram or table gives a precise piece of information on the trend of the selected variable.

This acquisition system writes recorded and elaborated signals to an Excel file. This file is useful in post processing work because it permits to calculate the experimental heat transfer coefficients and the pressure drops exhibited by the tested enhanced surface.

The Excel file lists, in chronological order, all the acquired measures. When steady-state conditions are reached and maintained for a few minutes, operating test conditions are changed varying the mass flow rate which flows through the test rig.

In post-processing operations all listed readings are elaborated. The one with the lowest heat balance deviation, during steady-state conditions, is taken as an experimental data point.

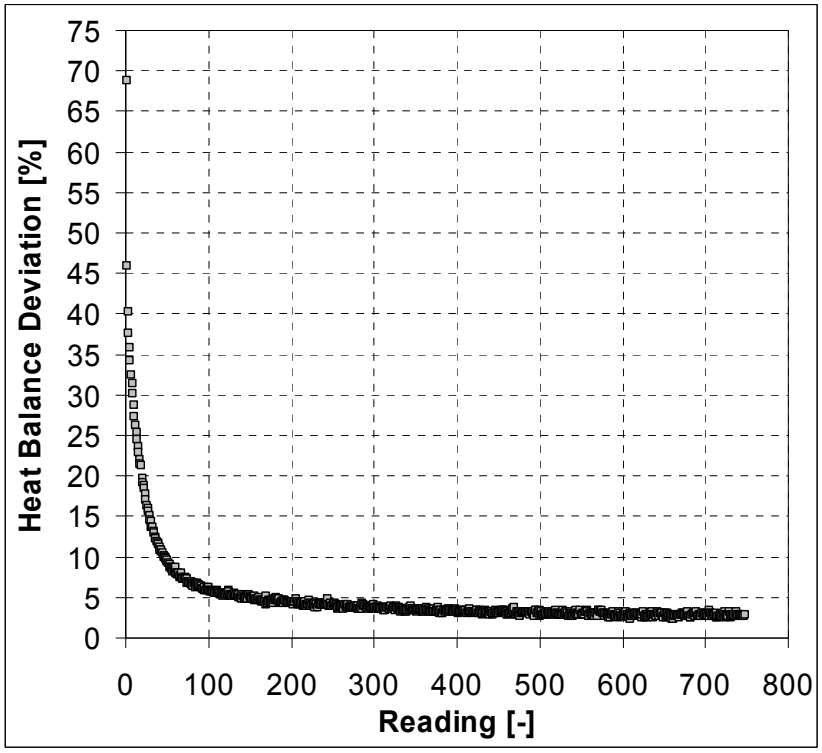

Figure 110. Experimental heat balance deviation plotted against readings.

Figure 110 shows an example of the behaviour of the test rig as a function of time (lecture). Generally speaking, a heat flux (i.e. 150 W) is imposed to the sample and a fixed air flow passes through it; after 700 lectures the system reaches the steady-state condition and a data point can be selected.

2.2.4 Heat Transfer and Pressure Drop Measurements: Techniques and Solutions

This paragraph describes the techniques and the components developed and implemented for heat transfer and pressure drop measurements during single-phase air flow through enhanced surfaces.

Considering heat transfer measurements, the attention will be focused on the technique used to heat the sample, on temperature measurement issues (uniformity and non-uniformity of the temperature profile) and on electric power measurements.

Pressure drop measurements are not as difficult as the heat transfer ones, but, in order to obtain a high accuracy measurement, the location and connection of static pressure taps must be given much attention.

2.2.4.1 Heat Transfer

Heating Technique

In general, there are two different ways to take heat transfer measures during single-phase air flow: the first one is by imposing a heat flux boundary condition, the second by imposing the wall temperature. This work concerns heat transfer measurements carried out by imposing constant heat flux as a boundary condition.

Heating by means of off-the-shelf electrical pads appears to be the simplest and cheapest technique. Unfortunately electrical pads are normally maden of silicon rubber and so, they are not stable at high temperatures (120 °C); moreover, temperature distribution on the heater surface appears to be non-uniform.

Another way to heat the sample could be by using the heating cartridges embedded in a copper block, but this technique was abandoned because it required a large amount of free volume. Since the heater had to be inserted within the stainless steel box, there was not sufficient space to hold it.

In this work, another heating technique has been implemented: the heater is obtained from a 7 mm copper plate with the same base area of the test sample; a guide is milled in the copper to hold the electrical wire resistance. This wire resistance is a nickel-chrome alloy presenting 1.37 Ω $m^{-1}$and it is drowned into high conductivity silicon paste. Electrical power is given by a stabilized direct current (DC) power supply providing up to 900 W. Figure 111 shows an example of the guide which is milled into the 7 mm copper plate. Four holes has been drilled to bolt the cover aluminum plate.

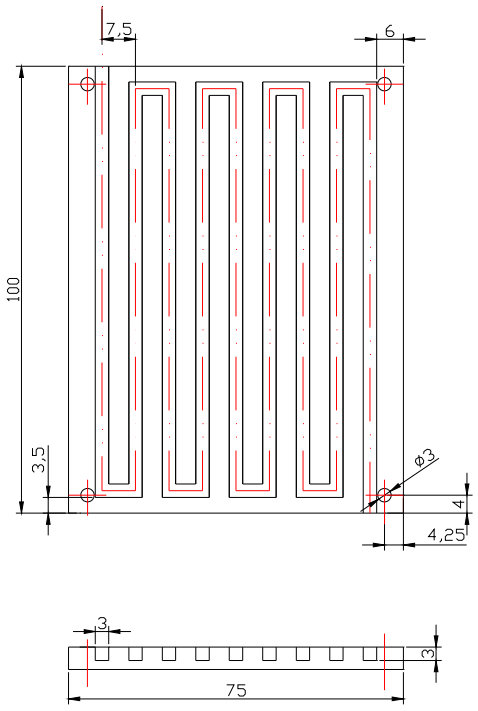

Figure 111. Drawing of the guide to be milled into the copper plate.

To evaluate the effective suitability of this heater, an infrared camera was used to film the temperature distribution of the heated surface in transient conditions. The heater was connected to the DC generator and an electric power variable between 50 and 150 W was applied.

Figure 112 shows a photo of temperature distribution taken with a thermo camera during a test on a copper heater prototype. A constant power of 150 W was supplied to the sample exchanging heat only with the ambient air in forced convection.

As it appears from the photo, there are no hot spots or lines in correspondence of the milled guide where the resistance wire was positioned; furthermore, the temperature is constant all over the surface.

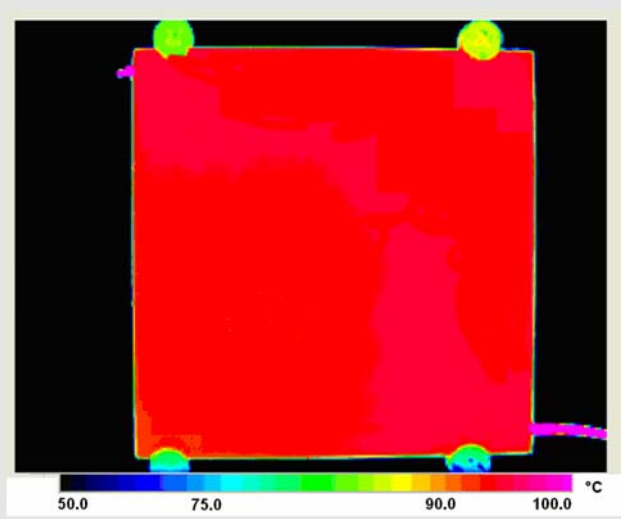

Figure 112. Thermo photo of the prototype heater powered with 150 W.

Electric Power Measurement

A DC stabilized generator able to supply up to 900 W is used to power the wire resistance embedded in the copper plate. In order to verify the accuracy of heat transfer measurements, this electric power has to be measured.

It can be measured in two different ways: it is possible to use an electronic power analyzer or to measure the voltage and the current independently.

In this work, the second method was followed: the voltage and the current are obtained from two EDP (Electrical Difference Potential) measures. The first one gives the effective EDP of the resistance wire inserted in the copper heater, the other is the EDP of a calibrated resistance (shunt).

If the resistance is known from Ohm law; the current is easily calculable from the measure of the potential difference.

$$R = \frac{V}{I} \quad [\Omega] \qquad \textbf{Eq. 205}$$

Where R is the wire resistance, while V and I are the electrical difference potential and the current, respectively.

The accuracy of this indirect measure is related to the nominal resistance accuracy: a calibrated shunt is used to obtain the best current evaluation.

This shunt is a stable calibrated resistance of 0.0993 Ω with an accuracy of ±0.03% which is inserted in the electrical circuit as shown in Figure 113.

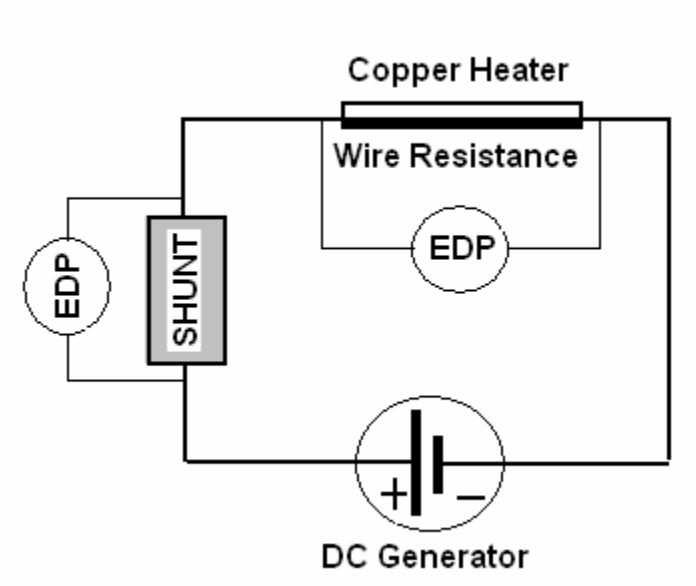

Figure 113. Schematic of the electrical difference potential measurements.

Therefore, with two accurate EDP measures it is possible to know the effective power supplied to the test sample by applying the following simple equation:

$$P_{EL} = V_R \cdot I = V_R \cdot \frac{V_S}{R_S} \quad [W] \qquad \textbf{Eq. 206}$$

Where the subscripts R and S refer to the wire resistance and to the shunt, respectively.
Applying the error analysis it appears that electric power uncertainty is always lower than ±0.15% of the reading.

Air Temperature and Heat Flow Rate Measurements

Temperature and heat flow rate measurements are closely linked. Hence, they are here presented together: the accuracy of air heat flow rate calculations depends on air temperature measures.
The wall temperatures of the different enhanced surfaces are also measured, but these will be discussed later, when the tested samples will be illustrated. In this paragraph, the attention is focused on air temperature and heat flow rate measurements.

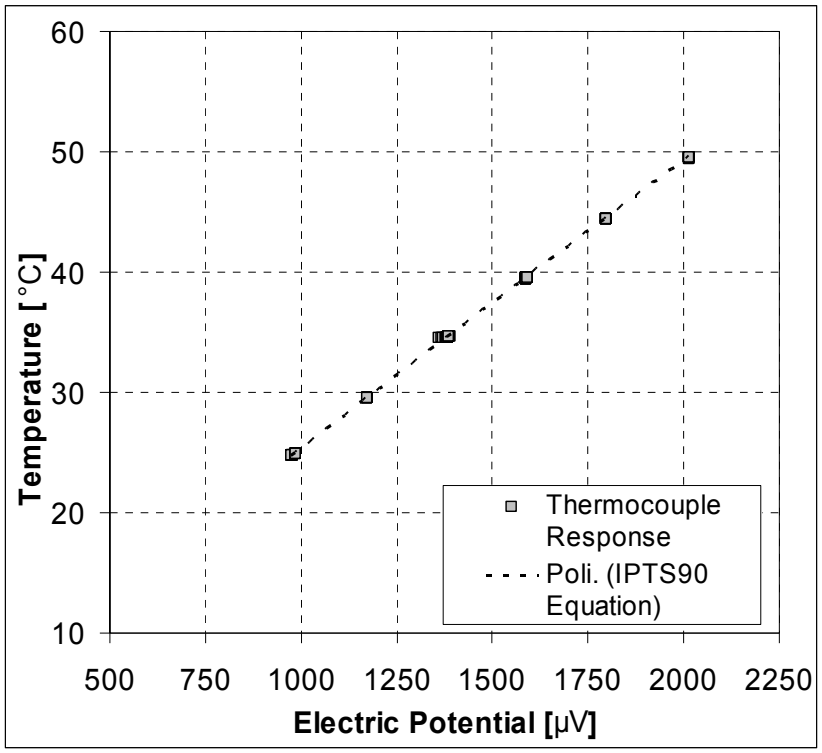

First of all, air temperature measurements were obtained by means of calibrated T-Type copper-constantan thermocouples.

These thermocouples, including all their measurement chains (ice point reference, digital voltmeter/switch multimeter) have been calibrated against a Pt100 thermistor with an accuracy of ±0.02 °C and different fitting curves have been developed. Furthermore, these fitting curves were in excellent agreement with IPTS90. Therefore, the IPTS90 curve was used in the calculations. The results of the calibration procedure permit to declare an uncertainty of temperature measures of ±0.05 °C.

Figure 114. An example of the calibration result. Comparison between the thermocouple readings and the Standard Equation IPTS90.

Figure 114 shows an example of the thermocouple calibration results; the calibration points obtained for each thermocouple have been compared with the standard equation IPTS90. All the calibrated temperature transducers which have been used in the test rig present a good agreement with the standard equation.

The measurement of the heat flow usually involves the measurement of the flow of a fluid and the determination of its entering and leaving enthalpy. The enthalpy depends on pressure and temperature.

For steady-state conditions, it is recommended that heat flow be measured by two independent methods [34]. This permits establishing the acceptability of the tests by obtaining a heat balance. In this new test facility the heat balance between the electric power and the air is constantly controlled.No heat balance will be perfect for one or more of the reasons listed below. In order to obtain a heat balance within a prescribed tolerance, some or all of the following causes of error will be considered.

- Losses or gains of heat from enclosures, pipes, wires, and connections. They shall be accounted for either a calibration or calculation procedure.
- Uniform velocity and temperature distribution at measuring location.
- The effect of thermal storage in such devices as duct walls, flow mixers, and straighteners during transient conditions. It must be made negligible or accounted for by calibration procedures, calculations procedures or measurements.
- Simplifications introduced as prescribed calculation procedures, such as the use of constant coefficients in equations and the use of typical or average values of physical properties of fluids.
- Unavoidable temperature or pressure fluctuations, with respect to time or space, of the fluid being measured.
- Small deviations in the accuracy, precision, and sensitivity of the test instruments.
- Effects of the action and interaction of:
    1. Performance oscillations of the instruments, especially of the self-balancing remote reading type.
    2. Performance oscillations of the apparatus for producing the test environment.
    3. Performance oscillations of the equipment being used.

From the foregoing it can be seen that some difficulties in obtaining acceptable heat balances cannot be overcome by merely specifying a high degree of instrument accuracy. As reported in ANSI/ASHRAE Standard 41.1-1986 [34], the determination of the average temperature of an airstream requires taking suitable precautions when dealing with the following:

- Non-uniformity of temperature across the airstream.
- Non-uniformity of air velocity.

- Thermal radiation to or from instrument sensing elements if exposed to the surrounding surfaces at temperatures different from that of the surrounding air.
- Heat conduction through stem or lead wires to or from an instrument sensing element if the stem or lead wires are exposed to temperatures different from that of the sensing element.
- Non-uniformity of the humidity ratio of the air when humidification or dehumidification is taking place.

Moreover, when temperature measurements are required in connection with the determination of heat flow rates, suitable precautions should be taken between the inlet and outlet measurement points for air, in order to acceptably minimize the effects of:

- Heat gains or losses when testing the apparatus ductwork, both steady-state and transient.
- Heat gains or losses due to air leakage from or into the test apparatus.
- The creation or suppression of recirculation or other abnormal airstream patterns caused by the presence of the test apparatus, which upset the normal thermal environment of the equipment being tested.
- Oscillations of temperature with time.
- Unsuitable instrument response time, resulting in unreliable readings, especially if air temperature oscillations have not been adequately damped.

Air discharged from coils or heat sinks may have non-uniform temperature distribution along with non-uniform velocity distribution, and one of the most difficult laboratory problems is to determine the true mean temperature. This can be accomplished in several ways [35]:

1. By measuring the temperature and the velocity at a large number of locations across the duct area. A weighted average temperature would then represent the true mean temperature, provided that sufficient observations are made.
2. By correcting any velocity non-uniformity and then determining the temperature at a large number of locations across the duct area. If the velocity is uniform, the average temperature should represent the true mean.

3. By mixing the air streams to the extent that any temperature non-uniformity is corrected. This is a very difficult thing to accomplish, but it would make it possible to measure the temperature at few points only and the result would be independent of any velocity non-uniformity which might exist.

The procedure suggested by Wile [35] is to combine methods (2) and (3) to the extent that (a) the air stream is reasonably well mixed and (b) the velocity pattern is made reasonably uniform.

In general, round or rectangular mixers, consisting of two sets of louvers producing a combination of shearing action and relative displacement on adjacent areas of the airflow, are most satisfactory [34].

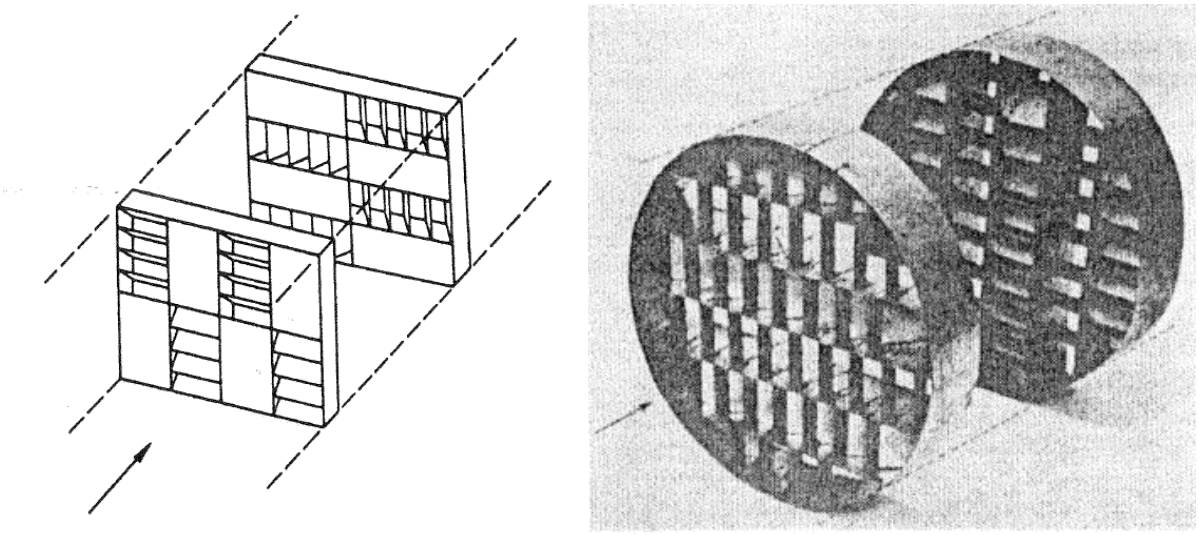

Figure 115. Examples of rectangular and circular mixing devices. [34].

Figure 115 illustrates two different mixing devices, for rectangular and circular ducts. Both consist of two mixers, one horizontal and one vertical. In 1947, Wile [35] suggested the use of two mixer assemblies, one for vertical mixing and the other for horizontal mixing.

Figure 116 shows the final form of the mixing devices located in the test section; temperature stems are highlighted in photos (B) and (D).

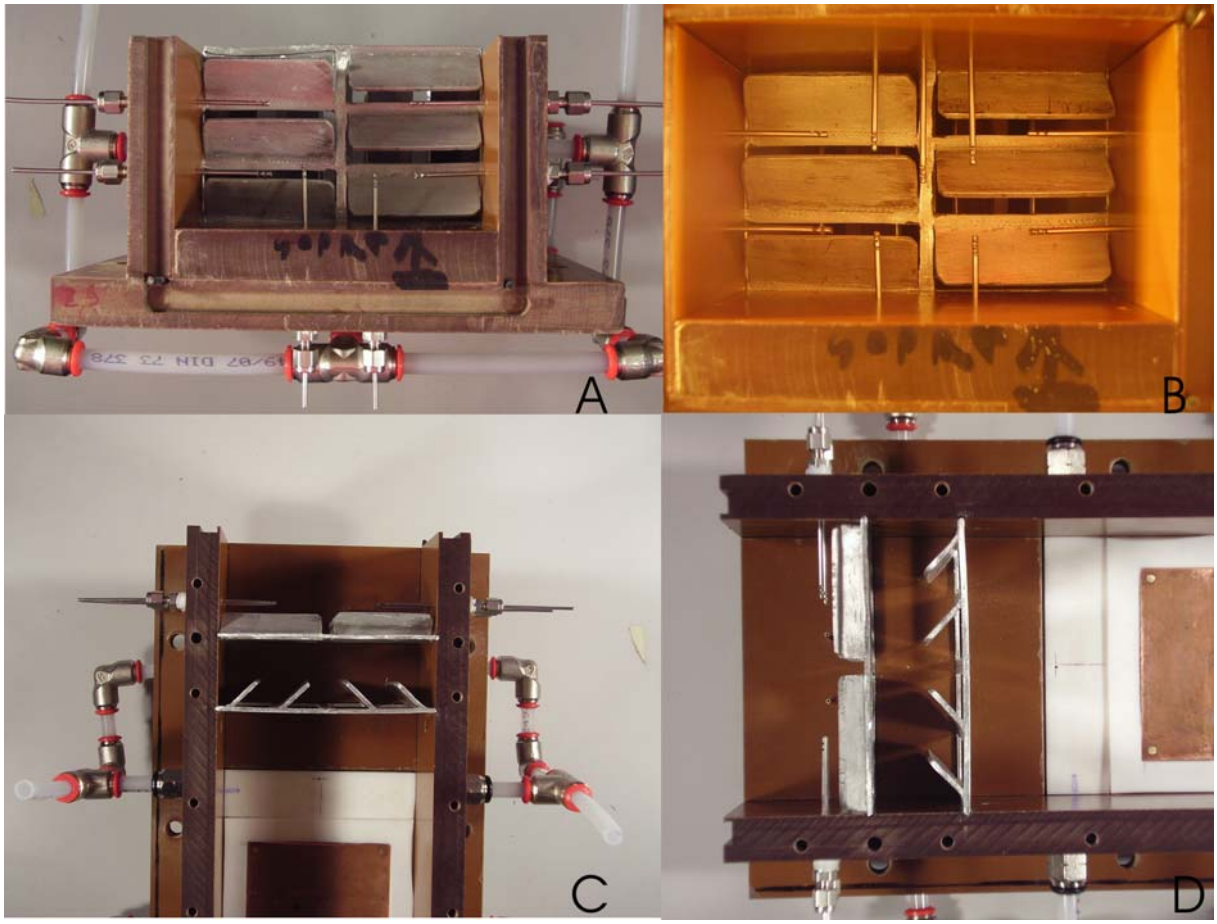

Figure 116. Photo of air mixer: (A) front view of the whole test section, (B) close-up of the horizontal mixer, (C) and (D) two top views of the mixer.

Figure 117 shows the executive drawing of the two mixers, designed as suggested by Wile [35] in order to deal with the non-uniformity of the temperature distribution of the air when it leaves the test sample.

The temperature probe is a 9 cm long 1/16" stainless steel tube in which a thermocouple is inserted. One end of the tube is closed by an epoxy droplet while the other is open to the ambient air.

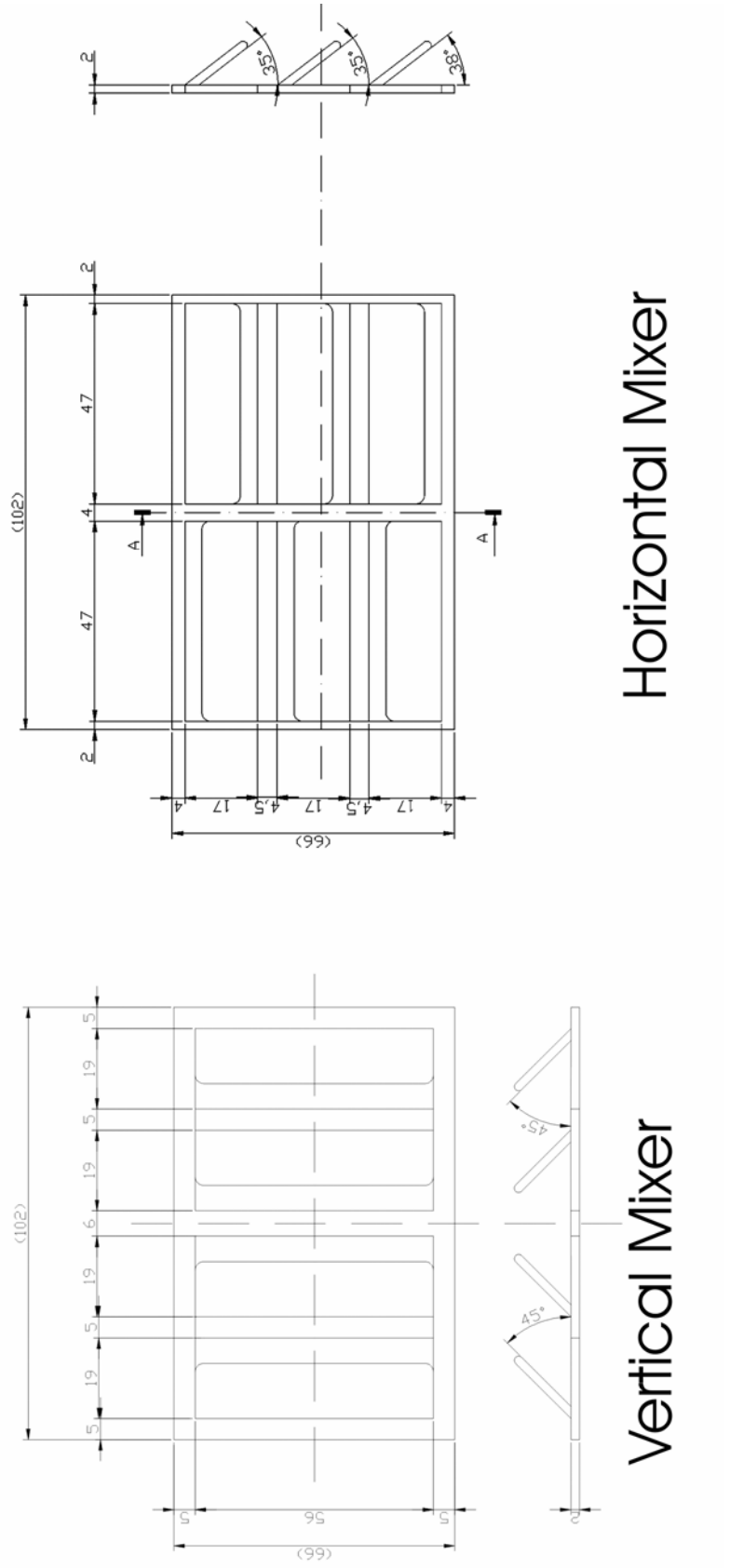

Figure 117. Drawing of the mixer devices.

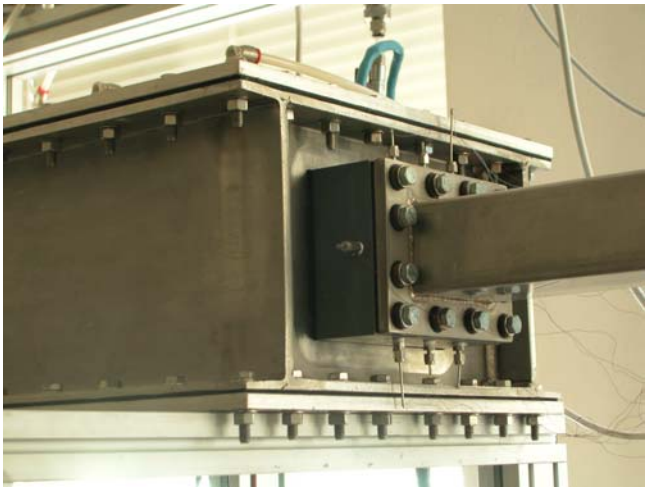

Figure 118. Close-up of the PVC block.

This device has been designed in order to improve thermocouple measurements, as it allows to insert the transducers in the fluid flow, shielding the sensor from thermal radiation but also allowing fluid-sensor contact.

As shown in photo (B) (close-up) of Figure 116, nine thermocouples were inserted at the exit of the sample, after the mixing devices, in order to measure the true mean air temperature. Nine thermocouples were also inserted at the inlet of the test section in order to measure the air stream temperature.

In the first experimental campaign, the inlet thermocouples were located inside the test section, while from the second experimental campaign onwards a PVC block was machined to hold the temperature probes transferring temperature measurements before the test section, as shown in Figure 118.

The air heat flow rate can be calculated as follows:

$$q_{air} = \dot{m}_{air}\left(h_{air,out} - h_{air,in}\right) = \dot{m}_{air} c_{s,air}\left(\overline{t}_{air,out} - \overline{t}_{air,in}\right) \qquad \textbf{Eq. 207}$$

Where $\dot{m}_{air}$ is the air mass flow rate, h_{air} is the specific air enthalpy, $c_{s,air}$ is the specific heat of humid air which is the sum of the $c_{p,air}$ and the term obtained by multiplying the humidity ratio x and the specific heat of the vapour $c_{p,v}$.

As described before, since after the compression the air is dehumidified and the humidity ratio does not change during the heat transfer process, the specific heat of humid air $c_{s,air}$, can be considered equal to that of dry air $c_{p,air}$.

Hence, the heat balance can be now expressed as:

$$P_{EL} = \dot{m}_{air} c_{p,air} \left(\overline{t}_{air,out} - \overline{t}_{air,in} \right) \qquad \textbf{Eq. 208}$$

It is important to perform a heat balance check in order to understand if any possible cause of systematic error has been successfully avoided.

2.2.4.2 Air Pressure Measurements

Experimental pressure drops are measured by means of a high accuracy differential pressure transducer which is connected to eight pressure taps, four upstream and four downstream of the test sample.

ASHRAE Standards 33-78 and 51-85 [33, 36] suggest measurement solutions to be implemented for pressure measurements. According to these standards [33, 36], four static pressure taps at the center of each of the four air duct sides are located both upstream and downstream to determine the air pressure drop of the test sample.

The four upstream static pressure taps are also connected to an absolute pressure transducer in order to measure the absolute pressure at the inlet of the test section. The standards also establishe the geometrical characteristics of the static pressure taps, which are displayed in Figure 119.

As suggested by the standards [36], a 1.5 mm (around 0.06 in) internal diameter was chosen for the static pressure taps. The surface around the pressure taps is free and smooth within a radius of 30 mm.

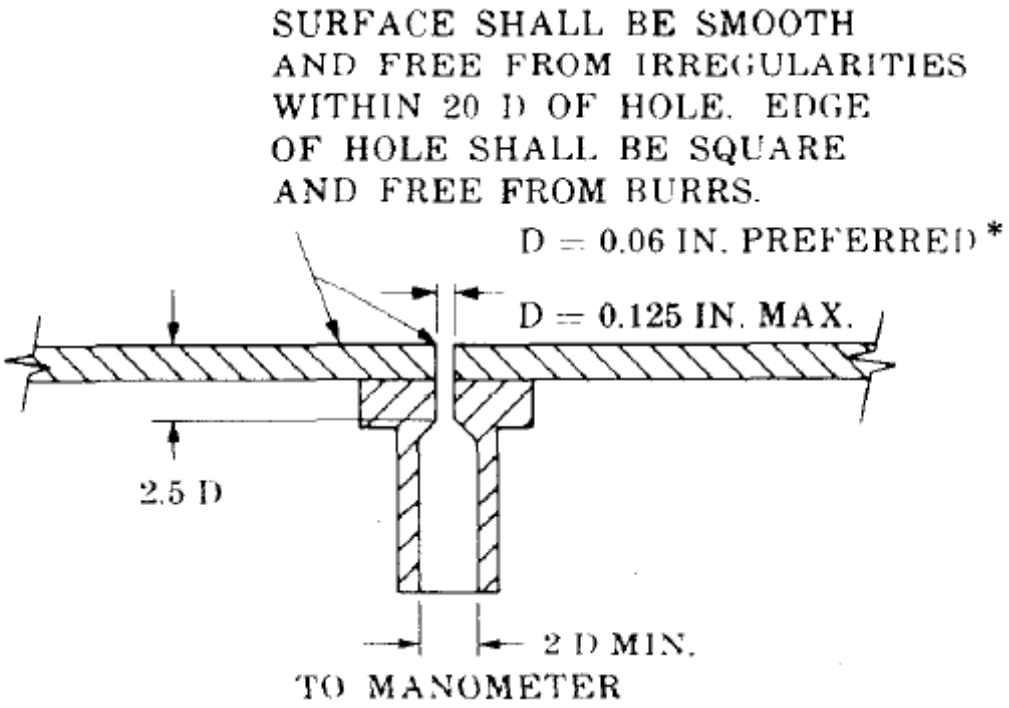

Figure 119. ASHRAE Standard 51-85 [36]: pressure tap drawing.

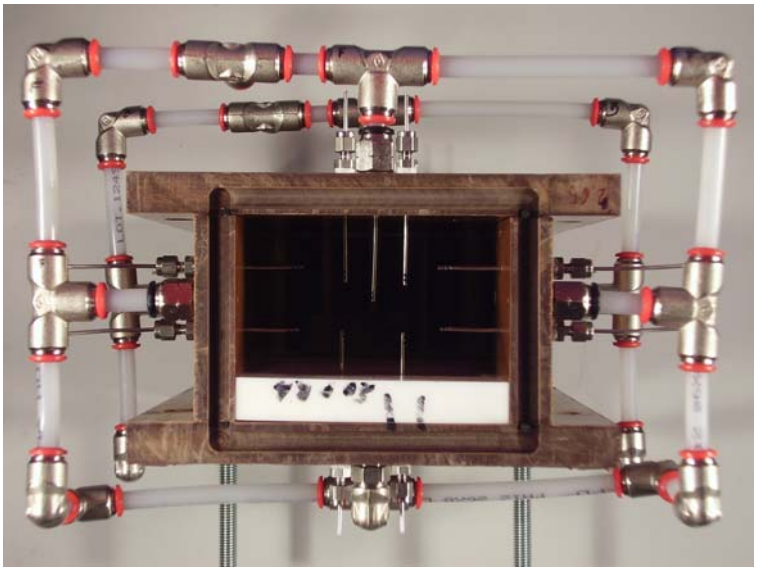

Figure 120. Frontal view of the bakelite channel: measuring pressure taps connected by pressure ducts.

Figure 120 shows the pressure ducts connecting the four static pressure taps to the pressure transducer. These connection ducts are made of Teflon.

Two absolute and two differential pressure transducers are implemented in the test rig to measure the absolute pressure of the air at the inlet of both the orifice flowmeter and the test section and air pressure drops across both the orifice plate and the test sample.

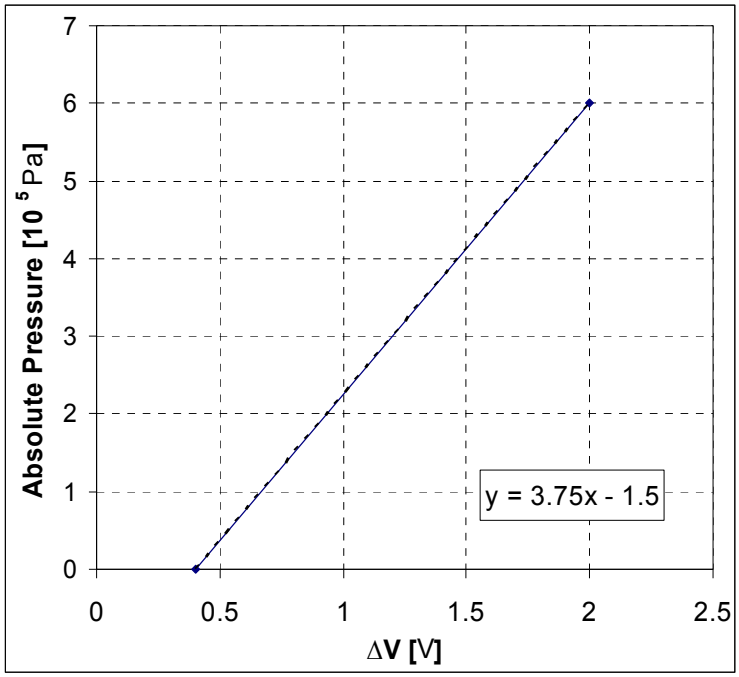

Figure 121. Absolute pressure plotted against the converted analogical output.

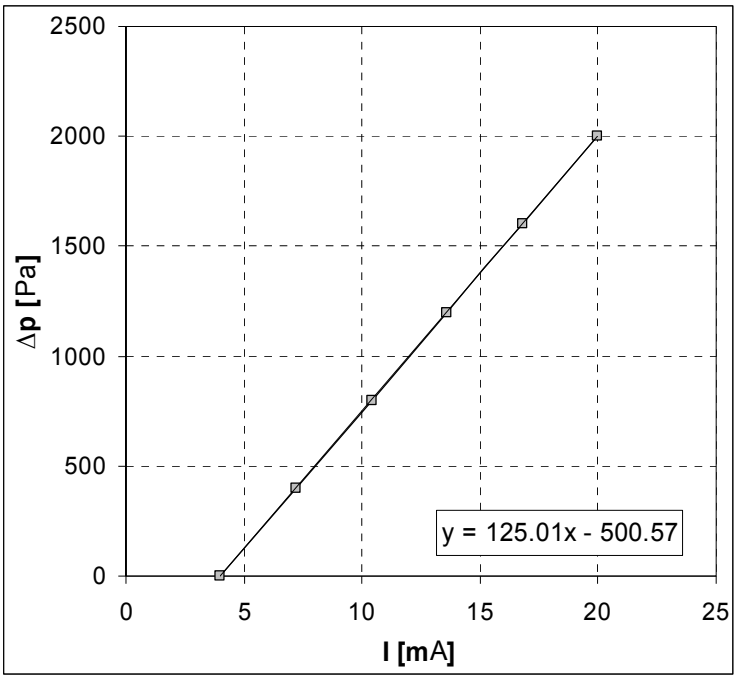

The absolute transducers, produced by Rosemount, have a 6 bar full scale with an accuracy of ±330 Pa (accuracy of ±0.055% of the full scale).

Figure 121 displays the calibration line of the calibrated transducers plotting absolute pressure against the converted analogical output. The 4-20 mA analogical output of this transducer was changed to 0.4-2 V by introducing a 100 Ω calibrated resistance.

The differential pressure transducer connected to the orifice flowmeter is an LPX 9381, a high accuracy instrument produced by Druck, with a full scale accuracy of ±2 Pa and 2000 Pa.

Figure 122. Differential pressure plotted against the analogical output for a LPX9381 Druck transducer.

Calibration line is plotted in Figure 122; calibration data are reported in the diagram.

Air pressure drops through the test sample are measured by means of a high accuracy differential pressure transducer selected with reference to the sample typology. If the specimen is a traditional finned surface, a Rosemount 500 Pa transducer with an accuracy of ±0.275 Pa is used.

In order to measure higher pressure drops a Druck transducer is implemented. This differential pressure instrument has an accuracy of ±1 Pa with a full scale of 1000 Pa.

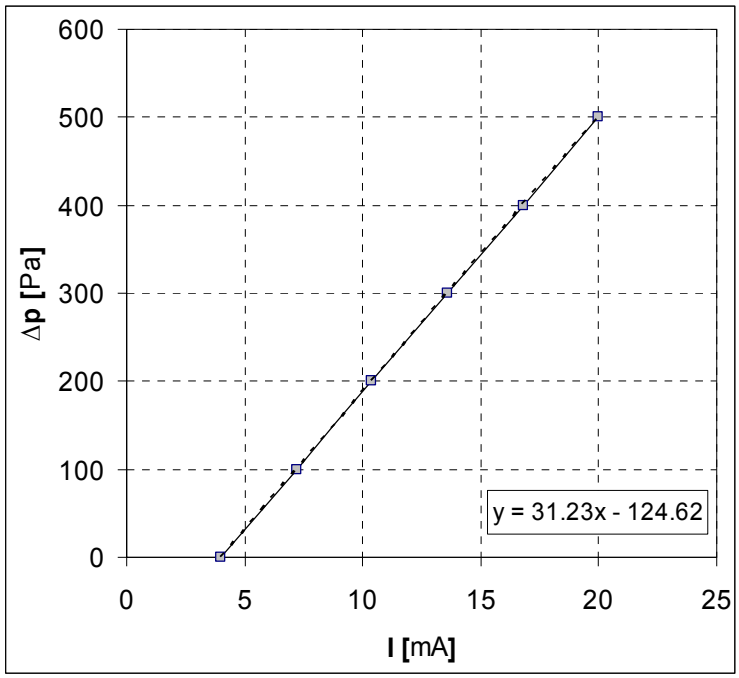

Figure 123. Differential pressure plotted against the analogical output of the Rousemount transducer.

Figure 123 reports the calibration data for a Rosemount differential pressure transducer, the default instrument installed in the test rig. If pressure drops exceed the full scale, this transducer is replaced by a Druck transducer, able to measure up to 1000 Pa of differential pressure.

Figure 124 and Figure 125 report two calibration certificates which refer to the Druck LPX9381 and Rosemount 3051S differential pressure transducers.

GE Druck

CALIBRATION CERTIFICATE
PRESSURE

UNIT UNDER TEST (UUT)

Manufacturer	: Druck
Type	: LPX 9381
Serial Number	: 2401162
Order No.	: Z10781.1.1
Pressure range	: 0 to 20 mbar d
Supply	: 10 to 30 Vdc
Output	: 4 to 20 mA
Calibration date	: 18/10/2006

CALIBRATOR INFORMATION (*1)

Manufacturer	: Pressurements
Model	: V1600/1
Serial number	: 3070111
Calibrated against	: UKAS Lab 0221
Manufacturer	: HP
Model	: 34401A
Serial number	: MY41019422
Calibrated against	: UKAS Lab 0221

SPECIFICATION (*2)

Non-linearity	: 0.100 %FS BSL
Temperature drift (-20 to 80 °C)	
Zero	: 0.01 %FS/°C
Span	: 0.01 %FS/°C

CALIBRATION DATA (0°C)

Applied Pressure mbar	Output mA	Deviation %FS BSL	Specification %FS BSL
0.0	4.001	-0.020	0.100
4.0	7.206	0.012	0.100
8.0	10.406	0.014	0.100
12.0	13.604	0.003	0.100
16.0	16.804	0.004	0.100
20.0	20.001	-0.013	0.100

COMMENTS

Certified by: Date: 18 OCT 2006

NOTES

(*1) Traceable to relevant International Standards (including NIST).
(*2) Consult data sheet for additional specifications.

Druck Ltd, Fir Tree Lane, Groby, Leicester LE6 0FH. Tel: (0116) 231 7100, Fax: (0116) 231 7101,Telex: 34173 Druck G
PS562 V2.00.01

Figure 124. Calibration certificate of a Druck LPX9381 differential pressure transducer.

EMERSON
Process Management

Q4

Emerson Process Management
GmbH & Co. OHG Weßling
Argelsrieder Feld 3
D-82234 Weßling, Germany
Tel. +49 (8153) 939-0

CALIBRATION TESTPROTOCOL Consistent with ISO 10474 - 3.1 / EN10204:2004 - 3.1
Prüfprotokoll konform mit ISO 10474 - 3.1 / EN10204:2004 - 3.1

Customer / Kunde

BIAGINI IMPIANTI Sas
di Ing. Marco Biagini
Via Pana' 56/B
35027
Noventa Padovana
ITALY

Manufacturer Information / Herstellerinformation

Order Number Auftrags Nummer:	**39072110**
Order Line / Unit Auftrags Line / Gerät:	**1 / 1**
Cust. ID Kund. ID	**N/A**
Order No. Best. Nummer:	**2007-335-01**

Device Information / Geräteinformation

Serial No / Seriennummer	**8449832**
Module SN: / Modul SN:	**3436195**
Output Mode / Ausgang	**Linear**
Model No / Modellnummer	**3051S2CD0A2F12A1BL4M5Q4**

Test Information / Prüfinformation

Factory Firma	**Emerson Process Management Weßling**
Station ID Stationsname	**IDM19**
Operator ID Mitarbeiter Nr.	**8004**
Test Date Prüfdatum	**15. Nov. 2007**

Equipment used / Verwendetes Equipment

Calibration Point (DP)

EqNumber	EqName
IDMB19	Multimeter
IDMD19	Loadbox
IDMG08	Pressure Controller

Calibration Data / Kalibrierdaten

Range: 0,00 to 500,00 PA

% of Range	Applied Pressure	Requested Pressure	Output (Analog)	% Span Error	Pass/Fail
100,00	5,00 MBAR	500,0000 PA	19,9986 (mA)	-0,0087	PASS
80,00	4,00 MBAR	400,0000 PA	16,7964 (mA)	-0,0225	PASS
60,00	3,00 MBAR	300,0000 PA	13,5968 (mA)	-0,0200	PASS
40,00	2,00 MBAR	200,0000 PA	10,3934 (mA)	-0,0412	PASS
20,00	1,00 MBAR	100,0000 PA	7,1854 (mA)	-0,0912	PASS
0,00	0,00 MBAR	0,0000 PA	3,9940 (mA)	-0,0375	PASS

This is to certify that the listed product meets the applicable Rosemount Specifications. Measuring and test equipment used in the manufacture and inspection of the listed product are traceable to the National Institute of Standards and Technology. The calibration System was designed to meet the intent of ANSI Z540-1-1994.

Hiermit bestätigen wir, dass vorgenannte Geräte / Systeme die Rosemount Spezifikationen erfüllen. Alle bei der Fertigung und Prüfung eingesetzten Meß- und Prüfmittel sind auf nationale Standards rückführbar. Das System wurde ausgelegt die Anforderungen nach ANSI Z540-1-1994 zu erfüllen.

Eva Kuntze (Worksinspector)

Figure 125. Calibration Certificate of a Rousemount 3051S differential pressure transducer.

2.2.5 Data Reduction

A simple scheme of data reduction is given in this paragraph. Since each test sample has got a specific test section configuration, it is not possible to generalize the post-processing data procedure. On the other hand, it is important to illustrate how the different parameters or results, such as non-dimensional numbers, the heat transfer coefficient and the friction factor, are defined.

Nevertheless, differently than in the previous chapter with two-phase flow, here the experimental uncertainty evaluation scheme is presented with the data reduction procedure. Hence, calculation results depend on the different test specimen; they will be reported in dedicated paragraphs.

As experimental uncertainty evaluation theory has been presented in paragraph 1.3.2.1, here it's not described again and only operating formulas are reported. The heat transfer and the pressure drop data reduction will be presented separately.

2.2.5.1 Heat Transfer

First of all, the heat balance between the electric power and the air-side heat flow rate must be verified:

$$P_{EL} = \dot{m}_{air} c_{p,air} \left(\overline{t}_{air,out} - \overline{t}_{air,in} \right) \qquad \textbf{Eq. 209}$$

where P_{EL} is the supplied electric power, $\dot{m}_{air}$ is the air mass flow rate, $c_{p,air}$ is the air specific heat at constant pressure and the last term is the air temperature difference between the inlet and outlet of the test section.

The mean air temperatures at the inlet and outlet of the test section are defined as:

$$\overline{t}_{air,in} = \frac{t_{1,in} + \ldots + t_{9,in}}{9} \qquad \textbf{Eq. 210}$$

$$\overline{t}_{air,out} = \frac{t_{1,out} + \ldots + t_{9,out}}{9} \qquad \textbf{Eq. 211}$$

The difference between the two terms of Eq. 209 must be always maintained within ±5.0%.

The product of the heat transfer coefficient *HTC* and the surface area efficiency Ω* is defined as:

$$HTC \cdot \Omega^* = \frac{P_{EL}}{A_{base} \cdot \Delta t_{ml}} \qquad \textbf{Eq. 212}$$

Where the reference surface, A_{base}, is the base area of the test sample and Δt_{ml} is the mean logarithmic temperature difference between the wall temperature and the air:

$$\Delta t_{ml} = \frac{\left(t_{w,in} - t_{air,in}\right) - \left(t_{w,out} - t_{air,out}\right)}{\ln\left[\frac{\left(t_{w,in} - t_{air,in}\right)}{\left(t_{w,out} - t_{air,out}\right)}\right]} \qquad \textbf{Eq. 213}$$

with $t_{w,in}$ and $t_{w,out}$ indicating the heated wall temperatures at the inlet and at the outlet of the base plate respectively. If the surface area efficiency is known or computable, it is possible to calculate the heat transfer coefficient value.
The heat transfer coefficient can be referred also to the total heat transfer area $A_{tot,}$ with the following equation:

$$\left(HTC \cdot \Omega^*\right)_{tot} = \frac{P_{EL}}{A_{tot} \cdot \Delta t_{ml}} \qquad \textbf{Eq. 214}$$

Since air temperature at the inlet of the test section is not controlled, it varies for the different tests within a limited range (21°C – 26°C), and in order to compare the different enhanced surfaces the mean wall temperatures for different air mass flow rates are calculated as follows. In the hypothesis that the product of heat transfer coefficient times the finned surface efficiency is constant along the sample and does not vary with air temperature (as air properties are almost constant), with reference to the mean air temperature across the sample $\overline{t}_{air}$ it is possible to calculate a normalized mean wall temperature $\overline{t}_w$:

$$\overline{t}_w = \overline{t}_{air} + \frac{P_{EL}}{HTC \cdot \Omega^* \cdot A_{base}} \qquad \textbf{Eq. 215}$$

Here this temperature is not intended as a design parameter, but it permits to compare different enhanced surfaces under the same inlet test conditions. Thus, the enhanced surface with the lowest mean wall temperature is the one with better performance.

Considering the experimental uncertainty evaluation, first of all it is important to point out that, since the experimental data points are punctual measures, the repeatability component of the uncertainty is not present.

The uncertainties of the transducers, including the related complete measuring chains used in the test rig, are summarized in Table 44.

Table 44. Uncertainties of the instruments and measurements implemented in the experimental set-up.

Transducer	***Uncertainty***
T-Type Thermocouple	± 0.05 °C
Absolute Pressure Transducer (end of scale 0.6 MPa)	± 0.055 FS%
Differential Pressure Transducer (Orifice, end of scale 2000 Pa)	± 0.1 FS%
Electric Power	± 0.13% of the reading
Air Flow Rate	± 0.8% of the reading

Starting with the air heat flow rate, as described before it is defined by the following equation:

$$q_{air} = \dot{m}_{air} c_{p,air} \left(\overline{t}_{air,out} - \overline{t}_{air,in} \right) \qquad \textbf{Eq. 216}$$

Deriving the equation, the sensitivity terms are:

$$\frac{\partial q_{air}}{\partial \dot{m}_{air}} = c_{p,air} \left(\overline{t}_{air,out} - \overline{t}_{air,in} \right) = \frac{q_{air}}{\dot{m}_{air}} \qquad \textbf{Eq. 217}$$

$$\frac{\partial q_{air}}{\partial c_{p,air}} = \dot{m}_{air} \left(\overline{t}_{air,out} - \overline{t}_{air,in} \right) = \frac{q_{air}}{c_{p,air}} \qquad \textbf{Eq. 218}$$

$$\frac{\partial q_{air}}{\partial \Delta t_{air}} = \dot{m}_{air} c_{p,air} = \frac{q_{air}}{\Delta t_{air}}$$ **Eq. 219**

From error analysis, the uncertainty of the mean air temperature is equal to 0.05 °C, while the uncertainty of the air temperature difference is equal to √2 times that of the experimental temperature measure. A "sequential perturbation" method was applied by using the REFPROP code to estimate the specific heat uncertainty. Considering a temperature measurement accuracy of ±0.05 °C and a pressure measurement accuracy of ±0.33 kPa, the estimated accuracy of the specific heat of the air was always lower than 1%, on the other hand a conservative value of 1% was taken for the calculations.
Finally, the experimental uncertainty of the air heat flow rate can be estimated with the following equation:

$$i_q = \sqrt{\left(\frac{\partial q_{air}}{\partial \dot{m}_{air}} \cdot i_{\dot{m}_{air}}\right)^2 + \left(\frac{\partial q_{air}}{\partial c_{p,air}} \cdot i_{c_{p,air}}\right)^2 + \left(\frac{\partial q_{air}}{\partial \Delta t_{air}} \cdot i_{\Delta t}\right)^2}$$ **Eq. 220**

The second term is the heat transfer coefficient defined by Eq. 212; its sensitivity coefficients are:

$$\frac{\partial\left(HTC \cdot \Omega^*\right)}{\partial P_{EL}} = \frac{1}{A_{base} \cdot \Delta t_{ml}} = \frac{HTC \cdot \Omega^*}{P_{EL}}$$ **Eq. 221**

$$\frac{\partial\left(HTC \cdot \Omega^*\right)}{\partial \Delta t_{ml}} = -\frac{P_{EL}}{A_{base} \cdot \Delta t_{ml}^2} = -\frac{HTC \cdot \Omega^*}{\Delta t_{ml}}$$ **Eq. 222**

Finally, the heat transfer coefficient uncertainty is given by:

$$i_{HTC} = \sqrt{\left(\frac{\partial\left(HTC \cdot \Omega^*\right)}{\partial \Delta t_{ml}} \cdot i_{\Delta t_{ml}}\right)^2 + \left(\frac{\partial\left(HTC \cdot \Omega^*\right)}{\partial P_{EL}} \cdot i_{P_{EL}}\right)^2}$$ **Eq. 223**

While the experimental uncertainty of the electric power is known and reported in Table 44, the uncertainty of the mean logarithmic temperature difference has to be evaluated as follows:

$$\Delta t_{ml} = \frac{\left(t_{w,in} - t_{air,in}\right) - \left(t_{w,out} - t_{air,out}\right)}{\ln\left[\frac{\left(t_{w,in} - t_{air,in}\right)}{\left(t_{w,out} - t_{air,out}\right)}\right]} = \frac{\Delta_1 - \Delta_2}{\ln\left(\frac{\Delta_1}{\Delta_2}\right)} \qquad \textbf{Eq. 224}$$

Where:

$$\Delta_1 = t_{w,in} - t_{air,in} \qquad \textbf{Eq. 225}$$

$$\Delta_2 = t_{w,out} - t_{air,out} \qquad \textbf{Eq. 226}$$

These two temperature differences present an uncertainty equal to √2 times that of the experimental temperature measure.
The sensitivity coefficients are:

$$\frac{\partial \Delta t_{ml}}{\partial \Delta_1} = \frac{2 \cdot \left(\Delta_2 - \Delta_1\right) \cdot \frac{1}{\Delta_2 \cdot \Delta_1} - \ln\left(\frac{\Delta_2}{\Delta_1}\right)}{\left(\ln\frac{\Delta_2}{\Delta_1}\right)^2} \qquad \textbf{Eq. 227}$$

$$\frac{\partial \Delta t_{ml}}{\partial \Delta_2} = \frac{-\left(\Delta_2 - \Delta_1\right) \cdot \frac{1}{\Delta_2} + \ln\left(\frac{\Delta_2}{\Delta_1}\right)}{\left(\ln\frac{\Delta_2}{\Delta_1}\right)^2} \qquad \textbf{Eq. 228}$$

Finally, the uncertainty of the mean logarithmic temperature difference is given by:

$$i_{\Delta t_{ml}} = \sqrt{\left(\frac{\partial \Delta t_{ml}}{\partial \Delta_1} \cdot i_{\Delta_1}\right)^2 + \left(\frac{\partial \Delta t_{ml}}{\partial \Delta_2} \cdot i_{\Delta_2}\right)^2} \qquad \textbf{Eq. 229}$$

2.2.5.2 Pressure Drops

Pressure drops are reported in terms of the pressure gradients, their uncertainty directly depends on the accuracy of the differential pressure transducer used for the measurements.

Table 45. Accuracy of the differential pressure transducers used for pressure drop measurements.

Instrument	***Accuracy***
Differential Pressure Transducer, Rosemount (Test Section, end of scale 500 Pa)	± 0.055 FS%
Differential Pressure Transducer, Druck (Test Section, end of scale 1000 Pa)	± 0.25 FS%

During the experimental campaign, the instruments listed in Table 45 were used in order to measure single-phase air pressure drops through the different test samples. The relative values listed in Table 45 are equal to ±0.275 Pa and ±2.5 Pa for the Rosemount transducer and for the Druck transducer, respectively.

Since different test samples present different pressure drop parameters, such as the friction factor, permeability, the inertia coefficient, etc., the experimental uncertainty of those values will be discussed in dedicated paragraphs.

2.3 Traditional Finned Surface Characterization

2.3.1 Introduction

In the following paragraphs, the experimental results of the study and characterization of a traditional finned surface for electronic cooling applications during single-phase air heat transfer will be presented. This work aims at experimentally validating the new test facility and at characterizing a traditional heat transfer surface which has been taken as a reference for successive comparisons.

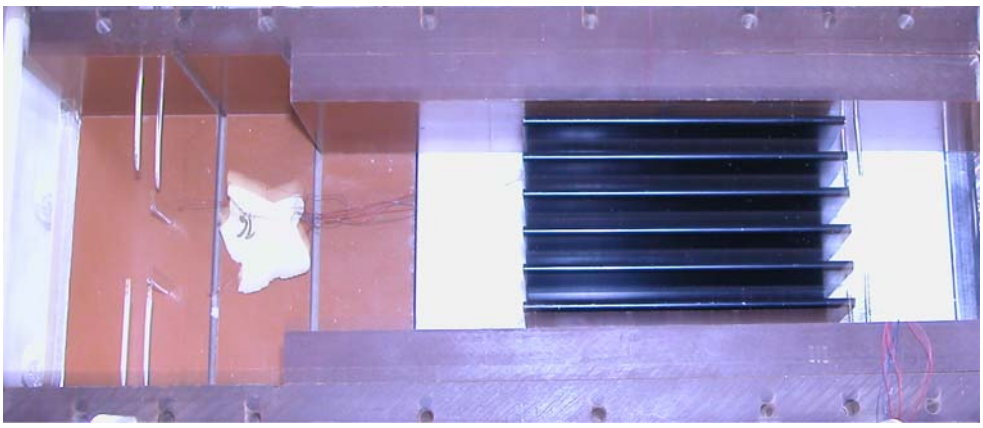

Figure 126. Close-up of the traditional finned surface located in the bakelite channel.

Figure 126 illustrates the test section arrangement for the thermo-fluid-dynamic characterization of the traditional finned surface.

This enhanced surface, measuring 100 x 70 x 60 mm, is obtained by extrusion of aluminum. It consists of six 48 mm high trapezoidal fins arranged over a 12 mm thick base. The most important geometrical characteristics of this heat transfer surface are listed in Table 46.

Table 46. Most important geometrical characteristics of the finned surface.

Traditional Aluminum Finned Surface	
Length of the Test Sample	100 mm
Height of the Sample	60 mm
Width of the Sample	70 mm
Number of Fins	6
Tip Fin Thickness	3 mm
Base Fin Thickness	5 mm
Fin Pitch	12 mm
Hydraulic Diameter*	14.27 mm
Thermal Conductivity	175±5 $Wm^{-1}K^{-1}$

*Hydraulic Diameter is defined as: $4 \cdot A_{eff} / P_{wet}$

The thermal conductivity of the aluminum alloy of the finned surface has been experimentally measured by Prof. Bonacina and Prof. Moro of the "Dip. di Fisica Tecnica" of the University of Padova by using a "Hot Disk" apparatus (for more information see: www.hotdisk.se).
As described in Figure 127, six holes were drilled into the base of the specimen in order to locate six calibrated T-Type thermocouples for measuring the wall temperature distribution during single-phase air heat transfer.

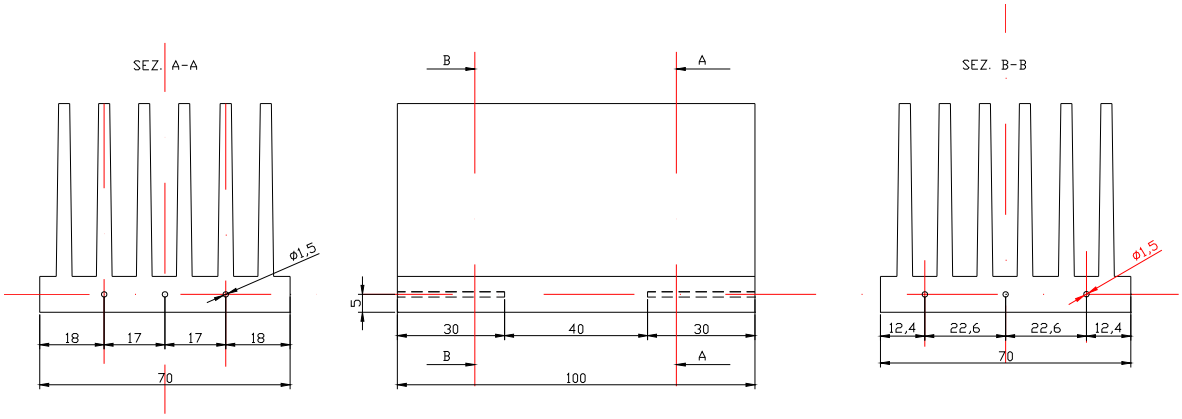

Figure 127. Drawings of the location of the six holes drilled in the specimen.

A suitable copper heater was designed to evenly heat the base of the sample. As described before, a guide was milled into a 7 mm thick copper plate, in which a calibrated wire resistance was inserted.

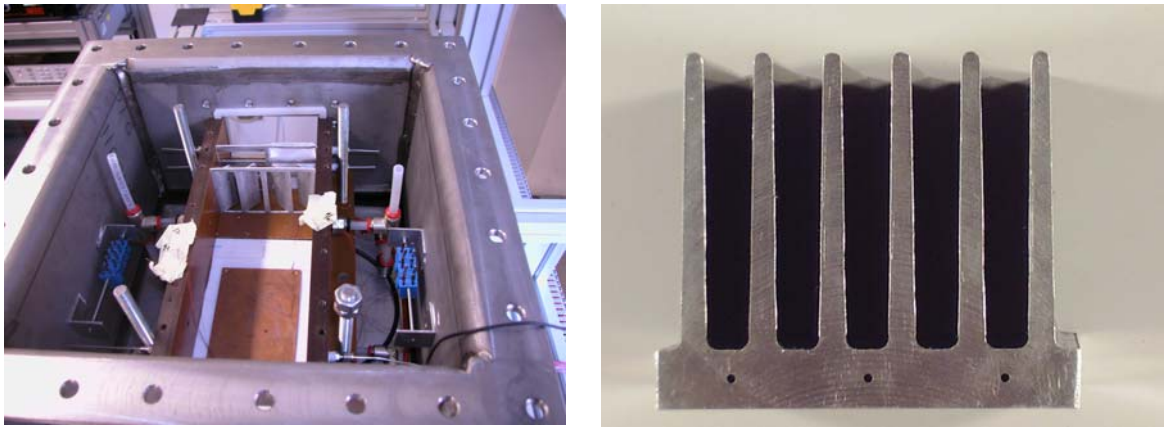

Figure 128. A photo of the test section arrangement (left) and a photo of the finned surface (right).

The test section arrangement for the finned surface campaign is shown on the left hand side of Figure 128; in this photo, the most important components are highlighted: the copper heater, the mixer and the machined Teflon plate. The photo on the right hand side of Figure 128, a close-up of the traditional finned surface, shows three of the six holes.

2.3.2 Experimental Uncertainty

The theory of experimental uncertainty, which is deeply analysed in paragraph 2.2.5, has been analytically applied to this case in order to give a general overview.

Now, the numerical results of the uncertainty of the experimental measurements are reported. In particular, the uncertainty of the air flow rate, of the heat transfer coefficients and of the pressure drops, in this order, will be pointed out.

2.3.2.1 Air Heat Flow Rate

As previously described, the air heat flow rate can be written as:

$$q_{air} = \dot{m}_{air} c_{p,air} \left(\overline{t}_{air,out} - \overline{t}_{air,in} \right) \qquad \textbf{Eq. 230}$$

As it appears from Eq. 230, the uncertainty of the air heat flow rate depends on the air mass flow rate and on the air temperature gain.

Table 47 reports the maximum and average experimental uncertainties of the air heat flow rate; these values are always lower than 2% and it appears that the maximum value depends on the air temperature gain uncertainty.

Table 47. Air heat flow rate experimental uncertainty.

	q_{air}	Δt_{air}	$\dot{m}_{air}$
i_m **[%]**	1.48	0.88	0.8
i_{max} **[%]**	1.68	1.20	0.8

At constant imposed heat flux, as the air mass flow rate increases, its temperature gain decreases, hence the value of the uncertainty of the heat flow rate increases as well. This is explained in Figure 129 and Figure 130, in which the uncertainty of the air heat flow rate is plotted against the air mass flow rate and the air temperature gain, respectively.

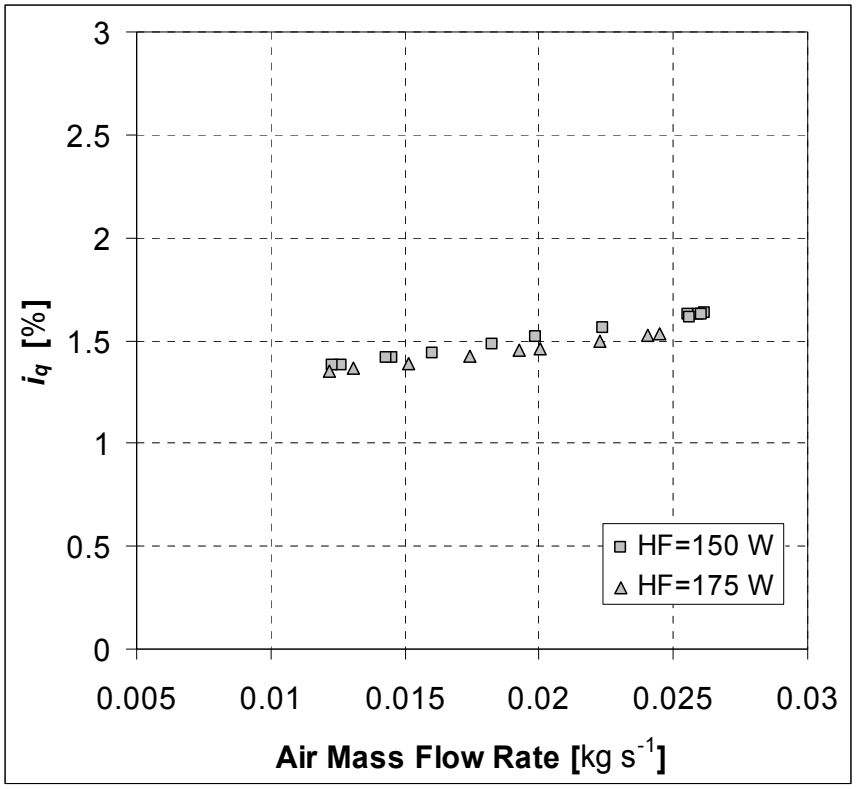

Figure 129. Uncertainty of the air heat flow rate plotted against the air flow rate. HF: Heat Flux [kW m^{-2}]

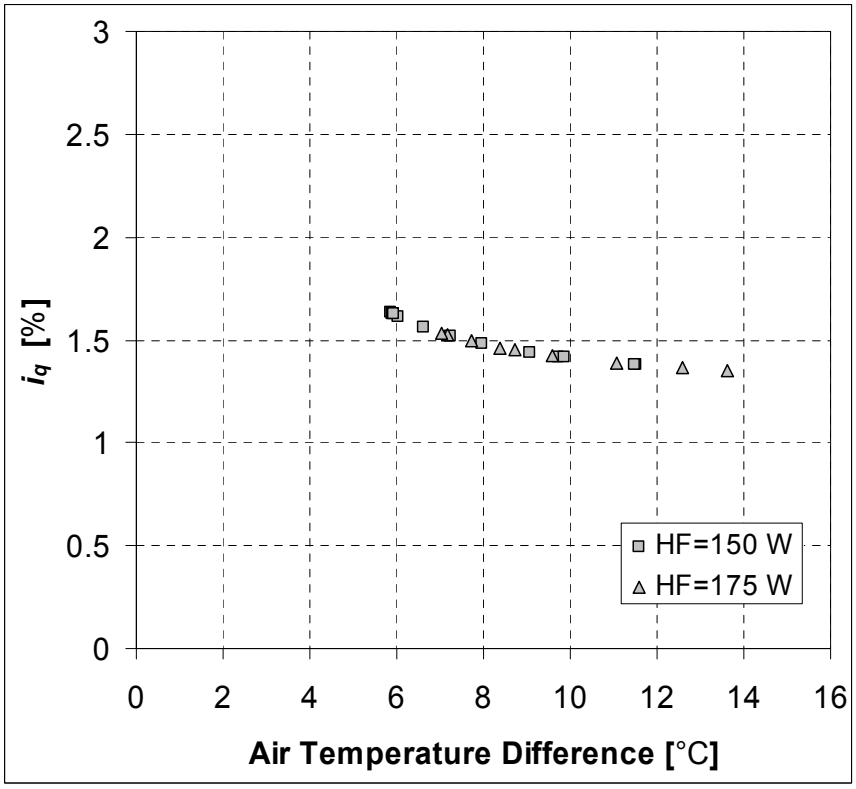

Figure 130. Uncertainty of the air heat flow rate plotted against the air temperature gain. HF: Heat Flux [kW m^{-2}].

2.3.2.2 Heat Transfer Coefficient

The uncertainty of the heat transfer coefficient depends on electric power measurements and on the mean logarithmic temperature difference, as described by Eq. 231:

$$\left(HTC \cdot \Omega^{*}\right)_{tot} = \frac{P_{EL}}{A_{tot} \cdot \Delta t_{ml}} \qquad \textbf{Eq. 231}$$

As it appears from the data reported in Table 48, the relative uncertainties of the mean logarithmic temperature difference and of the electric power are very low. The maximum value of the experimental uncertainty of the heat transfer coefficient is 0.72 W m^{-2} K^{-1}, while the average value is equal to 0.61 W m^{-2} K^{-1}.

Table 48. Heat transfer coefficient experimental uncertainty.

	HTC Ω*	Δt_{ml}	P_{EL}
i_m **[%]**	1.01	0.11	0.08
i_{max} **[%]**	1.028	0.15	0.08

In Figure 131 and Figure 132, the uncertainty of the heat transfer coefficient is plotted against the air mass flow rate and the mean logarithmic temperature difference respectively.
The heat transfer coefficient uncertainty is constant all over the range of operating test conditions.

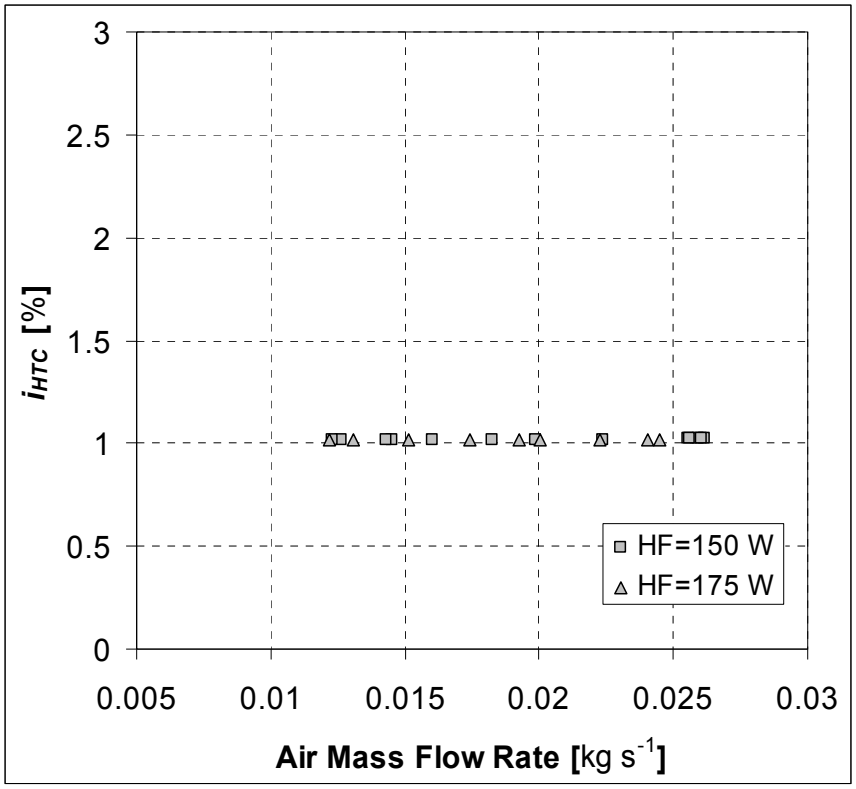

Figure 131. Uncertainty of the air heat transfer coefficient plotted against the air mass flow rate. HF: Heat Flux [kW m^{-2}].

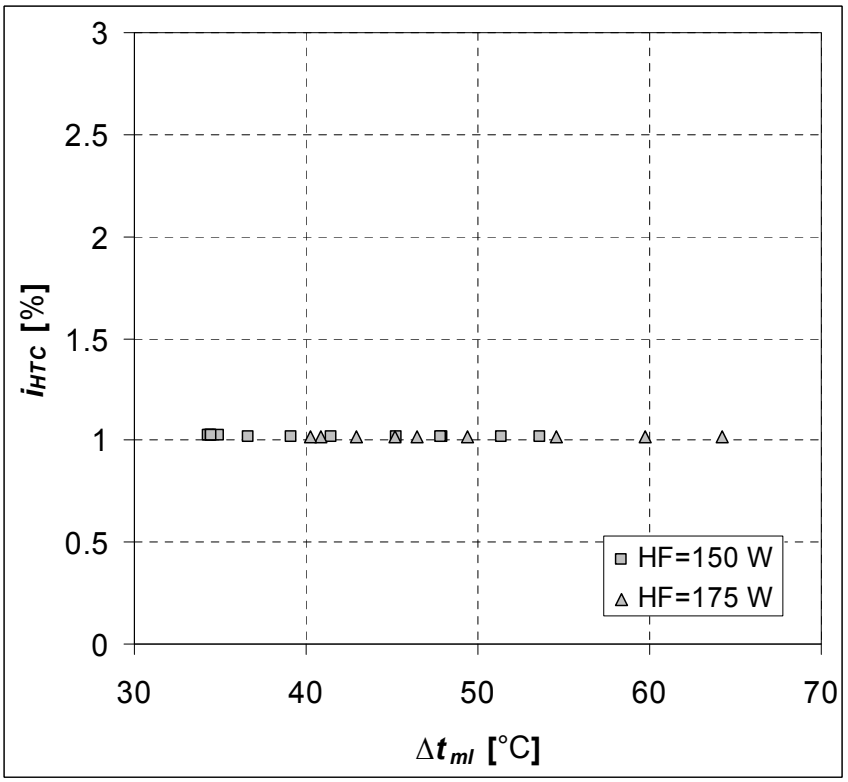

Figure 132. Uncertainty of the air heat transfer coefficient plotted against the air mean logarithmic temperature difference. HF: Heat Flux [kW m^{-2}].

2.3.2.3 Pressure Drops

Experimental pressure drops were measured at three different pressure value, namely, 0.101, 0.140 and 0.195 MPa, at the sample inlet. Measurements were carried out using a high accuracy differential pressure transducer with a full scale of 500 Pa and an overall uncertainty of ±0.275 Pa.

The uncertainty of pressure drop measurements is plotted against its experimental value in Figure 133. Since the absolute value of the uncertainty is constant, the relative value increases as the pressure drop decreases.

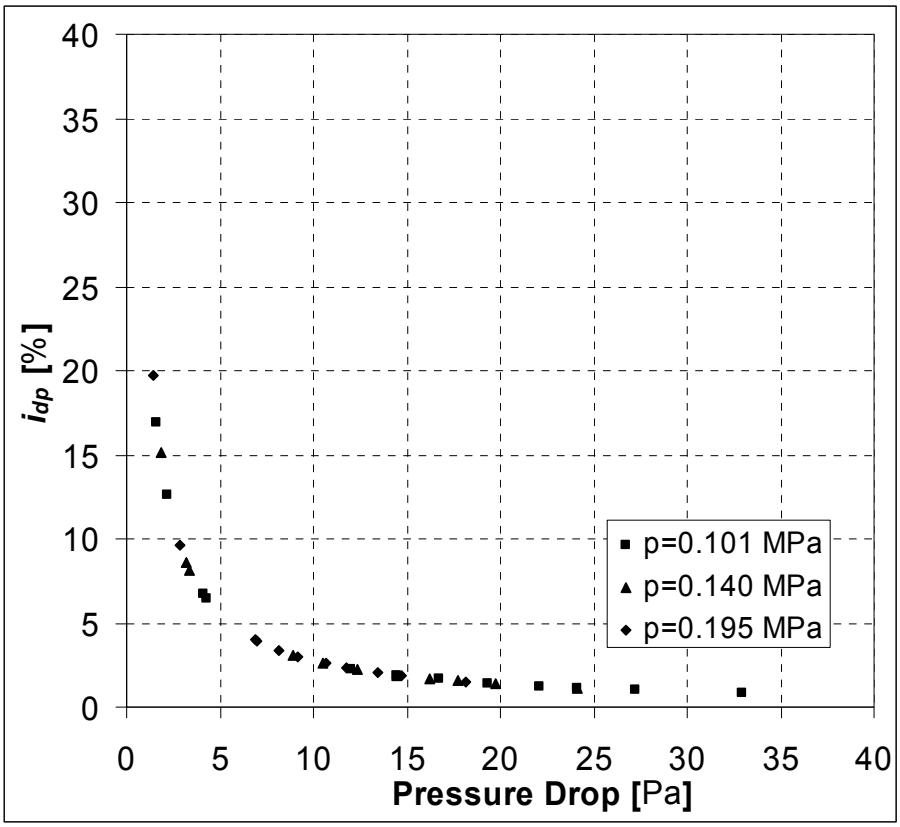

Figure 133. Uncertainty of the experimental pressure drop measurements plotted against their value as a function of the operating pressure.

Figure 134 shows the relative uncertainty of the experimental pressure drop measurement plotted against the air mass flow rate as a function of the operating pressure. The relative uncertainty increases as the mass flow rate decreases, and at 0.195 MPa it presents higher values than those exhibited at lower pressures.

Only measured pressure drops with an experimental uncertainty lower than 20% have been considered in the following analysis.

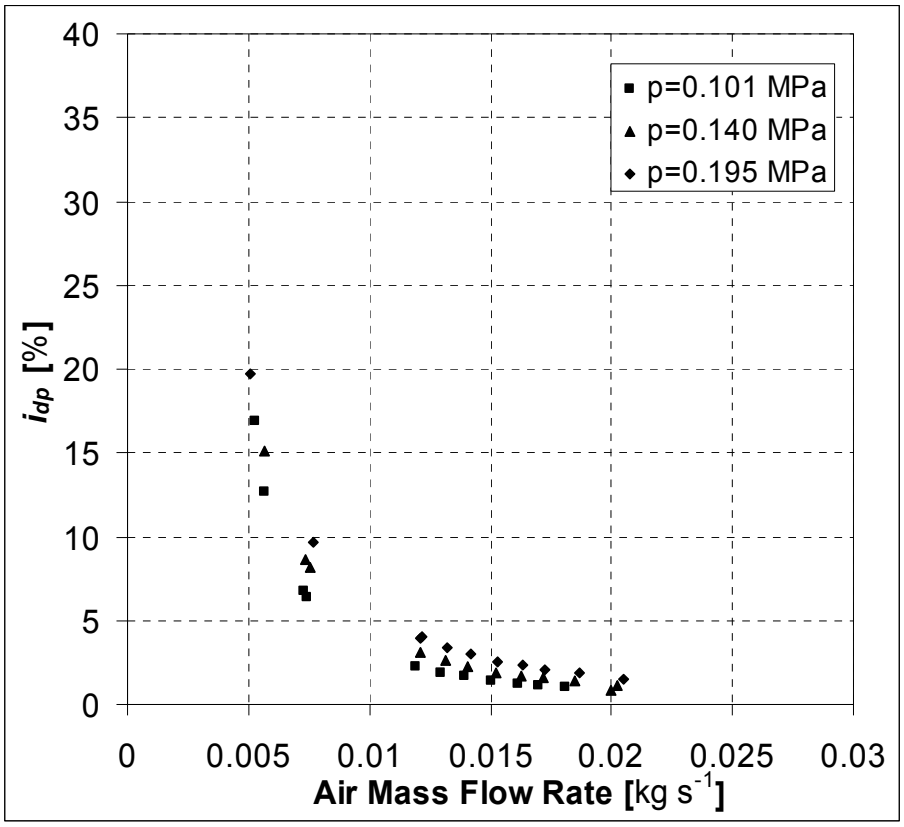

Figure 134. Uncertainty of the experimental pressure drop measurements plotted against the air mass flow rate as a function of the operating pressure.

2.3.3 Experimental Results

In the following paragraphs, the experimental results will be presented in terms of temperature distribution at the inlet and outlet of the test section, heat transfer coefficients, surface area efficiency and pressure drops.

2.3.3.1 Operating Conditions

The test sample was located inside the test section as shown in Figure 126 and Figure 128. The experimental data points refer to both adiabatic and heat transfer measurements carried out during single-phase air flow. Table 49 reports the most relevant operating test conditions.
Some tests were run in order to understand the effective behaviour of the test facility under different operating conditions. In particular, the temperature distribution at the inlet and outlet of the test section was controlled during both adiabatic and heat transfer operating conditions. The heat balance between the electric power supplied to the test sample and the measured air heat flow rate was also controlled.
Several data sets at different operating test conditions were collected. The mass flow rate was varied between 0.005 to 0.025 kg s^{-1}, adiabatic pressure drops were measured at three different pressures, 0.101 MPa, 0.140 MPa and 0.195 MPa, while heat transfer coefficients were measured imposing 150 and 175 W, corresponding to 21.4 and 25 kW m^{-2}, respectively.

Table 49. Operating test conditions.

Parameter	***Range***
Air Mass Flow Rate	0.005 – 0.025 kg s^{-1}
Absolute Pressure	0.101 – 0.195 MPa
Heat Flux	150 – 175 W
Air Frontal Velocity	0.8 – 4 m s^{-1}

2.3.3.2 Air Inlet Temperature Distribution

The temperature distribution at the inlet of the test section was measured by means of nine T-Type thermocouples, as showed in Figure 135. As suggested by ASHRAE Standard 33-78 [33], no individual dry bulb temperature reading of entering air on the measurement plane shall vary by more than around 0.6 °C (1 °F).

Figure 135. Photo of the thermocouples distribution at the inlet of the test section.

Figure 135 is a close-up of the thermocouples distribution at the inlet of the test section; the temperature transducers are clockwise numbered (TC1,..., TC9) starting from the upper center probe.

The thermocouples were inserted in the fluid through nine holes drilled in the bakelite walls. In particular, three holes were drilled in the ceiling wall: one in the center and two at a distance of 15 mm from the central one. These last two holes were copied in the bottom wall of the bakelite channel, while in the two side walls two probes divided the wall height into equal parts.

The results of 100 readings of each thermocouple (1 reading / 9 s) are reported in Figure 136: all the readings are within ±0.2 °C. There is not any apparent non-uniformity in the air temperature distribution at the inlet of the test section.

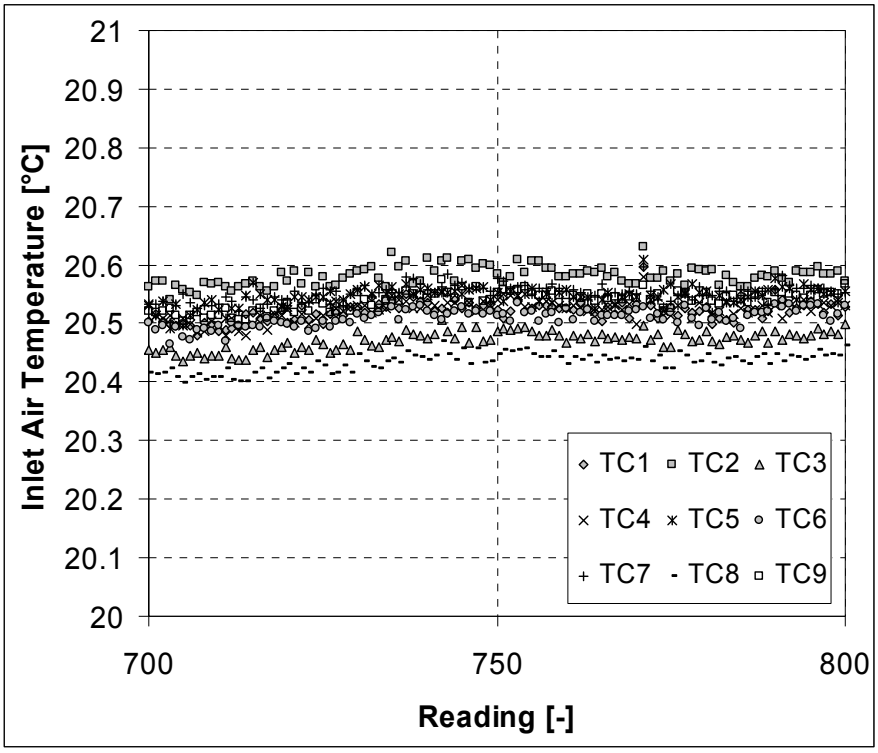

Figure 136. An example of the temperature distribution at the inlet of the test section.

2.3.3.3 Air Outlet Temperature Distribution

Figure 137 shows the thermocouples distribution at the outlet of the test section after the mixing device. Nine thermocouples were installed as at the inlet of the test section.

Figure 137. Photo of the thermocouples distribution at the outlet of the test section.

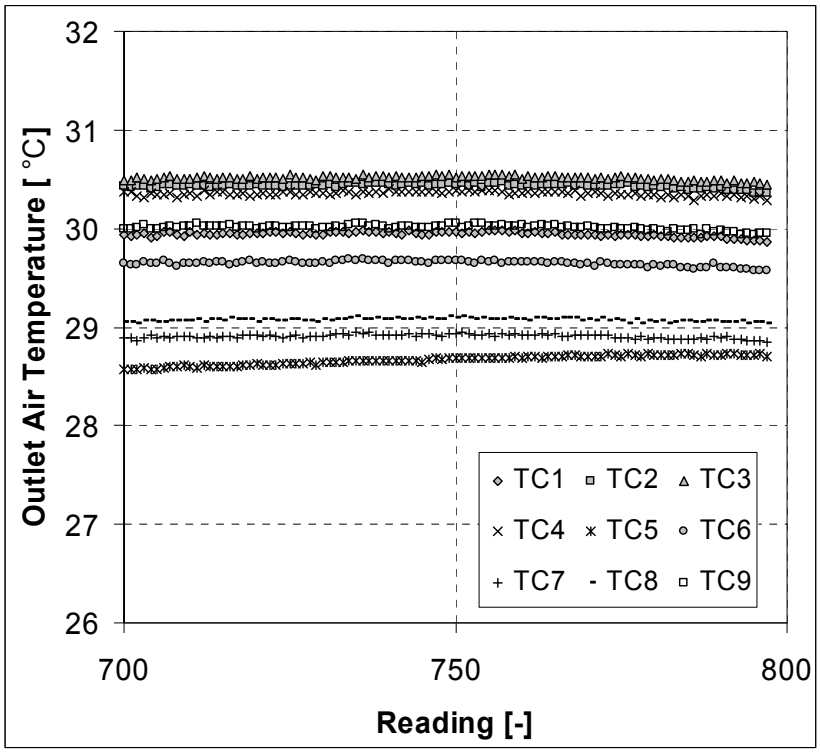

Figure 138. An example of the temperature distribution at the inlet of the test section.

Although a mixing device was designed and inserted at the exit of the test section, the air presented a non-uniform temperature distribution with a maximum difference of 1.6 °C (Figure 138). Still, because of the volume constraints of the system, there weren't any other possible technical solutions which could be implemented to solve this problem.

Nevertheless, the most important issue which must be satisfied to make the test reliable is the heat balance. If the comparison between the electric power and the air heat flow rate is verified within ±5%, mean average temperature estimates are also acceptable.

2.3.3.4 Heat Balance

For each experimental data point, the heat balance was evaluated. This comparison was carried out by calculating the following parameter, *HB*:

$$HB = \frac{q_{air} - P_{EL}}{P_{EL}} \cdot 100 \qquad \textbf{Eq. 232}$$

Where P_{EL} is the electric power and q_{air} is the air heat flow rate.

A positive value of *HB* means that the electric power is lower than the measured air heat flow rate; on the contrary, if the electric power is greater than the air heat flow rate, *HB* will be negative.

When the *HB* was within ±5% the steady state conditions were considered acceptable and the test point was recorded.

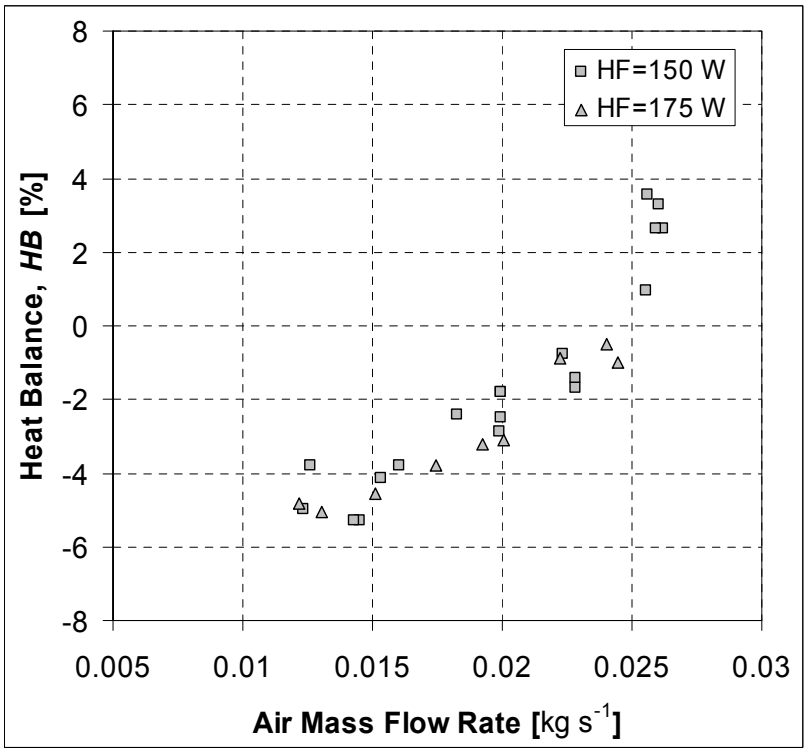

Figure 139. Heat balance deviation HB plotted against the air mass flow rate. HF: Heat Flux [kW m^{-2}].

Figure 139 plots the heat balance deviation, *HB,* against the air mass flow rate for the two sets of experimental data points. Generally speaking, for both imposed heat flow rates, 150 and 175 W, the deviation decreases as the mass flow rate increases. The deviation is always

negative; it means that the measured air heat flow rate is lower than the imposed electric power. Only few of the data points at a high air mass flow rate present a positive heat balance deviation. These experimental runs were carried out imposing 150 W.

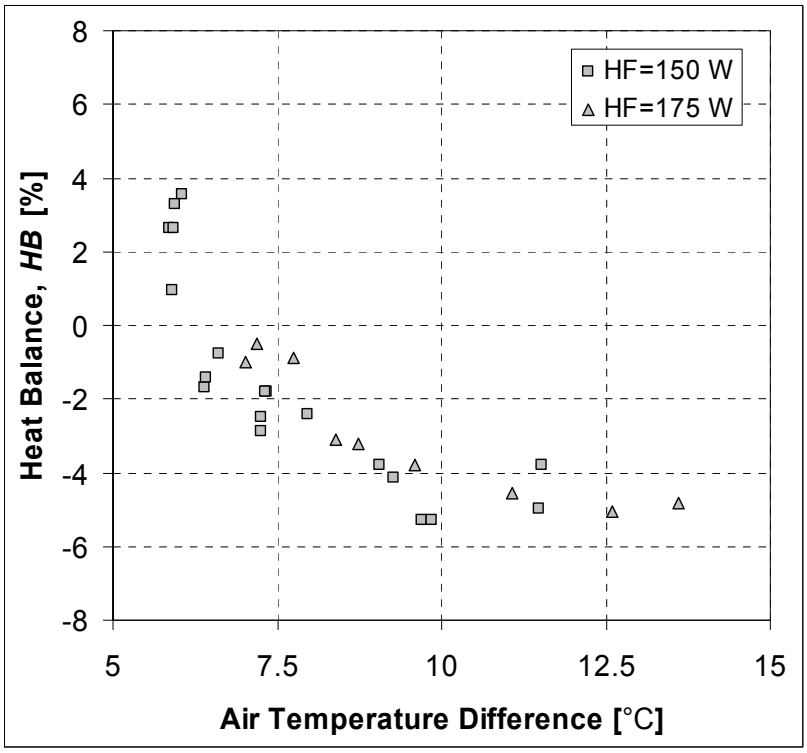

Figure 140. Heat balance deviation HB plotted against the air temperature difference.

As it appears from the diagram plotted in Figure 140, the deviation exhibits a dependence on the air temperature difference. With the exception of data points presenting a positive heat balance deviation, *HB* appears to increase as the temperature gain increases.

This behaviour can be explained with the higher difficulties in air flow mixing at a low air flow rate than at a high air flow rate. In fact, if some non-uniformities remain in the flow temperature distribution, mean air temperature estimation is affected by higher inaccuracy.

2.3.3.5 Heat Transfer Coefficient and Surface Area Efficiency

An extended surface (fin) is a device attached to the (primary) surface of a structure protruding in the adjacent fluid, where its sole purpose is to increase the heat transfer from the surface to the fluid or vice versa [37].

The heat transfer behaviour of an enhanced surface is defined by two important parameters: the effective heat transfer coefficient (*HTC*) and the surface area efficiency (Ω^*).

The measured heat transfer coefficient is the product of these two values, therefore, if it is possible to calculate one of them, the other will be evaluated.

$$\left(HTC \cdot \Omega^*\right)_{tot} = \frac{P_{EL}}{A_{tot} \cdot \Delta t_{ml}} \qquad \textbf{Eq. 233}$$

As it appears from Eq. 233, the global heat transfer behaviour is defined on the total heat transfer area, A_{tot} , which is equal to 0.06733 m^2.

The fin has a trapezoidal shape and its thickness varies from the base to the tip, passing from 5 mm to 3 mm. Since the thickness variation (2 mm) is small compared to the fin height (48 mm), it is possible to consider an equivalent rectangular fin with the thickness equal to the average value (4 mm).

The theory of fin efficiency is then applied to this equivalent rectangular fin, therefore it is possible to obtain the two parameters starting from the experimental global heat transfer behaviour.

One-dimensional fin efficiency theory is based on several important assumptions:

- There is a steady-state heat flow.
- The fin material is homogeneous and isotropic.
- There are no heat sources or sinks in the fin.
- The heat flow to or from the fin surface at any point is directly proportional to the temperature difference, at the same point, between the surface and the surrounding fluid (convective fins).
- The thermal conductivity of the fin material is constant.
- The heat transfer coefficient is the same all over the fin surface.
- The temperature of the surrounding fluid is uniform.

- The temperature at the base of the fin is uniform.
- Compared to its height, the fin thickness is so small that temperature gradients normal to the surface may be neglected (i.e. there is one-dimensional conduction).
- The heat transferred through the outermost edge of the fin is negligible compared to that dissipated through the sides (i.e. the tip of the fin is insulated).
- The width of the longitudinal fins is much larger than either the height or the base thickness (i.e. the temperature variation along the width is negligible).
- The end faces of the longitudinal fins along their width are adiabatic.

In his work, Razelos [37] has analyzed and discussed all cited assumptions. In particular, he affirms that, in longitudinal fins, the variation of the base temperature along their length can be overcome and the heat transfer from the fin can be obtained simply by using the average base temperature of the space.
The finned surface is located in the bakelite channel and the fin tips can be considered adiabatic as they touch the bakelite ceiling. As described before, the global heat transfer behaviour of the enhanced surface is obtained from the experimental measures using Eq. 212. The fin efficiency is iteratively calculated following the next simple algorithm:

$$\Omega = \frac{\tanh(mL)}{mL} \qquad \textbf{Eq. 234}$$

Where:

$$m = \sqrt{\frac{HTC}{\delta \cdot \lambda}} \qquad \textbf{Eq. 235}$$

And:

$$L = h \qquad \textbf{Eq. 236}$$

δ is half the equivalent fin thickness (2 mm), λ is the aluminum thermal conductivity, and it is equal to 175 ± 5 W m^{-1} K^{-1}, while *h* is the fin height.

Introducing, as a first step, the global heat transfer coefficient ($HTC\Omega^*$), the first estimation of the fin efficiency is calculated using Eq. 234 and the surface fin efficiency is given by:

$$\Omega^* = 1 - \frac{A_{fin}}{A_{tot}}(1-\Omega) \qquad \textbf{Eq. 237}$$

With this value, it is possible to calculate the first heat transfer coefficient; after few iterations its value remains constant and the procedure can be considered completed.

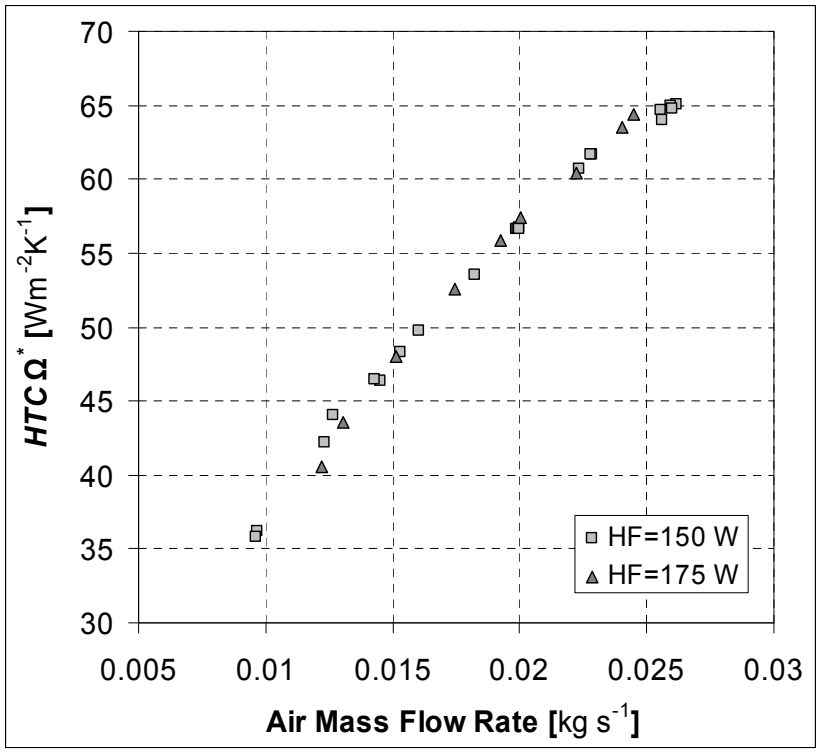

Figure 141. Global heat transfer behaviour of the finned surface plotted against the air mass flow rate. HF: Heat Flux [kW m^{-2}].

The product of the heat transfer coefficient and the surface fin efficiency is plotted against the air mass flow rate in Figure 141. As one can see, the global heat transfer coefficient increases linearly with the mass flow rate and it does not depend on the heat flux.

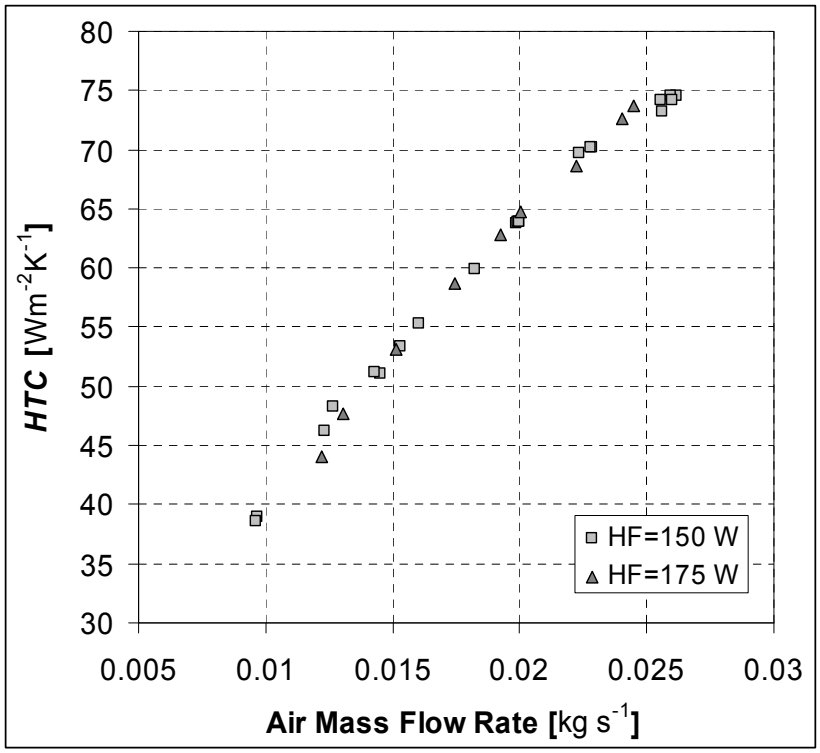

Figure 142. Heat transfer coefficient plotted against the air mass flow rate. HF: Heat Flux [kW m^{-2}].

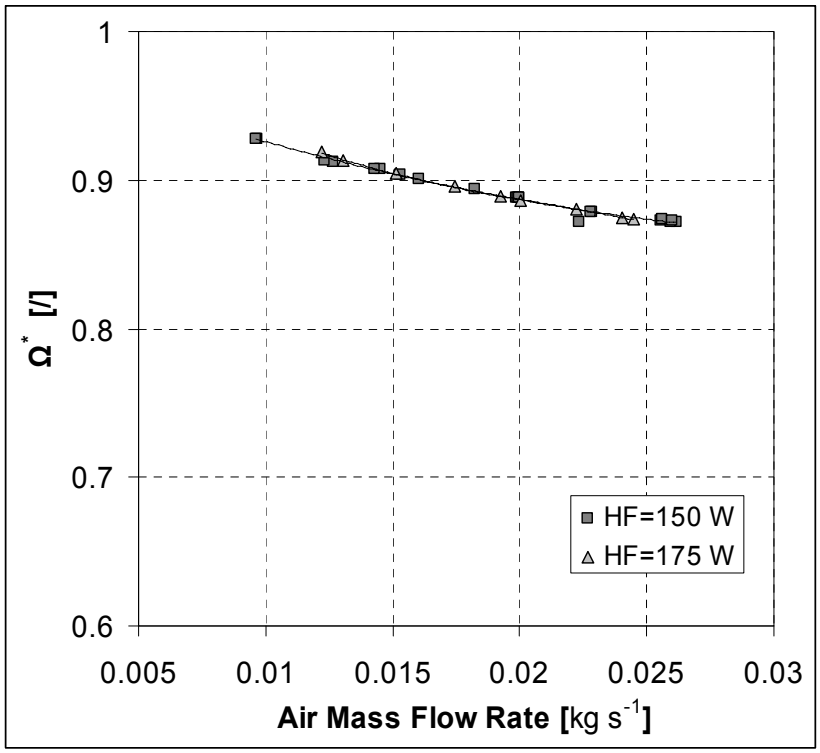

Figure 143. Surface area efficiency plotted against the air mass flow rate. HF: Heat Flux [kW m^{-2}].

Figure 142 and Figure 143 focus on the two terms of the global heat transfer behaviour: the heat transfer coefficient and the surface fin efficiency. The heat transfer coefficient presents the same behaviour of the product, while the surface fin efficiency decreases with the increasing of the heat transfer coefficient and of the air mass flow rate. In the range of operating test conditions, the surface fin efficiency varies between 0.87 and 0.93; again, the surface fin efficiency does not depend on the heat flux.

Experimental heat transfer coefficients have been compared with the results of some semi-empirical correlations proposed in the open literature. Analyzing the operating test conditions, it is possible to understand that the Reynolds number, referred to the hydraulic diameter, varies between 3000 and 9000, falling into the transition flow between the laminar region and the turbulent region. There is a lack of experimental works concerning the heat transfer coefficient and the fluid flow in this transition region, hence heat transfer phenomena have not been deeply investigated yet.

Moreover, as experimentally verified by Ghajar and Tam [38], the effect of the inlet configuration appears to influence heat transfer and fluid flow behaviours in the transition region, during single-phase liquid flow. In particular, Ghajar et al. [39] made local forced and mixed convective heat transfer measurements in a horizontal electrically heated stainless steel circular tube with re-entrant, square-edged and bell-mouth inlets under uniform wall heat flux conditions. They experimentally found that the heat transfer transition Reynolds number range for each inlet configuration can be estimated to be between 2000-8500 for the re-entrant inlet, 2400-8800 for the square-edged inlet and 3400-10500 for the bell-mouth inlet.

The same Authors experimentally investigated the heat transfer and the fluid flow during single-phase liquid flow covering all flow regimes (laminar, transition and turbulent) in a circular horizontal tube with three inlet configurations, finding that the heat transfer behaviour and the fluid flow depend on inlet boundaries conditions [39,40].

Ghajar et al. [41] have proposed an improved heat transfer correlation for the transition region developed on their experimental heat transfer measures during single-phase liquid flow in a horizontal circular tube. The results of this equation were compared with the experimental heat transfer coefficients measured during single-phase air heat transfer. Although the geometrical characteristics of the tested tube were different from our configuration, the heat transfer correlation was applied, considering the hydraulic diameter as the geometrical reference coordinate.

The correlation for heat transfer coefficient calculation in the transition region is the following:

$$Nu_{tr} = Nu_l + \left[e^{\left(\frac{a-\mathrm{Re}}{b}\right)} + Nu_t^c \right]^c \qquad \textbf{Eq. 238}$$

Where Nu_{tr} is the transition Nusselt number, while Nu_l and Nu_t are the Nusselt numbers referred to the laminar flow and the turbulent flow, respectively.

$$Nu_l = 1.24 \left[\frac{\mathrm{Re}\,\mathrm{Pr}\,d_h}{x} + 0.025\left(Gr\,\mathrm{Pr}\right)^{0.8} \right]^{0.33} \qquad \textbf{Eq. 239}$$

And:

$$Nu_t = 0.023\,\mathrm{Re}^{0.8}\,\mathrm{Pr}^{0.385}\left(\frac{x}{d_h}\right)^{-0.0054} \qquad \textbf{Eq. 240}$$

With the Reynolds number defined on the core cross-sectional area and based on the hydraulic diameter.
The constants depend on the different inlet configurations, as reported in Table 50.

Table 50. Constants in Eq. 238.

Inlet	***a***	***b***	***c***
Re-entrant	1766	276	-0.955
Square-edged	2617	207	-0.950
Bell-mouth	6628	237	-0.980

The finned surface is positioned as an obstacle in the test section, therefore the constants regressed for the square-edged and re-entrant inlet configurations are selected to calculate the transition Nusselt number.

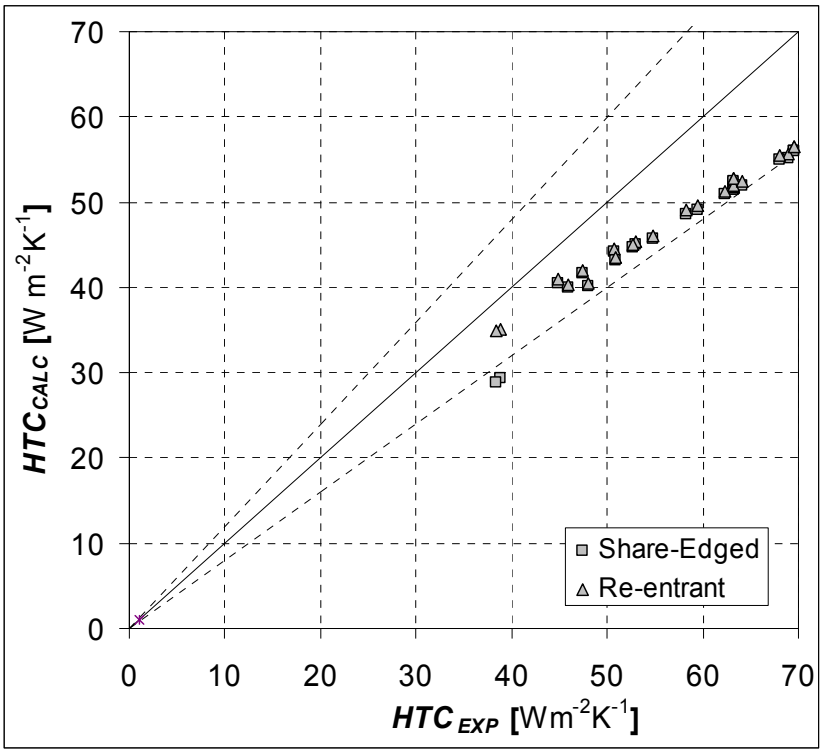

Figure 144. Calculated vs. experimental heat transfer coefficients. Model by Ghajar et al.

Generally speaking, even if it has been developed for circular ducts, the model proposed by Ghajar et al. is able to estimate experimental heat transfer coefficients with a quite good accuracy. The deviation, almost lower than 20%, rises as the mass flow rate increases, and experimental data points are underestimated. The two sets of constants exhibit near the same results excepted for the lowest experimental data points. This can be due to the different transitional Reynolds number: in fact, for square-edged inlet configuration it is equal to 2617 while it is 1677 for re-entrant configuration.

Another model was selected from the open literature in order to compare its results with the experimental heat transfer coefficients. This model was developed by Polley and Abu-Khader [42] using the most extensive and widely used source data on the performance of plate-fin surfaces, built by Kays and London [43].

This computational scheme is a power law correlation which combines the laminar and turbulent Nusselt numbers as follows.

The laminar Nusselt number is calculated with:

$$Nu_l = \left\{ 3.66^3 + 0.7^3 + \left(1.77 Gz^{1/3} - 0.7 \right)^3 + \left[\frac{4}{\pi} \left(\frac{2}{1+22\,\mathrm{Pr}} \right)^{1/6} Gz^{0.5} \right]^3 \right\}^{1/3} \quad \textbf{Eq. 241}$$

While the turbulent Nusselt number is given by:

$$Nu_t = 0.035 \sqrt{f}\,\mathrm{Re}\,\mathrm{Pr}^{1/3} \quad \textbf{Eq. 242}$$

Where the friction factor f is calculated with:

$$f = \left[\left(\frac{16}{\mathrm{Re}} \right)^3 + \left(\frac{0.078}{\mathrm{Re}^{0.25}} \right)^3 \right]^{1/3} \quad \textbf{Eq. 243}$$

The Nusselt number is given by:

$$Nu = \frac{HTCd_h}{\lambda_{air}} = \left[Nu_l^{10} + \left(\frac{1}{Nu_j^2} + \frac{1}{Nu_t^2} \right)^{-5} \right]^{0.1} \quad \textbf{Eq. 244}$$

Where the transition Nusselt number is defined by:

$$Nu_j = Nu_{l,\mathrm{Re}cr} e^{\left(\frac{\mathrm{Re}-\mathrm{Re}_{cr}}{730} \right)} \quad \textbf{Eq. 245}$$

The Authors suggested to use 2200 as the critical Reynolds number for cylindrical channels, while for rectangular ducts the value decreases to 1500.

The results of the application of this model are clearly illustrated in Figure 145. All data are underestimated by the proposed correlation; again, the deviation increases as the mass flow rate increases.

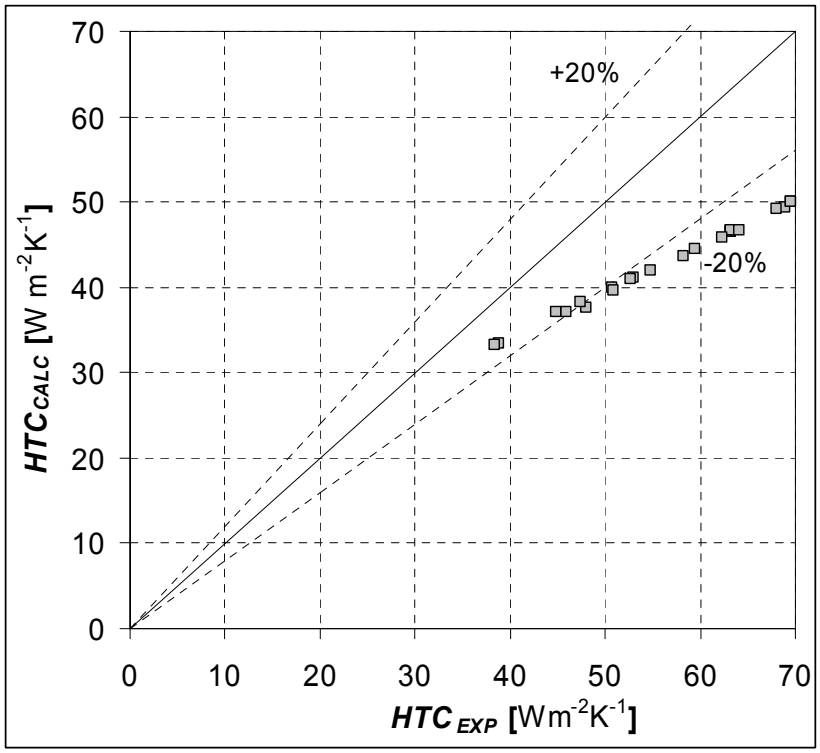

Figure 145. Calculated vs. experimental heat transfer coefficients. Model by Polley and Abu-Khader.

Table 21 reports the relative deviation, e_R, the absolute deviation, e_A, and the standard deviation σ_N calculated for the two evaluated models. The best agreements with the experimental data are exhibited by Ghajar et al. [41] correlations; however, both underestimate the data points.

Table 51. Deviations from the experimental values of the models.

Model	e_R **[%]**	e_A **[%]**	σ_N **[%]**
Ghajar et al. [41] Square-edged	-17.7	17.7	3.23
Ghajar et al. [41] Re-entrant	-16.0	16.0	3.18
Polley and Abu-Khader [42]	-24.5	24.5	4.19

2.3.3.6 Mean Wall Temperature

The wall temperature is one of the most important parameters in electronic cooling system design. Since the experimental data points were carried out under different ambient conditions (which vary, as they depend on atmospheric weather), the inlet air temperature was not constant. For this reason, a mean wall temperature has been calculated in order to compare experimental data points taken under different ambient conditions.

In the hypothesis that the product of the heat transfer coefficient times the finned surface area efficiency is constant along the sample and does not vary with air temperature (because air properties are almost constant) with reference to the mean air temperature across the sample, $\overline{t}_{air}$, it is possible to calculate a normalized mean wall temperature, $\overline{t}_{w}$:

$$\overline{t}_{w} = \overline{t}_{air} + \frac{P_{EL}}{HTC \cdot \Omega^{*} \cdot A_{tot}} \qquad \textbf{Eq. 246}$$

Calculations of mean wall temperatures were performed setting the air temperature at the inlet of the test section at 25 °C.

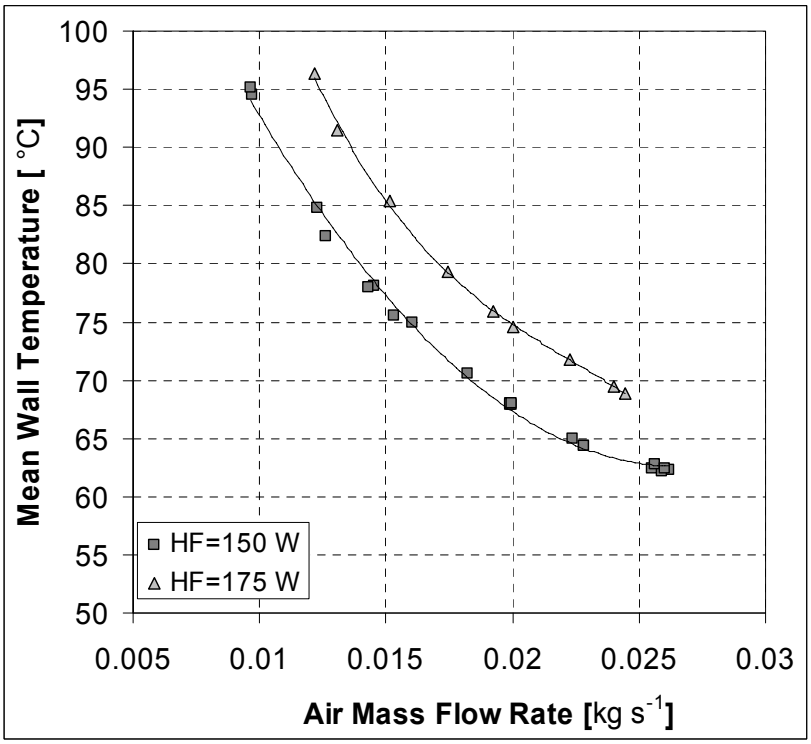

Figure 146. Mean wall temperature plotted against air mass flow rate. $t_{air,in}$=25 °C HF: Heat Flux [kW m^{-2}].

Figure 146 reports the results of the described calculations: the mean wall temperature is plotted against the air mass flow rate. The diagram illustrates that the wall temperature decreases as the mass flow rate increases, while it increases when the heat flux passes from 150 W to 175 W.

2.3.3.7 Pressure Drops

In this paragraph, the experimental pressure drops are analyzed. In this test equipment, it is possible to control the air flow rate and its pressure independently. Different data sets were collected varying the air flow rate at three different pressures: 0.101 MPa, 0.140 MPa and 0.195 MPa. As illustrated in paragraph 2.2.4.1, during this experimental campaign the temperature probes were located after the inlet pressure taps before the test sample.

As reported in Figure 147, two independent data sets, with and without the inlet temperature probes, were carried out to verify the influence of these transducers on the pressure drops. The measurements were collected at 0.140 MPa, and, as it appears from Figure 147, there is not any appreciable effect of the temperature probes on the pressure drops.

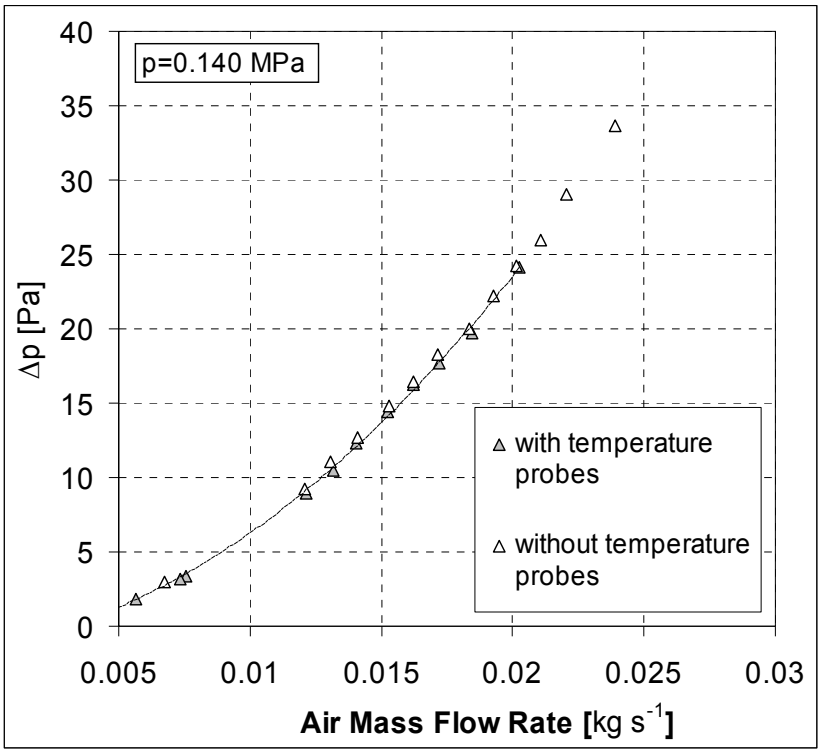

Figure 147. Pressure drop measurements with and without the inlet temperature probes.

The total pressure drop measured during adiabatic single-phase air flow through the finned surface is plotted in Figure 148. At constant mass velocity, the pressure drop increases with decreasing air absolute pressure, since the fluid density increases. The same trend is exhibited by the total pressure gradient, plotted in Figure 149.

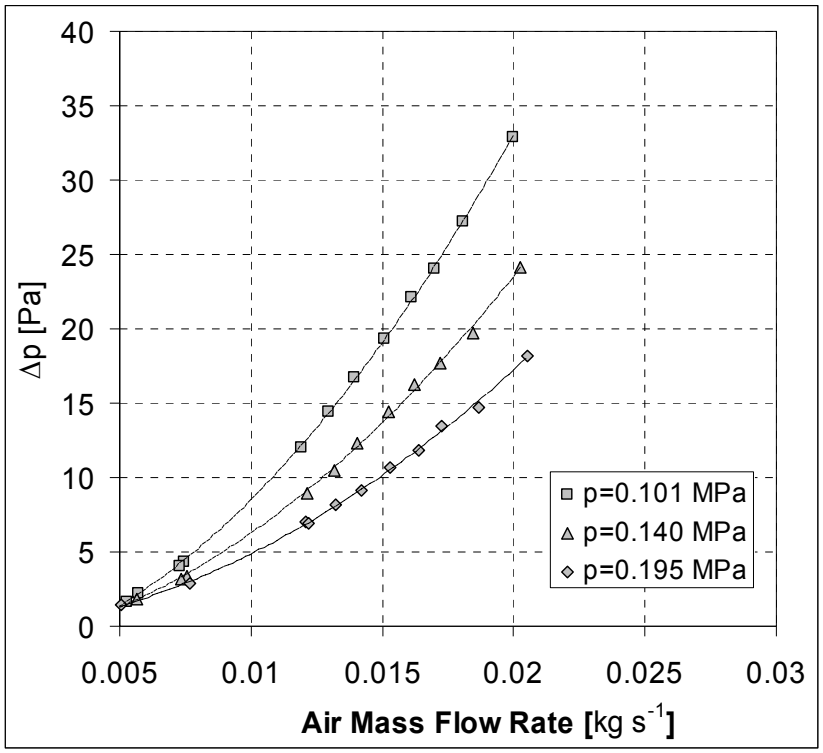

Figure 148. Total pressure drop plotted against the air mass flow rate.

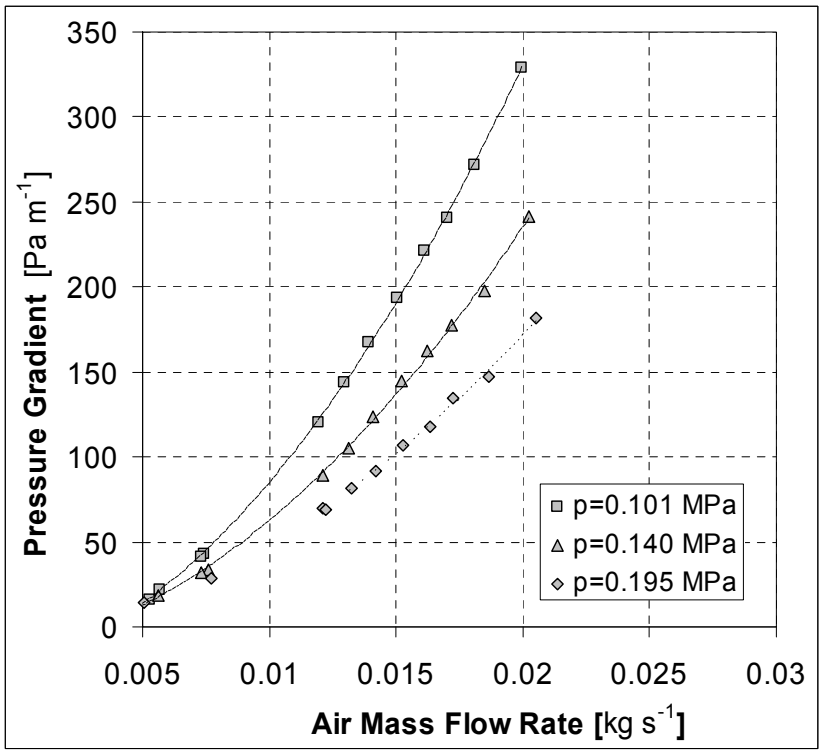

Figure 149. Total pressure gradient plotted against the air mass flow rate.

The designer is interested in the overall core pressure drop, including any entrance and exit loss, rather than merely the core friction pressure drop. On the other hand, if the experimental results are compared to the calculated ones, abrupt pressure drops have to be evaluated in order to obtain frictional ones.

Abrupt contraction and expansion additional pressure drops can be estimated using the *Kc* and *Ke* entrance and exit pressure loss coefficients suggested by Kays and London [43] for the multiple-tube flat duct heat exchanger. The abrupt pressure drops (Δp_{loc}) can be estimated using the following equation:

$$\Delta p_{loc} = \Delta p_{in} - \Delta p_{out} = \left[\frac{\rho u_{ch}^2}{2} \left(1 - \frac{A_{ff}}{A_{fr}} \right) + K_c \frac{\rho u_{ch}^2}{2} \right] - \left[\frac{\rho u_{ch}^2}{2} \left(1 - \frac{A_{ff}}{A_{fr}} \right) - K_e \frac{\rho u_{ch}^2}{2} \right] \quad \textbf{Eq. 247}$$

Therefore:

$$\Delta p_{loc} = K_c \frac{\rho u_{ch}^2}{2} + K_e \frac{\rho u_{ch}^2}{2} \quad \textbf{Eq. 248}$$

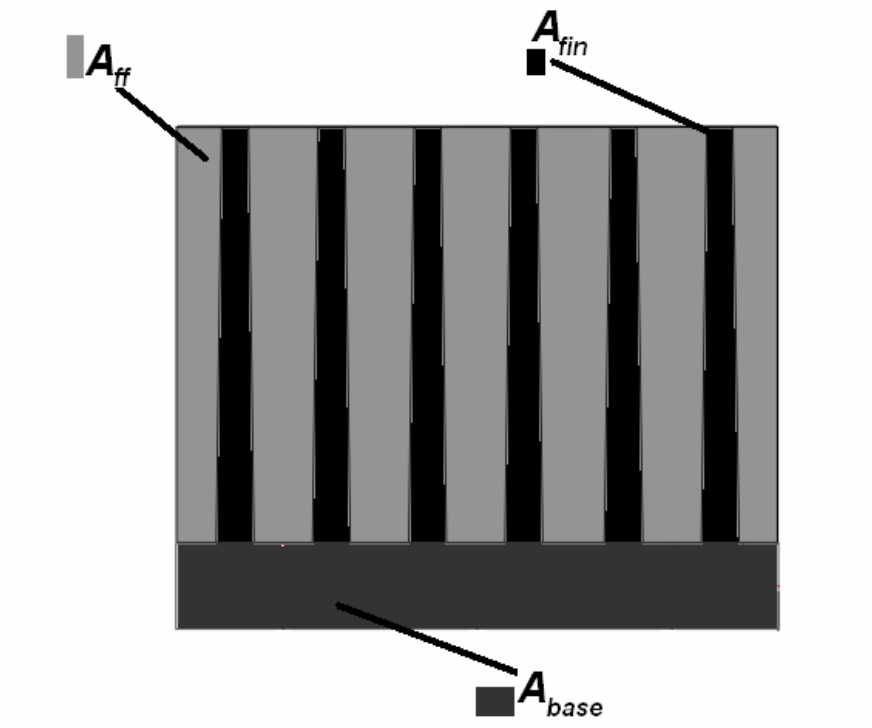

Figure 150. Frontal view of the finned surface.

Figure 150 reports a drawing of the frontal view of the finned surface with the most important areas which are used in the following to define different air velocities.

As suggested by Kays and London [43], u_{ch} is the channel velocity, linked to the frontal velocity by the ratio of free-flow area to frontal area (A_{ff}/A_{fr}).

$$u_{ch} = u_{fr} \frac{A_{ff}}{A_{fr}} \qquad \textbf{Eq. 249}$$

Where frontal area is the sum of the three areas: A_{ff}, A_{fin}, A_{base} highlighted in Figure 150; this velocity, Eq. 249, is used in the calculations called First Method.

Since the finned surface is inserted in the test section, as it would be in its application, the base is exposed to the fluid flow. Hence, the fluid field at the inlet of the test section is disturbed by the presence of the base, and a dead zone for the fluid flow might be present in front of the test sample. For this reason, it is possible that the approach velocity is different from the frontal velocity. Thus, also the inlet channel velocity can be higher than the frontal velocity.

The ratio of free-flow area to frontal area (A_{ff}/A_{fr}) is equal to 0.544. Considering the base thickness, frontal area decreases, and it would be 0.0035 m^2 instead of 0.0042 m^2 (as suggested in Figure 150, A_{fr} - A_{base}). Therefore, the approach velocity would be 1.2 times higher than the frontal velocity. Accordingly, using the predefined free-flow area to frontal area ratio, it is possible to determine the new inlet channel velocity which permits to calculate different local pressure drops.

Finally, the channel velocity to use in the calculation of the local pressure drops would be:

$$u_{ch} = 1.2 u_{fr} \frac{A_{ff}}{A_{fr}} \qquad \textbf{Eq. 250}$$

This channel velocity, Eq. 250, is used to calculate the abrupt pressure losses in the second way, called Second Method. The frictional pressure drops are obtained by subtracting the estimated local pressure losses from the total measured pressure drops. The results of the application of these two different methods are illustrated in Figure 151.

It is apparent that the Second Method exhibits lower frictional pressure drops than those obtained with the First Method.

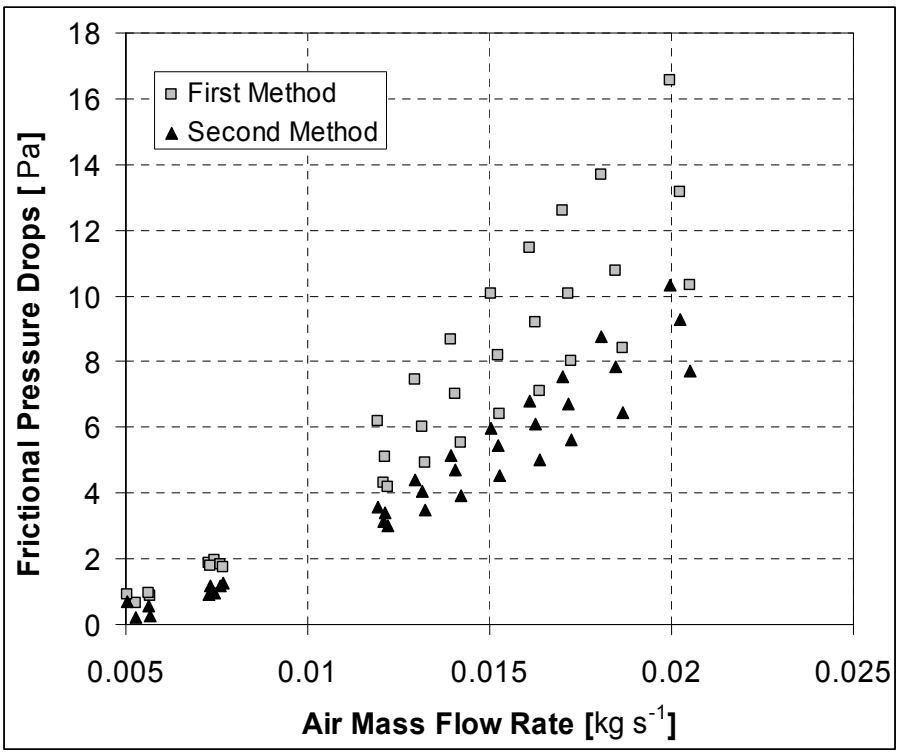

Figure 151. Estimated frictional pressure drops plotted against the air flow rate.

If the frictional pressure drops are calculated from the total pressure losses, the friction factor f can be evaluated considering the well-known Fanning equation:

$$\Delta p = 4 f \frac{l}{d_h} \frac{\rho u_{ch}^2}{2} \qquad \textbf{Eq. 251}$$

The channel velocity is the one only referred to the free-flow area to frontal area ratio, as suggested by Eq. 249.

In Figure 152, the friction factors were calculated only for the atmospheric data set, applying the two methods. The calculated values were compared with three semi-empirical correlations suggested in the open literature.

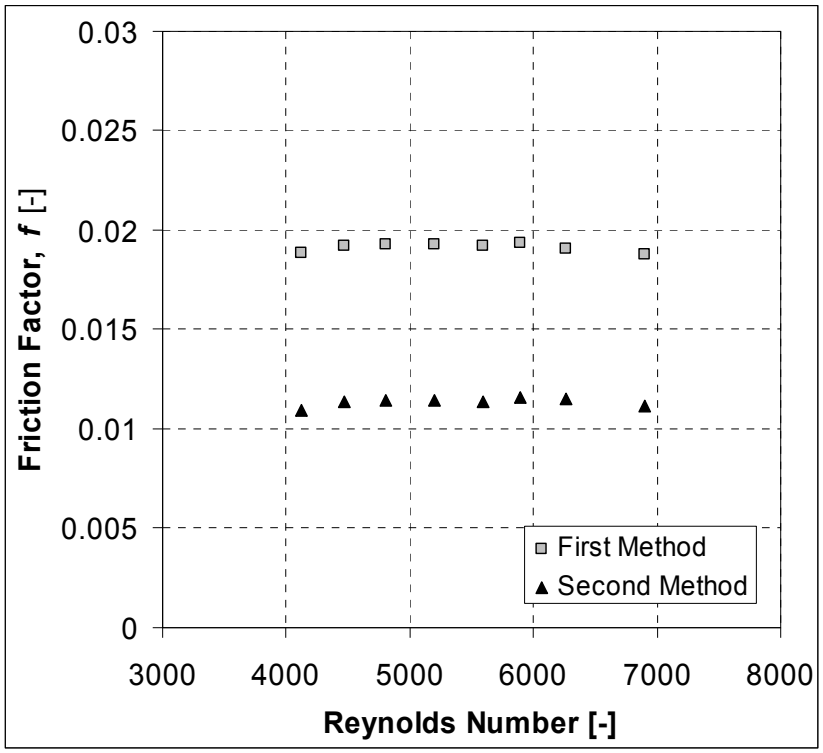

Figure 152. Friction factor f plotted against the Reynolds Number.

The three semi-empirical correlations are those suggested by Polley and Abu-Khader [42], Tam and Ghajar [39] and Phillips [44].

Polley and Abu-Khader [42] proposed to calculate the friction factor using the following simple equation:

$$f = \left[\left(\frac{16}{\mathrm{Re}} \right)^3 + \left(\frac{0.079}{\mathrm{Re}^{0.25}} \right)^3 \right]^{0.33333} \qquad \textbf{Eq. 252}$$

Tam and Ghajar [39] have studied the influence of the inlet configuration and of heating on the fluid flow.

As described before [41], the Authors [39] analyzed the transition flow regime considering three inlet configurations: re-entrant, square-edged and bell-mouth. The correlation for the friction factor evaluation in the transition flow region for the square-edged inlet configuration was:

$$f = \left[1 + \left(\frac{\mathrm{Re}}{4230}\right)^{-0.16}\right]^{-6.57} \left(\frac{\mu_f}{\mu_w}\right)^m \qquad \textbf{Eq. 253}$$

The dynamic viscosity ratio was proposed to take into account the temperature difference between the fluid and the wall during the heat transfer process. Since the data points were carried out under adiabatic test conditions, this ratio was set equal to 1.

Finally, the last equation was developed by Phillips [44] for micro-channel fluid flow. It covers both the developing and fully developed turbulent flow regions. The friction factor is given by:

$$f = A\,\mathrm{Re}^B \qquad \textbf{Eq. 254}$$

Where:

$$A = 0.09290 + \frac{1.01612}{l/d_h} \qquad \textbf{Eq. 255}$$

$$B = -0.26800 - \frac{0.32930}{l/d_h} \qquad \textbf{Eq. 256}$$

The Reynolds number is referred to the channel velocity (First Method).

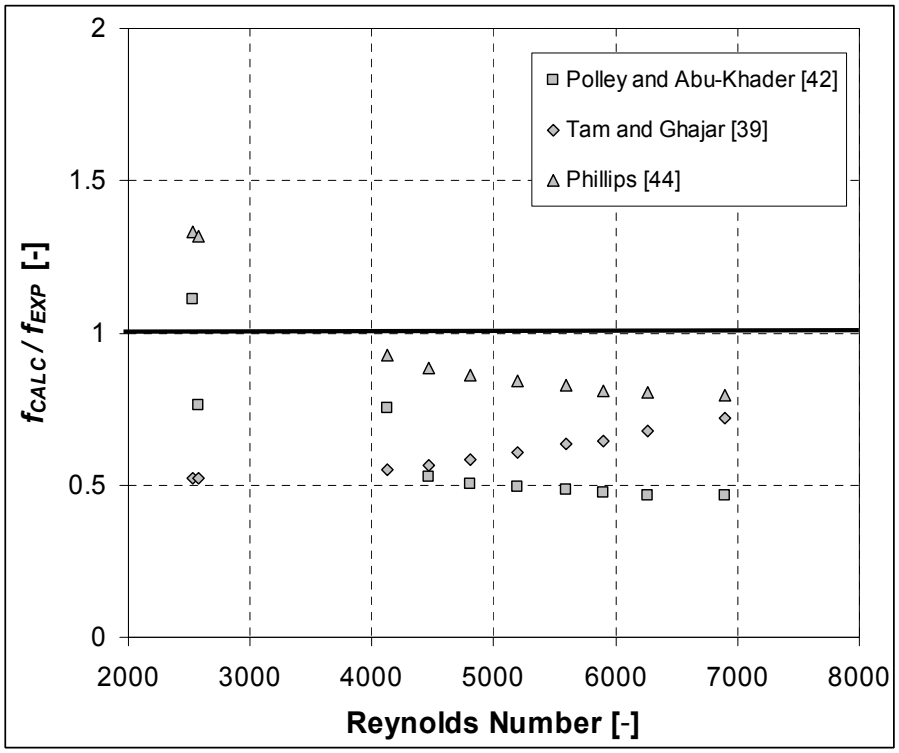

Figure 153. Calculated to experimental friction factor ratio plotted against the Reynolds Number referred to the channel velocity. Abrupt pressure losses evaluated with the First Method.

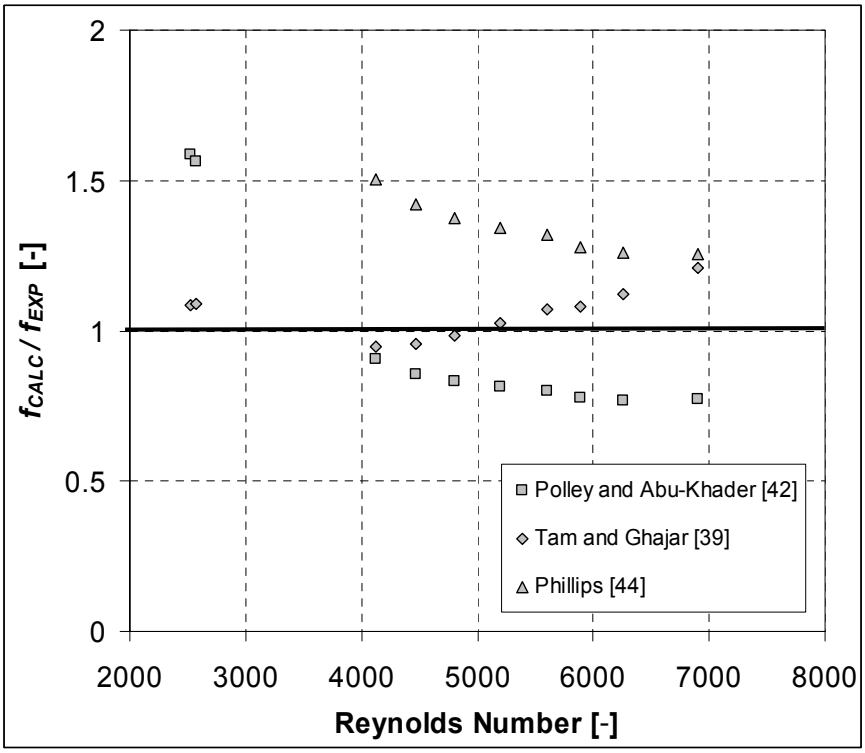

Figure 154. Calculated to experimental friction factor ratio plotted against the Reynolds Number referred to the channel velocity. Abrupt pressure losses evaluated with the Second Method.

Figure 153 and Figure 154 report the comparison between the experimental friction factors and those calculated with the three correlations.

In Figure 153, all applied models underestimate the experimental friction factors; in the diagram the experimental friction factors were calculated considering the First Method for abrupt pressure losses evaluation. The model proposed by Phillips [44] appears to be the most accurate, but it was developed for micro-channel applications. In Figure 154 the abrupt pressure losses were calculated using the Second Method; in this case the experimental friction factors are lower than those obtained by applying the First Method.

The most reliable model appears to be the one proposed by Tam and Ghajar [39], though it slightly overestimates the friction factor at high Reynolds number. The model proposed by Polley and Abu-Khader [42] slightly underestimates the friction factors (Figure 153). Phillips [44] equation overestimates the experimental results.

2.3.4 Conclusions

In this part of the work, a traditional finned surface has been thermo-fluid-dynamically characterized in a new experimental test rig. This experimental campaign was carried out to test and evaluate the new experimental test rig in a wide range of operating test conditions. In particular, both heat transfer coefficients and pressure drops were measured during single-phase air flow at different pressures.

Heat transfer measurements were performed in order to evaluate the thermal performance of the test section; in particular, the heat balance has been controlled for each selected data point. The temperature measurement technique was also controlled to verify the effective behaviour of the designed mixer. Adiabatic tests were carried out in order to measure air pressure drops through the finned surface at different pressures: 0.101 MPa, 0.140 MPa and 0.195 MPa.

From these first experimental test runs, the test facility can be considered reliable and the data points repeatable. Starting from these results and using this same test facility, five different aluminum metal foams have been experimentally characterized.

2.4 Transport Phenomena in Aluminum Foams

The aim of this part of the work was to experimentally investigate heat transfer and fluid flow during single-phase air flow through high porosity open-cell metal foams. Metal foams present random microstructures consisting of open cells randomly oriented and mostly homogeneous in size and shape. Most commercially available metal foams are based on aluminum, copper, nickel and metal alloys. Other very interesting stochastic porous materials are carbon foams, which are receiving special attention for their potential applications in several areas of thermal management.

Metal foams made of aluminum with porosity ranging from 0.903 to 0.956 and pores per inch (PPI) varying between 5 and 40 were used. In this chapter, the experimental results are presented in terms of heat transfer coefficients, pressure drops, permeability and inertia coefficient. In order to introduce this new topic, a brief overview is given of metal foams, looking at their foaming processes and their morphological structures.

2.4.1 Introduction

Generally speaking, metal foams are a class of cellular solids. The word *cell* derives from the Latin *cella:* a small compartment, an enclosed space. The research interest is in clusters of cells, to the Roman *cellarium*, to us *cellular solids*, which are an assembly of cells with solid edges or faces, packed together so that they fill space. Such materials are common in nature: wood, cork, sponge and coral are examples. A cellular solid is one made up of an interconnected network of solid struts or plates which form the edges and faces of cells.

Before talking about the metal foaming processes, it is worth mentioning that many foodstuffs are foams. Some, like meringue, are made by mechanical beating. Others, like breads, use a biological blowing agent (yeast). Others, like cornflakes, rely on a physical blowing agent (steam). And nature has devised her own ways of making foams either as part of the growth process of a single organism (as in bone, woods, cork and leaves) or as the product of a community of organisms (corals, sponges, nests of certain insects).

The cellular materials exhibit two predominant topologies: periodic (honeycomb) and stochastic (foamed). Examples of cellular solids are illustrated in paragraph 2.1. The simplest is a two-dimensional array of polygons which pack to fill a plane area like the hexagonal cells of the bee, honeycombs. More commonly, the cells are polyhedra which pack in three dimensions to fill space, foams.

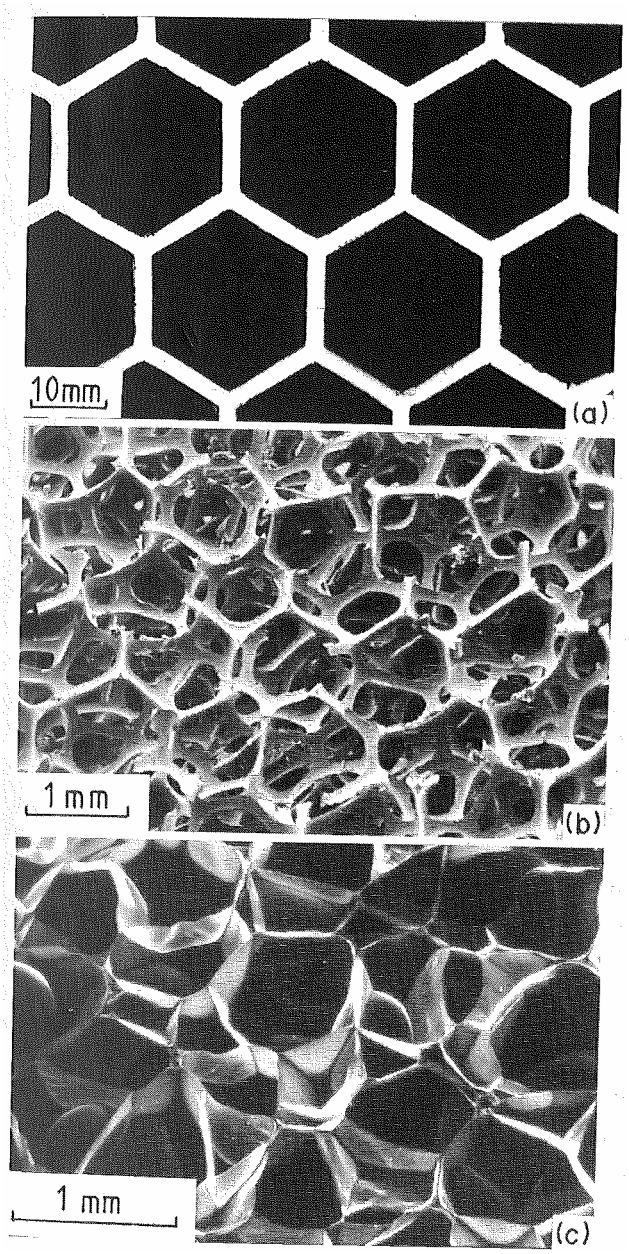

Figure 155. Example of cellular solids: (a) a two-dimensional honeycomb; (b) a three-dimensional foam with open cells; (c) a three-dimensional foam with closed cells. [45].

If the solid of which the foam is made is contained in the cell edges only (so that the cells connect through open faces), the foam is said to be open-celled. If the faces are solid too, so that the cell is sealed off from its neighbours, it is said to be closed-celled. Of course, some foams are partly open and partly closed.

Almost any materials can be foamed [45]. Polymers are the most common but metals, ceramics, glasses and even composites can be fabricated into cells. Different techniques are

used for foaming different types of solids. Considering the metal foams, they can be made using either liquid or solid state processing. Powdered metal and powdered titanium hydride or zirconium hydride can be mixed, compacted and then heated to the melting point of the metal to evolve hydrogen as a gas and form the foam. Mechanical agitation of a mixture of liquid aluminum and silicon carbide particles forms a froth which can be cooled to give the aluminum foam. Liquid metals can also be infiltrated around granules which are then removed; for instance, carbon beads can be burned off or salt granules can be leached out.

Metals can be coated onto an open-cell polymer foam substrate using electroless deposition, electrochemical deposition or chemical vapour deposition. Metal foams can also be made by an eutectic transformation: the metal is melted in an atmosphere of hydrogen and then cooled through the eutectic point, yielding the gas as a separate phase within the metal. Solid state processes use powder metallurgy. In the powder sintering method, the powdered metal is mixed with a spacing agent which decomposes or evaporates during sintering. Alternatively, a slurry of metal powder mixed with a foaming agent in an organic vehicle can be mechanically agitated to form a foam which is then heated to give the porous metal. Metal foams can also be formed by coating an organic sponge with a slurry of powdered metal, drying the slurry and firing to remove the organic sponge.

Foaming dramatically extends the range of properties available to the engineer. The enormous extension of properties creates applications for foams which cannot easily be filled by fully dense solids, and offers potential for engineering ingenuity. The low densities permit the design of light, stiff components such as sandwich panels and large portable structures, and of flotation of all sorts. In the last decades, these porous media have been largely studied because of their interesting properties that cover several different technical fields.

In fact, metal foams are lightweight structures, offering high strength and rigidity, high heat transfer surface area which improve energy adsorption and heat transfer in thermal applications [46].

Metal foams have considerable applications in multifunctional heat exchangers, cryogenics, combustion chambers, cladding on buildings, strain isolation, buffer between a stiff structure and a fluctuating temperature field, geothermal operations, petroleum reservoirs, compact heat exchangers for airborne equipment, air cooled condensers and compact heat sinks for power electronics.

2.4.2 The Structure of Metal Foams

2.4.2.1 Fundamental Structures and Definitions [45]

The structure of cells has fascinated natural philosopher for at least 300 years. Hooke examined their shape, Kelvin analysed their packing, and Darwin speculated on their origin and function. The subject is important to us here because the properties of cellular solids depend directly on the shape and structure of the cells.

The most important structural characteristic of a cellular solid is its relative density (ρ^*/ρ_s) (the density, ρ^* of the foam divided by that of the solid of which it is made, ρ_s).

The fraction of pore space in the foam is its porosity and it is simply:

$$\varepsilon = 1 - \frac{\rho^*}{\rho_S} \qquad \textbf{Eq. 257}$$

At first sight one might suppose that the cell size, too, should be an important parameter, and sometimes it is; but most mechanical and thermal properties depend only weakly on cell size.

Cell shape matters much more; when the cells are equiaxed the properties are isotropic, but when the cells are even slightly elongated or flattened the properties depend on direction.

There are important topological distinctions between two-dimensional cells (honeycombs) and three-dimensional cells (foams).

In three dimensions there is also the distinction between cells which are closed (that is, each cell is sealed off from its neighbours by membrane-like faces) and those which are open (so that the cells interconnected).

Another important parameter is connectivity. Considering the open-cell metal foams, the connectivity of cell edges is the number of edges that meet at a node or vertex: usually four, though it can be much higher.

The study of the geometry of foams has interested several relevant scientists. Plateau (1873), in his treatise on solid geometry, identified the cell shape as a rhombic dodecahedron (a 12-faced, garnet shaped figure), and it is certainly possible to partition space into an array of cells with this shape. But it is not the most efficient way to do so. For over a century, it was thought that the space-filling cell which minimizes surface area per unit of volume was Kelvin's tetrakaidecahedron with slightly curved faces. (Kelvin, 1887). Recently, using computer software for minimization of surface area, Weaire and Phelan (1994) have identified

a unit cell of even lower surface area per unit of volume. The unit cell is made up of six 14-sided cells (with 12 pentagonal and 2 hexagonal faces) and two pentagonal dodecahedra, all of equal volume. The 14-sided cells are arranged in three orthogonal axes with the 12-sided cells lying in the interstices between them, giving an overall simple cubic lattice structure.
Only the hexagonal faces are planar: all of the pentagonal faces are curved.
The Kelvin tetrakaidecahedron and the Weaire-Phelan unit cell are illustrated in Figure 156.

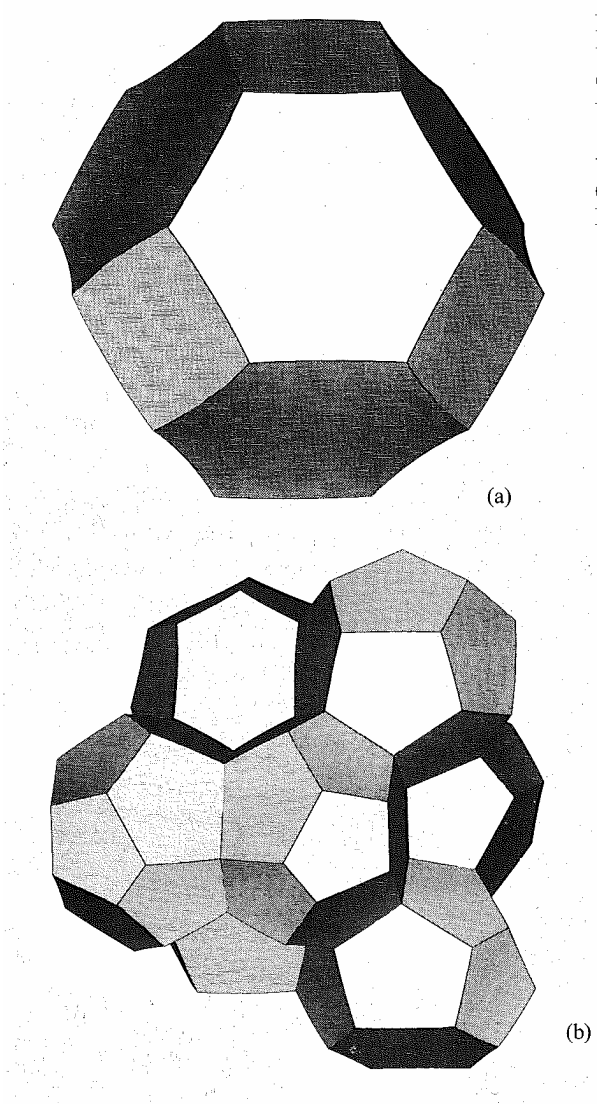

Figure 156. Examples of unit cell models: (a) Kelvin tetrakaidecahedron; (b) Weaire-Phelan unit cell [45].

In three dimensions a great variety of cell shapes is possible. Figure 157 shows most of the shapes that can be packed together to fill space, while Figure 158 shows the resulting cellular solids.

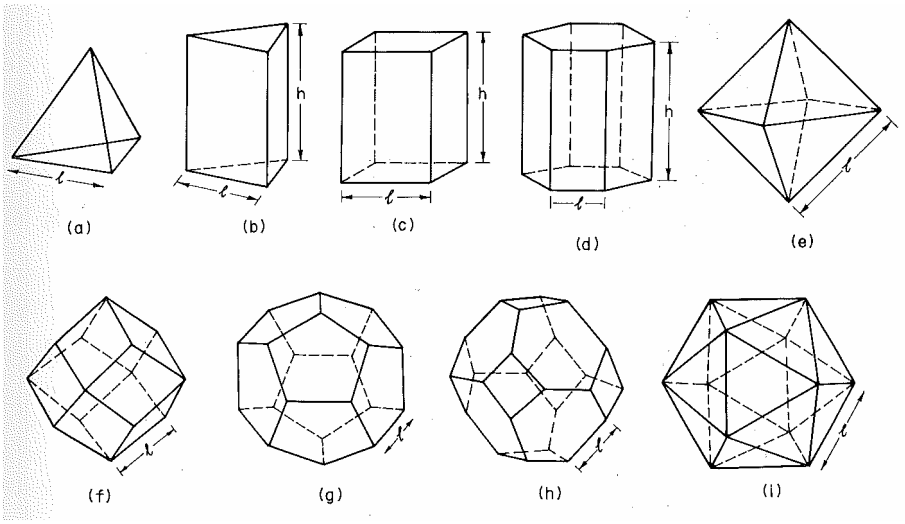

Figure 157. Three-dimensional polyhedral cells: (a) tetrahedron, (b) triangular prism, (c) rectangular prism, (d) hexagonal prism, (e) octahedron, (f) rhombic dodecahedron, (g) pentagonal dodecahedron, (h) tetrakaidecahedron, (i) icosahedron [45].

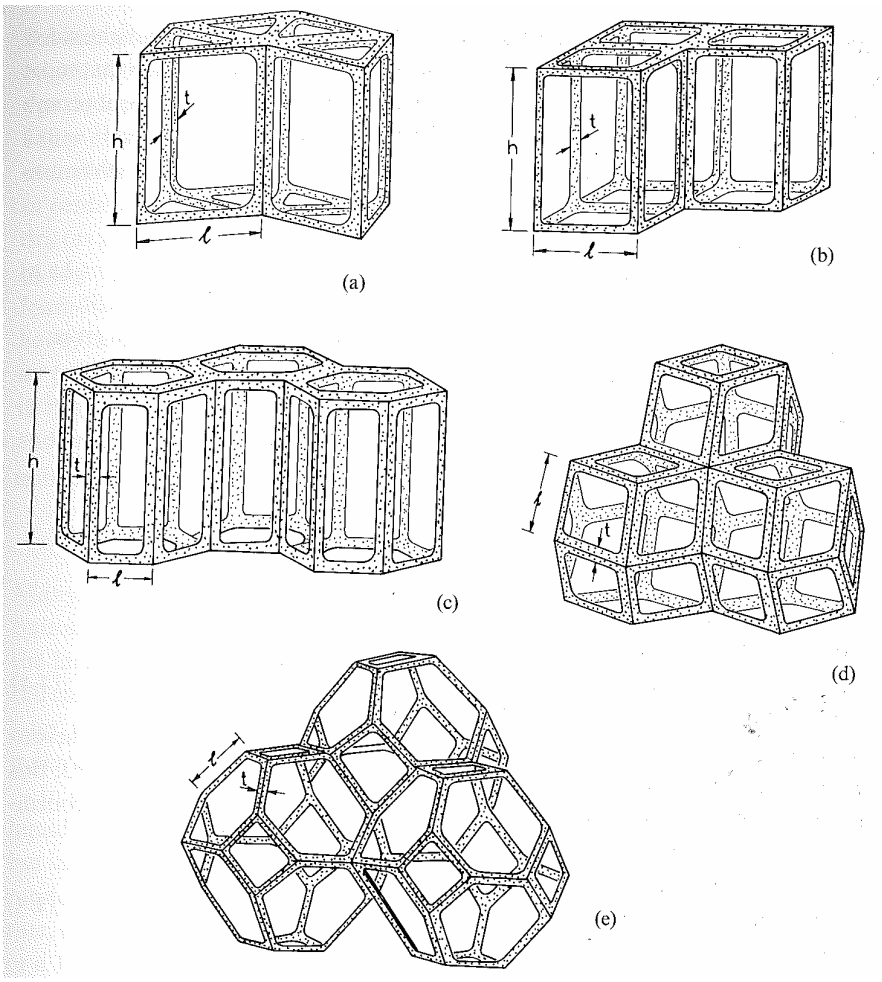

Figure 158. The packing of polyhedra to fill the space: (a) triangular prisms, (b) rectangular prisms, (c) hexagonal prisms, (d) rhombic dodecahedra, (e) tetrakaidecahedra.[45].

All of these unit cell packings have been suggested as idealizations for the cells in foams, together with others which, by themselves, do not pack properly unless distorted: the tetrahedron, the icosahedron and the pentagonal dodecahedron. Most foams, of course, are not regular packings of identical units, but contain cells of different sizes and shapes, with differing numbers of faces and edges.

If the foam is idealized as a packing of different polyhedra and these fill space without any distortions it is possible to calculate the relative density using the geometrical characteristic of the base polyhedron. Gibson and Ashby [45] suggest to use the tetrakaidecahedron because it gives the most consistent agreement with observed properties. The Authors derived geometric relationships for the tetrakaidecahedron unit cell, including the length of the edge of the hexagonal window, *l*.

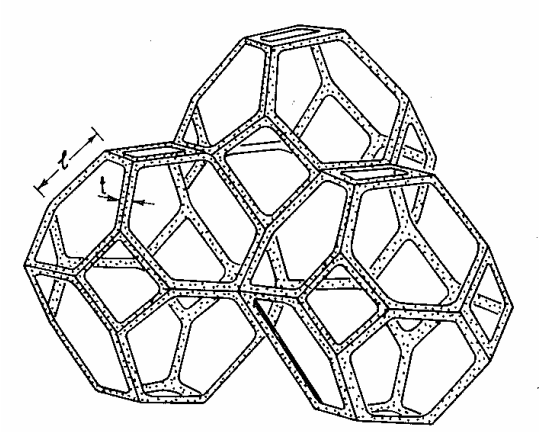

Figure 159. Tetrakaidecahedron structure.

The relative density is given by:

$$\frac{\rho^*}{\rho_S} = 1.06\left(\frac{t}{l}\right)^2 \qquad \textbf{Eq. 258}$$

Thus, measuring the fiber thickness *t* and the length of the edge of the hexagonal window *l*, it is possible to estimate the relative density of the open-cell metal foam.

For a tetrakaidecahedron unit cell, the following geometric relationships are valid.

V_C is the tetrakaidecahedron cell volume:

$$V_C = 11.31 l^3 \qquad \textbf{Eq. 259}$$

S_S is the surface area of the tetrakaidecahedron cell:

$$S_S = 36 t \cdot l \qquad \textbf{Eq. 260}$$

The length of the edge of the hexagonal window can be calculated using d_p, that is the diameter of a circle with an area equivalent to the hexagonal window (of six equilateral triangles of edge *l-t)*.

$$l = \frac{0.5498 d_p}{\left[1 - 0.971\left(1-\varepsilon\right)^{0.5}\right]} \qquad \textbf{Eq. 261}$$

The fiber thickness is obtainable by applying the following equations:

$$t = 0.971\left(1-\varepsilon\right)^{0.5} l = \frac{0.5338 d_p \left(1-\varepsilon\right)^{0.5}}{1 - 0.971\left(1-\varepsilon\right)^{0.5}} \qquad \textbf{Eq. 262}$$

Finally, the expression of the surface area per unit of volume is:

$$S_v = \frac{S_S}{V_C\left(1-\varepsilon\right)} = \frac{12.979\left[1 - 0.971\left(1-\varepsilon\right)^{0.5}\right]}{d_p\left(1-\varepsilon\right)^{0.5}} \qquad \textbf{Eq. 263}$$

Richardson et al. [47] applied similar equations derived for the pentagonal dodecahedron, and they found that the results were very close to those of the tetrakaidecahedron.

2.4.2.2 Other Unit Cell Models

Several Authors have proposed different unit cell idealizations in order to simplify the geometrical characterization of the porous media. The geometrical characteristics of a metal foam can present a wide variation between the nominal pore diameter calculated from the number of pores per inch (PPI) and the measured pore diameter, d_p.

The model suggested by Gibson and Ashby [45], and reported in the previous paragraph, descends from geometrical considerations about the possible structures which packed together can fill space.

Richardson et al. [47], according to Gibson and Ashby [45], propose the tetrakaidecahedron unit cell as a good idealization of the pore structure. In their work, the Authors [47] have also suggested an image technique to measure the mean pore diameter which has been partially applied here.

Calmidi [48] proposed an open-cell representation to approximate the metal foam structure as shown in Figure 160.

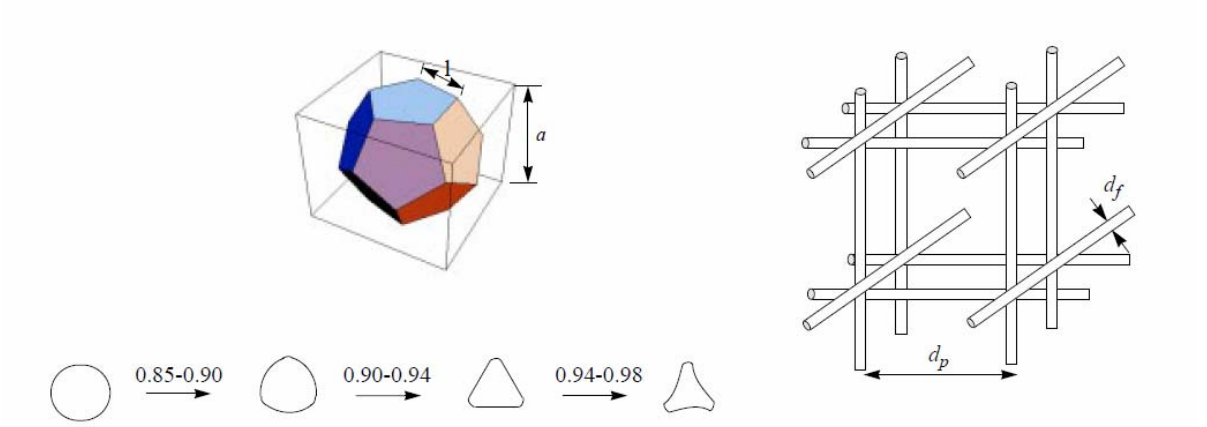

Figure 160. Calmidi [48] open-cell representation of metal foam and schematics of the fiber cross sections at different porosities.

It is shaped as a cube of unit volume, with porosity ε, with N^2 fibers of diameter d_f and N^2 pores of $(d_p)_c$ in each of the *x, y, z* directions. Noting that $N=1/(d_p)_c$ the ratio between the fiber diameter and the pore diameter is given by:

$$\frac{d_f}{(d_p)_c} = 2\sqrt{\frac{1-\varepsilon}{3\pi}}\frac{1}{G} \qquad \textbf{Eq. 264}$$

Where G is the shape function that takes into account the variation of the fiber cross section with porosity, according to Figure 160.

$$G = 1 - e^{-\frac{1-\varepsilon}{0.04}} \qquad \textbf{Eq. 265}$$

Bhattacharya et al. [49] have modified Eq. 264 to reflect the differences between the open-cell representation and the three-dimensional dodecahedron structure. First, with reference to Figure 160, $(d_p)_c$ has been replaced by the characteristic cell size, a, which can be determined by counting the number of cells in a given length of foam.

$$\frac{d_f}{a} = 2\sqrt{\frac{1-\varepsilon}{3\pi}}\frac{1}{G} \qquad \textbf{Eq. 266}$$

The cell size, a, is equivalent to the distance between two parallel pentagons of the dodecahedron structure, and it is equal to 2.23 times the length of the edge of the pentagonal face.

Next, Bhattacharya et al. [49] have made the equivalence between the two structures (cubic and dodecahedral), assuming that the square face formed by the cylinders has the same area as the pentagonal face formed by the fibers in the dodecahedron.

Hence, it is possible to recalculate $(d_p)_c$ as a function of the cell size, a:

$$\left(d_p\right)_c = 0.59a \qquad \textbf{Eq. 267}$$

By replacing a by $(d_p)_c$, Eq. 266 becomes:

$$\frac{d_f}{\left(d_p\right)_c} = 1.18\sqrt{\frac{1-\varepsilon}{3\pi}}\frac{1}{G} \qquad \textbf{Eq. 268}$$

In this paragraph, Bhattacharya et al. [49] model is presented according to the Authors, but in paragraph 2.4.3.3 it will be explained that, in Eq. 268, $(d_p)_c$ must be substituted by the cell size, a.

Finally, it is possible to define the surface area per unit of volume of the unit cell:

$$\left(S_v\right)_c = \frac{3\pi d_f}{\left(d_p\right)_c^2} \qquad \textbf{Eq. 269}$$

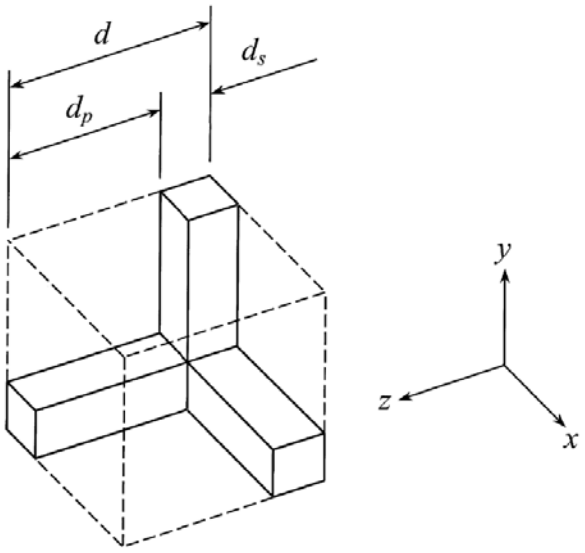

Figure 161. Fourie and Du Plessis [51] representative unit cell for cellular foams.

Du Plessis et al. [50] representative unit cell (RUC) is illustrated in Figure 161. Du Plessis et al. [50] assumed geometrical isotropy "on average" for the foamlike medium. The characteristic linear dimension of the RUC is *d*, which Calmidi [48] and then Bhattacharya et al. [49] called $(d_p)_c$.

With reference to the nomenclature defined in Figure 161, the ratio of the characteristic pore width $(d_p)_d$ to the characteristic RUC dimension *d* can be written as:

$$\frac{\left(d_p\right)_d}{d} = \sqrt{\frac{\varepsilon}{\chi}} = \frac{3-\chi}{2} \qquad \textbf{Eq. 270}$$

Where χ is the tortuosity, which is defined as the total tortuous pore length within a linear length scale, divided by the linear length scale in the porous medium.

Fourie and Du Plessis [51] proposed the following equation:

$$\chi = 2 + 2\cos\left[\frac{4\pi}{3} + \frac{1}{3}\cos^{-1}\left(2\varepsilon - 1\right)\right] \qquad \textbf{Eq. 271}$$

And also the specific surface area of the RUC can be calculated, using:

$$\left(S_v\right)_d = \frac{3}{d}\left(3 - \chi\right)\left(\chi - 1\right) \qquad \textbf{Eq. 272}$$

Finally, it is important to underline that for Du Plessis et al. [50] and Fourie and Du Plessis [51] the cell size, a, and $(d_p)_d$ are linked by:

$$a = \sqrt{3}d \approx 1.7320d \qquad \textbf{Eq. 273}$$

Bhattacharya et al. [49] modified the tortuosity model proposed by Du Plessis et al. [50] giving:

$$\frac{1}{\chi} = \frac{\pi}{4\varepsilon}\left[1 - \left(1.18\sqrt{\frac{1-\varepsilon}{3\pi}}\frac{1}{G}\right)^2\right] \qquad \textbf{Eq. 274}$$

Where G is the shape function defined by Eq. 265.

In Table 52, the three analysed models are summarized and compared, reporting the most important proposed equations.

Table 52. Representative foam structure models.

Parameter	***Link***
Representative Unit Cell	
Gibson and Ashby [45] ***tetrakaidecahedron****: t fiber thickness, l hexagonal face edge length, d_p equivalent diameter of the circle equal to the hexagonal face*	Figure 159
Calmidi [48] (a) and Bhattacharya et al. [49] (b) *(a)* ***cubic unit cell****: d_f fiber diameter and $(d_p)_c$ cubic cell characteristic length* *(b)* ***dodecahedron****: a characteristic cell size, l pentagon face edge length*	Figure 160
Du Plessis et al. [50] and Fourie and Du Plessis [51] ***RUC, representative unit cell****: d characteristic length, d_s fiber thickness, $(d_p)_d = d - d_s$*	Figure 161
Tortuosity	
Bhattacharya et al. [49] $\frac{1}{\chi} = \frac{\pi}{4\varepsilon}\left[1 - \left(1.18\sqrt{\frac{1-\varepsilon}{3\pi}}\frac{1}{G}\right)^2\right]$	Eq. 274
Fourie and Du Plessis [51] $\chi = 2 + 2\cos\left[\frac{4\pi}{3} + \frac{1}{3}\cos^{-1}\left(2\varepsilon - 1\right)\right]$	Eq. 271
Pore Dimensions	
Calmidi [48] $\frac{d_f}{\left(d_p\right)_c} = 2\sqrt{\frac{1-\varepsilon}{3\pi}}\frac{1}{G}$	Eq. 264
Bhattacharya et al. [49] (substitute $(d_p)_c$ with a) $\frac{d_f}{\left(d_p\right)_c} = 1.18\sqrt{\frac{1-\varepsilon}{3\pi}}\frac{1}{G}$	Eq. 268
Fourie and Du Plessis [51] $\frac{\left(d_p\right)_d}{d} = \sqrt{\frac{\varepsilon}{\chi}} = \frac{3-\chi}{2}$	Eq. 270

Surface Area per Unit of Volume	
Gibson and Ashby [45] $S_v = \frac{S_S}{V_C(1-\varepsilon)} = \frac{12.979\left[1-0.971(1-\varepsilon)^{0.5}\right]}{d_p(1-\varepsilon)^{0.5}}$	Eq. 263
Calmidi [48] and Bhattacharya et al. [49] ***(unit cell)*** $(S_v)_c = \frac{3\pi d_f}{(d_p)_c^2}$	Eq. 269
Du Plessis et al. [50] and Fourie and Du Plessis [51] ***(RUC)*** $(S_v)_d = \frac{3}{d}(3-\chi)(\chi-1)$	Eq. 272

2.4.3 Aluminum Metal Foams

2.4.3.1 Introduction and Geometrical Properties

Six aluminum metal foams (acquired from ERG Aerospace, Inc.) have provided in each test sample the most important structural characteristic: relative density. The test samples consist of a 40 mm thick foam core brazed between two 10 mm thick aluminum plates. The technical characteristics, provided by the supplier, of the six test samples used in this work are listed in Table 53.

Table 53. Properties of the aluminum foams provided by ERG Inc.

Sample	***PPI*** [pore/inch]	***Relative Density*** [%]	***Porosity***, ε [-]
S-1	5	7.9	0.921
S-2	10	4.4	0.956
S-3	10	6.6	0.934
S-4	10	9.7	0.903
S-5	20	6.8	0.932
S-6	40	7.0	0.930

As suggested by Richardson et al. [47], the fiber diameter and the length of the fiber between two adjacent vertices were measured by analyzing different high resolution photos. Four photos for each test sample were taken and the measurements were carried out using the tools of CorelDRAW 11 graphic software.

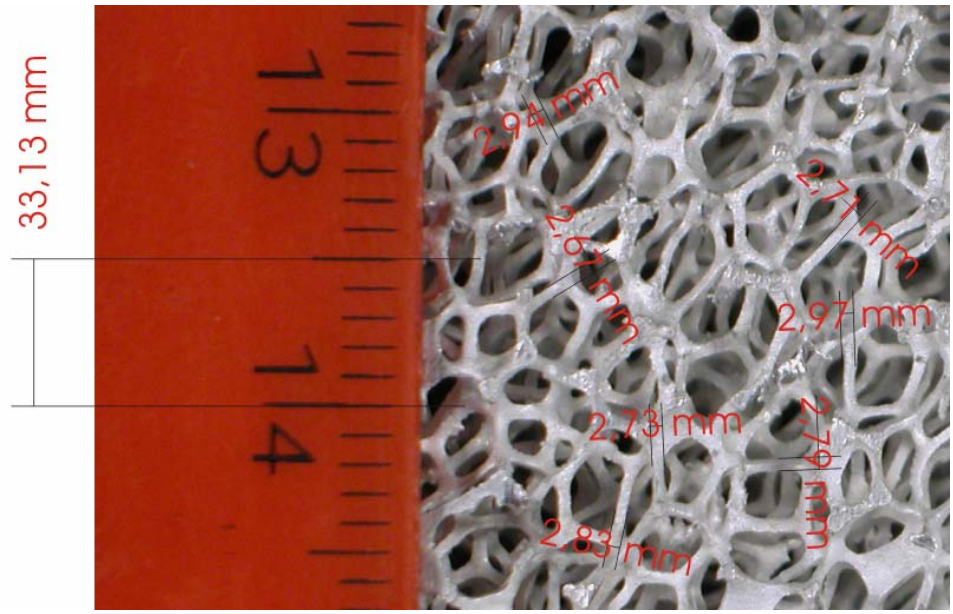

Figure 162. Photo of the fiber thickness measurement procedure (S-3: 10 PPI, ε=0.934).

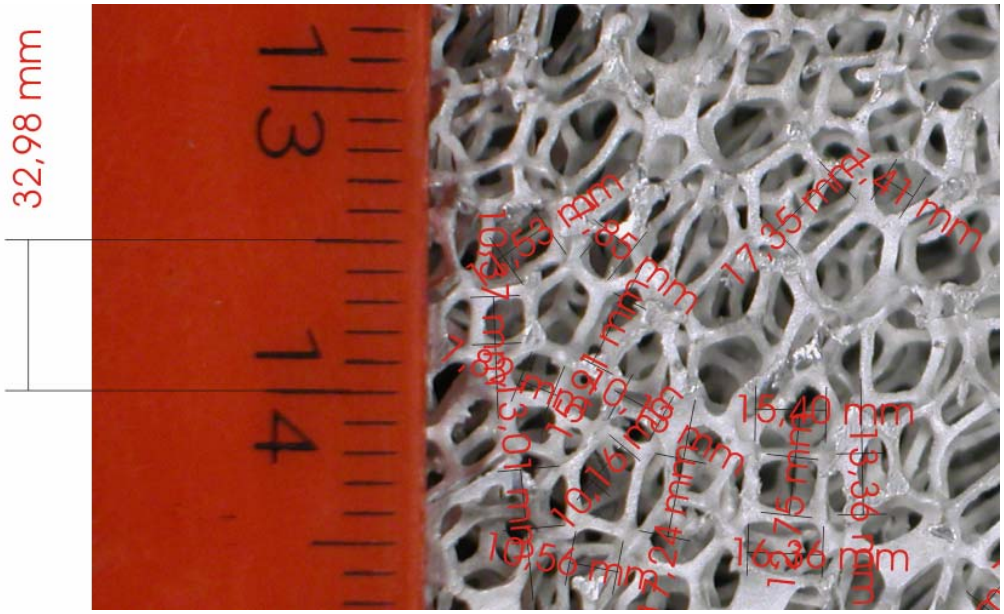

Figure 163. Photo of the edge measurement procedure (S-3: 10 PPI, ε=0.934).

Two examples of the measurement procedure are reported in Figure 162 and Figure 163; in particular, Figure 162 shows the fiber thickness measurement. Several measures for each photo were collected and then statistically analysed. The frequency of the different classes was calculated and then a normal distribution was applied.

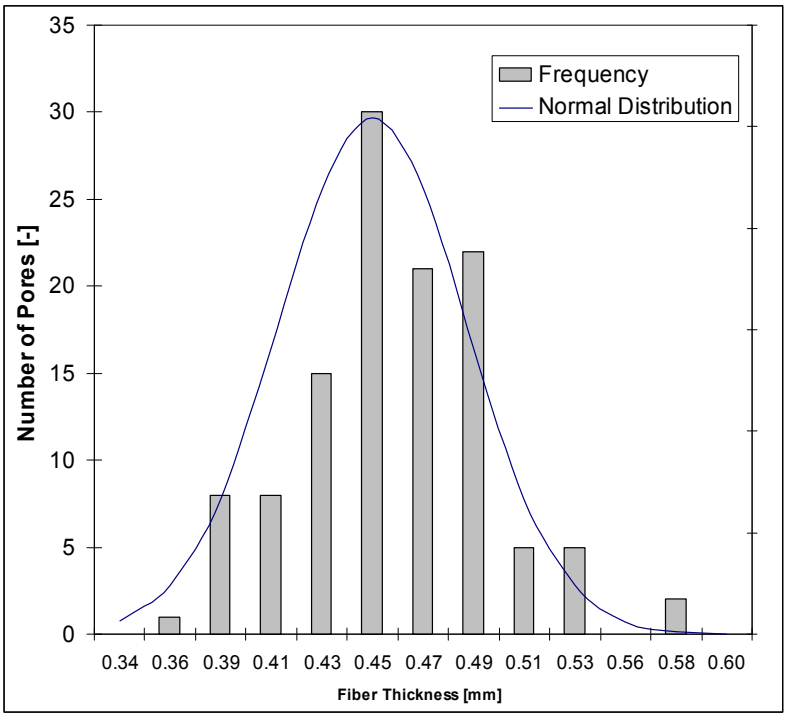

Figure 164. Distribution of the frequencies of fiber thickness measures.

An example of the statistical analysis is plotted in Figure 164; the normal distribution appears to fit well the observed frequencies of the fiber thickness.

Table 54. Fiber thickness measurement: t, d_f or d_s .

Sample	***PPI***	***Mean Value*** [mm]	***Maximum Value*** [mm]	***Minimum Value*** [mm]	***Standard Deviation*** [mm]
S-1	5	0.540	0.681	0.384	0.056
S-2	10	0.445	0.603	0.321	0.050
S-3	10	0.450	0.578	0.364	0.039
S-4	10	0.529	0.782	0.400	0.064
S-5	20	0.367	0.620	0.259	0.062
S-6	40	0.324	0.468	0.240	0.040

Table 55. Fiber length measurement: l.

Sample	***PPI***	***Mean Value*** [mm]	***Maximum Value*** [mm]	***Minimum Value*** [mm]	***Standard Deviation*** [mm]
S-1	5	1.959	3.574	0.917	0.518
S-2	10	1.351	2.376	0.630	0.339
S-3	10	1.785	2.862	0.838	0.423
S-4	10	1.870	3.050	0.922	0.441
S-5	20	1.218	2.009	0.644	0.271
S-6	40	1.072	1.756	0.454	0.254

The results of the measurements for all the experimental specimens are reported in Table 54 and Table 55, in terms of mean value, maximum value, minimum value and standard deviation of the measurements.

Finally, in Table 56, both the measured and the provided properties of the tested aluminum metal foams are summarized.

Table 56. Properties of the tested aluminum foams.

Sample	***PPI***	***Relative Density*** [%]	***Porosity*** [-]	***t, d_f or d_s*** [mm]	***Fiber Length*** [mm]
S-1	5	7.9	0.921	0.540	1.959
S-2	10	4.4	0.956	0.445	1.351
S-3	10	6.6	0.934	0.450	1.785
S-4	10	9.7	0.903	0.529	1.870
S-5	20	6.8	0.932	0.367	1.218
S-6	40	7.0	0.930	0.324	1.072

Although the models proposed for the structure modeling appear to be simple and easy to apply, they present some difficulties because the morphology of the porous medium is complicated and sometimes such defined parameters are hard to understand.

Therefore, in the following, some of the calculation results obtained by applying Gibson and Ashby [45], Calmidi [48], Bhattacharya et al. [49], Fourie and Du Plessis [51] representative models will be presented.

2.4.3.2 Gibson and Ashby [45] Representative Model

The Authors' representative unit cell is the tetrakaidecahedron; its most important characteristics have been discussed in paragraph 2.4.2.

Starting from the measured values, it is possible to follow two different ways: the first is to calculate the porosity starting from the measured properties, while the second consists in the fiber length evaluation using the measured fiber thickness and the relative density provided by the supplier.

The results listed in Table 57 were obtained using the measured geometrical properties. The porosity was calculated by applying Eq. 257 and Eq. 258; it is interesting to highlight that the tetrakaidecahedron structure appears to be in good agreement with the provided porosity. The greater deviation is observed for S-2, which presents the highest porosity, ε=0.956.

Three samples (S-2, S-3, and S-4) with PPI=10 and different relative density (or porosity) have been acquired in order to understand the influence of this property on heat transfer and fluid flow behaviours. For these three samples, the deviation between the calculated and the experimental porosity increases as the porosity decreases. Only one sample results to be underestimated (S-4).

Table 57. Results of Gibson and Ashby [45] model, part 1.

Sample	***PPI***	***t*** [mm]	***l*** [mm]	***Relative Density*** [%]	***Provided Porosity*** [-]	***Calculated Porosity*** [-]	$\frac{\varepsilon_{CALC}-\varepsilon}{\varepsilon}$ [%]
S-1	5	0.540	1.959	7.9	0.921	0.919	0.2
S-2	10	0.445	1.351	4.4	0.956	0.885	7.4
S-3	10	0.450	1.785	6.6	0.934	0.933	0.1
S-4	10	0.529	1.870	9.7	0.903	0.915	-1.4
S-5	20	0.367	1.218	6.8	0.932	0.904	3.0
S-6	40	0.324	1.072	7.0	0.930	0.903	2.9

The second way allows to calculate the hexagonal face edge length *l*, starting from the measured fiber thickness and the provided porosity; the results are summarized in Table 58. Again, only the sample which presents the higher porosity is not fitted by the model; the deviation between the calculated fiber length and that experimentally measured increases with the increasing of the number of pores per inch.

Table 58. Results of Gibson and Ashby [45] model, part 2.

Sample	***PPI***	***t*** [mm]	***Relative Density*** [%]	***l*** [mm]	***Calculated l*** [mm]	***Δl*** [mm]
S-1	5	0.540	7.9	1.959	1.979	0.020
S-2	10	0.445	4.4	1.351	2.183	0.832
S-3	10	0.450	6.6	1.785	1.801	0.016
S-4	10	0.529	9.7	1.870	1.747	-0.123
S-5	20	0.367	6.8	1.218	1.448	0.230
S-6	40	0.324	7.0	1.072	1.261	0.189

From this brief analysis of the model proposed by Gibson and Ashby [45], it appears that this is in great agreement with the experimental measures; only the sample which presents the highest porosity does not match the tetrakaidecahedron structure.

Table 59. Results of Gibson and Ashby [45] model, part 2.

Sample	***PPI***	***Relative Density*** [%]	***t*** [mm]	***l*** [mm]	S_v [m^2m^{-3}]	d_p [mm]
S-1	5	7.9	0.540	1.959	5559	3.252
S-2	10	4.4	0.445	1.351	6753	3.587
S-3	10	6.6	0.450	1.785	6680	2.961
S-4	10	9.7	0.529	1.870	5681	2.872
S-5	20	6.8	0.367	1.218	8187	2.380
S-6	40	7.0	0.324	1.072	9268	2.072

Table 59 lists the results of the calculations obtained by applying the representative model proposed by Gibson and Ashby [45], among which are the surface area per unit of volume (Eq. 263) and the diameter d_p.

2.4.3.3 The Other Structural Models: Calmidi [48], Bhattacharya et al. [49], Du Plessis et al. [50] and Fourie and Du Plessis [51].

In paragraph 2.4.2.2, two alternative structural models were presented and compared in order to propose alternative interpretations of foams. These models were developed in order to describe the heat transfer and fluid flow behaviours of different porous media.

In this paragraph, the model proposed by Calmidi [48] and rielaborated by Bhattacharya et al. [49] is compared against the representative idealization suggested by Du Plessis et al. [50] and Fourie and Du Plessis [51].

Figure 165 reports the comparison between the proposed tortuosity models, where tortuosity is a function of porosity. These calculations were performed using the porosities of the six test samples. As highlighted, the model proposed by Fourie and Du Plessis [51] decreases as the porosity increases, while the equation suggested by Bhattacharya et al. [49] increases. The two models present the same tortuosity for porosity, equal to 0.96.

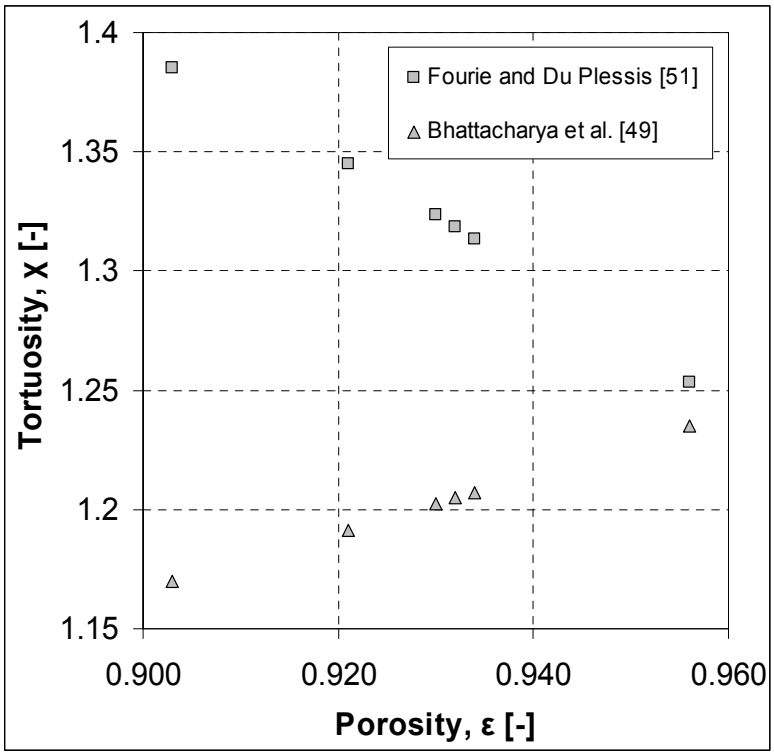

Figure 165. Comparison between the two tortuosity models, with tortuosity as a function of the porosity.

After this comparison, some calculations were done to evaluate the different experimental properties used in the heat transfer and fluid flow analyses.

Table 60. Results of the Calmidi [48] model.

Sample	***PPI***	***Relative Density*** [%]	***t*** [mm]	$d_f / (d_p)_c$ [mm]	$(d_p)_c$ [mm]
S-1	5	7.9	0.540	0.2126	2.541
S-2	10	4.4	0.445	0.2048	2.171
S-3	10	6.6	0.450	0.2071	2.170
S-4	10	9.7	0.529	0.2226	2.375
S-5	20	6.8	0.367	0.2079	1.765
S-6	40	7.0	0.324	0.2086	1.553

Using the relative density and the measured fiber thickness, it is possible to calculate the pore diameter suggested by Calmidi [48]; the results are listed in Table 60.

When the revised model proposed by Bhattacharya is applied, the calculation can be performed starting from the relative density and from the cell size or using the fiber thickness.

Table 61. Results of Bhattacharya et al. [49] model.

Sample	***PPI***	***Relative Density*** [%]	***t*** [mm]	$d_f / (d_p)_c$ [mm]	$(d_p)_c$ [mm]
S-1	5	7.9	0.540	0.1254	4.307
S-2	10	4.4	0.445	0.1209	3.680
S-3	10	6.6	0.450	0.1222	3.678
S-4	10	9.7	0.529	0.1313	4.025
S-5	20	6.8	0.367	0.1226	2.991
S-6	40	7.0	0.324	0.1231	2.632

The results reported in Table 61 appear quite strange, as the calculated pore diameter is far from those obtained applying Calmidi et al. [48] model. In fact, present authour suggests to $(d_p)_c$ with the cell size a in Eq. 268, paragraph 2.4.2.2.

Therefore, in Table 62, the results of the modified Bhattacharya et al. model are proposed. The calculated fiber thicknesses are in good agreement with the measured ones, and the new computed pore diameters are closer to those presented in Table 60. Hence in Eq. 268 it is important to substitute $(d_p)_c$ with the cell size, which is estimated to be 2.23 times the measured fiber length.

Table 62. Results of the modified Bhattacharya et al. [49] model.

Sample	***PPI***	***Relative Density*** [%]	d_f [mm]	***a*** [mm]	Calculated d_f [mm]	$(d_p)_c$ [mm]
S-1	5	7.9	0.540	4.369	0.548	2.577
S-2	10	4.4	0.445	3.013	0.364	1.778
S-3	10	6.6	0.450	3.981	0.486	2.349
S-4	10	9.7	0.529	4.170	0.548	2.460
S-5	20	6.8	0.367	2.716	0.333	1.603
S-6	40	7.0	0.324	2.391	0.294	1.410

Finally, the calculation results obtained by applying Fourie and Du Plessis [51] model are reported in Table 63. The characteristic cell length $(d_p)_d$ is calculated using again the measured fiber thickness. Comparing the characteristic unit cell lengths proposed by the different Authors, it can be seen that there is a great agreement.

Table 63. Results of the Fourie and Du Plessis [51] model.

Sample	***PPI***	***Relative Density*** [%]	d_s [mm]	d_s / d [-]	Calculated d [mm]	$(d_p)_d$ [mm]
S-1	5	7.9	0.540	0.1725	3.132	2.592
S-2	10	4.4	0.445	0.1266	3.514	3.069
S-3	10	6.6	0.450	0.1567	2.868	2.418
S-4	10	9.7	0.529	0.1926	2.744	2.216
S-5	20	6.8	0.367	0.1592	2.303	1.937
S-6	40	7.0	0.324	0.1617	2.003	1.679

Finally, in Table 64 the three models are applied to calculate the surface area per unit of volume of the representative unit cell.

The highest values have been obtained by the equation suggested by Calmidi [48], while the lowest are exhibited by Fourie and Du Plessis [51] model.

Table 64. Unit cell surface area per unit of volume models.

Sample	***PPI***	***Relative Density*** [%]	S_v [m^2m^{-3}]		
			Calmidi [48]	Bhattacharya et al. [49]	Fourie and Du Plessis [51]
S-1	5	7.9	789	766	547
S-2	10	4.4	889	1327	378
S-3	10	6.6	900	768	553
S-4	10	9.7	883	823	680
S-5	20	6.8	1110	1346	698
S-6	40	7.0	1266	1535	812

2.4.4 Experimental Results

2.4.4.1 Introduction

As reported in the brief initial overview, numerous Authors have investigated heat transfer and fluid flow through cellular structure materials and, in particular, through foams. Considering the heat transfer behaviour of metal and non-metal foams, this topic has been experimentally studied by different research groups all over the world, among which: Calmidi and Mahajan [25], Calmidi [48], Hsieh et al. [26], Kim et al. [27], Hwang et al. [28], Kim et al. [29], Dukhan and Chen [53], Giani et al. [54], Fu et al. [55], Younis and Viskanta [56].

Pressure drops during single-phase flow through porous media, foams, have been experimentally measured by several scientists such as Richardson et al. [47], Bhattacharya et al. [49], Beavers and Sparrow [52], Paek et al. [57], Liu et al. [58], Hamaguchi et al. [59] and Vafai and Tien [60].

Moreover, heat transfer and fluid flow have been modeled by various Authors; a complete synthesis of the proposed correlations for heat transfer coefficient and pressure drop estimation has been suggested by Mahjoob and Vafai [61].

The experimental results concerning heat transfer and fluid flow of air through five aluminum metal foams will be presented in the following paragraphs.

2.4.4.2 Set-up Arrangement

The test facility was set up in order to allow heat transfer and pressure drop measurements for single-phase air flow through different Al 6101 alloy aluminum foams. Five of the six previously characterized samples were tested: S-1, S-2, S-3, S-4, S-6. The remaining, S-5, with 20 PPI and a porosity of 0.932, will be characterized in a different experimental campaign.

The samples were located in the bakelite channel on a copper heater measuring 100 x 100 mm, which was designed as described in paragraph 2.2.4.1 and illustrated in Figure 166. The aluminum foam samples were equipped with twelve T-Type calibrated thermocouples, inserted in twelve holes drilled into two guides milled all around the two aluminum plates. Six thermocouples were inserted in the upper plate and six in the bottom one (Figure 168). They were used to measure the temperatures of the two plates during the heat transfer measurements.

A new mixer was designed to ensure uniform distribution of air at the exit of the test sample; the device was different from the one developed for the finned surface measurements.

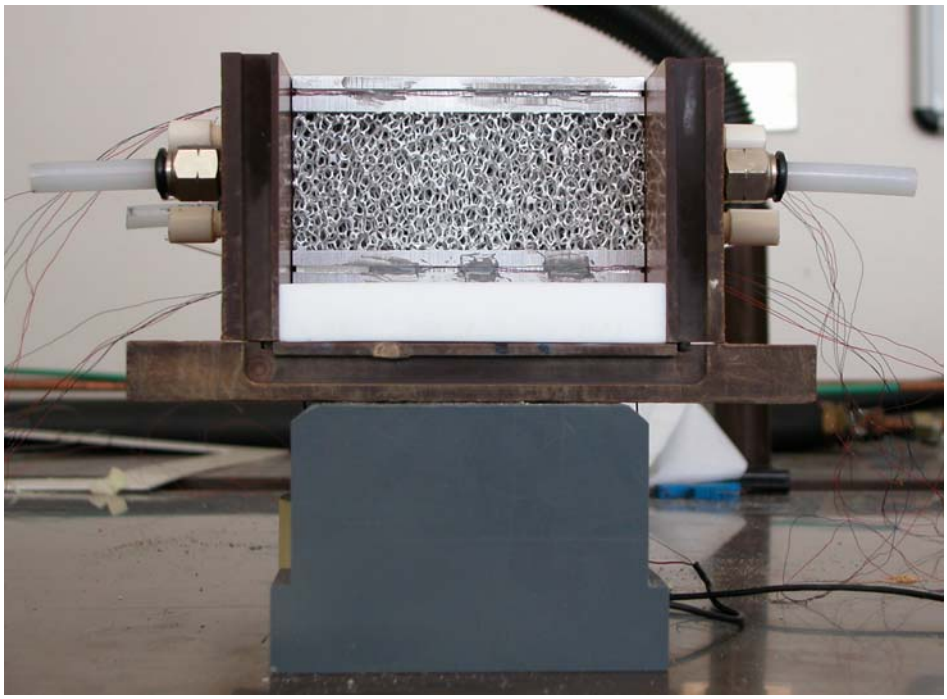

Figure 166. Photo of an instrumented test sample inserted in a part of the bakelite channel during the assembly work.

Figure 167 shows a top-view photo of the new mixer. When the air arrives, it is vertically mixed by several horizontal fins; it is then displaced by the vertical obstacles and, finally, two horizontal blocks are inserted.

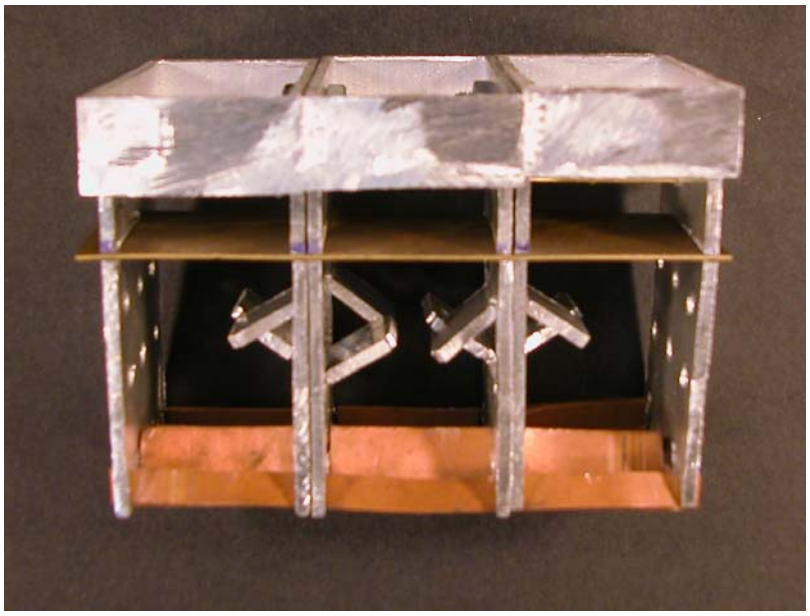

Figure 167. Top view photo of the new mixer especially designed for the aluminum foam tests.

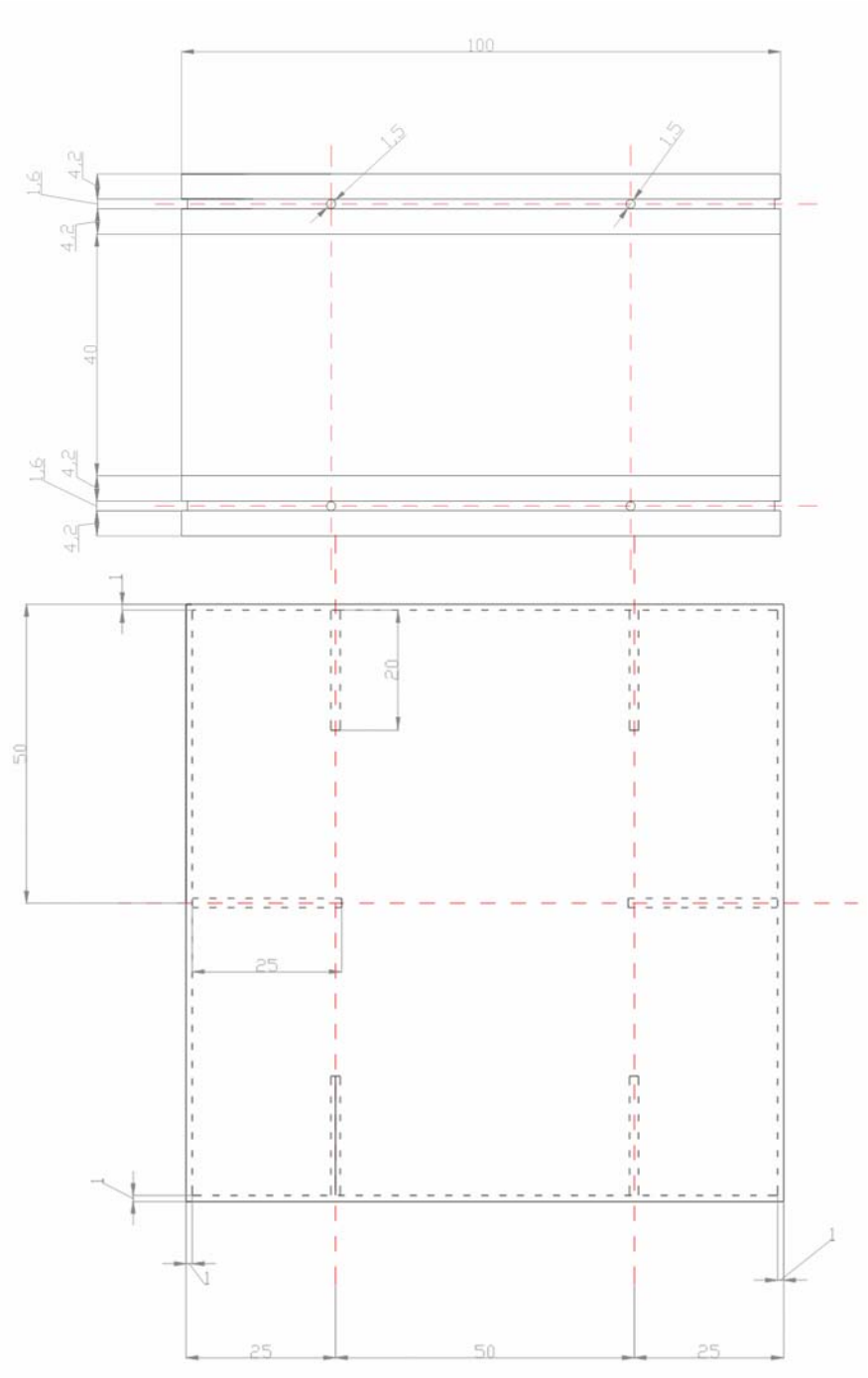

Figure 168. Executive drawing of the test sample.

The shape of this mixer was designed to allow it to be located after the test sample, before the temperature probes.

The other technical solutions have been discussed in paragraph 2.2.4. The fully equipped test section for the foam heat transfer and pressure drop measurements is illustrated in Figure 169.

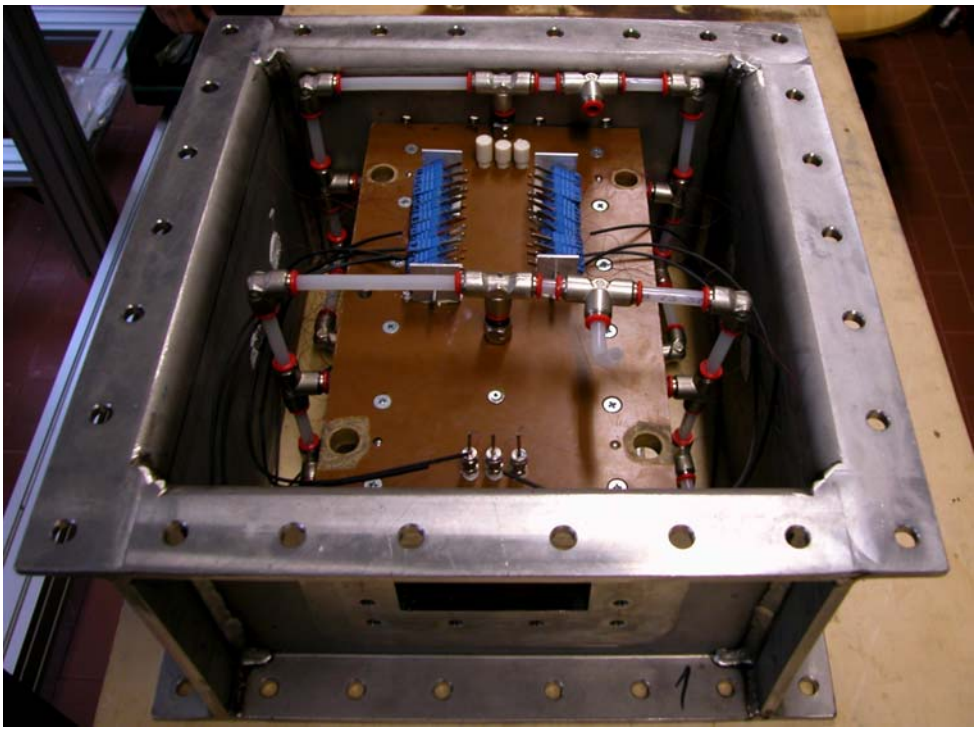

Figure 169. Photo of the fully equipped test section.

Sixteen calibrated T-Type thermocouples were inserted at the inlet and outlet of the test section to measure temperature distributions: eight of them were located at the inlet and eight at the outlet.

Three of the eight temperature probes inserted at the outlet of the test section are evident in Figure 169, which also show the pressure measurement lines.

2.4.4.3 Data Reduction

In paragraph 2.2.5, the data reduction procedure was presented, but not all calculated parameters were analyzed, because some of them are exclusive to each test sample. While the heat transfer coefficient can be calculated by the Eq. 212 defined in paragraph 2.2.5.1 using the base area, the pressure drops can be analyzed differently.

In particular, the foams are characterized by two important parameters which describe the fluid flow through their structure: the permeability, K, and the inertia coefficient, f. As suggested by Beavers and Sparrow [52], which based their analysis on the first study on non-Darcy flow in porous media proposed by Reynolds (1900), the experimental pressure gradient may be represented by the form:

$$\left(-\frac{dp}{dz}\right)_{EXP} = \frac{\mu \cdot u}{K} + \frac{\rho \cdot f \cdot u^2}{\sqrt{K}} \qquad \textbf{Eq. 275}$$

Beavers and Sparrow [52] present the following rationale to support the form of Eq. 275. For very low speed flow, i.e. Darcy flow, it is well established that the pressure gradient is a linear function of the velocity. At higher velocities, departures from Darcy's law are due to inertial effects, first such as separation (i.e. form drag) and later such as turbulence. Inertia effects are reckoned to be proportional to ρu^2.

K is the permeability of the porous media, which, according to Darcy's law, is the measure of the flow conductance of the matrix; it is expressed in m^2 (Kaviany) [62]. The second term reports the quadratic dependence of the pressure drop on the velocity and defines the inertia coefficient, f. The other quantities are the air dynamic viscosity, μ, the air density, ρ, and the air frontal velocity at the inlet of the foam, u.

The collected experimental data points allow to estimate the permeability K and the inertia coefficient f. In fact, Eq. 275 can be rewritten as:

$$\left(-\frac{dp}{dz}\right)_{EXP} \cdot \frac{1}{u} = \frac{\mu}{K} + \frac{\rho \cdot f \cdot u}{\sqrt{K}} = a + b \cdot u \qquad \textbf{Eq. 276}$$

The experimental results have shown that the pressure gradient divided by the air velocity is a linear function of the air velocity, and the two constants *a* and *b* allow to calculate the permeability and inertia coefficient, respectively.

$$K = \frac{\mu}{a}$$ **Eq. 277**

And:

$$f = \frac{b\sqrt{K}}{\rho}$$ **Eq. 278**

2.4.4.4 Experimental Uncertainty

As in the case of the traditional finned surface, the theory of experimental uncertainty is not presented here, because it has been analyzed in paragraph 1.3.2.1.

Starting from the air heat flow rate, the maximum and average experimental values of its uncertainty are reported in Table 65.

Table 65. Air heat flow rate experimental uncertainty.

	q_{air}	Δt_{air}	$\dot{m}_{air}$
i_m [%]	1.33	0.41	0.8
i_{max} [%]	1.41	0.71	0.8

The experimental uncertainty of the air heat flow rate is always lower than ±1.5%, this is due to the uncertainty of the air temperature difference, which is low because the air temperature gain through the heated samples is always higher than 9.9 °C.

Considering the product of the heat transfer coefficient and the surface area efficiency, called global heat transfer coefficient, its uncertainty analysis is summarized in Table 66.

Table 66. Heat transfer coefficient experimental uncertainty.

	$HTC\ \Omega^*$	Δt_{ml}	P_{EL}
i_m [%]	1.03	0.11	0.08
i_{max} [%]	1.02	0.19	0.08

The uncertainty of the heat transfer coefficient is almost constant and equivalent to ±1%, its maximum value is 9.7 W m^{-2} K^{-1}.

Finally, the pressure drop uncertainty depends on the differential pressure transducer used in the experimental campaign. In order to measure the air pressure drops through the aluminum foam, the Rosemount instrument has been substituted by the Druck one (1000 Pa full scale). This differential pressure transducer has an accuracy of ±1 Pa, hence the average uncertainty on the experimental pressure drops is ±0.27%, with a maximum value of ±0.91%. Considering the permeability and inertia coefficient, they present an uncertainty of ±0.8% and ±1.4%, respectively.

2.4.4.5 Operating Test Conditions

Heat transfer coefficient and pressure drop measurements during air flow through five aluminum metal foams were carried out. The most important experimental test conditions are listed in Table 67. The heat balance between the electric power supplied to the test sample and the measured heat flow rate was also controlled.

The measurements were taken imposing three different heat fluxes: 250 W, 325 W and 400 W, which correspond to 25.0, 32.5 and 40.0 kW m^{-2}, respectively. The air flow rate was varied between 0.01 and 0.025 kg s^{-1}, while the pressure at the inlet of the test section was always set around the value of that of ambient conditions.

Table 67. Operating test conditions.

Parameter	***Range***
Air Mass Flow Rate	0.01– 0.025 kg s^{-1}
Absolute Pressure	Near Ambient Conditions
Heat Flux	250, 325 and 400 W
Air Frontal Velocity	2.0 – 5 m s^{-1}

The most important properties of the studied Al6001 alloy aluminum foams are summarised in Table 56 for reader convenience.

Table 68. Properties of the tested aluminum foams.

Sample	***PPI***	***Relative Density*** [%]	***Porosity ε*** [-]	***Fiber Thickness*** [mm]	***Fiber Length*** [mm]
S-1	5	7.9	0.921	0.540	1.959
S-2	10	4.4	0.956	0.445	1.351
S-3	10	6.6	0.934	0.450	1.785
S-4	10	9.7	0.903	0.529	1.870
S-5	20	6.8	0.932	0.367	1.218
S-6	40	7.0	0.930	0.324	1.072

In the following, the experimental results in terms of heat balance, heat transfer coefficient, pressure drop, permeability and inertia coefficient will be presented for S-1, S-2, S-3, S-4, S-6 samples, then the heat transfer behaviour of all the tested specimens will be compared.

2.4.4.6 5 PPI Aluminum Foam Sample: S-1

The experimental measurements of 5 PPI aluminum foam with a porosity of 0.921 are here presented.

In Figure 170, the *HB* calculated value is plotted against the air mass flow rate. The heat balance decreases as the flow rate increases; the measured air heat flow rate is always lower than the supplied electric power, and it appears to be independent of the heat flux.

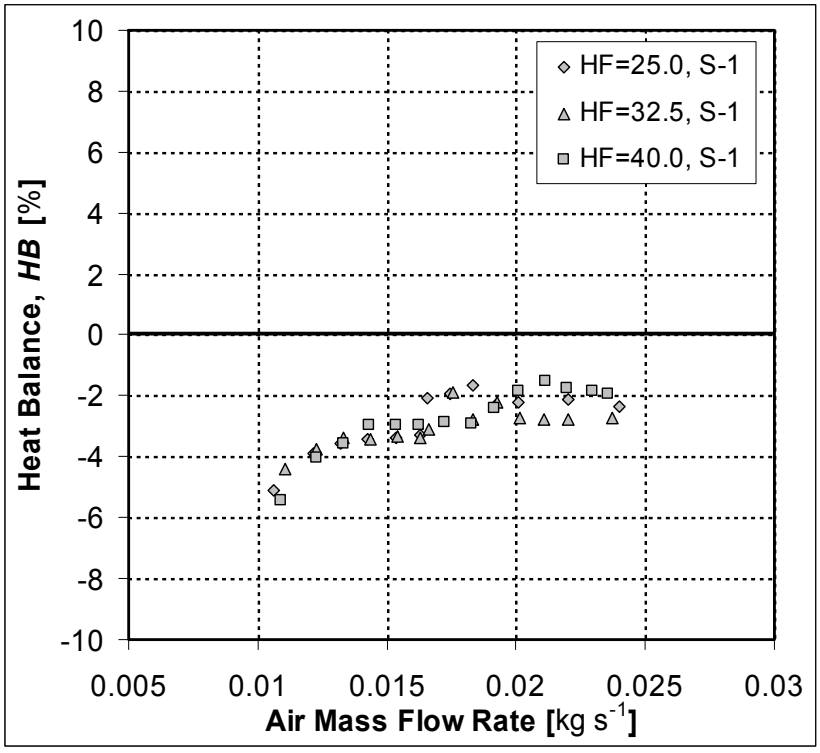

Figure 170. Heat balance plotted against air mass flow rate. HF: Heat Flux [kW m^{-2}]

Figure 171 and Figure 172 report the heat transfer results. The global heat transfer coefficient and the mean wall temperature are plotted against the air mass flow rate as a function of the imposed heat flux. The global heat transfer coefficient appears to be independent from the imposed heat flux.

It increases with increasing air flow rate and it varies between 591 and 816 W m^{-2} K^{-1}. The mean wall temperature, calculated according to Eq. 215, imposing $t_{air,in}$=25 °C , decreases as the air flow rate increases. At a constant mass flow rate, the temperature increases with the electric power.

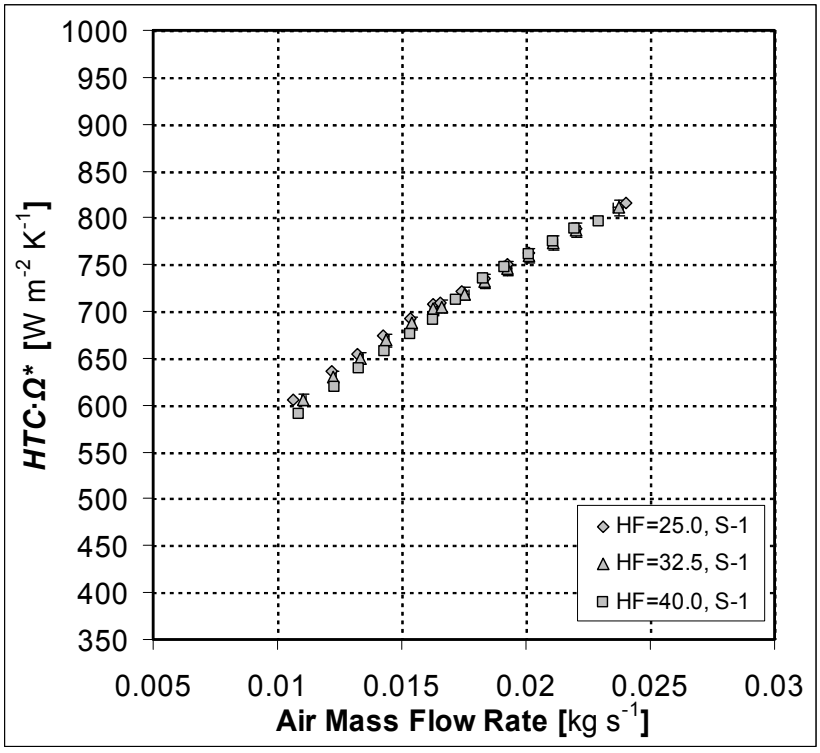

Figure 171. Global heat transfer coefficient of the S-1 plotted against air mass flow rate. HF: Heat Flux [kW m^{-2}]

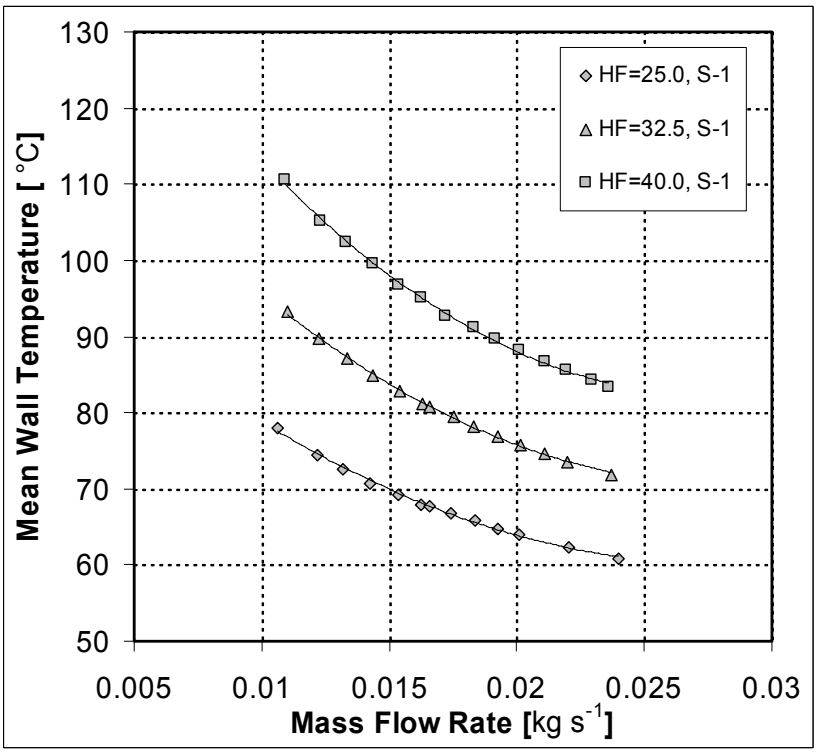

Figure 172. Mean wall temperature evaluated using Eq. 215. t_{air}*=25* °C. *HF: Heat Flux* [kW m^{-2}].

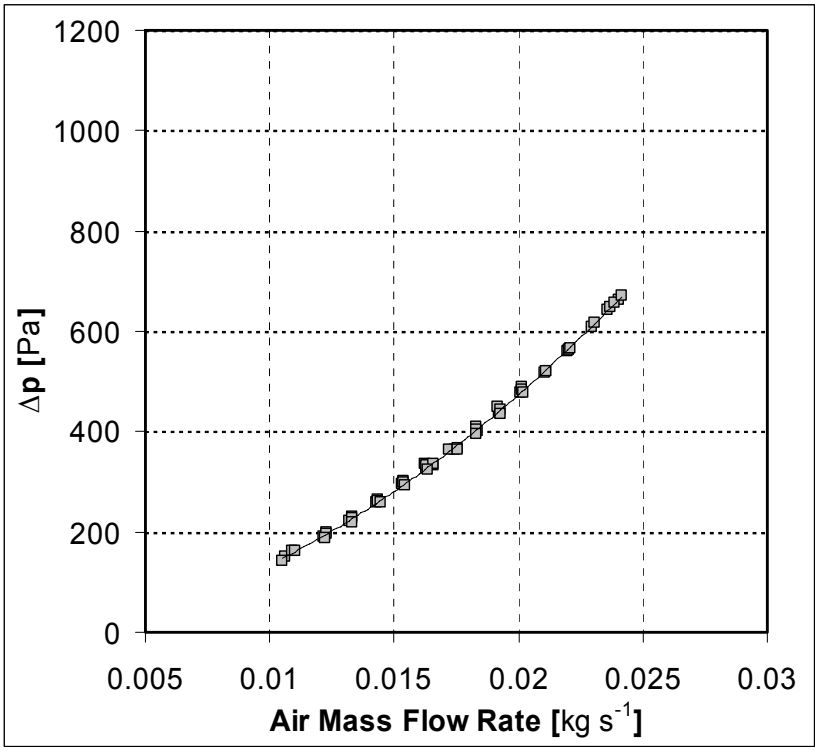

Figure 173. Experimental pressure drops plotted against air mass flow rate.

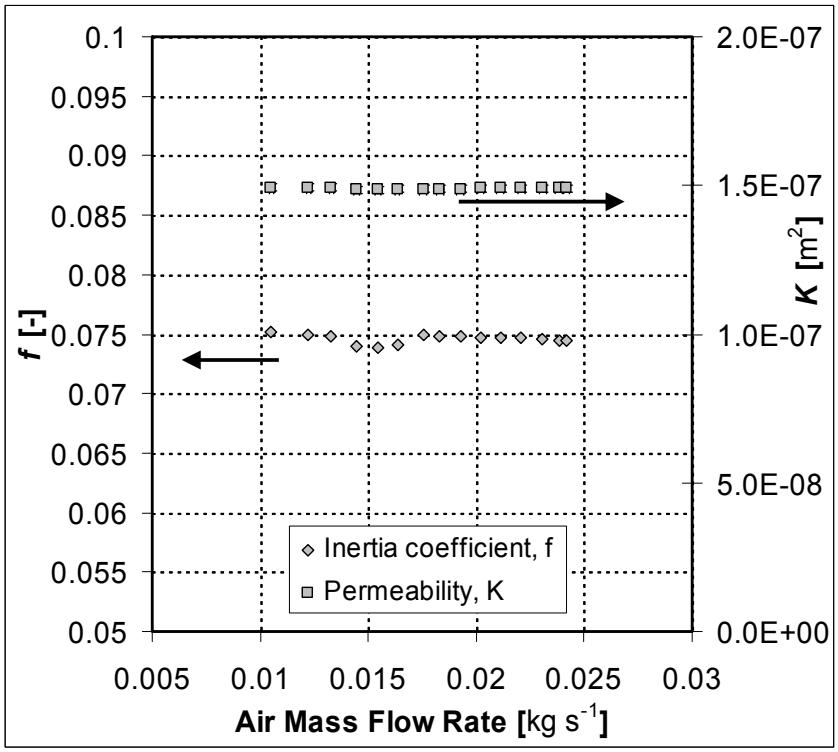

Figure 174. Inertia coefficient f and permeability K plotted against air mass flow rate.

The fluid flow results are reported in Figure 173 and Figure 174. In particular, Figure 173 plots the pressure drop as a function of the flow rate; it appears that the pressure losses increase as the mass flow rate increases, rising from 149 to 664 Pa when the air flow rate changes from 0.011 to 0.024 kg s^{-1}.

Figure 174 illustrates the inertia coefficient, f, and the permeability, K, plotted against the air mass flow rate. These values appear to be constant for all operating test conditions; the inertia coefficient varies between 0.074 and 0.075, while the permeability ranges between 1.484 and 1.493 (10^{-7}) m^2

2.4.4.7 10 PPI Aluminum Foam Sample: S-2

The experimental measurements of 10 PPI aluminum foam with a porosity of 0.956 are here presented.

As it appears from the next figures, only two data sets were carried out for this test sample, imposing 250 W and 325 W. In fact, since the sample has low heat transfer performance, the wall temperature sharply increases as the electric power increases. Thus, in order to prevent any possible damage to the test section, the experimental tests were stopped at 325 W.

First of all, the heat balance between the electric power and the measured heat flow rate is presented. Figure 175 plots the *HB* deviations against the air mass flow rate.

The heat balance is quite constant with the flow rate; the measured air heat flow rate is always lower than the supplied electric power.

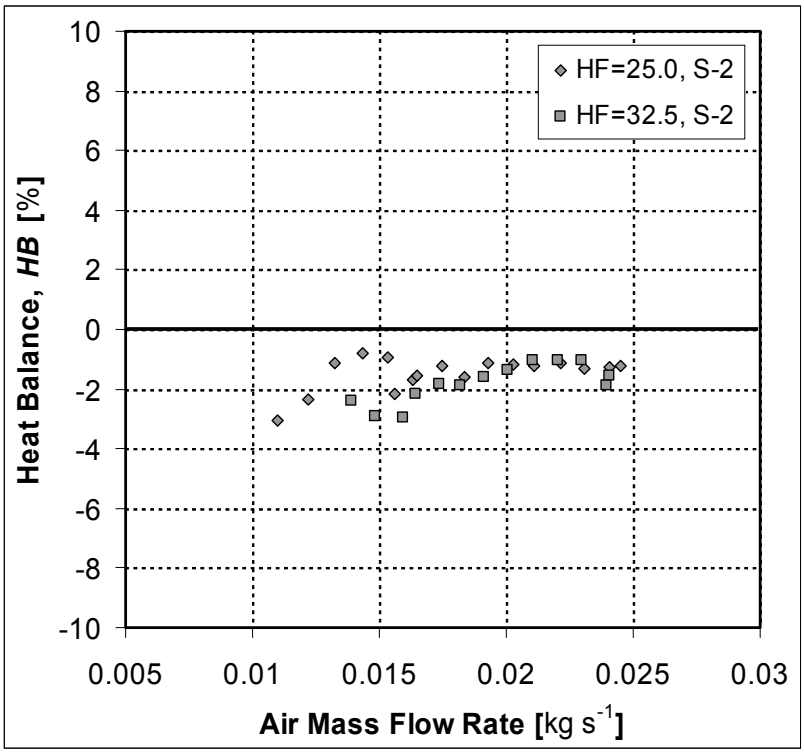

Figure 175. Heat balance plotted against air mass flow rate. HF: Heat Flux [kW m^{-2}].

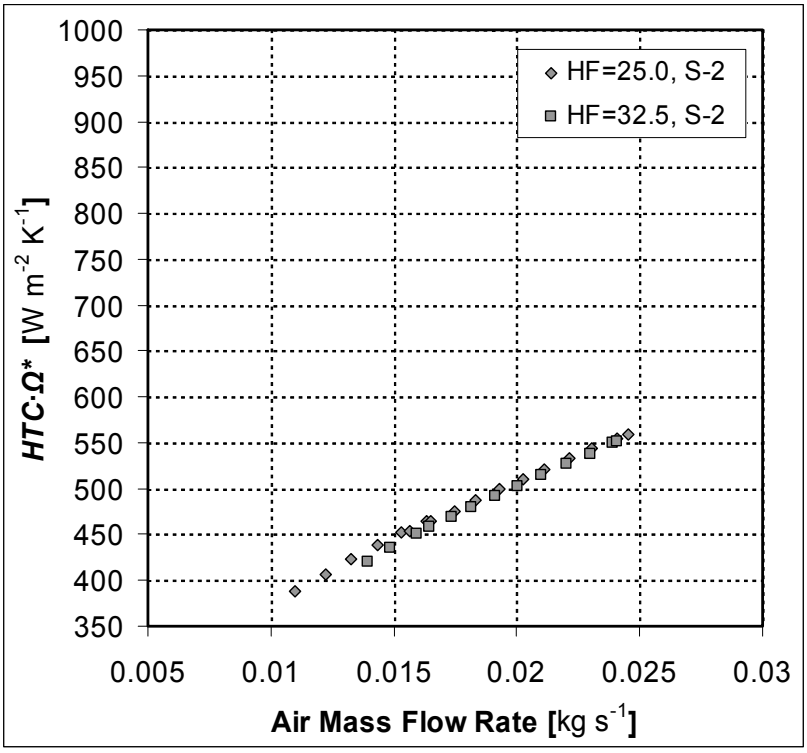

Figure 176. Global heat transfer coefficient of S-2 plotted against air mass flow rate. HF: Heat Flux [kW m^{-2}].

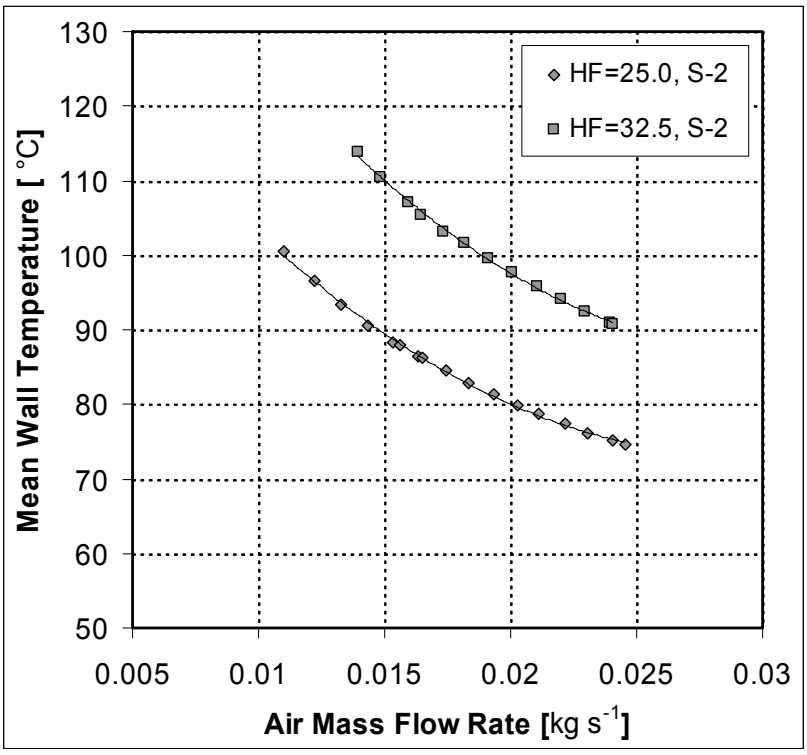

Figure 177. Mean wall temperature evaluated using Eq. 215. t_{air}*=25* °C*. HF: Heat Flux* [kW m^{-2}].

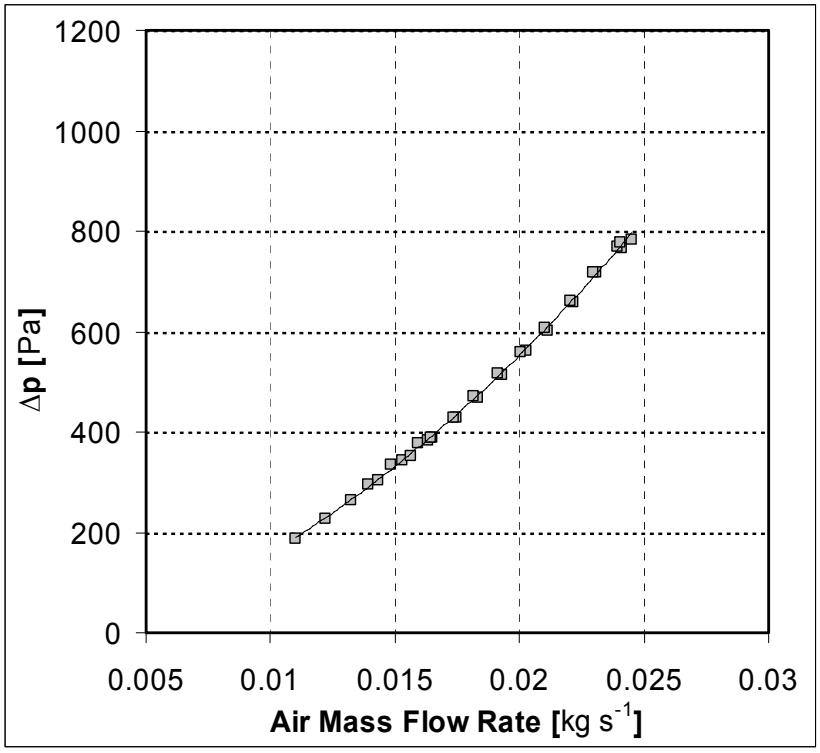

Figure 178. Experimental pressure drops plotted against air mass flow rate.

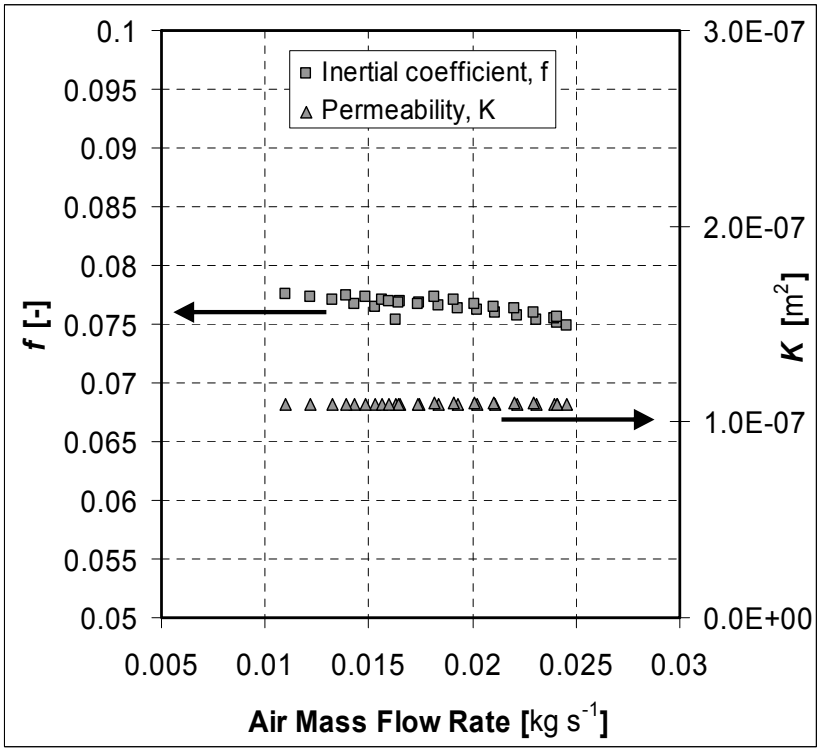

Figure 179. Inertia coefficient f and permeability K plotted against air mass flow rate.

Figure 176 and Figure 177 report the heat transfer results. The global heat transfer coefficient and the mean wall temperature are plotted against the air mass flow rate as a function of the imposed heat flux. The global heat transfer coefficient appears to be independent from the imposed heat flux. It increases with increasing air flow rate, varying between 388 and 560 W m^{-2} K^{-1}. The mean wall temperature, calculated according to Eq. 215, imposing $t_{air,in}$=25 °C, decreases as the air flow rate increases. At constant mass flow rate, the temperature increases with the imposed electric power.

The fluid flow results are reported in Figure 178 and Figure 179. In particular, Figure 178 plots the pressure drops as a function of the flow rate; it appears that the pressure losses increase as the mass flow rate increases, varying between 188 and 784 Pa.

Figure 179 illustrates the inertia coefficient, f, and the permeability, K, plotted against the air mass flow rate. These values appear to be quite constant for all operating test conditions. The inertia coefficient varies between 0.075 and 0.078, while the permeability ranges between 1.087 and 1.095 (10^{-7}) m^2.

2.4.4.8 10 PPI Aluminum Foam Sample: S-3

The experimental measurements of 10 PPI aluminum foam with a porosity of 0.934 are here presented.

First of all, the heat balance between the imposed electric power and the measured air heat flow rate is presented in Figure 180, plotted against the air mass flow rate. *HB* is negative, and it decreases when the air flow rate rises from 0.01 to around 0.017 kg s^{-1}, where *HB* is equal to zero. Then, the deviation increases as the air flow rate increases.

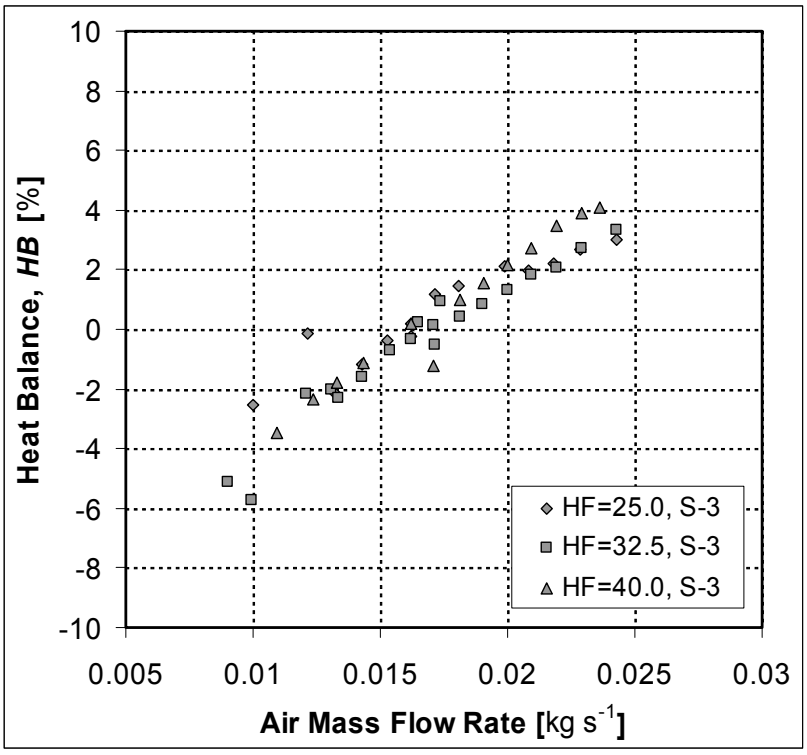

Figure 180. Heat balance plotted against air mass flow rate. HF: Heat Flux [kW m^{-2}].

Figure 181 and Figure 182 report the heat transfer result. The global heat transfer coefficient and the mean wall temperature are plotted against the air mass flow rate as a function of the imposed heat flux. The global heat transfer coefficient appears to be independent from the imposed heat flux and it increases when the flow rate increases, varying between 486 and 753 W m^{-2} K^{-1}. The mean wall temperature, calculated according to Eq. 215, imposing $t_{air,in}$=25 C, decreases as the air flow rate increases. At constant mass flow rate, the temperature increases with the electric power.

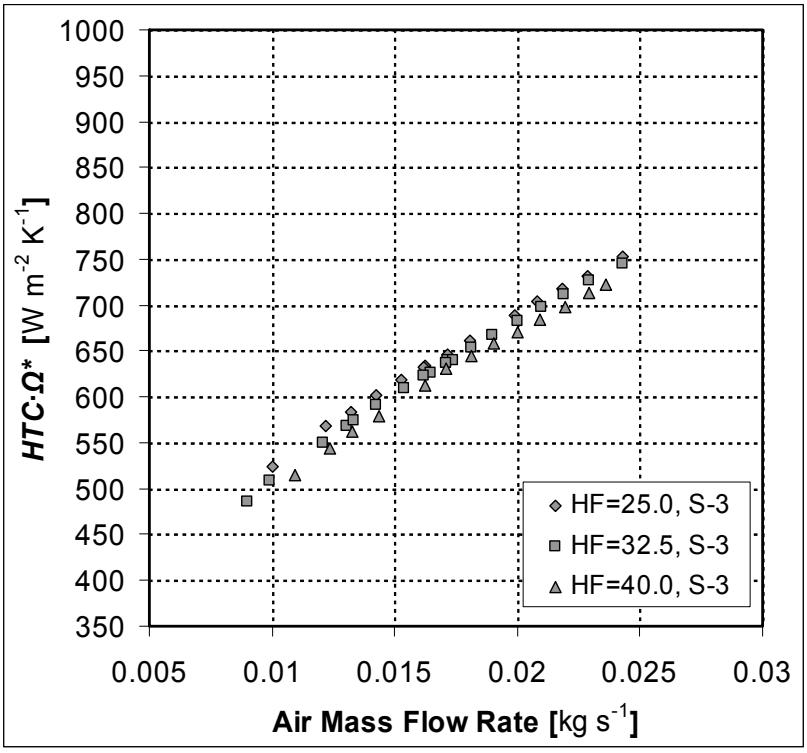

Figure 181. Global heat transfer coefficient of S-3 plotted against air mass flow rate. HF: Heat Flux [kW m^{-2}].

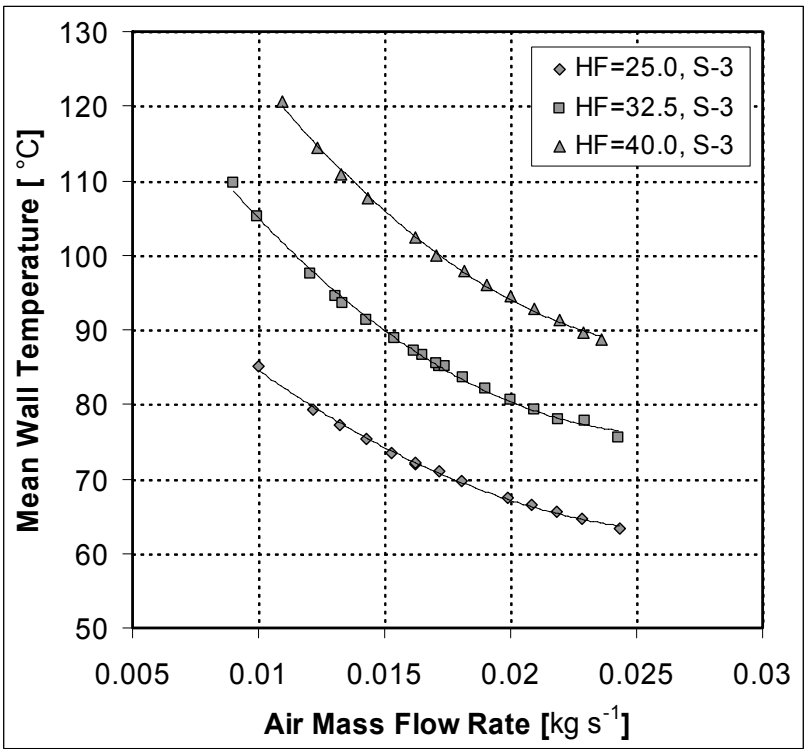

Figure 182. Mean wall temperature evaluated using Eq. 215. t_{air}*=25* °C*. HF: Heat Flux* [kW m^{-2}].

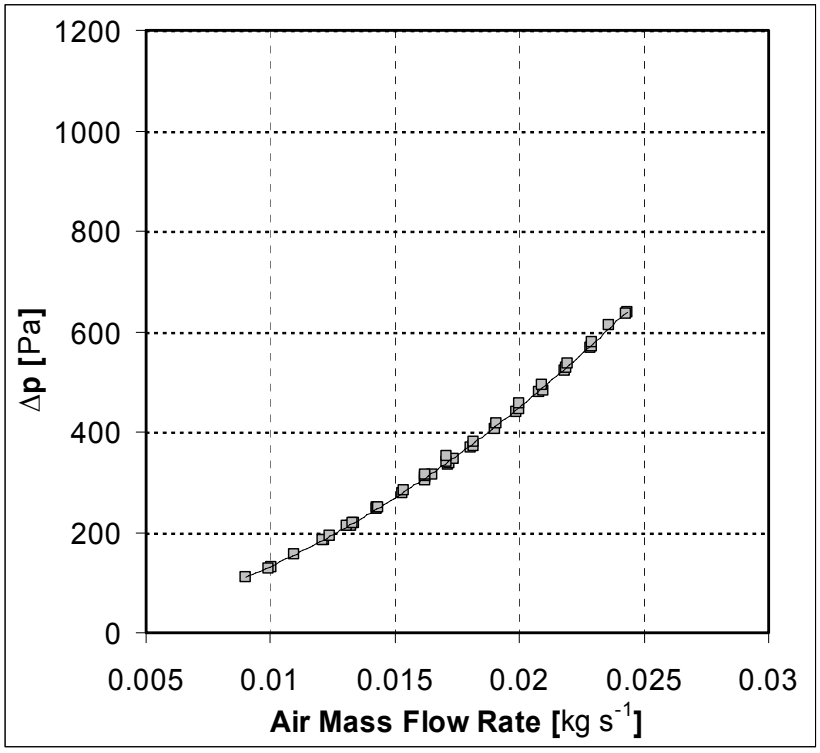

Figure 183. Experimental pressure drops plotted against air mass flow rate.

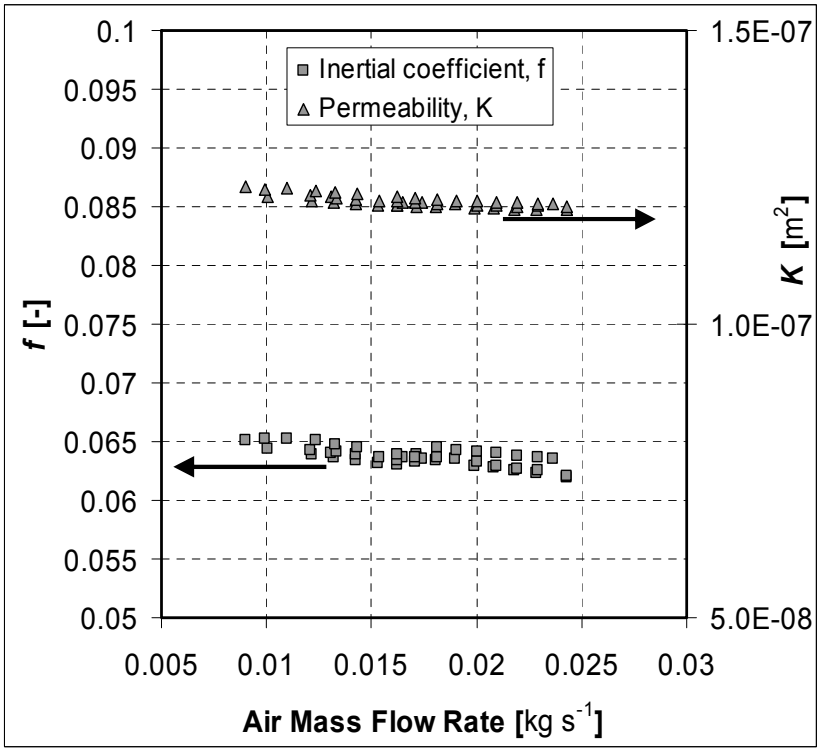

Figure 184. Inertia coefficient, f and permeability K plotted against air mass flow rate.

The fluid flow results are reported in Figure 183 and Figure 184 In particular, Figure 183 plots the measured pressure drops as a function of the flow rate; it appears that the pressure losses increase as the mass flow rate increases, passing from 110 to 638 Pa when the air mass flow rate varies from 0.01 to 0.025 kg s^{-1}.

Figure 184 illustrates the inertia coefficient, f, and the permeability, K, plotted against the air mass flow rate. These values appear to be constant for all operating test conditions. The inertia coefficient varies between 0.062 and 0.065, while the permeability ranges between 1.194 and 1.233 (10^{-7}) m^2.

2.4.4.9 10 PPI Aluminum Foam Sample: S-4

The experimental measurements of 10 PPI aluminum foam with a porosity of 0.903 are here presented.

First of all, the heat balance between the electric power and the measured heat flow rate is presented. Figure 185 plots the *HB* calculated value against the air mass flow rate. The heat balance decreases as the flow rate increases and the measured air heat flow rate is always lower than the supplied electric power.

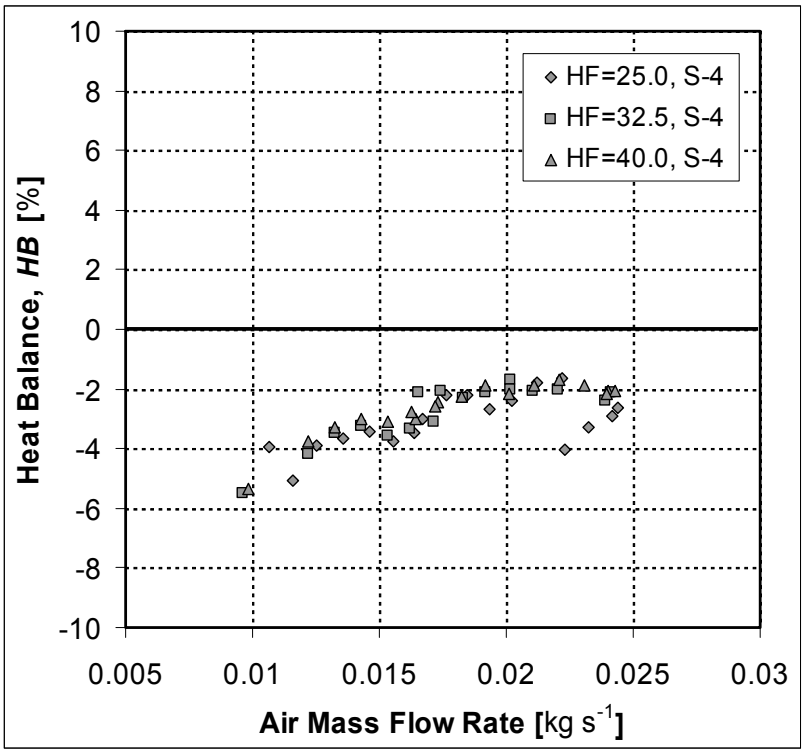

Figure 185. Heat balance plotted against air mass flow rate. HF: Heat Flux [kW m^{-2}].

Figure 186 and Figure 187 report the heat transfer results. The global heat transfer coefficient and the mean wall temperature are plotted against the air mass flow rate as a function of the imposed heat flux. The global heat transfer coefficient appears to be independent from the imposed heat flux; it increases with increasing flow rate and varies between 656 and 947 W m^{-2} K^{-1}. The mean wall temperature, calculated according to Eq. 215, imposing $t_{air,in}$=25 °C, decreases as the air flow rate increases. At constant mass flow rate, the temperature increases with the electric power.

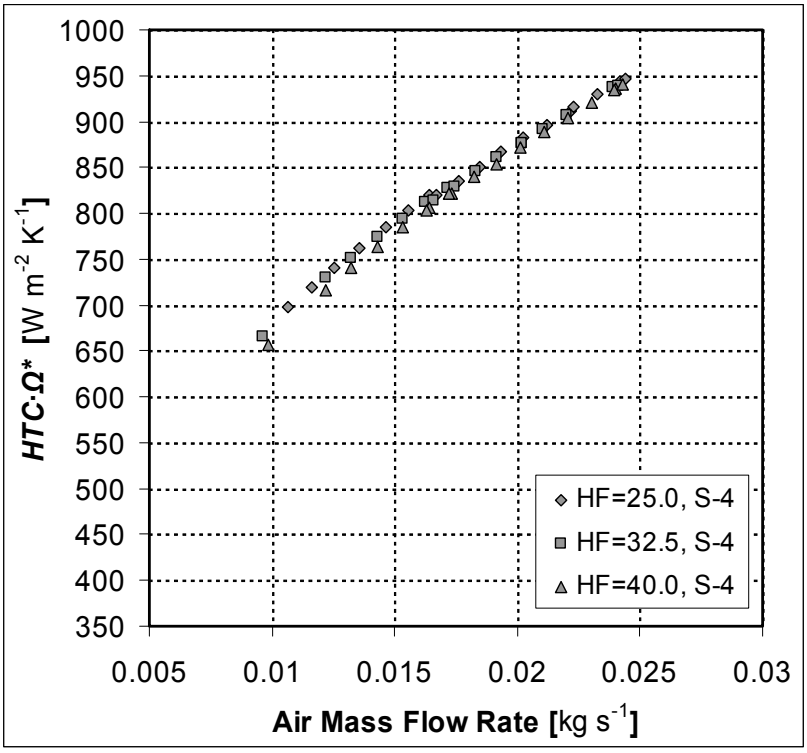

Figure 186. Global heat transfer coefficient of S-4 plotted against air mass flow rate. HF: Heat Flux [kW m^{-2}].

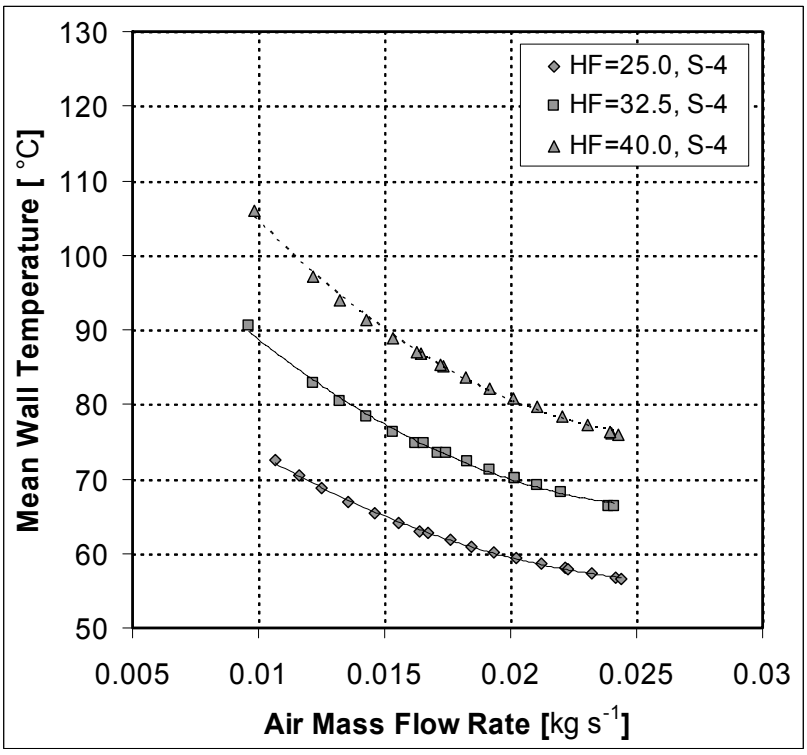

Figure 187. Mean wall temperature evaluated using Eq. 215. t_{air}*=25* °C*. HF: Heat Flux* [kW m^{-2}].

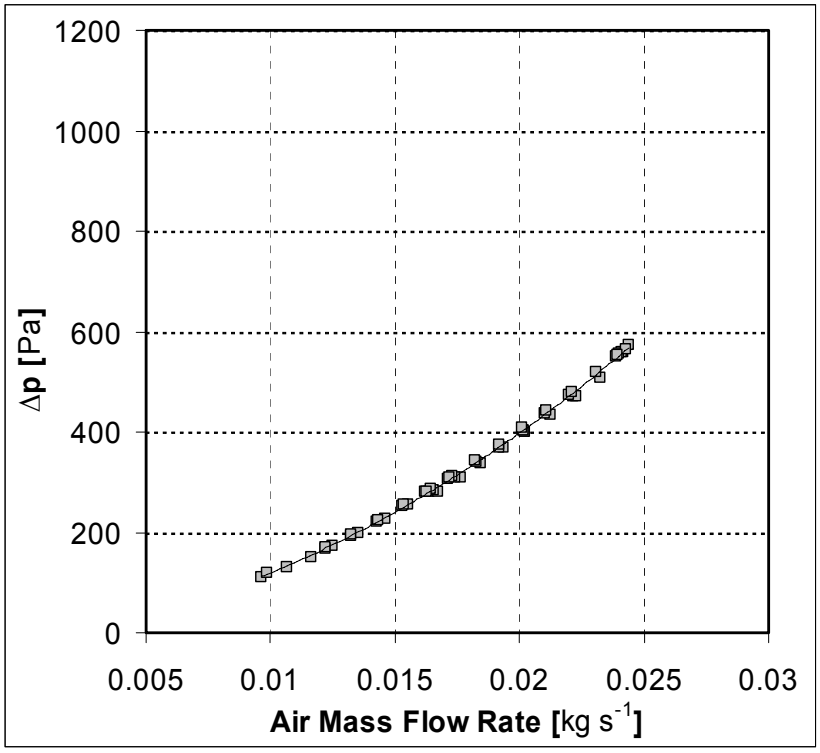

Figure 188. Experimental pressure drops plotted against air mass flow rate.

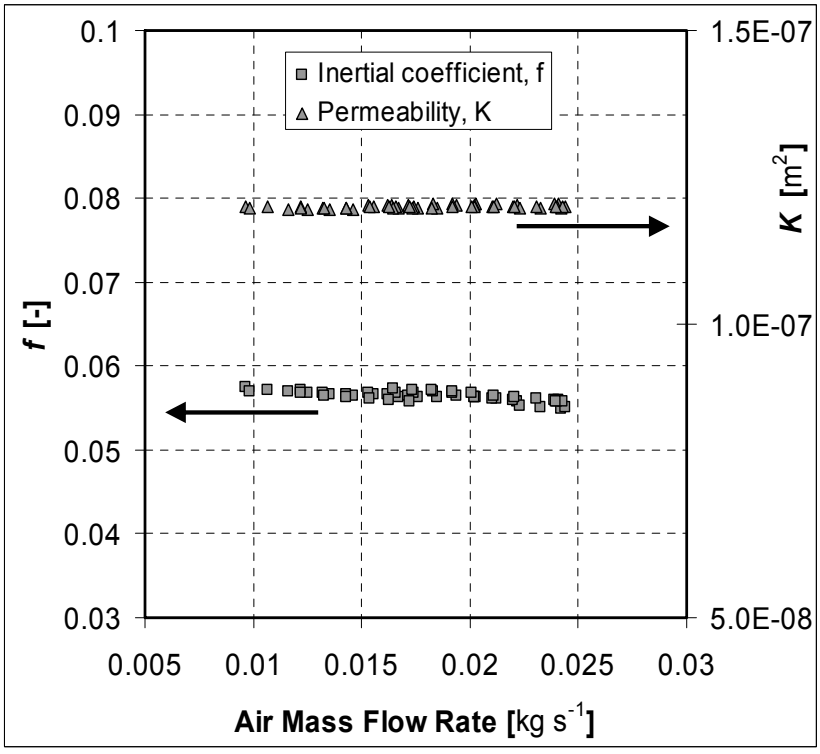

Figure 189. Inertia coefficient, f and permeability K plotted against air mass flow rate.

The fluid flow results are reported in Figure 188 and Figure 189 In particular, Figure 188 plots the pressure drops as a function of the air flow rate; it appears that the pressure losses rise as the mass flow rate increases, varying between 111 and 573 Pa.

Figure 189 illustrates the inertia coefficient, f, and the permeability, K, plotted against the air mass flow rate. These values appear to be constant for all operating test conditions. The inertia coefficient varies between 0.055 and 0.057, while the permeability ranges between 1.194 and 1.204 (10^{-7}) m^2.

2.4.4.10 40 PPI, Aluminum Foam Sample: S-6

The experimental measurements of 40 PPI aluminum foam with a porosity of 0.930 are here presented.

First of all, the heat balance between the imposed electric power and the measured air heat flow rate is presented. Figure 190 plots *HB* against the air mass flow rate. The heat balance decreases as the flow rate increases; at high air mass flow rate the air heat flow rate tends to the value of the supplied electric power and the deviation tends to zero.

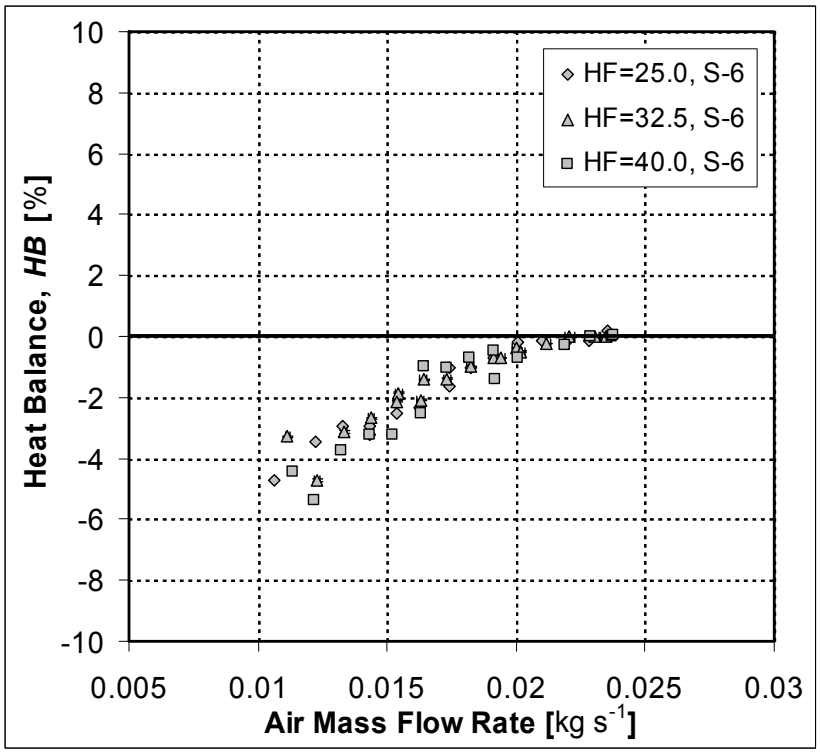

Figure 190. Heat balance plotted against air mass flow rate. HF: Heat Flux [kW m^{-2}].

Figure 191 and Figure 192 report the heat transfer results. The global heat transfer coefficient and the mean wall temperature are plotted against the air mass flow rate as a function of the imposed heat flux. The global heat transfer coefficient appears to be independent from the imposed heat flux; it increases when the air flow rate increases and varies between 537 and 773 W m^{-2} K^{-1}. The mean wall temperature, calculated according to Eq. 215, imposing $t_{air,in}$=25 °C , decreases as the air flow rate increases. At constant mass flow rate, the temperature increases with the electric power.

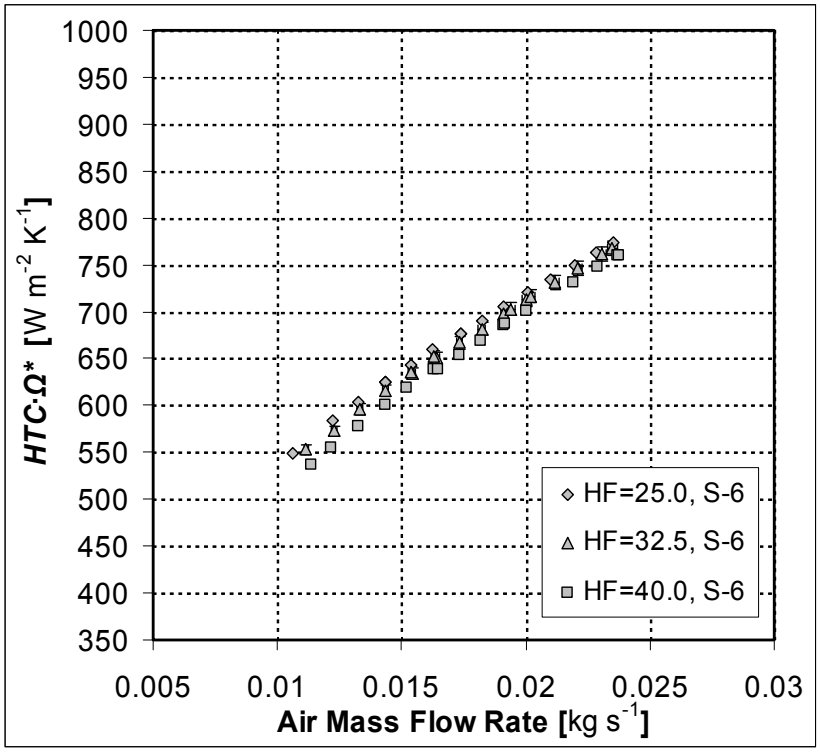

Figure 191. Global heat transfer coefficient of S-6 plotted against air mass flow rate. HF: Heat Flux [kW m^{-2}].

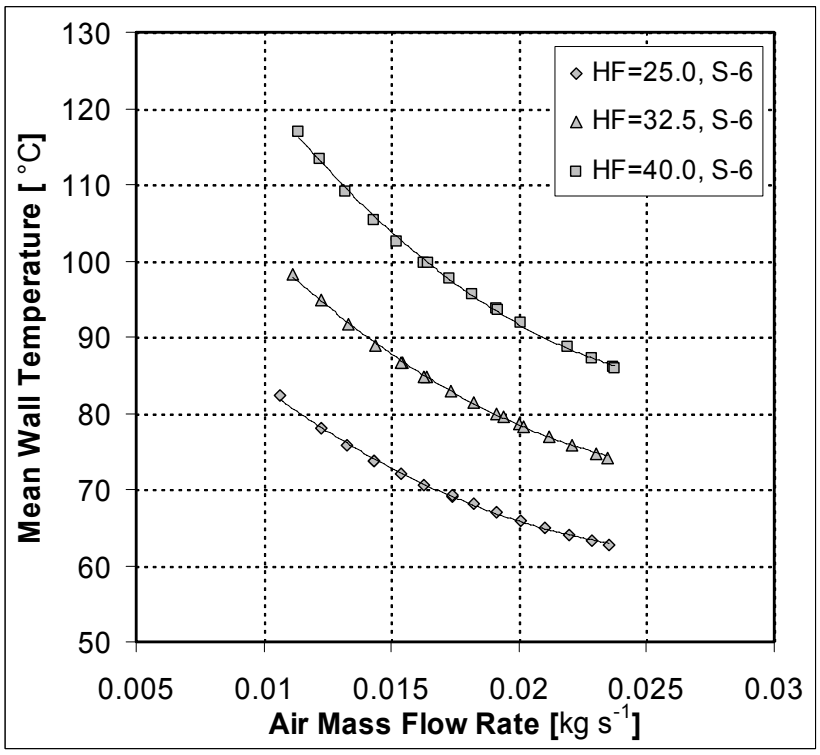

Figure 192. Mean wall temperature evaluated using Eq. 215. t_{air}*=25°C. HF: Heat Flux* [kW m^{-2}].

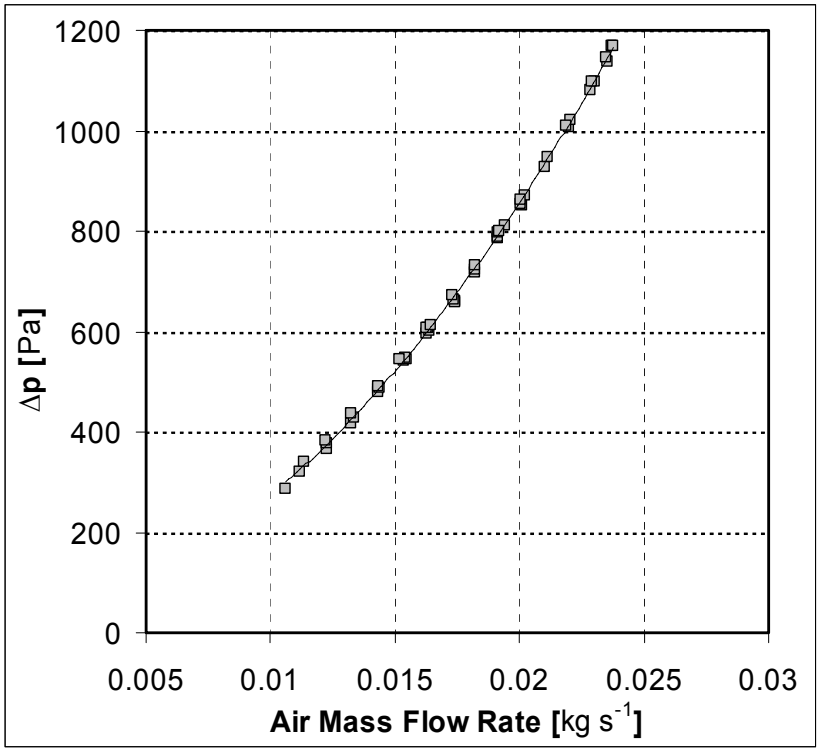

Figure 193. Experimental pressure drops plotted against air mass flow rate.

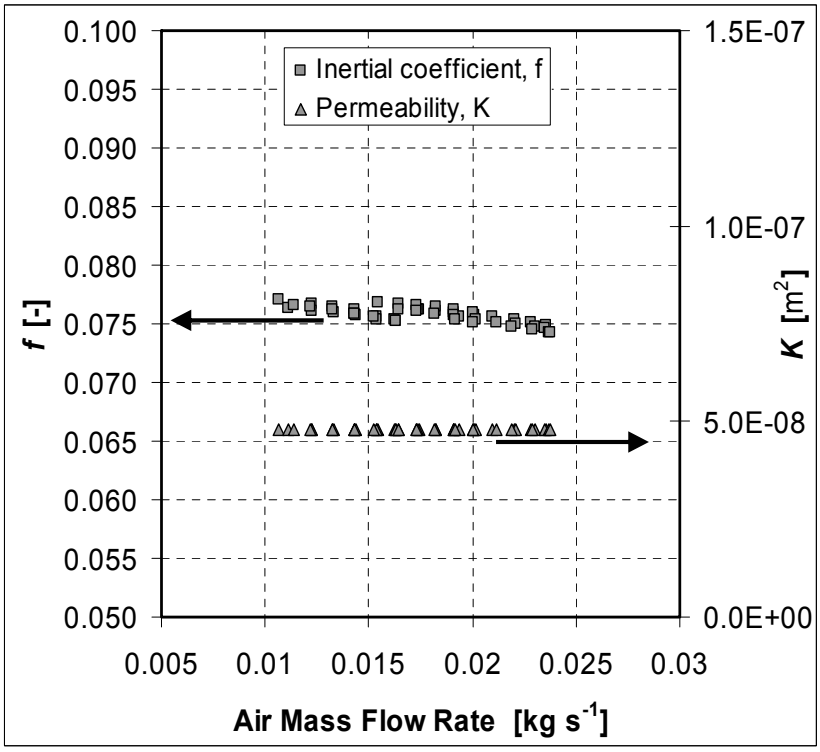

Figure 194. Inertia coefficient f and permeability K plotted against the air mass flow rate.

The fluid flow results are reported in Figure 193 and Figure 194. In particular, Figure 193 plots the pressure drops as a function of the flow rate; it appears that the pressure losses rise as the air mass flow rate increases, varying between 288 and 1168 Pa.

Figure 194 illustrates the inertia coefficient, f, and the permeability, K, plotted against the air mass flow rate. These values appear to be constant for all operating test conditions. The inertia coefficient varies between 0.074 and 0.077, while the permeability ranges between 0.477 and 0.481 (10^{-7}) m^2.

2.4.4.11 Comparison Between the Tested Aluminum Foams

The comparison between the global heat transfer behaviours of the different tested aluminum foams are now presented. As already mentioned, five of the six acquired aluminum foams have been tested. They present different structural properties which influence their global heat transfer performance during single-phase air flow. These properties are listed in Table 68.

First of all, all the tested metal foams were compared in order to find the one with the best heat transfer behaviour in the investigated range of operating conditions.

Figure 195, Figure 196 and Figure 197 plot the global heat transfer coefficient, which is the product of the heat transfer coefficient and the surface area efficiency, against the air mass flow rate for three imposed heat fluxes.

The data set referred to S-2, shown in Figure 197, was simulated. In fact, the experimental data points were not carried out, as the wall temperatures at 32.5 kW m^{-2}, taken during the preview measurements, were too high. This procedure is acceptable, since the experimental heat transfer coefficients appear to be independent from the imposed heat flux (Figure 176).

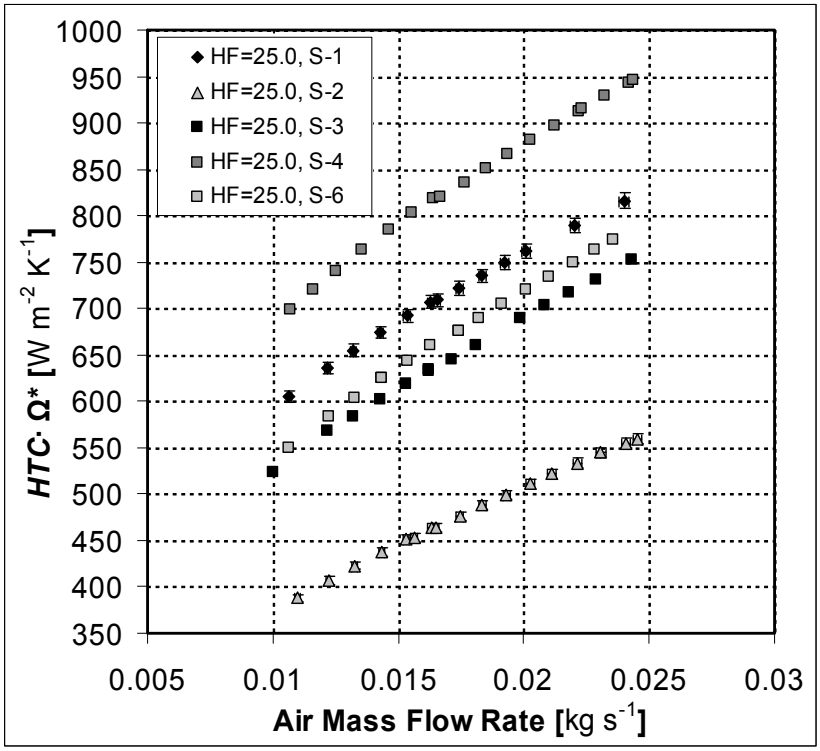

Figure 195. Comparison between the tested aluminum foams: global heat transfer coefficient plotted against air mass flow rate. HF=25.0 kW m^{-2}.

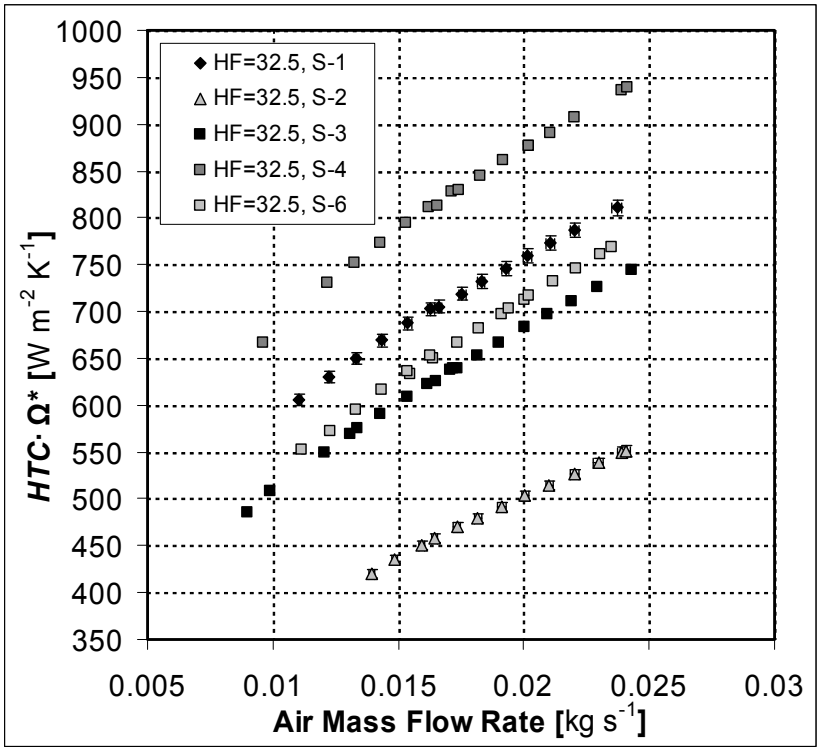

Figure 196. Comparison between the tested aluminum foams: global heat transfer coefficient plotted against air mass flow rate. HF=32.5 kW m^{-2}.

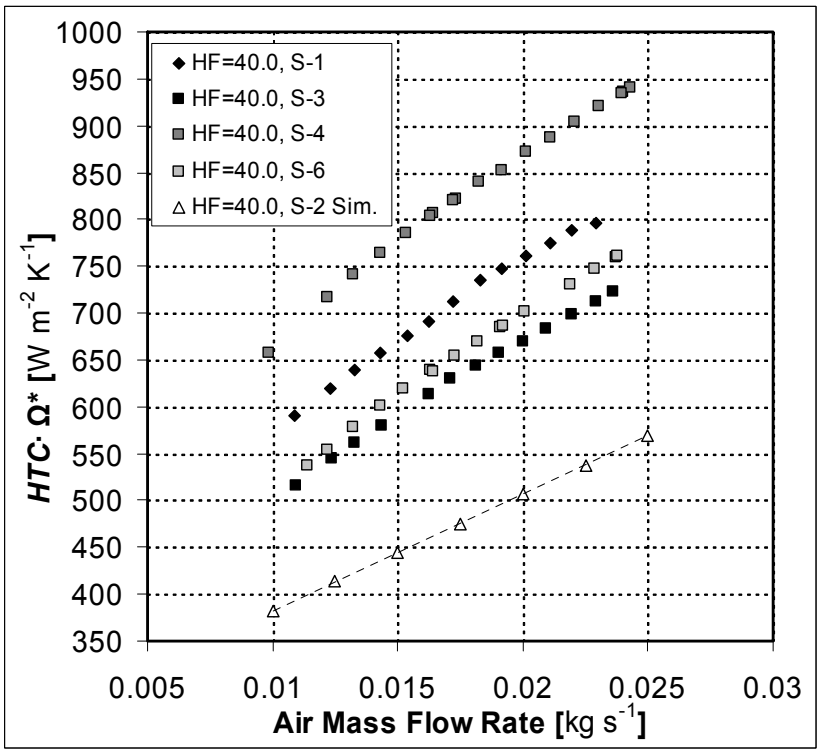

Figure 197. Comparison between the tested aluminum foams: global heat transfer coefficient plotted against air mass flow rate. HF=40.0 kW m^{-2}.

The global heat transfer coefficient of the different aluminum foams shows the same trend for all the imposed heat fluxes. In particular, the best heat transfer behaviour was exhibited by the 10 PPI aluminum foam, which presents the lowest porosity (ε=0.903), while the worst was that of another 10 PPI sample, the one presenting the highest porosity (ε=0.956).

Looking at Figure 195, it appears that the 40 PPI aluminum foam exhibits a global heat transfer coefficient lower than that of the 5 PPI aluminum foam. On the other hand, the 40 PPI metal foam presents a heat transfer area higher than that of the 5 PPI aluminum foam, because the heat transfer area increases as the number of pores per inch increases, as reported in Figure 198.

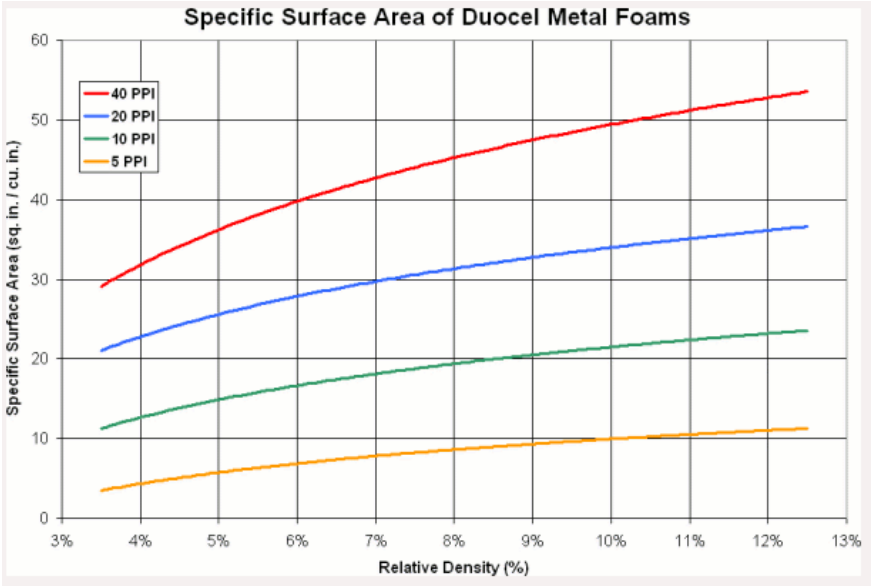

Figure 198. Surface area per unit of volume plotted against relative density. (1 in^2in^{-3} *= 39.37* m^2m^{-3}*) [63].*

A possible explanation for this behaviour is the following. Since the global heat transfer coefficient is referred to the base area, it takes into account both the total heat transfer area and the surface area efficiency; therefore, the surface area efficiency worsens the mere increasing of the surface area. Their combined effects produce an overall worsening of the heat transfer behaviour.

From the experimental wall temperatures it appears that the surface area efficiency of these aluminum foams is very low. In fact, each test sample was instrumented with twelve T-Type thermocouples: six inserted in the upper plate and six in the bottom plate.

During the experimental measurements, these temperatures were acquired; the upper wall temperatures were independent of both the imposed heat flux and the air mass flow rate. For

instance, for S-4, at 40 kW m^{-2}, passing from 0.01 kg s-1 to 0.025 kg s^{-1}, the mean base temperature varies from 102 °C to 72 °C, while the upper mean wall temperature changes only between 34 and 24 °C.

As experimentally and numerically determined by Dukhan et al. [64], in a metal foam, the temperature decays exponentially with the distance from the heated base. The Authors have experimentally demonstrated that the temperature of the foam reaches that of the ambient at a dimensionless distance from the heated base of approximately 0.3. Applying this result to our samples, it follows that a layer of more than 2.5 cm of the foam thickness is at around ambient temperature and so the related heat transfer is negligible.

With increasing heat transfer area, this phenomenon grows and the fin efficiency decreases. Therefore, it is important to find the right equilibrium between the increasing of the heat transfer area and the worsening of the surface efficiency. As evident from Figure 195, Figure 196 and Figure 197, the best heat transfer compromise is represented by the 10 PPI sample, the one with the lowest porosity: ε=0.903. According to Figure 198, as compared with the other two 10 PPI samples, this one has the highest surface area and the thickest fiber. As it is well-known, the fin efficiency depends on the fin thickness, more precisely it increases as the fin thickness increases, hence the 10 PPI sample S-4 may also present the highest efficiency.

For all the tested foams, the global heat transfer coefficient linearly increases with the air mass flow rate. S-3, presenting 10 PPI and 0.934 of porosity, exhibits almost the same global heat transfer behaviour of the 40 PPI foam sample.

Figure 199, Figure 200 and Figure 201 report the mean wall temperature plotted against the air mass flow rate as a function of the imposed heat flux. The mean wall temperature has been computed imposing 25 °C air temperature at the inlet of the test section (Eq. 215), in this way it has been possible to compare data points acquired under different ambient conditions, $21°C<t_{air,in}<26°C$.

In Figure 201, the data for S-2 are simulated in the hypothesis that the heat transfer coefficient is independent from the imposed heat flux. S-2 appears to be far from all the other tested samples, presenting the worst mean wall temperature. The lowest wall temperatures are exhibited by the 10 PPI sample S-4, which presents also the highest global heat transfer coefficients.

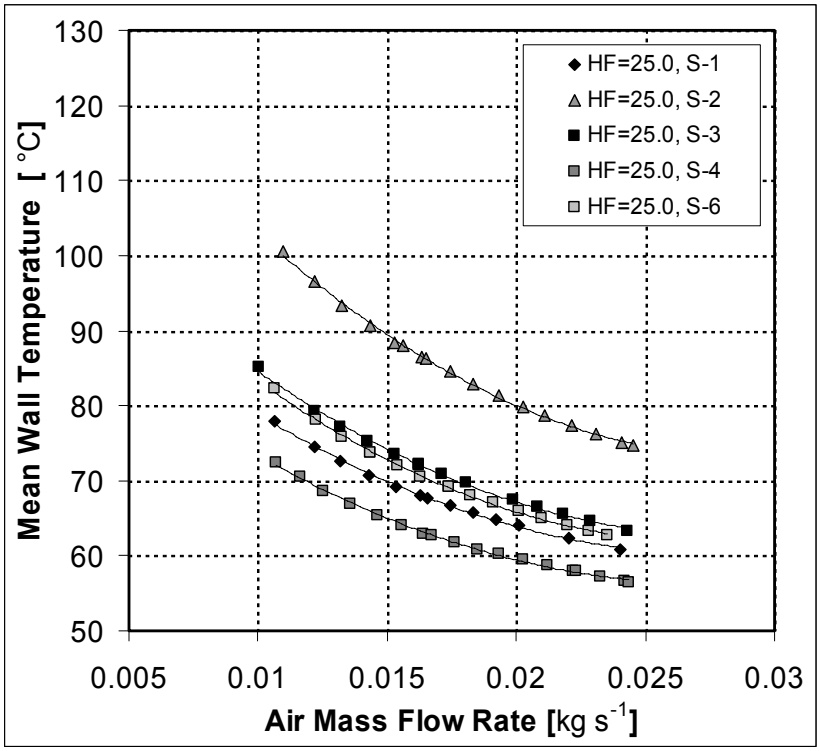

Figure 199. Comparison between the tested aluminum foams: mean wall temperature evaluated using Eq. 215. t_{air}*=25*°C. *HF=25.0* kW m^{-2}.

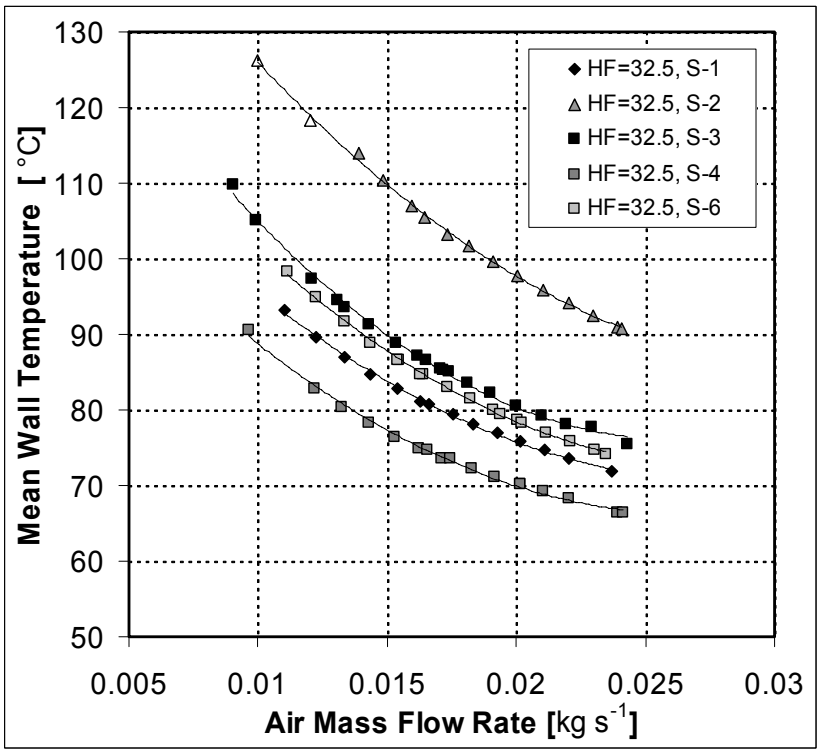

Figure 200. Comparison between the tested aluminum foams: mean wall temperature evaluated using Eq. 215. t_{air}*=25*°C. *HF=32.5* kW m^{-2}. *Blank triagles refer to estimated values.*

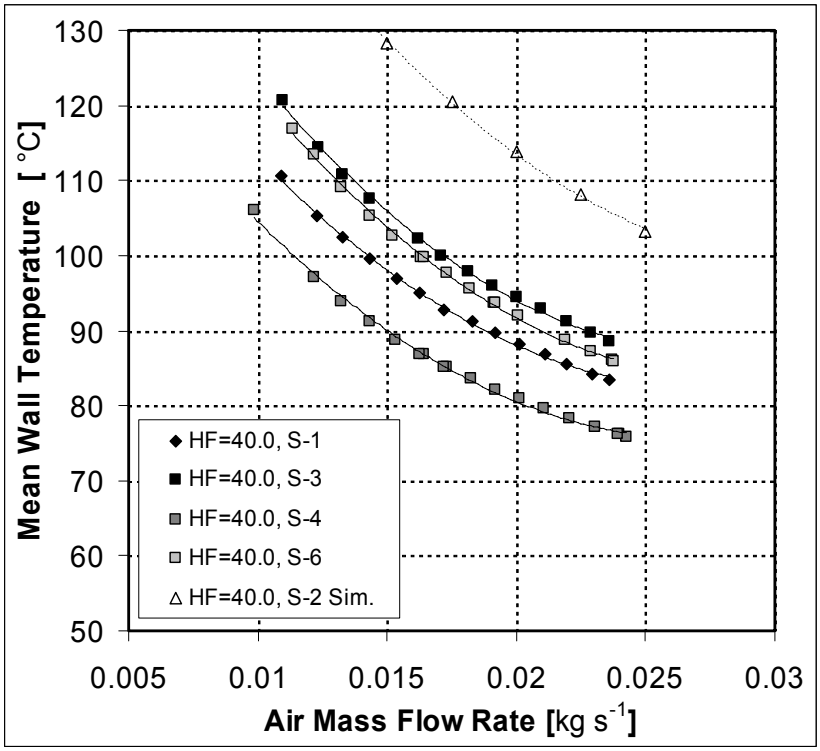

Figure 201. Comparison between the tested aluminum foams: mean wall temperature evaluated using Eq. 215. t_{air}=25°C. HF=40.0 kW m^{-2}. *Blank triagles refer to estimated values.*

As the heat flux increases, also the temperature difference between the best and the worst sample rises. For instance, at 0.015 kg s^{-1}, the temperature difference is around 25 K at 25 kW m^{-2}, while it becomes 35 K at 32.5 kW m^{-2} and 40 K at 40 kW m^{-2}.

The experimental pressure drops of the different aluminum foams are presented in Figure 202. The highest pressure drops has been measured for the 40 PPI S-6 sample, while the lowest ones has been obtained for S-4. It is interesting to point out that the pressure drops of the 40 PPI sample are two times higher than those measured for S-4, the 10 PPI sample. The pressure drops measured for S-1 and S-3 are almost the same, but at high mass flow rate the 5 PPI sample S-1 presents higher pressure losses than the 10 PPI sample. At low mass flow rate, i.e. at around 0.01 kg s^{-1}, S-1, S-2, S-3 and S-4 present the same pressure drops.

The permeability, K, and the inertia coefficient, f, for all the tested aluminum foams are reported in Table 69. S-1, S-2 and S-6 have almost the same inertia coefficients, while the permeability of the 40 PPI sample, S-6, is one half and one third, respectively, of that of S-2 and of S-1. S-3 and S-4 present the same permeability, while the inertia coefficient of S-3 is 0.064 and that of S-4 is 0.056.

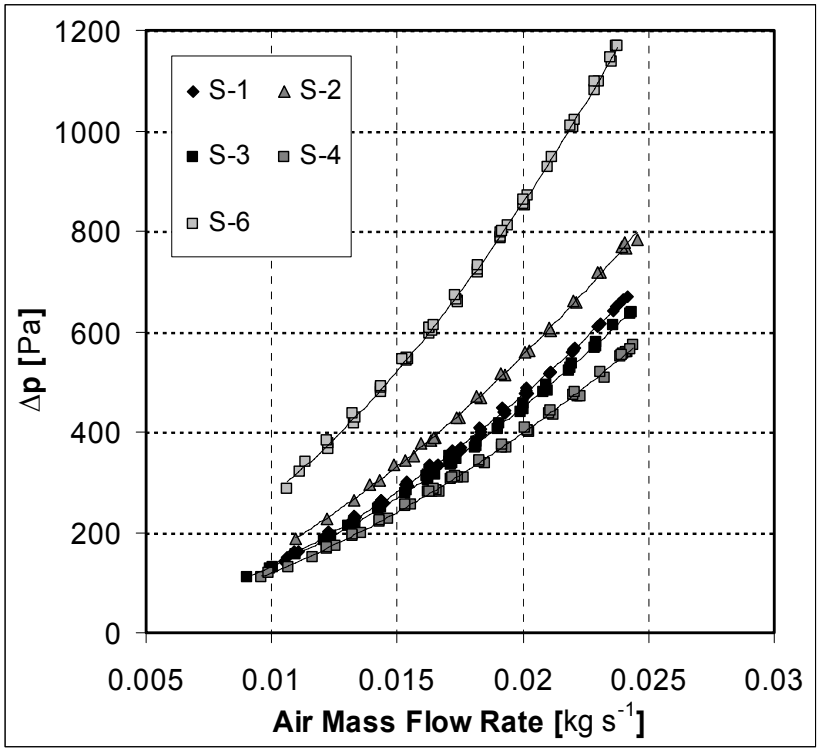

Figure 202. Comparison between the tested aluminum foams: experimental pressure drops plotted against air mass flow rate.

Table 69. Permeability and inertia coefficient values for the tested aluminum foams.

Sample	***PPI***	***Relative Density*** [%]	***Porosity*** [-]	***Permeability,* K** 10^{-7} [m^2]	***Inertia Coeff.,* f** [-]
S-1	5	7.9	0.921	1.489	0.074
S-2	10	4.4	0.956	1.092	0.076
S-3	10	6.6	0.934	1.209	0.064
S-4	10	9.7	0.903	1.200	0.056
S-5	20	6.8	0.932	-	-
S-6	40	7.0	0.930	0.479	0.076

2.4.4.12 Comparison Between Three 10 PPI Aluminum Foams with Different Porosity

Three 10 PPI aluminum foam samples were analysed in order to study the effect of porosity on heat transfer behaviour during single-phase air flow. The experimental results are illustrated in Figure 203, Figure 205 and Figure 206, where the global heat transfer coefficient, the computed mean wall temperature and the pressure drop are plotted against the air mass flow rate.

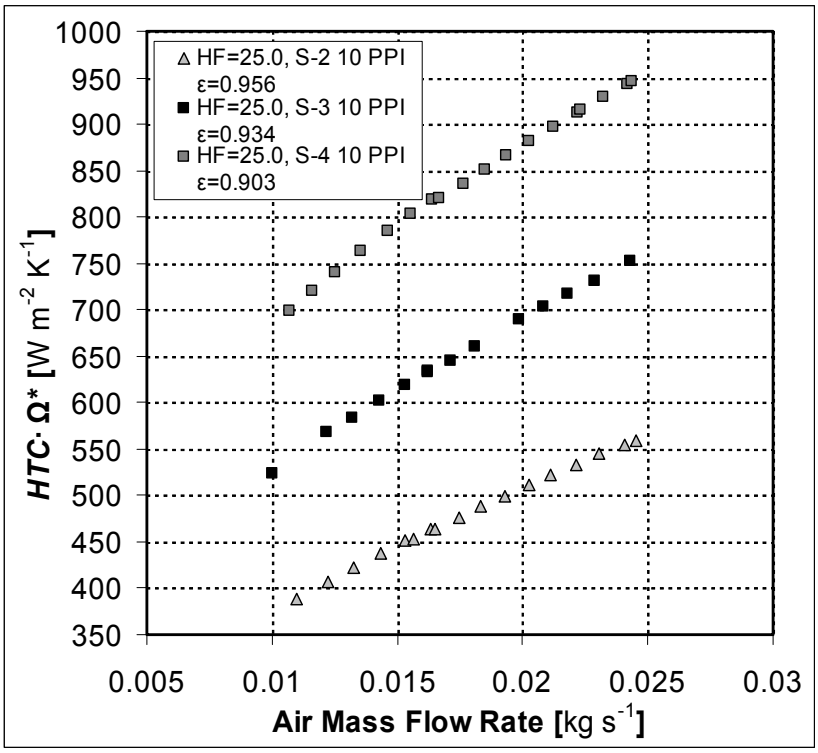

Figure 203. Comparison between the different 10 PPI aluminum foams: global heat transfer coefficient plotted against air mass flow rate. HF=25 kW m^{-2}.

As the relative density increases, i.e. the porosity decreases, the global heat transfer behaviour gets better and better. As it appears from Figure 203, the global heat transfer coefficients presented by S-4 are 1.73 and 1.27 times higher than those measured for S-2 and S-3.

According to Figure 198, this experimental evidence can be explained considering both the increasing of the surface area of the heat transfer and the improvement of the surface area efficiency. As described in the previous paragraph, the surface area efficiency of S-4 may be higher than those of S-2 and S-3, because its fiber thickness is higher than theirs and, in addition, its pores are larger than those of S-2.

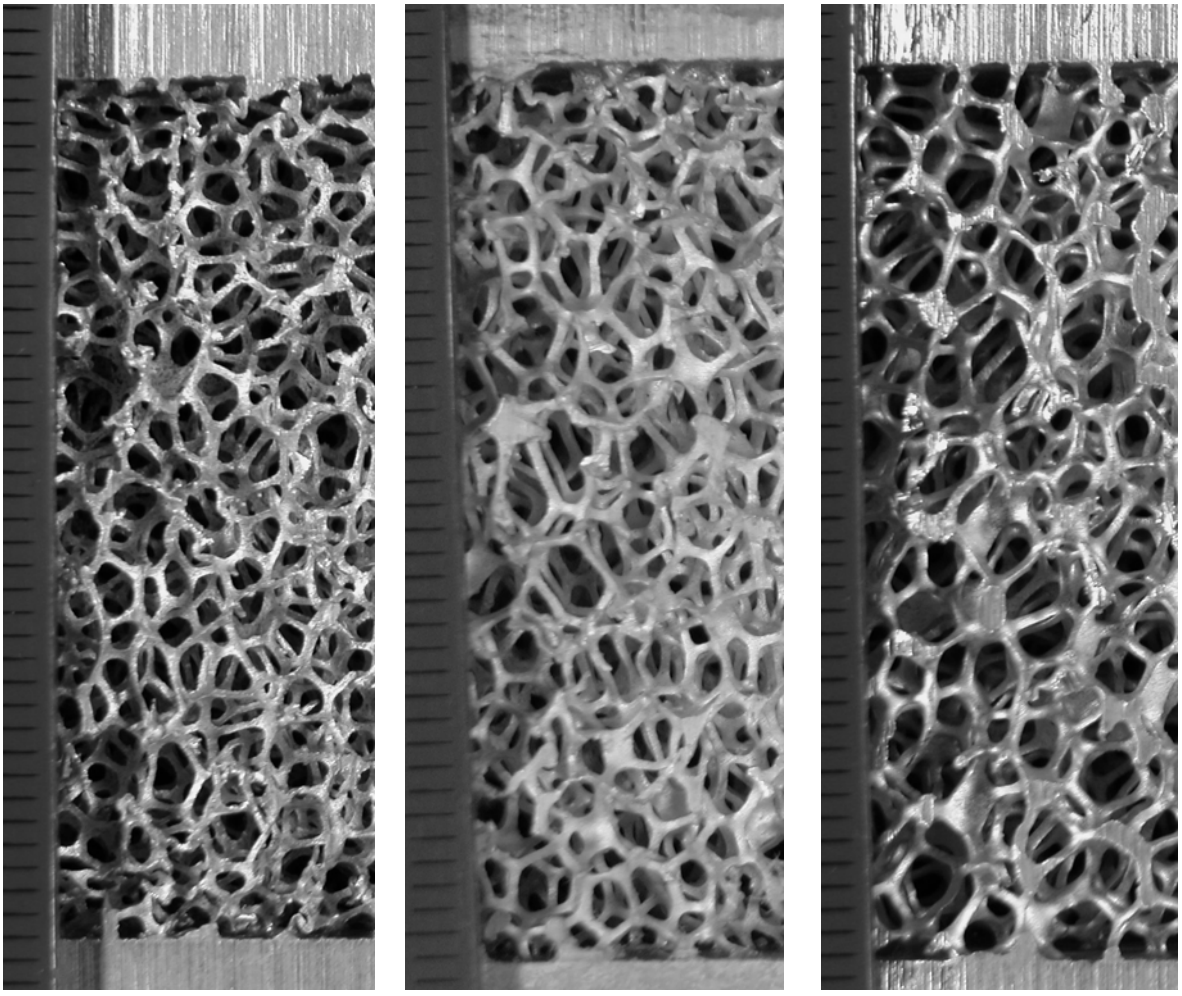

Figure 204. Photos of the different 10 PPI samples: left side photo, S-2 ε=0.956; central photo, S-3 ε=0.934, right side photo, S-4 ε=0.903.

Table 70. Properties of the 10 PPI tested samples.

Sample	***PPI***	***Relative Density*** [%]	***Porosity*** [-]	***Fiber Thickness*** [mm]	***Fiber Length*** [mm]
S-2	10	4.4	0.956	0.445	1.351
S-3	10	6.6	0.934	0.450	1.785
S-4	10	9.7	0.903	0.529	1.870

Figure 204 shows three photos of the different 10 PPI aluminum foams. Comparing the foam pores, it appears that S-2 presents the smallest ones, while S-4 is made of the thickest and longest fibers, which improve the surface area efficiency. Table 70 confirms these qualitative results reporting the fiber length and thickness for the three foam samples.

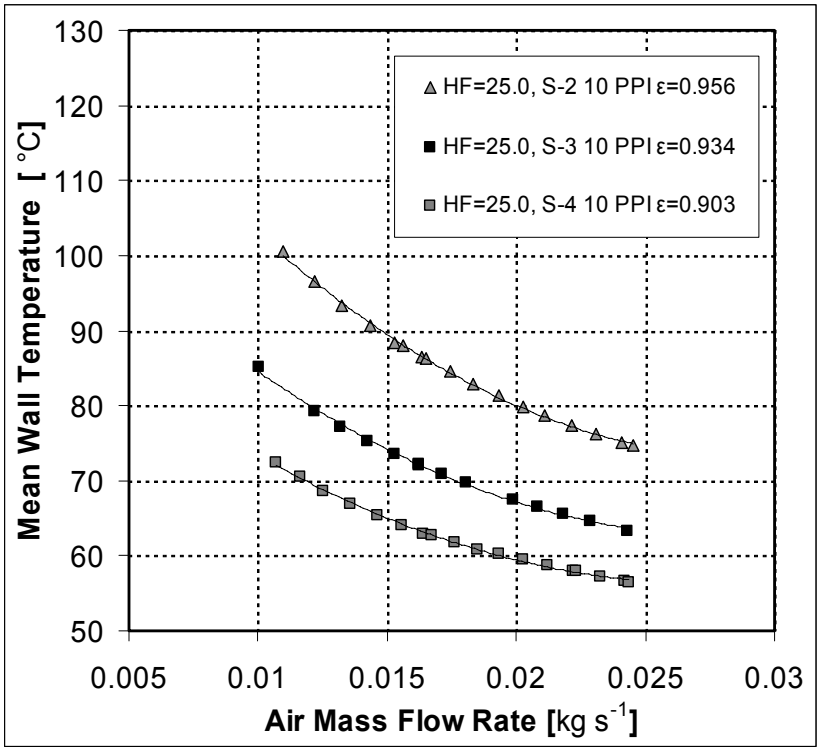

Figure 205. Comparison between the different 10 PPI aluminum foams: mean wall temperature evaluated using Eq. 215. t_{air}*=25* °C. *HF=25* kW m^{-2}

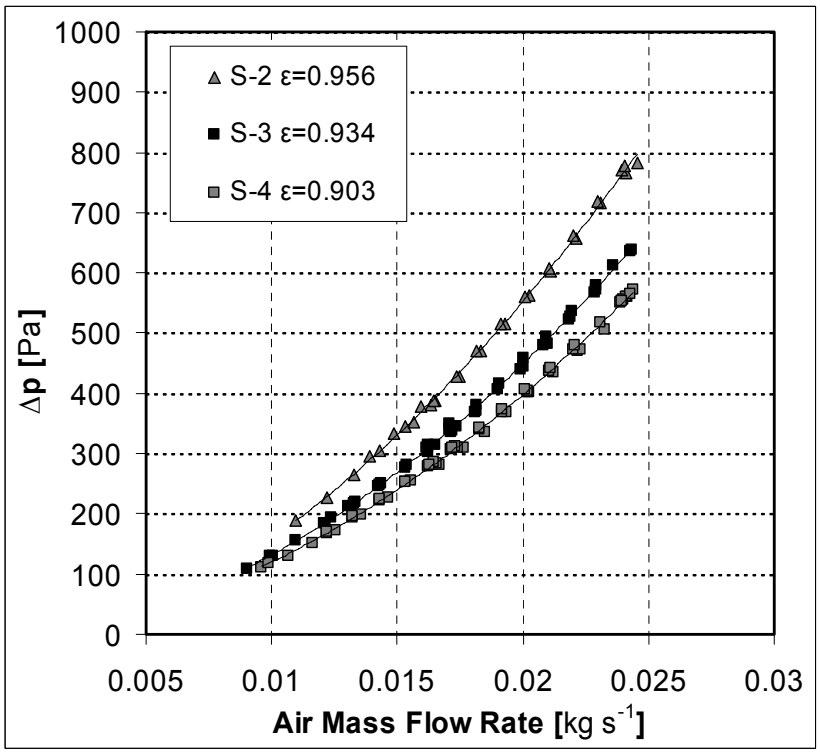

Figure 206. Comparison between the different 10 PPI aluminum foams: experimental pressure drops plotted against air mass flow rate.

The mean wall temperatures for the three test samples, calculated imposing an air temperature of 25 °C at the inlet of the test section (Eq. 215), are plotted in Figure 205. Again, S-4 presents the best behaviour as compared with the other two test samples.

Figure 206 illustrates the experimental pressure drops measured for the three 10 PPI foam samples plotted against the air flow rate. S-2, the foam with the highest porosity, equal to 0.956, presents also the highest pressure drops, while S-4 exhibits the lowest ones.

The inertia coefficient, *f*, appears to be a function of the porosity, i.e. relative density; in fact, it increases as the porosity increases. Considering the permeability *K*, S-3 and S-4 present almost the same value, which is around 1.2 10^{-7} m^2, while for S-2 the permeability is around 1.09 10^{-7} m^2 (Table 71).

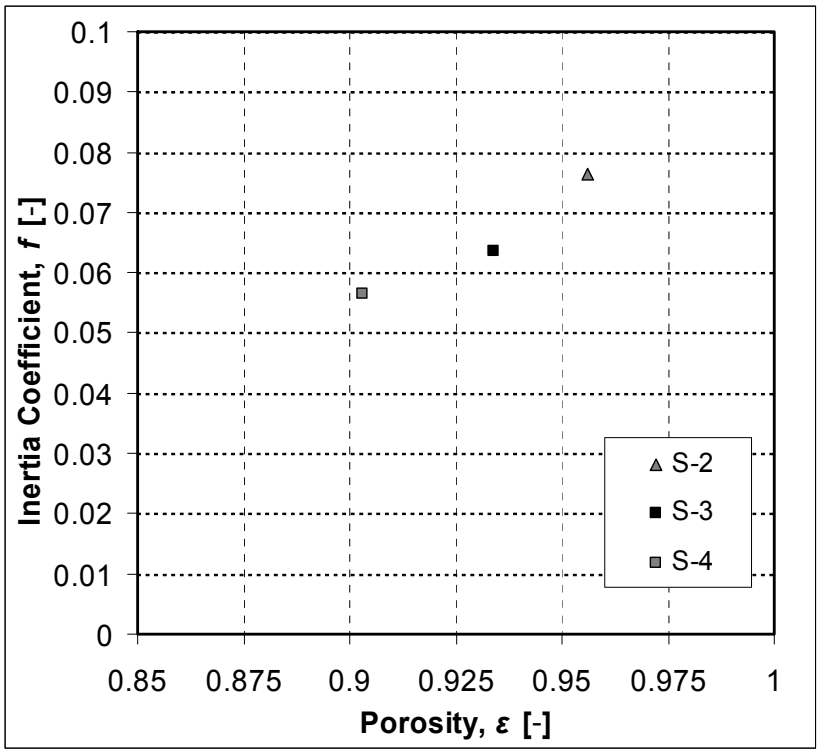

Figure 207. Comparison between the different 10 PPI aluminum foams: experimental inertia coefficient plotted against air mass flow rate.

Table 71. Permeability and inertia coefficient values for the three 10 PPI aluminum foams.

Sample	***PPI***	***Relative Density*** [%]	***Porosity*** [-]	***Permeability,* K** 10^{-7} [m^2]	***Inertia Coeff.,* f** [-]
S-2	10	4.4	0.956	1.092	0.076
S-3	10	6.6	0.934	1.209	0.064
S-4	10	9.7	0.903	1.200	0.056

2.4.4.13 Traditional Finned Surface vs. Aluminum Metal Foams

The comparison between the heat transfer behaviour of the traditional finned surface which had been previously tested and those of the considered aluminum foams is now outlined. The traditional finned surface has been characterized in order to evaluate the new test facility and so as to become a reference surface for the alternative enhanced structures.

Thus, in this paragraph, the measured global heat transfer coefficient for the finned surface referred to the base area is plotted, together with those exhibited by the aluminum foams, against the air mass flow rate. The traditional finned surface performs slightly better than S-2, which is the sample with a PPI of 10 and the highest porosity.

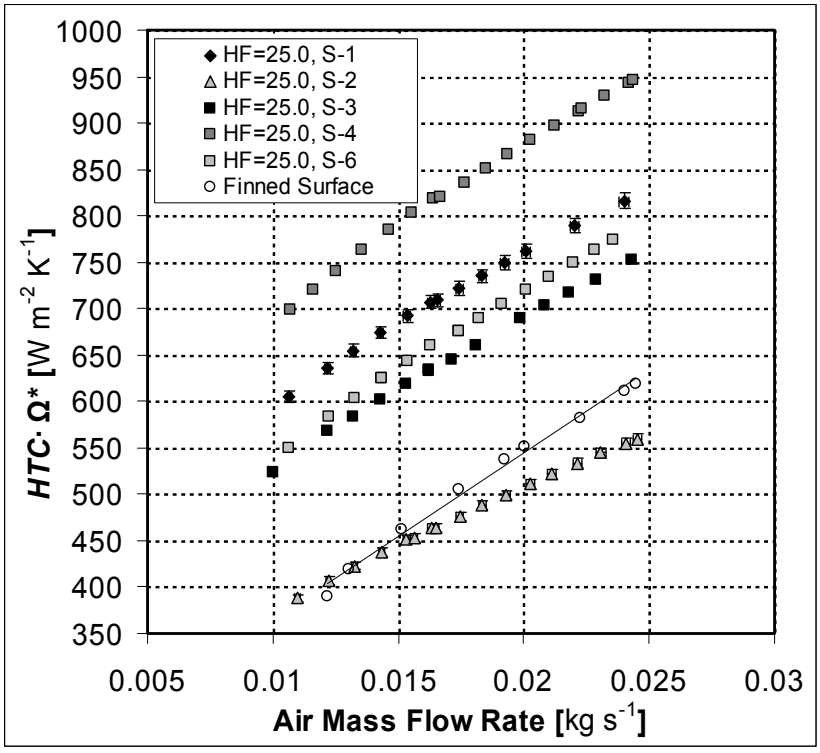

Figure 208. Traditional finned surface vs. aluminum foams: global heat transfer behaviour plotted against air mass flow rate. HF=25 kW m^{-2}.

On the other hand, when the heat transfer behaviour of the finned surface is compared with those of the other aluminum foams, it is evident that these new enhanced surfaces present interesting heat transfer capabilities.

At high mass flow rate, the global heat transfer coefficient measured for S-4, the best of the aluminum foams, is around 1.5 times the one obtained for the traditional finned surface, while at low mass velocity this ratio reaches the value of 2.

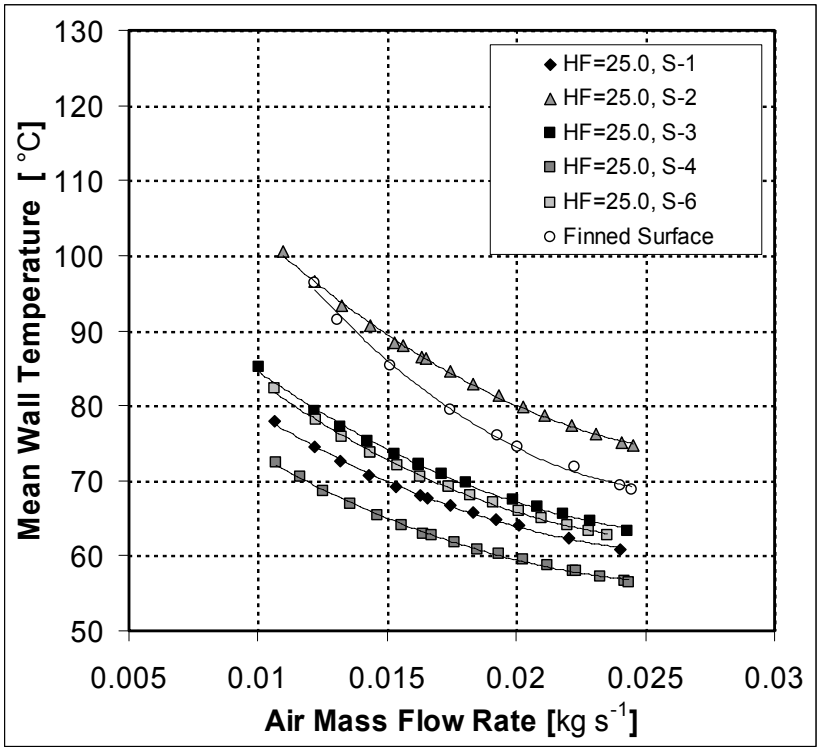

Figure 209. Traditional finned surface vs. aluminum foams, mean wall temperature evaluated using Eq. 215. t_{air}*=25* °C. *HF=25* kW m^{-2}.

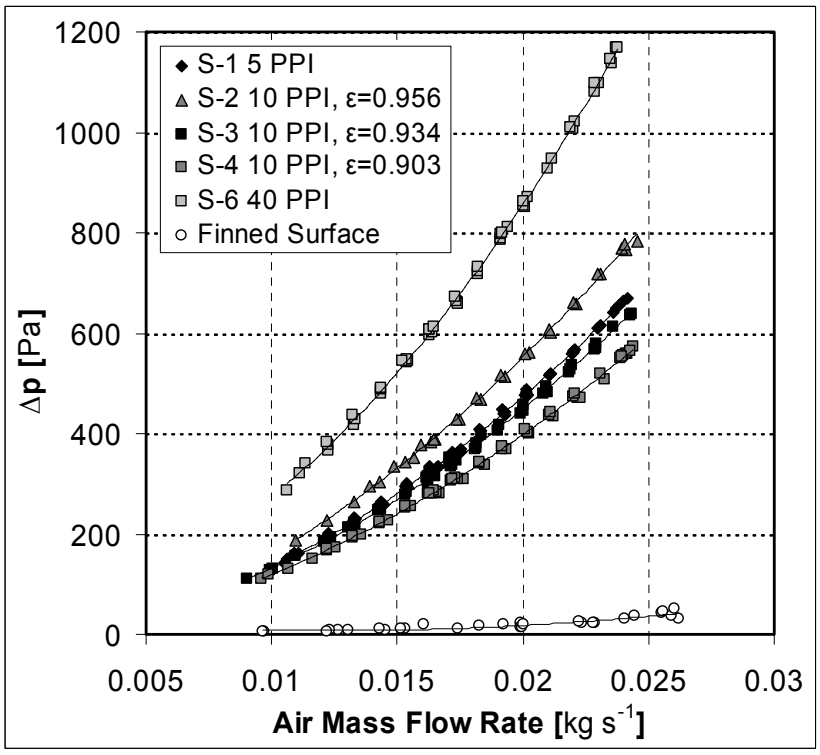

Figure 210. Traditional finned surface vs. aluminum foams: experimental pressure drops plotted against air mass flow rate.

As shown in Figure 209, at 25 kW m^{-2} the traditional finned surface and S-2 are again the samples with the highest calculated mean wall temperatures. At high air mass flow rate the wall temperature calculated for the finned surface is lower than that obtained for S-2.

The other side of the coin is represented by the fluid flow behaviour, since the pressure drops exhibited by the aluminum foams are orders of magnitude higher than those of the traditional finned surface. As reported in Figure 210ined for S-2.

The other side of the coin is represented by the fluid flow behaviour, since the pressure drops exhibited by the aluminum foams are orders of magnitude higher than those of the traditional finned surface. As reported in Figure 210, at 0.025 kg s^{-1} the best aluminum foam, S-4, loses around 600 Pa, while the traditional finned surface losses only 50 Pa; the ratio between these two pressure drops is 12. In the case of the 40 PPI sample the ratio becomes 24.

The tested stochastic materials appear to be suitable only where a high air pressure load is available.

2.5 Conclusions

One of the most crucial challenges in the field of air cooling applications is to increase the upper limit of the heat flow rate dissipated per unit area. High heat flux dissipators and compact heat sinks are more and more demanded in many different applications where an efficient heat transfer would allow the overcoming of the limits of air cooling.

From this point of view, there is a growing necessity for new enhanced surfaces able to replace the traditional finned ones.

This part of this Ph. D. thesis reports the design, development and building of the new experimental set-up devised to fully characterize the thermal-fluid-dynamic behaviour of several different enhanced surfaces during single-phase air heat transfer. The new experimental facility was built in the laboratory of the Dipartimento di Fisica Tecnica of the University of Padova.

The design or selection of all components implemented in the test rig have been deeply analyzed in order to give a clear and synthetic overview of each decision made to create a high accuracy test equipment. The designed set-up is an open-circuit type wind tunnel with rectangular cross section where it is possible to analyse specimens with finned surfaces, offset strip pins, cellular structure materials both stochastic and periodic and microgeometries.

The cellular structure materials and new enhanced surfaces hitherto proposed in the open literature present pressure drops which are higher by orders of magnitude than those of the traditional finned surfaces at the same operating conditions. Hence, here, in order to characterize a variety of enhanced surfaces under a wide range of operating test conditions, compressed air has been selected as a coolant. The heating technique and the air flow rate, electric power, air temperature and pressure measurements have been discussed and the implemented experimental solutions have been presented.

This new test rig is able to carry out single-phase air heat transfer measurements at different pressures, varying the air flow rate between 0.05 and 0.025 kg s^{-1} and heating the test sample up to 900 W. The experimental heat transfer coefficients and the pressure drops during single-phase air flow through a traditional finned surface have been measured and reported. This finned surface has also been taken as a reference for successive comparisons, which have involved a new enhanced heat transfer surface class, aluminum foams.

Metal foams are a class of cellular structured materials with a stochastic, interconnected pore distribution, mostly uniform in size and shape. In the last decades, these porous media have

been largely studied because of their interesting properties, covering several different technical fields. In fact, metal foams are lightweight materials, offering high strength and rigidity and high heat transfer surface area which improve energy absorption and heat transfer in thermal applications.

Metal foams have considerable applications in the making of multifunctional heat exchangers, cryogenics, combustion chambers, cladding on buildings, strain isolation buffers between a stiff structure and a fluctuating temperature field, geothermal operations, petroleum reservoirs, compact heat exchangers for airborne equipment, air cooled condensers and compact heat sinks for power electronics.

Six 40 mm thick Al 6101 alloy (aluminum) foams were acquired from ERG Aerospace, Inc. They present different numbers of pores per inch (5-40 PPI) and varying porosity (from 0.903 to 0.956). Three of them are 10 PPI samples with different porosities: 0.903, 0.934 and 0.956. These samples were acquired to study the effects of porosity on heat transfer and fluid flow behaviours during air forced convection.

A systematic measuring technique has been developed to measure the most important geometrical characteristic of the tested aluminum foams. Four photos of each side of the specimens have been taken. Then a large number of thickness and length measurements of the fibers have been taken and statistically analysed. Five of the six test samples have been experimentally characterized in the new test facility.

The global heat transfer coefficients (obtained multiplying the effective heat transfer coefficient by the surface area efficiency) have been measured during single-phase air heat transfer. Also the pressure drops of the air through these new cellular structure materials have been measured.

The 10 PPI sample with the lowest porosity presents the best heat transfer behaviour, exhibiting the highest heat transfer coefficients and the lowest pressure drops under the investigated range of operating conditions. The results obtained for the three 10 PPI aluminum foams confirm that the global heat transfer coefficients and the pressure drops strongly depend on the porosity. The global heat transfer coefficient increases as the porosity decreases; conversely, the pressure drops decrease.

The surface area efficiency of these new enhanced surfaces appears to be very low: after a few millimetres, around a centimetre, from the heated wall, the temperature is around ambient

temperature. Therefore, the global heat transfer coefficient of the metal foam is worsened by its surface area efficiency.

The tested aluminum foams have been compared with the traditional finned surface, which has exhibited the same global heat transfer coefficient as the worst aluminum foam (the 10 PPI sample with the highest porosity). The global heat transfer coefficient measured for the best aluminum foam (10 PPI, ε=0.903) is around 1.7 times higher than the one obtained for the finned surface. On the other hand, this foam presents pressure drops which are 12 times higher than those of the traditional surface.

These new enhanced surfaces appear to be suitable when high pressure loads are available; for instance, aluminum foams might be used to cool aeronautical electronics systems.

Finally, the 20 PPI test sample will be tested and compared with the other ones and, of course, with the finned surface.

Other six 20 mm thick aluminum foams were acquired from ERG Aerospace to study their surface area efficiency. These new samples will be tested, then they will be compared with the ones already experimentally characterized. The collected experimental data points will generate a wide database of heat transfer coefficients and pressure drops, which will be used to test the available heat transfer and fluid flow correlations and to select new suitable correlations. The test rig will be also used to develop and test other enhanced surfaces which might improve the applicability of air cooling to electronics applications.

2.6 Nomenclature

A_{base}	base area [m^2]
A_{eff}	effective heat transfer area [m^2]
A_{ff}	effective free-flow cross sectional area [m^2]
A_{fr}	frontal area [m^2]
C	coefficient of discharge
c_p	specific heat capacity [J kg^{-1} K^{-1}]
c_s	specific heat capacity of the humid air [J kg^{-1} K^{-1}]
D	stainless steel internal diameter [m]
d	orifice diameter [m]
d_h	hydraulic diameter [m]
d_p	pore diameter [m]
d_s	fiber thickness [m]
e_A	mean absolute deviation [%]
e_P	percent deviation [%]
e_R	mean relative deviation [%]
f	friction factor
g	gravitational acceleration [m s^{-1}]
G	shape function
HB	heat balance [%]
HTC	heat transfer coefficient [W m^{-2} K^{-1}]
$HTC\ \Omega^*$	"global" heat transfer coefficient [W m^{-2} K^{-1}]
Kc, Ke	abrupt contraction and expansion coefficients
i	uncertainty [%]

I	current [A]
$\dot{m}$	air mass flow rate [kg s^{-1}]
p	pressure [Pa]
P_{EL}	Electric Power
Δp	pressure difference [Pa]
PPI	pore per inch
q	heat flow rate [W]
R	*Ohm* resistance [Ω]
t	temperature [°C] or fiber diameter [m]
Δt_{ml}	mean logarithmic temperature difference [K]
u	velocity [m s^{-1}]
V	tension [V]
x	humidity ratio [kg_v kg_{da}^{-1}]

Non-dimensional Number

Pr	Prandtl number
Re	Reynolds number
Gr	Grashof number
Gz	Graetz number

Greek Symbols

β	diameters ratio [-]

ε	porosity or gas expansion factor
μ	dynamic viscosity [kg m^{-1} s^{-1}]
σ_N	standard deviation
ρ	density [kg m^{-3}]
χ	tortuosity
Ω	fin efficiency [-]
Ω^*	surface area efficiency [-]

Subscripts

air	air
CALC	calculated
ch	channel
EXP	experimental
f	fluid
in	inlet
l	laminar
loc	local
out	outlet
t	turbulent
tr	transition
w	wall

2.7 References

[1] Etemoglu A.B., A brief survey and economical analysis of air cooling for electronic equipments. *Int. J. of Heat and Mass Transfer*, 34 (2007): 103-113.

[2] Kandlikar S.G., Garimella S., Li D., Colin S., King M.R., Heat transfer and fluid flow in minichannels and microchannels, Elsevier.

[3] Tasaka M., Aihara T., Hayashi C., Heat Transfer and Pressure Loss Characteristics of Very Compact Heat Sinks with Plate Fins Cooled by Jets, *Heat Transfer – Japanese Research*, 27 (6) (1998): 399-414.

[4] Kim S.Y., Lee M.H., Lee K.-S., Heat Removal by Aluminum –Foam Heat Sink in a Multi-Air Jet Impingement, *IEEE Trans.,* 28 (1) (2005): 142-148.

[5] El-Sheikh H. A., Garimella S.V., Heat Transfer form Pin-Fin Heat Sink under Multiple Impinging Jets, *IEEE Trans.* 23 (1) (2000): 113-120.

[6] Brignoni L.A., Garimella S.V., Experimental Optimization of Confined Air Jet Impingement on a Pin Fin Heat Sink, *IEEE Trans.,* 22 (3) (1999): 399-404.

[7] Go. D.B., Maturana R.A., Fisher T.S. Garimella S. V., Enhancement of external forced convection by ionic wind, *Int. J. of Heat and Mass Transfer*, 51 (2008): 6047-6053.

[8] McGlein R.J., Jachuck R., Lin S., Integrated thermal management techniques for high power electronic devices, *Applied Thermal Engineering* 24 (2004): 1143-1156.

[9] Zhang H.Y., Pinjala D., Wong T.N., Toh K.C., Joshi Y.K., Single-phase liquid cooled microchannel heat sink for electronic packages, *Applied Thermal Engineering,* 25 (2005): 1472-1487.

[10] Hetsroni G., Mosyak A., Segal Z., Ziskind G., A uniform temperature heat sink for cooling electronic devices, *Int. J. of Heat and Mass Transfer,* 45 (2002): 3275-3286.

[11] Gillot C., Bricard A., Schaeffer C., Single and two-phase heat exchanger for power electronic components, *Int. J. of Thermal Science*, 39 (2000): 826-832.

[12] Webb R.L., Next generation Devices for Electronic Cooling With Heat Rejection to Air, *Trans. of the ASME*, 127 (2005): 2-10.

[13] Knight R.W., Goodling J.S., Gross B.E., Optimal thermal design for air cooled forced convection finned heat sinks - Experimental verification, *IEEE Trans.*, (1992): 206-212.

[14] Mohamed M.M., Air cooling characteristics of a uniform square modules array for electronic device heat sink, *Applied Thermal Engineering* 26 (2006): 486-493.

[15] Xu G., Xue J., Cheng Y., Zhu W., Luo L., Heat Transfer Characteristics of Small-Sized Plate-Fin Heat Sink Array in Supercomputer, *IEEE Trans.* (2006).

[16] Kim S. J., Kim D.-K., Oh H.H., Comparison of Fluid Flow and Thermal Characterizatiocs of Plate-Fin and Pin-Fin Heat Sinks Subject to a Parallel Flow, *Heat Transfer Engineering*, 29(2) (2008): 169-177.

[17] Jonsson H., Palm B., Thermal and Hydraulic Behaviour of Plate Fin and Strip Fin Heat Sinks Under Varying Bypass Conditions, *IEEE Trans*., 96-103.

[18] Saini M., Webb R.L., Heat Rejection Limits of Air Cooled Plane Fin Heat Sinks for Computer Cooling, *IEEE Trans.* 26 (1) (2003): 71-79.

[19] Tian J., Kim T., Lu T.J., Hodson H.P., Queheillalt D.T., Sypeck D.J., Wadley H.N.G., The effect of topology upon fluid-flow and heat-transfer within cellular copper structures, *Int. J. of Heat and Mass Transfer*, 47 (2004): 3171-3186.

[20] Ashby M.F., Evans A., Fleck N.A., Gibson L.J., Hutchinson J.W., Wadley H.N.G., Metal Foam. A design Guide, Butterworth Heinmann, 2000.

[21] Gallego N.C., Klett J.W., Carbon foams for thermal management, *Carbon*, 41(2003): 1461-1466.

[22] Kim T., Zhao C.Y., Lu T.J., Hodson H.P., Convective heat dissipation with lattice-frame materials, *Mechanics of Materials*, 36 (2004): 767-780.

[23] Wen T., Tian J., Lu T.J., Queheillalt D.T., Wadley H.N.G., Forced convection in metallic honeycomb structures, *Int. J. of Heat and Mass Transfer*, 49 (2006): 3313-3324.

[24] Lu T.J., Heat transfer efficiency of metal honeycombs, *Int. J. of Heat and Mass Transfer* 42 (1999): 2031-2040.

[25] Calmidi V.V., Mahajan R.L., Forced Convection in High Porosity Metal Foams, *J. of Heat Transfer*, 122 (2000): 557-565.

[26] Hsieh W.H., Wu J.Y., Shih W.H., Chiu W.C., Experimental investigation of heat-transfer characteristics of aluminum-foam heat sink, *Int. J. of Heat and Mass Transfer,* 47 (2004): 5149-5157.

[27] Kim S.Y., Kang B.H., Kim J.H., Forced convection from aluminum foam materials in an asymmetrically heated channel, *Int. J. of Heat and Mass Transfer*, 44 (2001): 1451-1454.

[28] Hwang J.-J, Hwang G.-J., Yeh R.-H, Chao C.-H., Measurement of interstitial Heat Transfer and Frictional Drag for Flow Across Metal Foams, *Tran. of the ASME*, 124 (2002): 120-129.

[29] Kim T., Fuller A.J., Hodson H.P., Lu T.J., An experimental study on thermal transport in lightweight metal foams at high Reynolds numbers, *Proc. of International Symposium of Compact Heat Exchangers*, Grenoble, France, 2002, 227-232.

[30] Del Col D., Fantini F., Mancin S., Rossetto L., Zilio C., Single phase heat transfer and pressare drops in cellular structures, *Proc. of XXIV Congresso Nazionale UIT sulla Trasmissione del Calore,* Napoli, June 21-23, 2006.

[31] Cavallini A., Mancin S., Rossetto L., Zilio C., Forced convection in enhanced surfaces: heat transfer and pressure drop measurement, *Proc. of the 62° Congresso Nazionale ATI, Fisciano Salerno,* 2007.

[32] EN ISO 5167-1:1991/A1:1998, "Orifice plates, nozzles and Venturi tubes inserted in circular cross section conduits running full".

[33] ASHRAE STANDARD 33-78, Method of Testing Forced Circulation Air Cooling and Air Heating Coils, 1978.

[34] ANSI/ASHRAE STANDARD 41.1-1986 (RA 2006), Standard Method for Temperature Measurement.

[35] Wile D.D., Air flow measurement in the laboratory, *Journal of ASRE*, June 1947.

[36] ASHRAE STANDARD 51-85, Laboratory methods of testing fans rating, 1985.

[37] Razelos P., A Critical Review of Extended Surface Heat Transfer, *Heat Transfer Engineering*, 24 (6) (2003): 11-28.

[38] Ghajar A.J., Tam L.-M., Flow regime map for a horizontal pipe with uniform wall heat flux and three inlet configurations, *Experimental Thermal and Fluid Science*, 10 (1995): 287-297.

[39] Tam L.-M., Ghajar A.J., Effect of Inlet Geometry and Heating on the Fully Developed Friction Factor in the Transition Region of a Horizontal Tube, *Experimental Thermal and Fluid Science*, 15 (1997): 52-64.

[40] Tam L.-M., Ghajar A.J., The unusual behaviour of local heat transfer coefficient in a circular tube with bell-mouth inlet, *Experimental Thermal and Fluid Science*, 16 (1998):187-194.

[41] Ghajar A.J., Tam L.-M., Tam S.C., Improved Heat Transfer Correlation in the Transition Region for a Circular Tube with three Inlet Configurations Using Artificial Neural Networks, *Heat Transfer Engineering*, 25 (2) (2004): 30-40.

[42] Polley G.T., Abu-Khader M.M., Interpreting and Applying Experimental Data for Plate-Fin Surfaces: Problems with Power Law Correlation. *Heat Transfer Engineering*, 26 (2005):15-21.

[43] Kays W.M., London A. L., Compact Heat Exchanger, 3rd Edition, Krieger, Malabar, Florida, 1984.

[44] Phillips R.J., Forced Convection, Liquid Cooled, Microchannel Heat Sinks, M.S. Thesis, Dept. Mechanical Engineering. MIT, Cambridge, MA, 1987.

[45] Gibson L.J., Ashby M.F., Cellular Solids – Structure and properties, 2nd Edition, Cambridge Solid State Science Series, Cambridge University Press, 1997.

[46] Mahjoob S., Vafai K., A synthesis of fluid and thermal transport model for metal foam heat exchanger *Int. J. of Heat and Mass Transfer*, doi:10.1016/j.ijheatmasstransfer.2007.12.012

[47] Richardson J.T., Peng Y., Remue D., Properties of ceramic foam catalyst supports: pressure drop, *Applied catalysis A: General*, 204 (2000): 19-32.

[48] Calmidi V.V. Transport phenomena in high porosity metal foams, Ph.D. Thesis, University of Colorado, Boulder, CO, 1998.

[49] Bhattacharya A., Calmidi V.V., Mahajan R.L., Thermophysical properties of high porosity metal foams, *Int. J. of Heat and Mass Transfer*, 45 (2002): 1017-1031.

[50] Du Plessis J.P., Montillet A., Comiti J., Legrand J., Pressure drop prediction for flow through high porosity metallic foams, *Chemical Engineering Science,* 21 (1994):3545-3553.

[51] Fourie J.G., Du Plessis J.P., Pressure Drop modelling in cellular metallic foams, *Chemical Engineering Science,* 57 (2002): 2781-2789.

[52] Beavers G.S., Sparrow E.M., Non-Darcy Flow Through Fibrous Porous Media, *J. of Applied Mechanics,* December 1969, 711-714.

[53] Dukhan N., Chen K.C., Heat transfer measurement in metal foam subjected to constant heat flux, *Experimental Thermal and Fluid Science*, 32 (2007): 624-631.

[54] Giani L., Groppi G., Tronconi E., Heat Transfer Characterization of Metallic Foams, *Industrial Engineering Chemical Research,* 44 (2005): 9078-9085.

[55] Fu X., Viskanta R., Gore J.P., Measurement and correlation of volumetric heat transfer coefficents of cellular ceramics, *Experimental Thermal and Fluid Science,* 17 (1998): 285-293.

[56] Younis L.B., Viskanta R., Experimental determination of the volumetric heat transfer coefficient between stream of air and ceramic foam, *Int. J. Heat and Mass Transfer*, 36 (6) (1993): 1425-1434.

[57] Paek J.W., Kang B.H., Kim S.Y., Hyun J.M., Effective Thermal Conductivity and Permeability of Aluminum Foam Materials, *Int. J. of Thermophysics*, 21 (2) (2000): 453-464.

[58] Liu J.F., Wu W.T., Chiu W.C., Hsieh W.H., Measurement and correlation of friction characteristic of flow through foam matrixes, *Experimental Thermal and Fluid Science*, 30 (2006): 329-336.

[59] Hamaguchi K., Takahashi S, Miyabe H., , "Heat Transfer Characterization of Matrix: in Case of Foamed Metal", *Trans. Japanese Soc. Mech. Eng*., 49 (1983)

[60] Vafai K., Tien C.L., Boundary and inertia effects on convective mass transfer in porous media, *Int. J. of Heat and Mass Transfer*, 25 (1982): 1183-1190

[61] Mahjoob S., Vafai K., A synthesis of fluid and thermal transport models for metal foam heat exchangers, *Int. J. of Heat and Mass Transfer*, 51 (2008): 3701-3711.

[62] Kaviany M., Principle of Heat Transfer in Porous Media, Mechanical Engineering Series, 2nd Ed., Springler ed., 1995

[63] ERG Aerospace Inc. Web Site, www.ergaerospace.com

[64] Dukhan N, Quinoñes-Ramos P., Cruz-Ruiz E., Vélez-Reyes M., Scott E.P., One-dimensional heat transfer analysis in open-cell 10-ppi metal foam, *Int. J. of Heat and Mass Transfer,* 48 (2005): 5112-5120.

CONCLUSIONS

This Ph. D. thesis, in which single-phase and two-phase flow through enhanced heat transfer surfaces have been experimentally studied and analyzed, consists of two separate parts. Therefore, the most important issues highlighted with respect to each argument are pointed out at the end of the related chapter. Here, some final remarks will be made, aiming at giving some hints for future possible research works.

The experimental work concerning two-phase flow has involved the condensation of R410A, a halogenated refrigerant, inside a microfin tube. The condensation heat transfer coefficients and the pressure drops at a saturation temperature of 40 °C have been measured under a wide range of operating conditions. A large number of experimental heat transfer coefficients for the condensation of different synthetic and natural refrigerants inside microfin tubes have been selected from the open literature and collected to complete a database of around 4000 experimental measures. After that, a model for the computation of the heat transfer coefficient during condensation inside micro-finned tubes has been developed and validated against the experimental database.

Considering the importance of environmental issues, other experimental campaigns are needed to characterize the condensation heat transfer properties of other refrigerants, for validating and improving the proposed model.

The experimental work concerning single-phase flow has involved the design, development and building of a new test facility for the thermal-fluid-dynamic characterization of several different enhanced surfaces and microgeometries during air forced convection. This experimental test rig has been designed to allow the study and development of new enhanced heat transfer surfaces for electronic cooling applications able to overcome the thermal limits of air cooling.
The new facility has been tested characterizing a traditional finned surface. The experimental heat transfer coefficients and the pressure drops measured during single-phase air forced convection were repeatable. These results have confirmed the reliability of the new experimental set-up. Subsequently, five aluminum metal foams, a new class of enhanced

surfaces, have been tested. In this Ph. D. thesis their heat transfer coefficients and the pressure drops measured during air forced convection have been presented and analysed.
According to the experimental results, during single-phase air heat transfer metal foams exhibit interesting heat transfer properties but, on the other hand, they are also characterized by high pressure losses. These stochastic materials appear to be suitable for electronics cooling systems when high air pressure loads are available.

More experimental work is needed to completely understand the thermal-fluid-dynamic behaviour of these new enhanced surfaces, in order to define the best design parameters. As a consequence, considering possible future work in this field, other metal foams of different thicknesses may be tested to fully characterize their thermal behaviour. The collected results could be used to develop new simple heat transfer correlations which can lead to the design of efficient heat sinks for advanced electronics cooling systems.

Acknowledgements

The support of the University of Padova, through the project CPDA044932, and of MIUR, through the PRIN Project 2007TALBHJ_003, are gratefully acknowledged.

Bibliography

[1] Cavallini A., Censi G., Da Riva E., Del Col D., Mancin S., Shell and tube minichannel condenser for low refrigerant charge, *Proc. of 8t^h ISHMT-ASME Heat and Mass Transfer Conference" Hyderabad*, India, 3-5 January 2008.

[2] Cavallini A., Del Col D., Doretti L., Mancin S., Rossetto L., Zilio C., Visualization of the heat transfer enhancement during condensation in a microfin tube, *Proc. of FEDSM2006, 2006 ASME Joint U.S. - European Fluids Engineering Summer Meeting*, Miami, Florida, July 17-20 2006.

[3] Cavallini A., Del Col D., Mancin S., Rossetto L., Thermal performance of R410A condensing in a microfin tube, *Proc. of International Refrigeration and Air Conditioning Conference at Purdue*, West Lafayette, IN, USA, July 17-20 2006.

[4] Del Col D., Fantini F., Mancin S., Rossetto L., Zilio C., Single phase heat transfer and pressure drops in cellular structures, *Proc. of XXIV Congresso Nazionale UIT sulla Trasmissione del Calore*, Napoli, 21-23 June 2006.

[5] Cavallini A., Del Col D., Mancin S., Rossetto L., An updated model for condensation of halogenated refrigerants inside enhanced tubes, *Proc. of IIR Congress, International Congress of Refrigeration 2007*, Beijing, 21-26 August 2007

[6] Cavallini A., Del Col D., Mancin S., Rossetto L., Condensation of pure and near-azeotropic refrigerants in micro-fin tubes: a new computational procedure, *Int. J. of Refrigeration*, 32 (2009): 162-174, doi:10.1016/j.ijrefrig.2008.08.004.

[7] Cavallini A., Mancin S., Rossetto L., Zilio C., A new experimental test rig for the thermal-fluid-dynamic characterization of enhanced surfaces during single phase air flow, *Proc. of XXV Congresso Nazionale UIT sulla Trasmissione del Calore Trieste*, 18-20 June 2007.

[8] Cavallini A., Mancin S., Rossetto L., Zilio C., Forced convection in enhanced surfaces: heat transfer and pressare drop measurements, *Proc. of 62° Congresso Nazionale ATI, Fisciano*, 11-14 September 2007.

[9] Cavallini A., Mancin S., Rossetto L., Zilio C., Experimental single phase air heat transfer through an aluminum metal foam, *Proc. of 8th IIR Gustav Lorentzen Conference,* Copenhagen, 1-10 September 2008.

[10] Cavallini A., Mancin S., Rossetto L., Zilio C., Air flow in aluminum foam: heat transfer and pressure drops measurements, *Proc. of the 1s^t European Conference on Microfluidics - Microfluidics 2008 - Bologna*, 10-12 December 2008.

[11] Cavallini A., Mancin S., Rossetto L., Zilio C., Heat transfer performance of aluminum foams during single phase air flow, *Proc of. Thermal Issues in Emerging Technologies, ThETA 2*, Cairo, Egypt, 17-20 December 2008.

Ringraziamenti

Dopo tutto questo inglese, i ringraziamenti li scriverò in italiano.
Giunto alla fine di questo percorso non so cosa mi riserverà il futuro, però sono molto felice di aver condiviso gran parte del mio tempo con persone speciali. Non vi sarà un ordine, né gerarchico né di importanza... dimenticherò sicuramente qualcuno ma non se ne abbia a male perché... si sa... sono fatto così, ho sempre la testa fra le nuvole...
Ringrazio tutti Voi, tutte le persone con cui ho lavorato, riso, scherzato e litigato in questi ultimi tre anni...
Professoressa Rossetto, un grazie speciale è riservato a Lei, che ha saputo guidarmi, insegnarmi, spronarmi, ringraziarmi, consigliarmi... grazie per avermi voluto ancora lì, per la stima che ripone in me e per le aspettative che spero non deludere mai!
Un grazie al professor Cavallini... per la possibilità offertami durante il primo anno a Purdue, per le parole con cui si è congratulato alla fine della presentazione e per tutte le volte che è passato in laboratorio a vedere come procedevano i lavori...
Un grazie al duo Doretti-Zilio, Zilio-Doretti che come avvocato e procuratore non sono una garanzia ma come Mentori-Amici sono imbattibili... grazie per come mi avete insegnato a fare ricerca.. se mi sono appassionato a questo lavoro è un vostro merito e un vostro regalo...
Non ho finito... grazie per essermi stati vicini e per avermi messo sempre di fronte alle mie possibilità e alle mie responsabilità... grazie per la profonda stima che sento provate per me.
Marko Matkovic, grazie per avermi fatto capire il senso più profondo della parola “Ricerca”, facendomi per primo scoprire questo mondo.... grazie per le lunghe chiacchierate giù all’impianto e grazie per avermi fatto capire che la passione oltre le capacità ti permette di spingerti sempre un po’ più avanti...
Un grazie a Davide Del Col, per avermi dato la possibilità di lavorare ad un interessante progetto europeo e per avermi portato con se all’estero affinché facessi esperienza...

Manuela... grazie per il tuo cinismo... la sincerità e la schiettezza con la quale mi hai sempre trattato e finalmente posso scriverlo: “Scusa se quella volta non sono venuto a farti sorveglianza!”...

Lorenzo.... quanti consigli mi hai dato.... tutti messi in pratica anche se non riuscirò mai raggiungere il Maestro!!!!

Un grazie a Silvano Masin che mi ha insegnato quel poco che di idraulica so e senza il quale non avrei mai costruito questo impianto... grazie anche per le risate che ci facevamo costruendolo...

Placido... che dire... grazie... per la pazienza, per il tempo che mi hai dedicato, per le soluzioni che hai trovato... per i consigli, gli scherzi e l’allegria con la quale abbiamo sempre lavorato.

Roberto, grazie per come mi hai insegnato a usare le mani per costruire qualcosa, grazie per la pazienza che avevi quando sbagliavo un pezzo o, peggio, l’attrezzo. Grazie per il tempo e il buonumore e i discorsi che abbiamo fatto. Grazie per avermi sempre consigliato nella maniera giusta e per aver costruito quasi la totalità dei pezzi da me così pazzamente pensati... magari un giorno, seguendo i tuoi consigli, progetteremo qualcosa di veramente facile e semplice da costruire e utilizzare!

Marco... insostituibile nei quadri elettrici che per rimangono oscuri per quanto tu abbia provato ad insegnarmeli.... mi dispiace dirti che hai perso tempo, ancora faccio scintille con i cavi della macchina... grazie per le perle di saggezza politico giuridica con le quali porti l’allegria in officina!

Michele... il rugby ci unisce e il basket ci divide... grazie per la priorità che mi ha sempre fatto credere di avere (tanto lo so che fai con tutti così!!!)... è certo che senza i tuoi ordini e i tuoi mandati non sarei riuscito a costruire un bel niente..

grazie per gli spunti di riflessione sulla vita che scambiamo, grazie per l’aperitivo del venerdì sera...

Franco.... grazie per la tua disponibilità e la caparbietà con la quale hai sempre trovato tutti gli articoli e le tesi che malauguratamente ti ho chiesto: devo confessarti che l’articolo in giapponese non lo nemmeno letto, non si capiva nulla...

Fabio, grazie per avermi aiutato nella costruzione dell'impianto e quelle volte i cui venivi a salvarmi dai pezzi in acciaio inox che minacciavano di cadermi addosso.
Carlo.... grazie per la tua gentilezza e disponibilità ... e per le discussioni sul rugby...
Enrico... quanti caffè a parlare del nulla... quante discussioni sulla vita, la musica, la coca-cola e le mentos....e il propano... e i trasduttori sensoriali...e churn flow...
Andrea... grazie per la parola e per i consigli... grazie per le chiacchierate di basket, windsurf, calcio....e scambio termico bifase!
Stefano Bort... è il tuo turno... è sempre piacevole stare in tua compagnia... non vedo l'ora che sia di nuovo primavera per sederci dopo pranzo dieci minuti al sole, sulla panchina...a raccontarci e consigliarci...
Stefano Schiav... tra poco sarai papà, oggi 11 gennaio 2009 ti sposi.. che dire complimenti! Grazie per le simpatiche discussioni politiche che ci siamo fatti...
Paolo.... basta con quelle formule... andiamo via che altrimenti qui ci restiamo!! Grazie per i pranzi... per le tue provocazioni e la tua arguta ironia...
Un grazie a tutti gli Amici: gli andati e i ritrovati... coloro che comunque, nel bene e nel male, ci sono sempre...
Franco, un grazie particolare lo riservo a te.... alle parole di conforto e tranquillità che sai dare... ai consigli sempre giusti...
Grazie alla mitica Via Rudena 57.... e a quelli che passano di là!!!!!!!!
Un Grazie speciale alla mia Adorata Famiglia: Mamma, Nonna, Giulia e Gigi...
Un grazie alla mia Amata: Ste.
...alla Signora Paola, al Signor Guidali (Angelo), a Gio, a Betz e a Devis...
Ecco, ho finito... di decantar le vostre lodi... miei cari che mi avete accompagnato... questa esperienza è finita... spero vogliate condividere con me la Gioia di essere riuscito a raggiungere questo obiettivo... grazie ancora a tutti Voi!